Effect of Particle Size on the Hydration Kinetics and Microstructural Development of Tricalcium Silicate

THÈSE N° 4102 (2008)

PAR

Maria Mercedes COSTOYA FERNANDEZ

Diploma of advanced studies in chemical engineering, University of Vigo, Espagne
et de nationalité espagnole

EPFL

ÉCOLE POLYTECHNIQUE
FÉDÉRALE DE LAUSANNE

Suisse
2008

ABSTRACT

Impure tricalcium silicate (Alite, C_3S) is the most important and abundant phase of Portland cement. It reacts quickly with water to give calcium hydroxide (CH) and calcium silicate hydrate (C-S-H) which is the most important phase for strength development. It is well known that the C_3S particle size distribution plays an important role on the hydration kinetics, microstructural development and final properties of hydrated cement pastes.

The general aim of the present investigation was to gain insight on the effect of particle size on the hydration kinetics and microstructural development of alite pastes. In this study, alite was synthesized and separated into different gradations. The hydration kinetics was investigated by means of isothermal calorimetry and chemical shrinkage. The microstructural developments of the different gradations of alite were studied and compared using different techniques such as: SEM, TEM, XRD, He pycnometry, N_2 adsorption, etc.

The hydration kinetics during the different stages of the hydration was observed to be dependent on the initial particle size of the grains and also related with the defect concentration on the surface of the grains. Higher rates of reaction were observed for powders with higher specific surface area. A linear relationship between the rate constant and the specific surface area was observed. Further, it was observed that the hydration kinetics of multi-sized system during the nucleation and growth process can be modeled as the linear addition of individual particles. The microstructural development of C_3S pastes at later ages was found to be poorly affected by the initial particle size; the nature of the hydration products is the same. The only differences concern the capillary porosity and the C-S-H density. Slightly higher values of capillary porosity and C-S-H density were measured for smaller particles. The most likely explanation can be related with a different initial arrangement of the grains.

Keywords: Synthesis; Ca_3SiO_5; Particle size; Hydration Kinetics; Microstructure; C-S-H

RÉSUMÉ

Le silicate tricalcique impur, appelé également alite, est la phase la plus abondante du ciment Portland. Cette phase réagit rapidement avec l'eau pour former du silicate de calcium hydraté (C-S-H), la phase la plus importante pour le développement en résistance, et l'hydroxyde de calcium (CH). Des travaux antérieurs ont montré que la distribution de taille des particules de C_3S joue un rôle important dans la cinétique d'hydratation et le développement microstructural conduisant aux propriétés finales des pâtes de ciment.

L'objectif général de ce travail était de qualifier l'effet de la taille des particules sur la cinétique d'hydratation et sur le développement microstructural des pâtes d'alite. Dans cette étude, l'alite a été synthétisée et séparée en différentes fractions. La calorimétrie isotherme et le retrait chimique ont permis d'établir la cinétique d'hydratation. Les développements microstructuraux des pâtes composées de différentes fractions d'alite ont été étudiés et comparés en utilisant différentes techniques telles que le MEB, le MET, la DX, la pycnométrie à hélium et l'adsorption d'azote.

Au cours de l'hydratation, il a été observé que les cinétiques dépendaient de la taille initiale des grains de C_3S, mais également de la concentration des défauts à leur surface. Des taux de réaction plus élevés ont été observés pour les poudres à plus grande surface spécifique. Une relation linéaire a été établie entre la constante du taux de réaction et la surface spécifique dans le régime de germination-croissance. En outre, il a été constaté que la cinétique de l'hydratation des systèmes de taille multiple peut être modélisée par l'addition linéaire de la cinétique d'hydratation des particules individuelles. Il a été montré que la taille initiale des particules a peu d'effet sur le développement microstructural des pâtes de C_3S d'âges avancés et que la nature des produits d'hydratation est la même. De légères différences ont toutefois été trouvées dans la porosité capillaire et la densité du C-S-H.

Mots-clés: synthèse; Ca_3SiO_5; taille de particules; cinétique d'hydratation; microstructure; C-S-H.

_____

ZUSAMMENFASSUNG

Unreines Tricalcium Silikat, auch Alit genannt, ist die häufigste Phase in Portland Zement. Es reagiert schnell mit Wasser und bildet zu Calcium Silikat Hydrat (C-S-H), welches hauptverantwortlich für die Festigkeitsentwicklung ist , und Calcium Hydroxide (CH). Es ist bekannt, dass die Korngrössenverteilung von C_3S einen wichtigen Einfluss auf die mikrostrukturelle Entwicklung und damit auf die Endeigenschaften der hydratisierten Zementpasten hat.

Das Hauptziel der vorliegenden Arbeit bestand darin, den Effekt der Korngrösse auf die Hydratationskinetik und die mikrostrukturelle Entwicklung von Alit-Pasten zu beschreiben. Alit wurde für diese Studie synthetisiert und in verschiedene Fraktionen aufgeteilt. Die Hydratationskinetik wurde mittels isothermaler Kalorimetrie und Messungen des chemischen Schwindens untersucht. Die mikrostrukturelle Entwicklung der Pasten (bestehend aus verschiedenen Alit-Fraktionen), wurde mittels verschiedenen Techniken wie REM, TEM, XRD, Helium-Pycnometrie und Stickstoff-Adsorption untersucht und verglichen.

Es wurde beobachtet, dass die Kinetik während der unterschiedlichen Hydratationsphasen von der Partikelgrösse und den Defekten an den Kornoberflächen abhängt. Die Reaktionsrate nimmt mit der spezifischen Oberfläche der Körner zu. Zwischen der Reaktionskonstante und der spezifischen Oberfläche wurde ein linearer Zusammenhang während der Nukleations- und Wachstumsphase beobachtet. Die Hydratations-Kinetik von Systemen welche aus mehreren Korngrössen bestehen, kann mittels gewichteter Summe der einzelnen Partikelgrössen modelliert werden. Es konnte gezeigt werden, dass die Korngrösse kaum Einfluss auf die spätere mikrostrukturelle Entwicklung von C_3S Pasten hat, da die Hydratationsprodukte unverändert bleiben. Kleine Unterschiede wurden einzig bei Kapillarporosität und Dichte der C-S-H Phasen festgestellt.

Schlüsselwörter: Synthese; Ca_3SiO_5; Partikelgrösse, Hydratationskinetik, Mikrostruktur, C-S-H

ACKNOWLEDGEMENTS

TABLE OF CONTENTS

GLOSSARY

Abbreviations of tricalcium silicate (C_3S) used in this study

C: CaO

S: SiO_2

H: H_2O

Pure C_3S: triclinic polymorph (TI)

Alite: monoclinic polymorph (MIII)

PSD: particle size distribution

w/c: water/cement ratio

XRD: x-ray diffraction

IC: isothermal calorimetry

SEM: scanning electron microscopy

SEM-IA: scanning electron microscopy-image analysis

SE: secondary electron

BSE: backscattered electron

BSE-IA: backscattered electron-image analysis

EDS: energy dispersive spectroscope

TEM: transmission electron microscopy

Ch.Sh: chemical shrinkage

TGA: thermogravimetric analysis

NMR: nuclear magnetic resonance

OPC: ordinary Portland cement

C-S-H: calcium silicate hydrates

CH: portlandite/calcium hydroxide

CHAPTER 1: INTRODUCTION

1.1 Background

Over the past few decades, several computer models have been developed to simulate the cement microstructure during hydration using various approaches. There are many factors which influence the hydration that have been considered to be key points in the development of a model. For example, the morphology of the hydration product layer, the effect of particle characteristics, whether the mechanism of hydration product formation is topochemical or through-solution. A literature review for the different theories is presented in [1].

It is well known that the initial particle size of the powder has an important impact on the hydration kinetics, microstructure and its final properties [2-7]. Nevertheless, there are only a limited number of models based on the effect of the particle size distribution and, in most of them, the hydration kinetics are investigated by means of surface area rather than individual particles. This is because it is very difficult to separate the powder into very narrow particle size distributions. The effects of particle size, distribution, composition, shape and texture however, are important parameters that should be taken into account.

The effect of particle size and their interaction with other components has been considered in the development of a new model (***µic***) that has been recently developed at EPFL to simulate the microstructural development of cementitious materials [8]. This model, and others like it, needs to be validated against experiment results with model cementitious systems before they can be used as predictive tools to reduce experimental work.

1.2 Objectives and Scopes of this Study

The investigation of Ordinary Portland Cement (OPC) hydration is very complex due to the simultaneous and different nature of the chemical reactions that take place. Although tricalcium silicate (C_3S) does not represent the hydration of OPC due to differences in its composition and final properties, it can be used as first approach to simplify the investigation of the hydration kinetics.

This thesis aims to gain insight into the differences that the initial particle size has on the hydration kinetics and microstructural development of C_3S. To do so, tricalcium silicate has been synthesized and fractionated in different narrow particle size distributions. The hydration kinetics of the different stages of the hydration, both at early and later ages, were investigated by the combination of several techniques such as isothermal calorimetry (IC), chemical shrinkage (Ch.Shr) and backscattered electron image analysis (BSE/IA)

Some of the main open questions that will be answered in this work are the following:

- Why does the reaction slow down after the dissolution peak?
- What brings the induction period to an end?
- What are the reaction kinetics during the nucleation and growth process?
- What is the mechanism that governs the hydration at later ages?
- What is the influence of particle size on hydration kinetics?
- What is the influence of the initial particle size on the microstructural evolution of C_3S pastes?
- Does the initial particle size have an influence on the formation of the hydration products?

Furthermore, the experiments concerning the kinetics and the microstructural development of tricalcium silicate hydration have been performed for the future development and validation of $\boldsymbol{\mu ic}$.

1.3 Outline of the Thesis

This thesis consists of six chapters and three appendices.

Chapter 2 describes the synthesis protocols, the characterization, and the separation into different particle size distributions for the alite and the pure C_3S used during this investigation. Furthermore, it explains the role that ions like Al and Mg play on the grain growth.

Chapter 3 gives a review of the literature on hydration kinetics of tricalcium silicate. It presents the key points and the most controversial aspects, details the techniques and the measurement protocols developed in this investigation, and presents the results on the influence of the particle size on the different stages of hydration: dissolution, induction period, nucleation and growth and later period. The investigation of the hydration kinetics was done by isothermal calorimetry for the first 24 hours after mixing and chemical shrinkage and backscattered electron image analysis-BSE/IA to examine later age hydration kinetics.

Chapter 4 describes the role that the initial powder particle size has on the microstructural development of C_3S pastes. Qualitative and quantitative analysis of the microstructural development during hydration was investigated by scanning electron microscopy (SEM) together with thermogravimetric analysis (TGA), helium pycnometry. Important key points in the investigation of the microstructure such as the degree of hydration, porosity, and density of the products the products are detailed in this chapter.

Chapter 5 gives a detailed characterization of C-S-H, the most important binding phase in the hydration of C_3S. The morphology (SEM), chemical composition as measured by EDS analysis in the SEM, and the chemically bound water in C-S-H as calculated from thermogravimetric analysis are presented. The pore size characterization of C-S-H was done by nitrogen adsorption.

Chapter 6 presents a discussion of the most important findings of this work, summarizes the most important conclusions and proposes future work in this area of research.

REFERENCES

[1] Menashi D. Cohen, Ruben D. Cohen, Modelling of the hydraiton of tricalcium silicate. Journal of materials science 23 (1988) pp. 2816-3820

[2] Tenoutasse N. and De Donder A., Silicates Industriels, 35, (1970). pp. 301

[3] G. Frigioine, S. Marra, Relationship between particle size distribution and compressible strength in Portland cement, Cement and Concrete Research 6 (1976) pp. 113-128

[4] T. Knudsen, The dispersion model for hydration of Portland cement. I. General concepts, Cement and Concrete Research 14 (1984) pp. 622- 630

[5] Scrivener, K.L. Development of Microstructure during the Hydration of Portland cement, Ph. D Thesis University of London (1984)

[6] J.M. Pommersheim, Effect of particle size distribution on hydration kinetics, in Materials Research Society Symposium Proceedings 85, L.J. Struble and P.W. Brown (EDS.) Materials Research Society, Pittsburgh (1987) pp. 301-306

[7] Dale P. Bentz, Edward J. Garboczi, Claus J. Haecker and Ole M. Jensen, Effects of cement particle size distribution on performace properties of Portland cement-based materials, Cement and Concrete Research 29 (1999) pp. 1663-1671

[8] Shashank Bishnoi, Vector modelling of hydrating cement microstructure and kinetics, Ph. D Thesis École Polytechnique Fédéral de Lausanne (2008)

CHAPTER 2: SYNTHESIS OF PURE PHASES

This Chapter describe the synthesis protocols of the pure phases necessary for the hydration study and their characterization, and their separation into different gradations to investigate the reaction rates of individual particles.

2.1 Polymorphism of Tricalcium Silicate

Tricalcium silicate exhibits 7 different polymorphs depending on the sintering temperature or the impurities added for the synthesis [1-4]: three triclinic, three monoclinic and one trigonal; where the letters indicate the formal crystallographic symmetry and the numbers designate variants of a particular symmetry. The phase transformations are recapitulated below:

$$T1 \xleftrightarrow{\ 620^oC\ } T2 \xleftrightarrow{\ 920^oC\ } T3 \xleftrightarrow{\ 980^oC\ } M1 \xleftrightarrow{\ 990^oC\ } M2 \xleftrightarrow{\ 1060^oC\ } M3 \xleftrightarrow{\ 1070^oC\ } R$$

The transformation sequence is at least partially reversible when cooling: optical data supports the existence of two triclinic forms between 620 and 980ºC and two other monoclinic forms between 980 and 1070ºC [4].

Impurities play an important role on the phase transformations: they do not only influence the sequence of phase transformations but they also help stabilize Ca_3SiO_5 itself [4]. The impurities play a dual role: they are partly responsible for the stability of Ca_3SiO_5 in clinker at room temperature and they have a strong influence on which alite polymorph is obtained when sintering. It has been reported [4] that even the R phase can be preserved and stabilised at room temperature, although it appears that in most clinkers,

alite is in fact a mixture of polymorphs with some individual crystals being sometimes zoned. The close structural similarity of all these polymorphs justifies the use of the collective term "alite" to describe the family of phases closely related to R-Ca_3SiO_5 (M, T and other variants).

Depending on the impurities, only certain polymorphs can be stabilised at room temperature such as M1 and M3 , a mixture of them or T2 [4 and16]. The triclinic, monoclinic and trigonal structure of C_3S can be contained in OPC, the monoclinic form being normally predominant [1]. The most common doping ions for the synthesis of tricalcium silicate are Al^{3+}, Mg^{2+} and Fe^{3+} with smaller amounts of K^+, Na^+ and SO_3. The limits of substitution of those ions in C_3S have been reported by Hahn et al. [10]. In the case of MgO (Ca^{2+} are substituted by Mg^{2+}), the limit is 2.0% at 1550ºC and decreases with temperature to 1.5% at 1420ºC. For Al_2O_3, the limit found is 1.0%, for all temperatures and the substitution is partly of 2 Al^{3+} for $Ca^{2+}+Si^{4+}$ and partly of 4 Al^{3+} for 3 Si^{4+} and a vacant octahedral site. For Fe_2O_3, the limit is 1.1%, and substitution was of 2 Fe^{3+} for $Ca^{2+}+Si^{4+}$. It was also concluded that the limit of substitution for MgO was not affected by the incorporation of Al^{3+} or Fe^{3+} or both, nor vice versa, but Al^{3+} and Fe^{3+} competed for the same sites and the limit for one was decreased in the presence of the other. More recently a study on substitution limits was published by Stephan and is summarised in Table 2.1 [17].

The complex polymorphism of C_3S introduces problems of quantitative phase analysis of clinkers by X-ray diffraction. The diffracted energy of a single reflection in the R phase is split into several closely spaced reflections in the lower-symmetry phases, and the extent to which these reflections overlap those of the belite phase tends to increase as the symmetry of the C_3S decreases. Minor shifts in atomic positions within the lower-symmetry alite phases alter the absolute reflection intensities, making it difficult to secure satisfactory calibration; the usual assumption which is made- that the multiple reflections contain the same total diffracted energy as the associated single R reflection- remains unproven [4].

Table 2.1: Modification of C_3S with foreign oxides and type of substitution [17]. Data given in wt.%.(∗ The limit of substitution depend on the temperature of synthesis)

Modification	Fe_2O_3	Al_2O_3	MgO (1500 °C)∗
T I	0–0.9	0–0.45	0–0.55
T II	0.9–1.1	0.45–1.0	0.55–1.45
M I			1.45–2.0
M II			>1.2
Type of substitution	2 Fe for 1 Ca + 1 Si	Al for Ca, Si and hole	1 Mg for 1 Ca

2.2 Protocol Development for the Synthesis of Pure Phases

2.2.1 Synthesis of Pure Tricalcium Silicate.

Conventional preparation of pure tricalcium silicate (pure C_3S) [5,6,19,20] requires long resident times (about 10 hours) at high sintering temperatures ($\sim$1600ºC) due to the low ion diffusion rates for solid-state reactions.

Pure triclinic silicate, (Ca_3SiO_5, C_3S), was prepared from a 1:3 stoichiometric mixture of high purity quartz powder and $CaCO_3$ (both Merck). After homogenizing a water suspension of these materials, the blend was first dried at 100°C during 24h. The dried mass was then pressed into pellets of 3.5 cm in diameter. The pellets were then heated at 1650°C for 10h an electric furnace and cooled rapidly on a platinum dish according to the firing cycle in Figure 2.1. This procedure was repeated until no reflections due to free lime could be observed by X-ray diffraction. The reburning process was done without regrinding the pellets. As shown §2.2.2.2 no significant differences were found in means of particle sizes by regrinding the pellets before every reburning cycle.
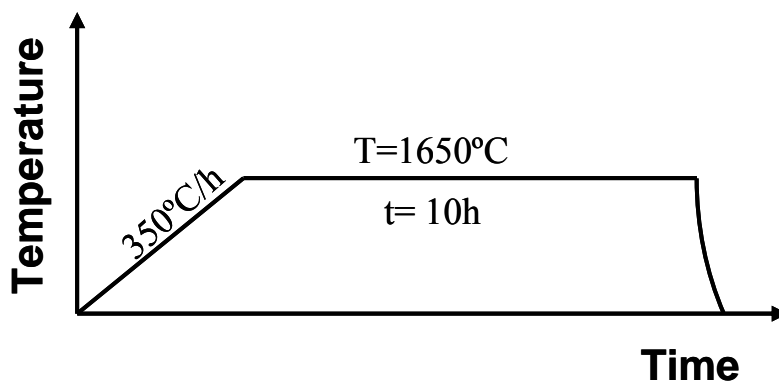
Figure 2.1: Cycle used for pure C_3S synthesis

The product resulting from this process was identified using X-ray diffraction as the triclinic T1 form (Figure 2.2) [15].
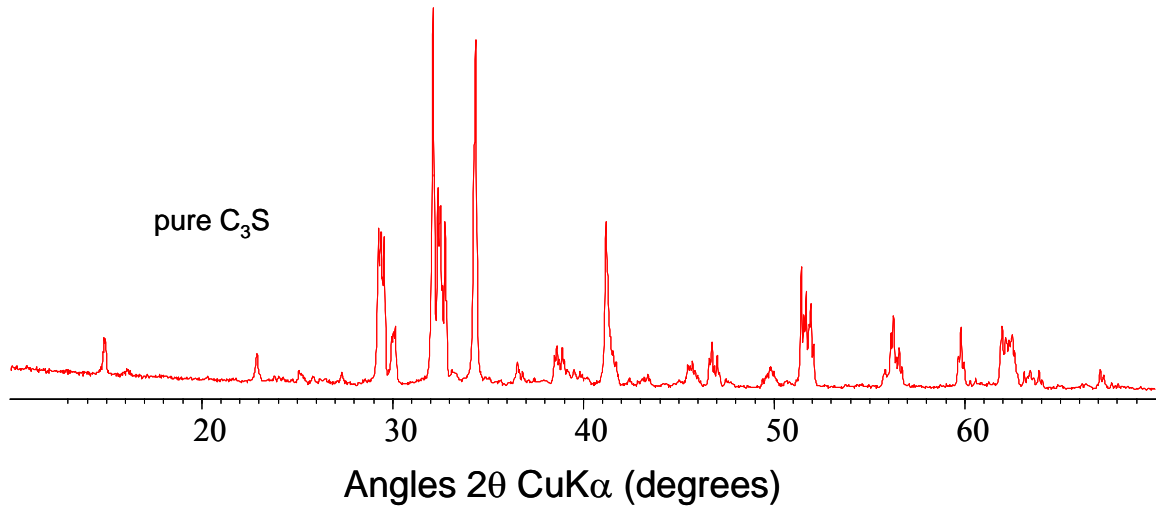
pure C_3S

Figure 2.2 : XRD of pure C_3S (polymorph T1)

The free lime content was determined by both Rietveld analysis and chemical analysis after dissolving in ethanol-glycerin [18]. It was found to be less than 0.5%.

To break agglomerates of C_3S crystals that are formed in this solid state synthesis 45 minutes of mechanical grinding with an automatic mortar grinder followed by 12 hours of ball milling with a turbula powder blender (0.5 cm zirconium balls) was done. The morphology of the grains was characterized by backscattered electron imaging of polished cross sections of the powder before and after grinding. Figure 2.3 shows the morphology of the C_3S powder. The clusters of C_3S crystals formed during the sintering process are detailed.
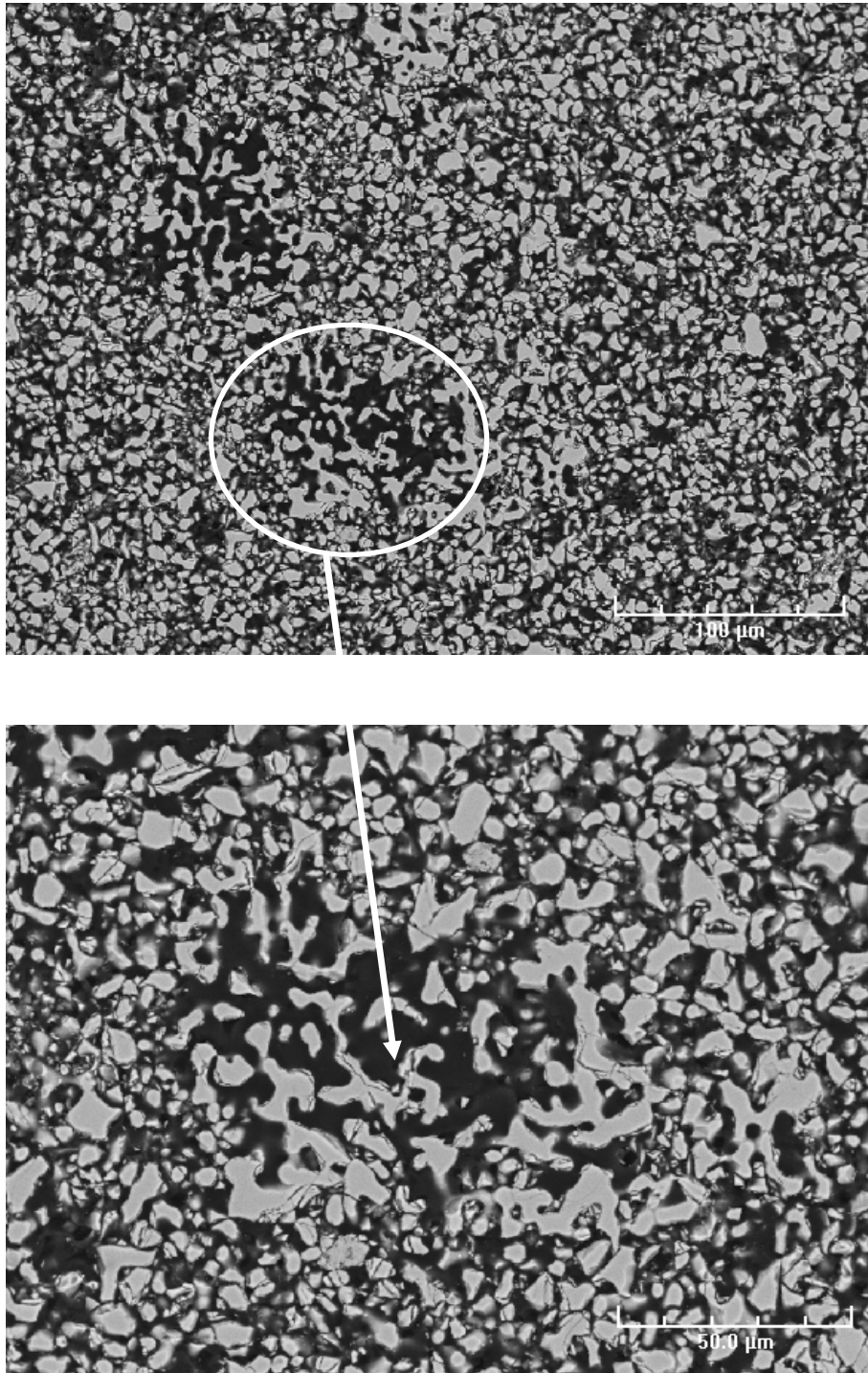
Figure 2.3: BSE images of the synthesized pure C$_3$S before grinding showing agglomerates
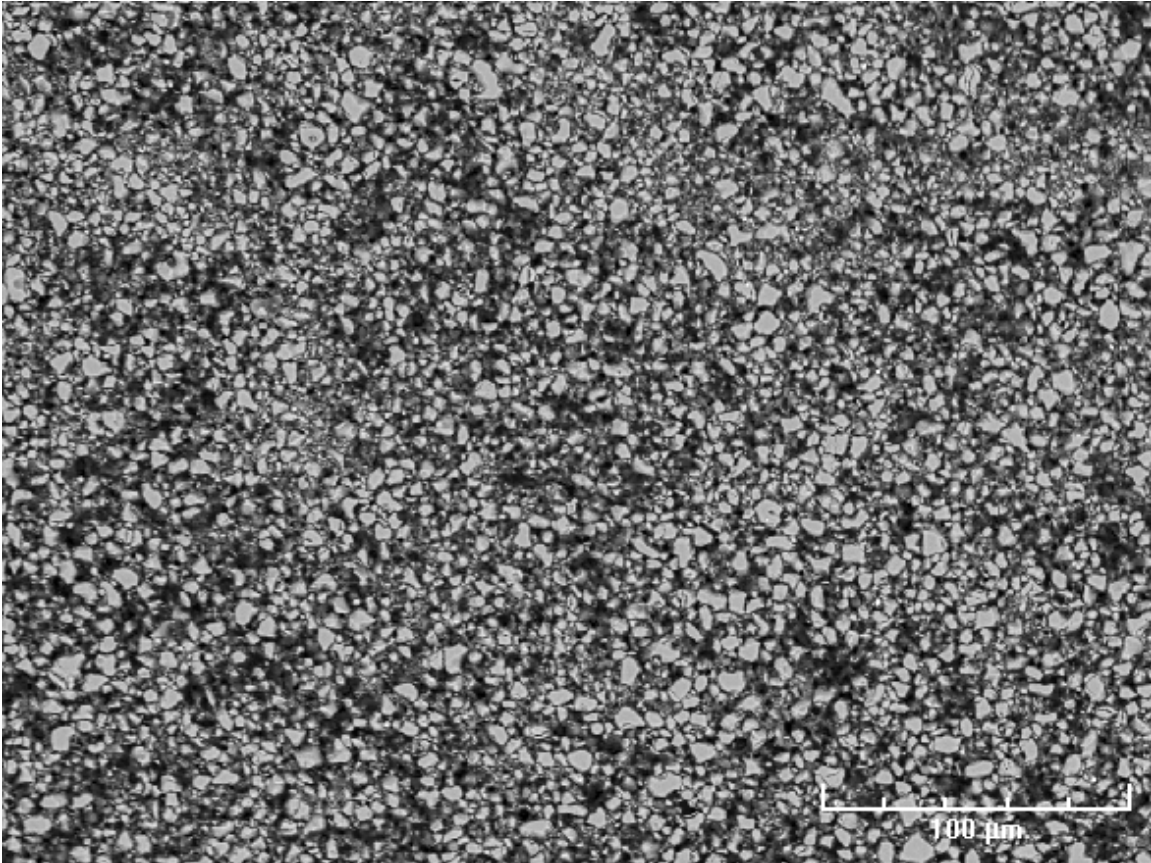
Figure 2.3.b: BSE images of synthesized pure C$_3$S after 12 hours ball milling

The particle size distribution of the powder was measured by laser granulometry analysis (Mastersizer 2000, Malvern Instruments Inc.) using isopropanol as dispersant and ultrasound to disagglomerate the particles before the measurement. Figure 2.4 shows the particle size distribution obtained for the synthesized powder compared with that of typical OPC. Pure C$_3$S particle size distribution presents 2 main particle size populations: one around 0.5 µm and the bigger at 6 µm. The particles size obtained from this synthesis protocol range between 0.1 and 30 µm, too small to compare with the psd of OPC.

In order to obtain a particle size distribution closer to that of OPC, a new synthesis protocol adding Al and Mg ions was developed and is described in the next section.
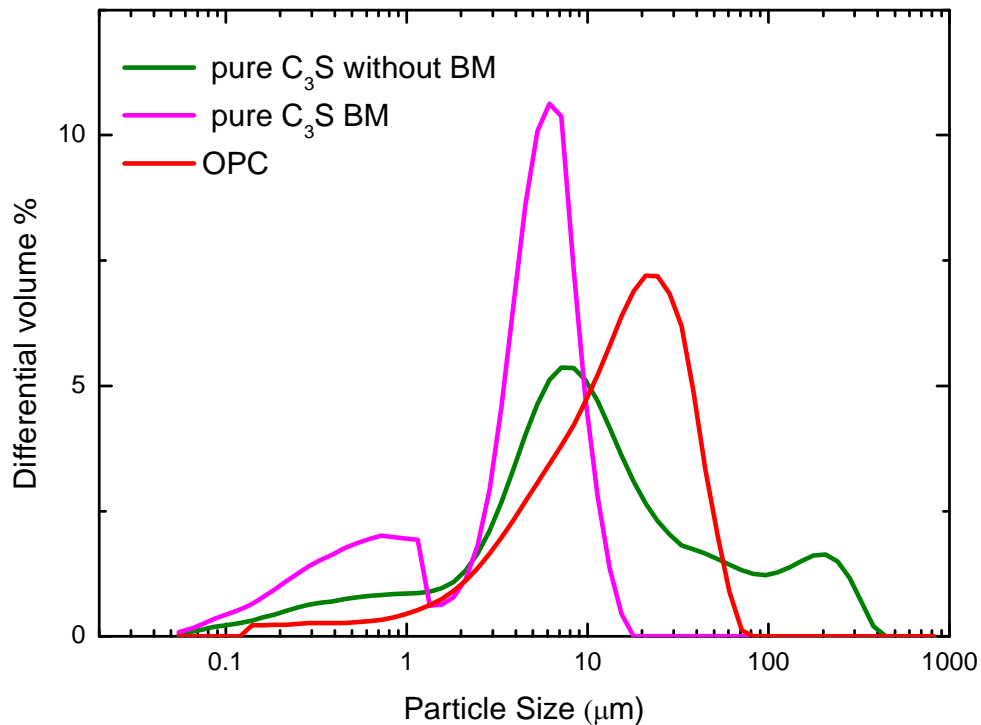
Figure 2.4: Particle size distribution of pure C$_3$S compared with OPC (BM: ball milling)

2.2.2 Synthesis of Alite.

The reason for adding Al and Mg to the blends lies in the nucleation and grain growth processes: small amounts of magnesium ions increase the quantity of the liquid phase and decrease the viscosity of the mix [9], which allows a better diffusion of the chemical species and favours the growth of larger grains compared to pure C$_3$S. Mg ions improve the burnability of the blend and favour the reduction of free lime [9]. In addition, Ca^{2+} is substituted by Mg^{2+} in the lattice and the combination of Al and Mg ions stabilise the T1, T2 and M3 polymorphs at room temperature [10]. Skibsted and al. [11] reported the first direct evidence for guest ions substitution in alite and belite by the observation of Al substitution using ^{27}Al magic-angle spinning (MAS) NMR. They concluded that for the case of both minerals Al^{3+} preferentially substitutes Si^{4+} sites.

The alite phase was prepared by mixing calcium carbonate (CaCO$_3$), silica dioxide (SiO$_2$), aluminum oxide (Al$_2$O$_3$) and magnesium oxide (MgO) (all from Merck) with the molar ratios that are given in table 2.2. Three blends were prepared in order to assess the

influence of Al and Mg ions on particle growth, size and composition. The mixture preparation was the same as for pure tricalcium silicate synthesis.

Table 2.2: Molar ratio composition of the synthesized powders

Molar Ratio	C1	C2	C3
CaO	3	2.92	3
SiO_2	0.88	0.97	0.88
Al_2O_3	0.05	0.02	0
MgO	0.05	0.11	0.06

2.2.2.1 Influence of the temperature on the grain growth

The influence of the temperature on the grain growth was studied on the second composition, C2, at temperatures of 1450ºC and 1500ºC. Figure 2.5 shows that small variations of temperature have a large impact on the grain growth : higher temperatures allow a more efficient migration of the ions to the interstitial sites and therefore a faster grain growth. Since the aim is to increase the size of the alite grain, the higher temperature was selected for the synthesis.
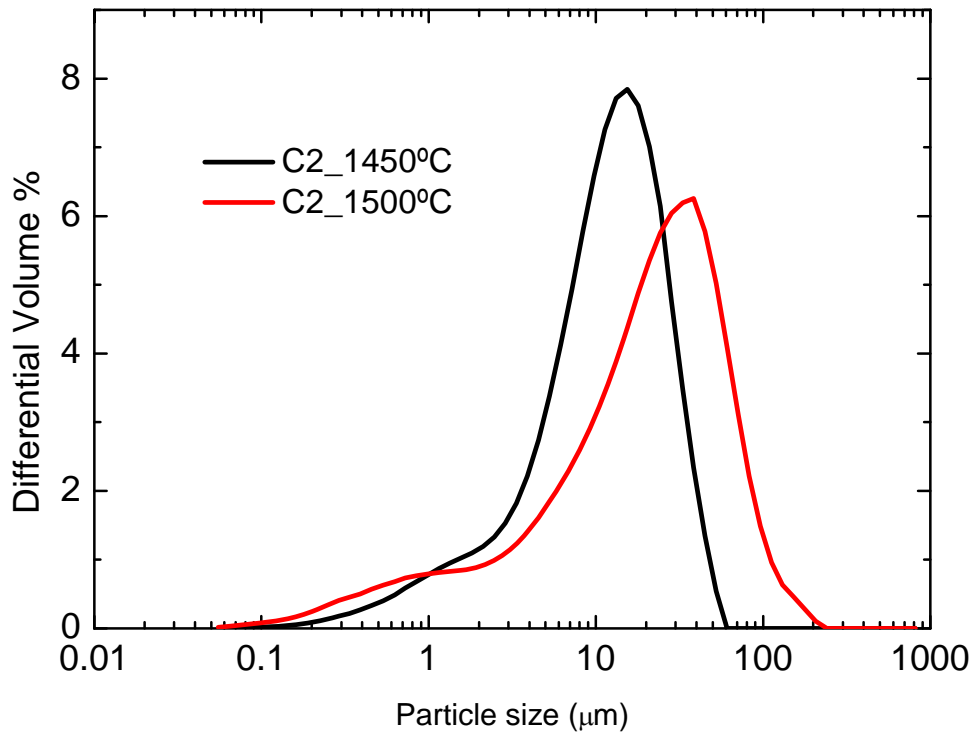
Figure 2.5: Effect of the burning temperature on the grain growth

2.2.2.2 Influence of grinding between clinkering cycles

The influence of grinding the material between each thermal clinkering cycle was investigated with alite C1. Two identical pellets were fired three times, one being ground between each thermal circle while the other was ground after the 3rd cycle only. In both cases the pellets were fired at 1450ºC and ground 1h of mechanically grinding followed by 5 min by hand in a mortar. As reflected in Figure 2.6 no significant differences in means of particle sizes were found.
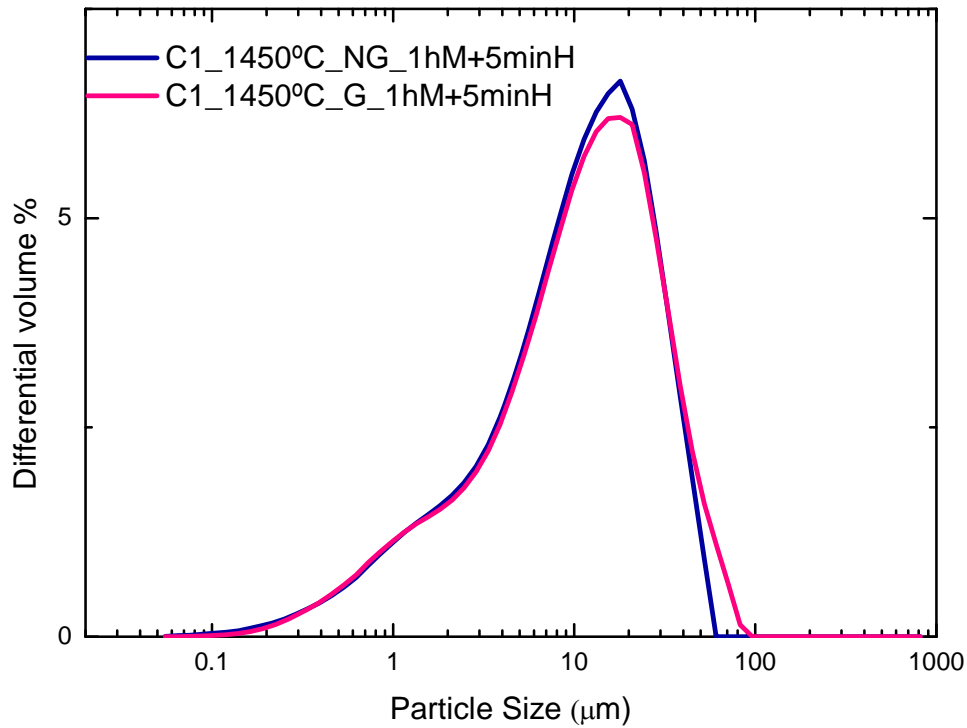
Figure 2.6: Influence of the grinding between each cycle of temperature (M: mechanical grinding, H: hand mixing in a mortar, G: grounded and NG: not grounded)

2.2.2.3 Effect of Al and Mg ions on the grain growth

The following step of the study was to investigate the effect of Al and Mg ions on the alite grain growth. To do so, the different compositions shown in Table 2.2 were fired at 1500ºC and then ground using the same protocol. Figure 2.7 shows the particle size distribution of the synthesized powders.
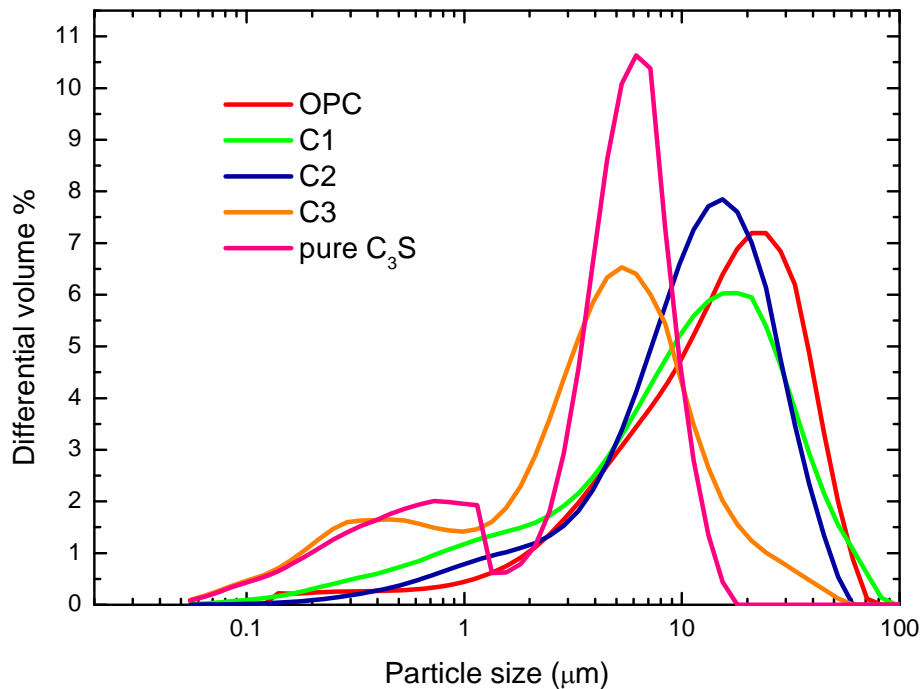
Figure 2.7: PSDs of different wt % compositions of Mg and Al ions

The C1 and C2 compositions containing Al ions present bigger particle size compared to C3. Subsequently, it can be concluded that the Al ions plays the major role on the grain growth. Al ions coordinate themselves in the lattice and increase the quantity of liquid phase while decreasing its viscosity, allowing a better diffusion of the chemical species and favoring the grain growth [12]. Despite the fact that aluminium has a major influence on the growth of the grains, the Mg ions help to decrease the viscosity of the liquid which favors the mass diffusion and decreases the final C_3A content of the samples [13]. MgO catalyze the dissolution reaction of C_3A in the liquid phase, which hinders C_3A formation and promotes the presence of Al^{3+} ions as interstitial in C_3S. Moreover MgO helps to reduce the CaO percentage in the liquid phase by improving the combination of free lime [9].

The polymorph identification was made by X-ray diffraction based on the paper written by Courtial [14]. The XRD patterns of the three powders synthesized in the same conditions (Temperature: 1500ºC;3F: 3 times fired; NG: not-ground between cycles) are presented in Figure 2.8.
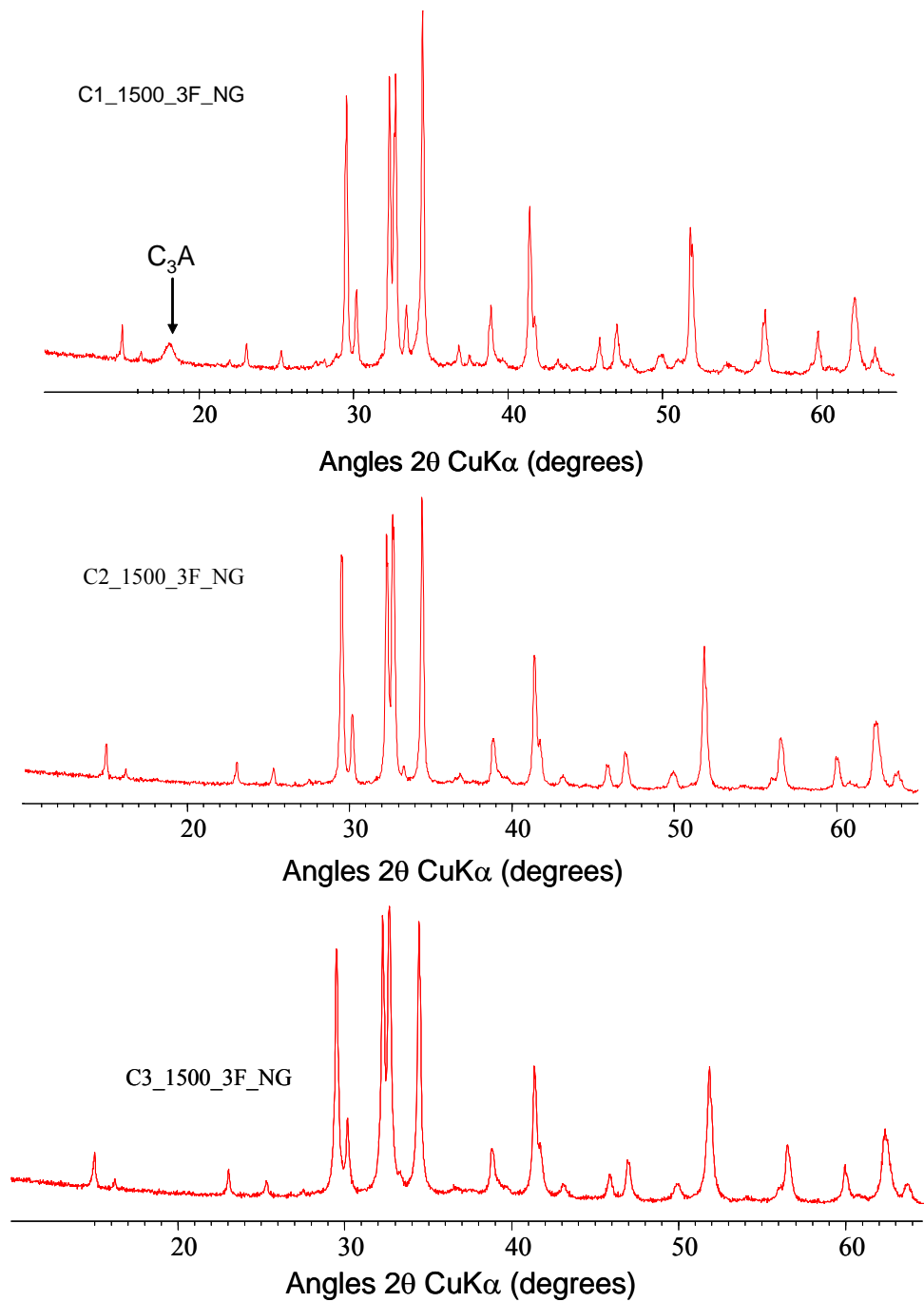
Figure 2.8: XRD for powders of compositions C1, C2 and C3 fired at 1500ºC

The X-ray diffraction patterns look very similar, but the use of five angular windows in the diffraction patterns is sufficient to discriminate them as reported in [14] (Figure 2.9). The five angular windows (W1-5) needed for the identification of the polymorphs M1, M2 and M3 are shown in Figure 2.10 (left). The difference between the M1 and M3 polymorphs becomes evident when looking at the W3 and W5 angular windows. However these windows are not able to assess the presence of an eventual superstructure. The only significant difference discriminating the diffraction patterns of M1 and M2 alites lies in W3 (second peak).

The M1 and the M3 structures can be identified by inspection of W1,W2 and W4. Several Bragg lines characteristic of the presence or the lack of superstructure appear in these windows. The second peak of the doublet W1 is characteristic of the M1 structure. The same applies in W2 and W4 [14].

The synthesized powders (C1, C2 and C3) were analyzed by X-ray diffraction using the following conditions:

- $2\theta = 10°$ to $60°$
- Interval step of $0.017°$
- Active length of 120s
- Active length (2θ) of $2.122°$

Figure 2.10 (right) shows the X-ray diffraction patterns produced from the different powders for the five angular windows. From the analysis of their angular windows compositions C1 and C2 were identified as polymorph M3 and composition C3 is polymorph M2.
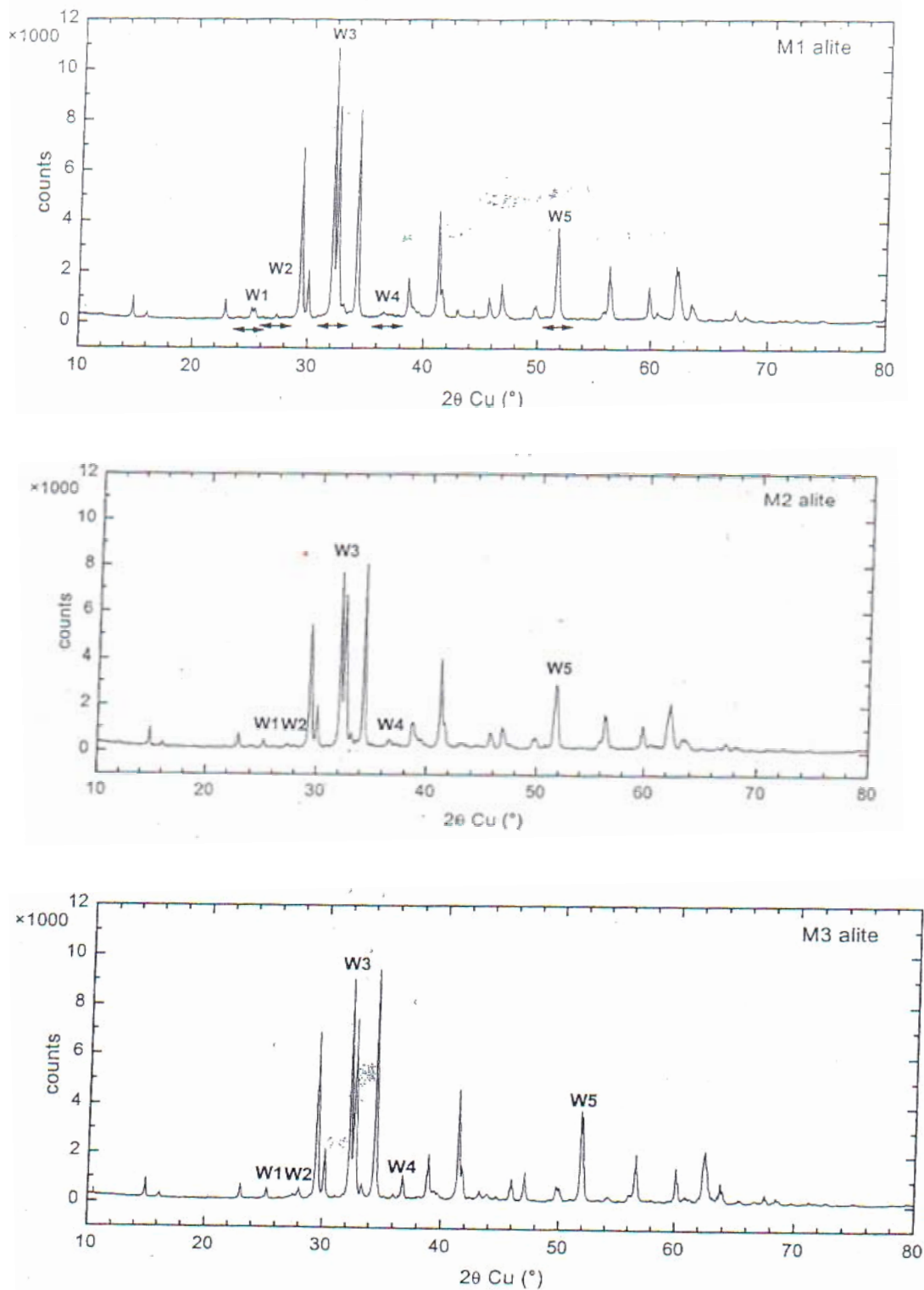
Figure 2.9: Powder X-ray diffraction patterns of three synthetic alites M1, M2, AND M3 [14]
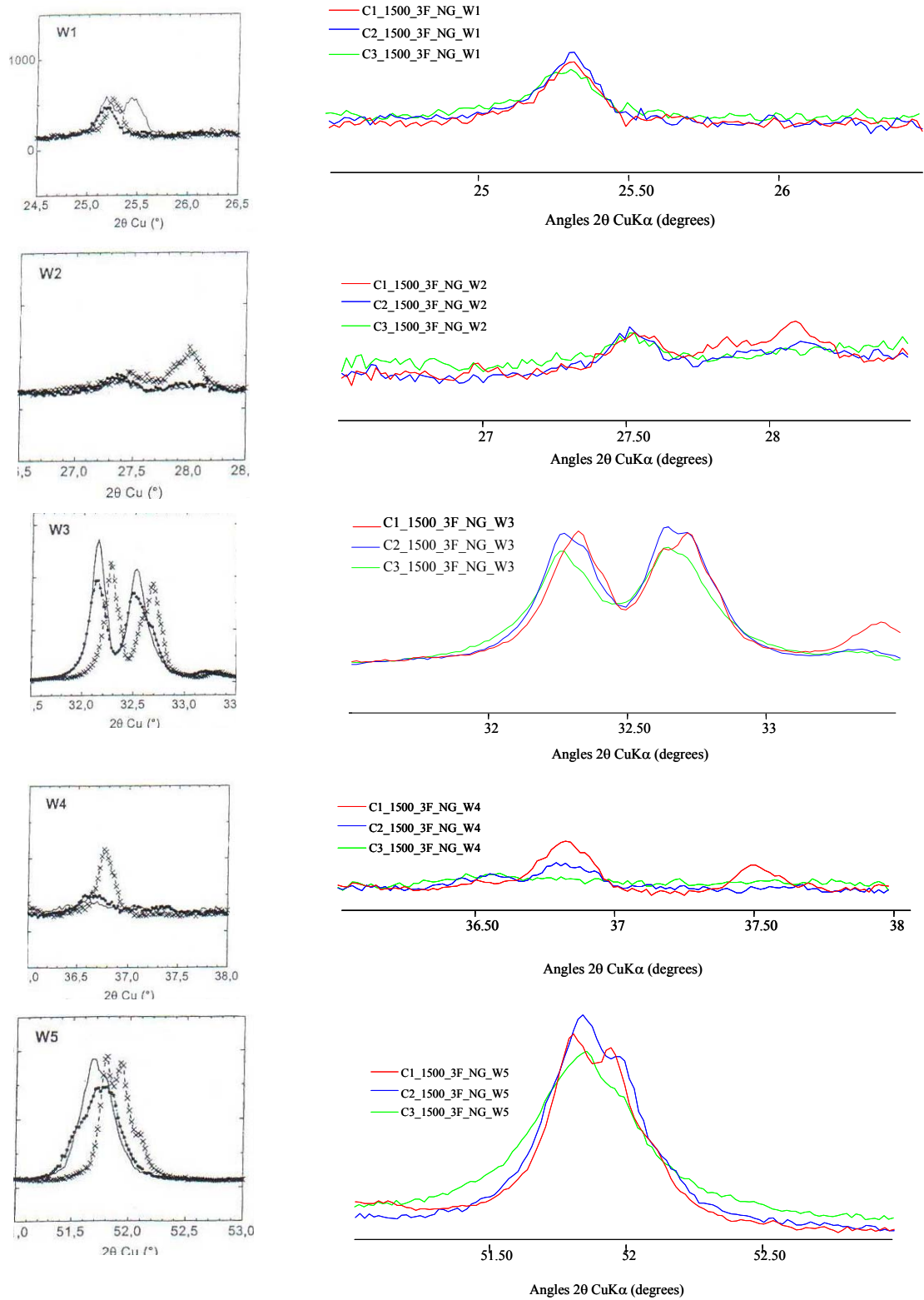
Figure 2.10: The five angular windows (W1,W2,W3,W4,W5) used for the identification of the alite M1, M2 and M3 polymorphs [14] (left) and the five angular windows for the 3 synthesized powders C1, C2 and C3 (right)

Rietveld refinement was used to quantify the % wt. of C_3S, C_3A and CaO in the final products. Figure 2.11. Table 2.3 detail the weight percentages of C_3S, C_3A and free lime for the different sintesized alites.

- ■ C_3S_M3 94.80 %
- ■ C_3A_cubic 4.86 %
- ■ CaO 0.35 %

Angles 2θ CuKα (degrees)

- ■ C_3S_M3 100.00 %
- ■ C_3A_cubic 0.00 %
- ■ CaO 0.00 %

Angles 2θ CuKα (degrees)

- ■ C_3S_M3 100.00 %
- ■ CaO 0.00 %

Angles 2θ CuKα (degrees)
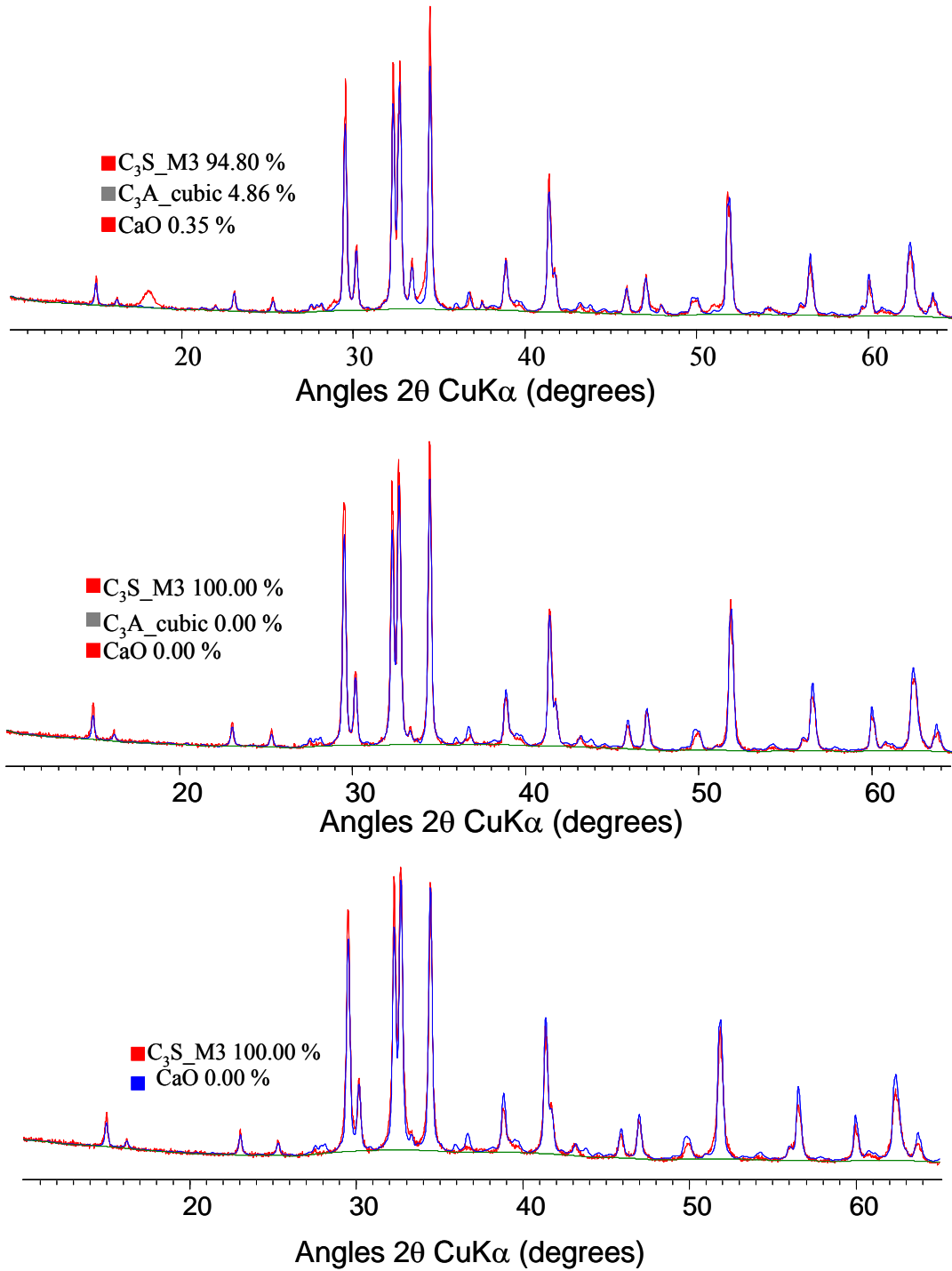
Figure 2.11: Rietveld analysis for Alite of compositions C1 (top), C2 (middle) and C3(bottom)

Table 2.3: Weight percentages of C_3S, C_3A and CaO in the different alite compositions

wt. %	Alite-C1	Alite-C2	Alite-C3
C_3S_M3	94.80	100	100
C_3A	4.86	0	0
CaO	0.35	0	0

Based on XRD characterization and Laser Granulometry Analysis, C2 (1% Al_2O_3 and 2% MgO) was selected for its purity (no traces of C_3A or CaO were found) and closest psd compared to OPC for hydration kinetics study. Both C_3A and CaO react very quickly with water and their presence would cause an acceleration of the kinetics. The similarity in morphology of alite-C2 and OPC was also observed by backscattered electron imaging of the powder (Figures 2.12 and 2.13).

Rietveld analysis of alite-C1 showed a high C_3A content (around 3%wt) and the analysis of the particle size distribution of alite-C3 showed very small crystallites compared with OPC.
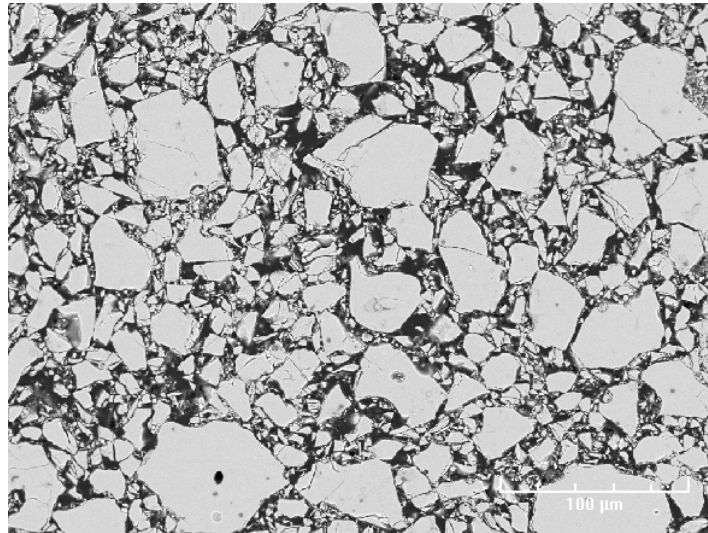
Figure 2.12: Synthesized Alite-C2. SEM image (800x,BSE)
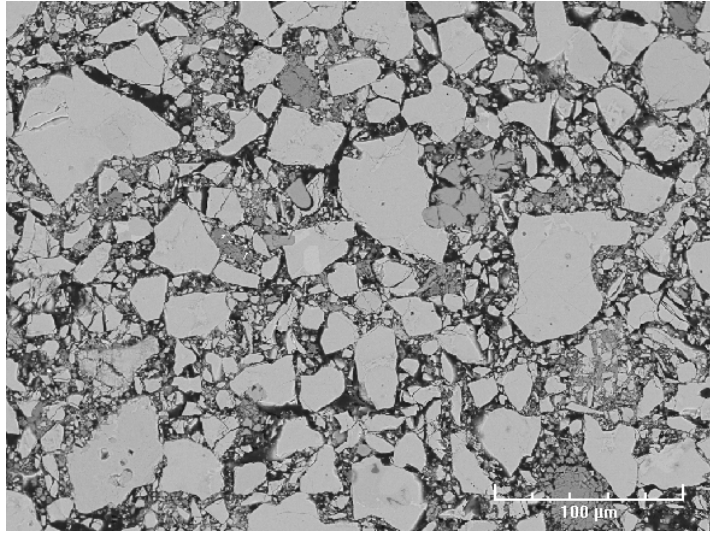
Figure 2.13: OPC. SEM image (800x,BSE)

2.3 Separation of Alite Powder into Different Particle Size Distributions

Two methods were used to separate the alite-C2 into different particle size distributions needed for the hydration studies.

The first method employed was sieving for separating the biggest particles. Consecutive sieves of 100, 71, 50, 36 and 25 μm were used to obtain the different narrow particle size distributions represented in Figure 2.14.

The smaller fractions were then decanted using isopropanol as dispersant matrix (Figure 2.15). Equal amounts (100 g) of powder were used for the decantation in columns of 250 mL and 3.5cm of diameter. The mixture of powder with isopropanol was vibrated in an ultrasonic bath for 15 min to insure a homogeneous mixing of the powder and then was left for decantation for a week. The supernatant solution was eliminated carefully with a pipette and the different fractions obtained were washed 4 times with isopropanol.
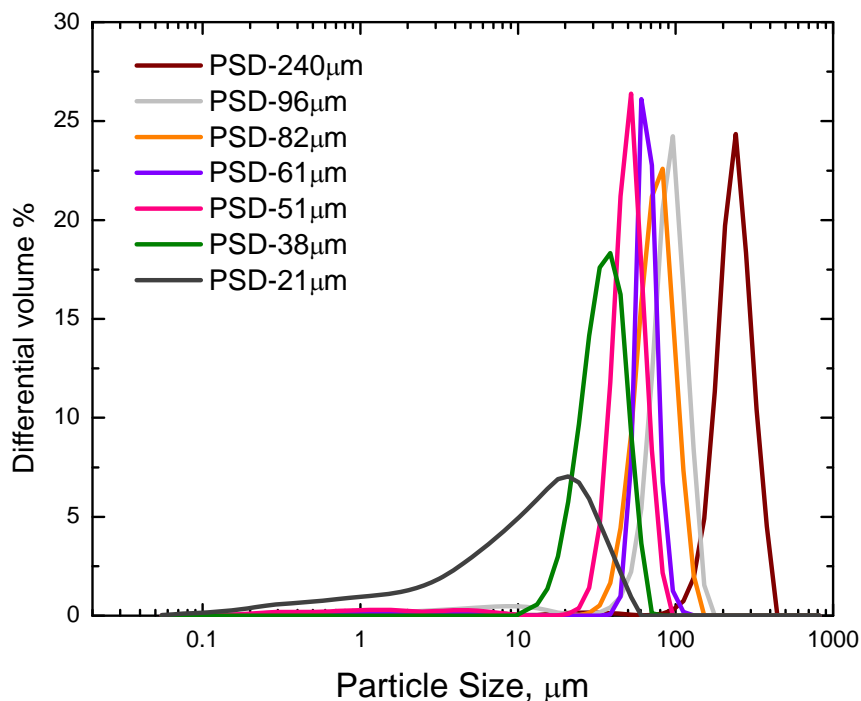
Figure 2.14: PSDs obtained by sieving
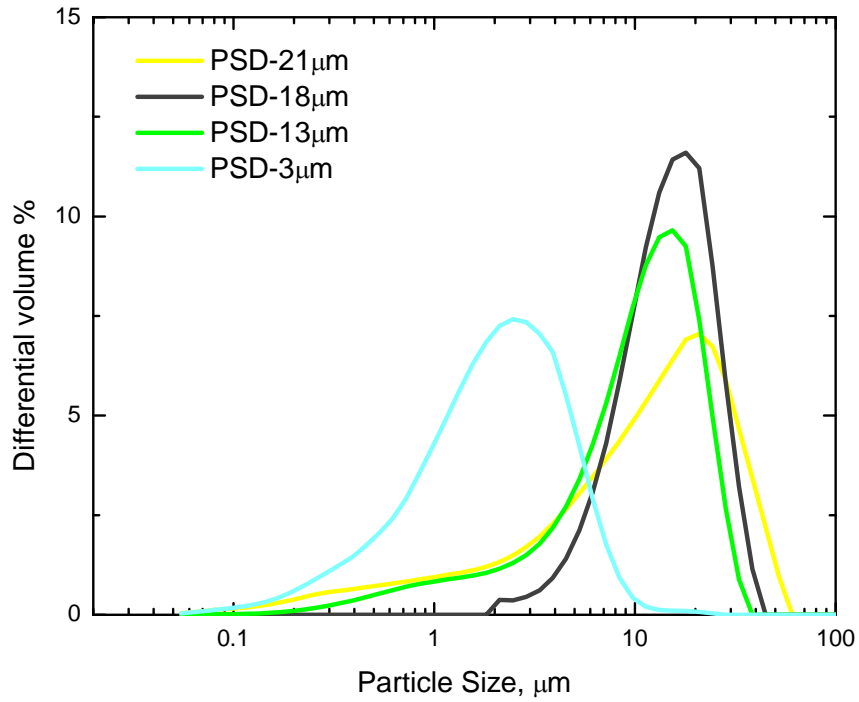
Figure 2.15: PSDs obtained by decantation
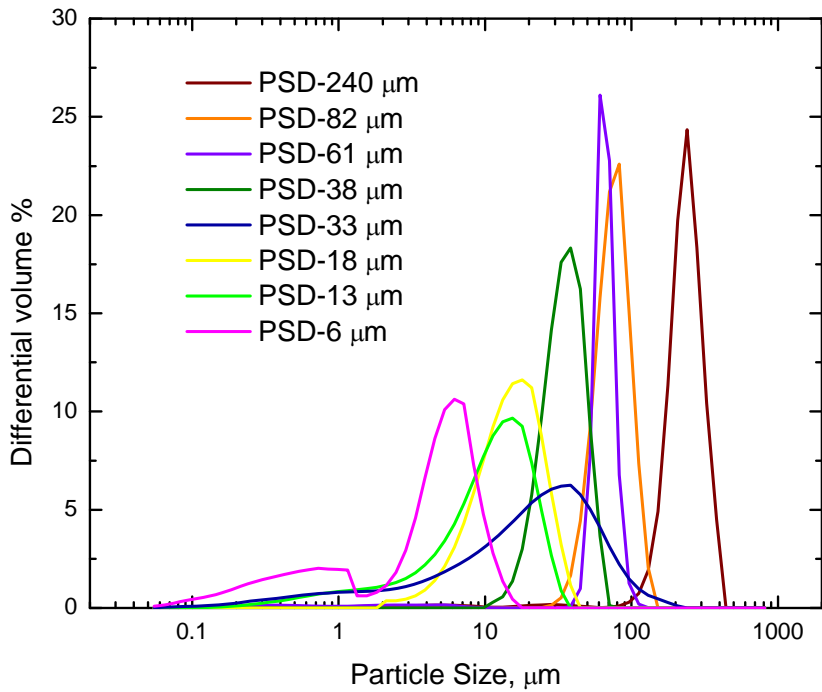
Figure 2.16: PSDs used for the hydration study

The specific surface area for the different gradations measured by BET, Blaine (ASTM method C204-96a) and calculated from their particle size distribution measured by granulometry laser analysis assuming spherical particles are presented in Table 2. As a consequence of the limitations of each of the methods used for the derivation of the surface area, the total values should be looked under suspect. For instance, Blaine method will work better for smaller gradations. The specific surface area measured by Blaine is derived from the resistance to flow air through the powder. Then, gradations with higher porous bed of the powder (coarse particles) will lead to a much faster air flow leading to higher error in the measurement. The densities of each powder calculated by He pycnometry is presented in the same table (Table 2.4). The nomenclature of the different particle sizes used during the hydration study is given in the same table.

Table 2.4: Table of median sizes, surface areas (BET and Blaine) and densities for the different gradations

Particle Size Distribution	Median psd (µm)	Blaine (cm^2/g)	Calculated from PSDs (cm^2/g)	Density by He pycnometry (g/cm^3)
OPC-33 µm	33	3066	6105	3.11
PSD-240µm	240	-	84.3	3.15
PSD-96µm	96	766	488	3.13
PSD-82µm	82	610	268	3.14
PSD-61µm	61	835	1275	3.13
PSD-51µm	51	1081	1361	3.11
PSD-38µm	38	1212	591	3.15
PSD- 33µm/Alite	33	1905	5497	3.15
PSD-18µm	18	2393	1602	3.17
PSD-13µm	13	3059	4564	3.15
PSD-21µm	21	5255	1739	3.13
PSD-6µm/pure C$_3$S	6	2952	22989	3.13

REFERENCES

[1] H.F.Taylor, Chement chemistry, Thomas Telford, London 1997.

[2] M. Bigare, A. Guinier, C. Mazieres, N. Yannaquis, W. Eysel, Th. Hahn, Polymorphism of tricalcium silicate and its solid solution, J. Am. Ceram. Soc. 50 (1967). 609-619.

[3] I. Maki, K.Nakagawa, K. Hiraiwa, T. Nonami, Microscopic study on the polymorphism of Ca_3SiO_5, Cem. Concr. Res. 8 (1978) 407-414.

[4] Peter C. Hewlett, in Chemistry of Cement and Concrete (Fourth edition, 1998), pp. 107-110.

[5] M. Malki, P. Echegut, Electrical conductivity of the Ca-SiO2 system in the solid and the molten states, Journal of Non-Crystalline Solids 323 (2003) 131-136

[6] Meducin,F. Étude des phases silicatées du ciment hydraté sous haute pression et haute temperature, Ph.D Thesis Université Paris (2001)

[7] H.Y. Ghorab, E.A. Kishar and Abou Elfetouh, Studies on the stability of the calcium sulfoaluminate hydrates. Part II: effect of alite, lime, and monocarboaluminate hydrate, Cement and Concr. Res. 28 (1998) 53-61

[8] Ángeles G. De La Torre, Sebastián Bruque, Javier Campo, Miguel A.G. Aranda, The superstructure of C_3S from synchrotron and neutron powder diffraction and its role in quantitative phase analysis, Cement and Concr. Res. 32 (2002) 1347-1356

[9] Xiaocum Liu, Yanjun Li, Influence of MgO on the formation of Ca_3SiO_5 and $3CaO.3Al_2O_3.CaSO_4$ minerals in alite-sulphoaluminate cement, Cem. Concr. Res. 32 (7) (2002) 1125-1129

[10] T. Hahn, W. Eysel and E. Woermann, 5th Int. Symp. On the Chem. Cement, Vol. 1, p. 61, Tokyo, 1969.

[11] J. Skibsted, H.J. Jakobsen, C.J. Hall, Direct observation of aluminium guest ions in the silicate phases of cement minerals by Al-27 mass NMR-spectrocscopy, Chem. Soc. Faraday Trans. 90 (1994) 2095-2098

[12] N. Antón et al, Liquid phase sintering of CMC´s based on clinker Porland, J. of European Ceram. Society 20 (12) (2001) 2215-2224

[13] X. Liu et al., Effect of MgO on the composition and properties of alite-sulphoaluminate cement, Cem. Concr. Res. 35 (9) (2005) 1685-1687

[14] M. Courtial, M.-N. de Niorfontaine, F. Dunstetter, G. Gasecki and M. Signes-Frehel, Polimorphism of tricalcium silicate in Portland cement: A fast visual identification of structure and superstructure, Powder Diffr., 18 (2003) 7-15

[15] Golovastikov, N. I., Matveeva, R. G. and Belov, N. V., Crystal structure of the tricalcium silicate $3CaO \cdot SiO_2=C_3S$. Kristallografiya, 20 (1975) 721-729

[16] Maki I, Chromi S., Microscopic study on the polymorphsm of Ca3SiO5, Cement and Concr. Res. 8 (1978) 407-14

[17] Dietmar Stephan, Sebastian Wistuba , Crystal structure refinement and hydration behaviour of $3CaO \cdot SiO_2$ solid solutions with MgO, Al_2O_3 and Fe_2O_3, J. of European Ceram. Society 26 (2006) 141-148

[18] American Standard ASTM C 114

[19] Brunauer Stephen, Hayers J.C., Hass W.E., The heats of hydration of tricalcium silicate and β-dicalcium silicate, Journal Of Physical Chemistry 58 (3) (1954) 279-285

[20] Feldman, R.F., Helium flow and density measurement of the hydrated tricalcium silicate - water system, Cement and Concr. Res. 2 (1) (1972) 123-136

CHAPTER 3: EFFECT OF THE PARTICLE SIZE ON THE EARLY HYDRATION KINETICS OF TRICALCIUM SILICATE

This chapter presents a study on different particle sizes of alite as a way of understanding its hydration kinetics.

Most previous studies on the kinetics of hydration are complicated by the fact that a wide range of particle sizes are used. It is recognised that the particle size affects the hydration kinetics, and has been previously studied focusing on the overall effect of the surface area [1-5]. However, there is still not a good understanding on how particle size affects the hydration kinetics of cement, and if the size of particle affects the mechanisms involved.

This chapter focuses on the effect of the initial particle size on the different stages of hydration: dissolution, induction period, nucleation and growth and diffusion. To do so, the kinetics of several alite gradations was continuously monitored by a combination of two techniques: isothermal calorimetry and chemical shrinkage. SEM-image analysis was used as a complementary technique to link the hydration kinetics at early ages with the long term microstructural development as will be described in Chapter 4.

3.1 State Of The Art on the Hydration of Tricalcium Silicate

The broad patterns of reactions occurring during the hydration of tricalcium silicate are more or less understood, although the underlying mechanisms are not all fully resolved. The hydration products formed are calcium hydroxide (CH) and a poorly crystalline calcium silicate hydrate (C-S-H), as shown in Eq.3. 1 [6]]:

$$C_3S + (3-x+n)H \rightarrow C_xSH_n + (3-x)CH \qquad \text{Eq.3. 1}$$
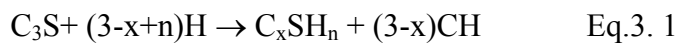
in which n, the water to silicate ratio (H/S), is approximately 4 in the case of saturated pastes. The typical range of values for the CaO to SiO_2 ratio (C/S) for cement pastes varies from 1.2 to 2.1. In the case of pure C_3S pastes however, the C/S ratio of C-S-H is around 1.7-1.8 [6, 7].Thus the amount of water necessary for complete reaction of C_3S corresponds to a water to cement ratio (w/c) of about 0.42 [6].

Overall the hydration of C_3S is an exothermal process and can be monitored continuously using isothermal calorimetry. A typical heat evolution curve for C_3S is given in Figure 3. 1. It is characterised by a strong peak in the first minutes after mixing. There is then a period of low heat evolution during which the concentration of calcium ions increases slowly [6]. After the induction period, a second exothermal peak is produced at around 10 hours from the massive precipitation of hydration products. The reaction then slows down and continues at a lower rate as long as water is provided to the system.
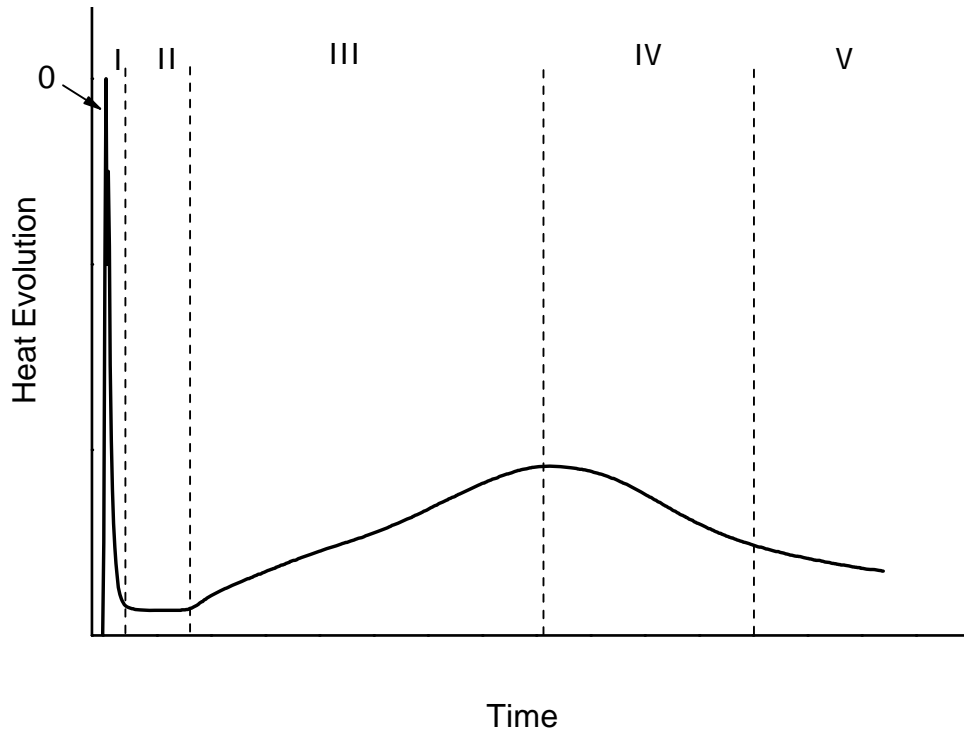
Figure 3. 1: Typical isothermal calorimetry curve for C_3S paste

Although there is a consensus about the general pattern of hydration, the fundamental mechanisms that govern the hydration, especially the early age stages (periods 0, I & II) are not yet fully understood, and are a source of great controversy. The main points of controversy concern the following questions:

a) why does the reaction slow down after the dissolution peak?

b) what brings the induction period to an end?

c) what are the reaction kinetics during the nucleation and growth process?

d) what is the influence of particle size on hydration kinetics?

Many authors have tried to answer the above questions. The following section describes the main theories that have been proposed.

a) Why does the reaction slow down after the dissolution peak?

The first part of the isothermal calorimetry curve **(Periods 0 and I)** corresponds to an initial dissolution (~15min) of ions upon contact with water followed by the reduction in dissolution rate commonly reffered to as the "first deceleration period". The proposed hypotheses to explain this dissolution are based either the poisoning of C_3S dissolution sites or by the formation of a protective layer of hydration product around the grain surface.

- Some authors [8-10] proposed that this step of slowing down of the dissolution could be a protonation or hydrolysis of the silicate and oxygen ions at the C_3S surface, followed by a congruent dissolution of the material. [11-13] introduced the concept of a superficially hydrolyzed layer (*Boundary layer theory*) in which the surface of the C_3S grain is protonated and becomes less reactive.

- Others [14-19] proposed that calcium and silicate ions at the surface of the grains pass rapidly into solution as simple hydrated ionic species. The rapid dissolution ends with the formation of a protective coating layer of a type of C-S-H somewhat different and less stable than that formed later on [14,15,18,19].

To date, neither of these mechanisms has been proven correct.

b) What brings the induction period to an end?

Period II, during which a low heat evolution is detected, is known as the "induction period". This period lasts for about 1-2 hours, depending on several parameters, such as the presence of additives, the mineralogy of cement, and its particle size. There are two main hypotheses which have been proposed to explain the mechanism that ends the induction period.

- Several authors propose that the induction period ends when hydration becomes dominated by nucleation and growth of the C-S-H [20-24].

- Others proposed that the product of the initial reaction forms a protective layer on the C_3S particles. The induction period ends when this is destroyed or rendered more permeable by ageing or phase transformation [14,18,25,26].

There is no general agreement on the mechanism that ends the induction period. Additionally, some hypotheses have been proposed which are not mutually exclusive [27].

Young et al. [16] found that the onset of crystallisation of portlandite could be correlated with the end of the induction period. During the induction period the calcium and hydroxide concentrations rises to a level at which the nucleation of portlandite occurs. The nucleation rate in solution is low at low degrees of supersaturation but increases rapidly as a higher critical supersaturation is reached. This theory implies that seeding with portlandite crystals would shorten the induction period, whereas this in fact prolongs the induction period. However, the addition of CH at the beginning of hydration has been shown to decrease the initial dissolution peak. Seeds of CH can also be poisoned by the presence of silica in solution.

- Fierens and Verhaengern [21] suggested that there is no protective layer around the grains but that water is only chemisorbed by interaction with surface defects and that the length of the induction period depends on the probability of C-S-H nucleation, which increases with increasing defect concentration. They further stated that unlike the induction period, the dissolution peak does not depend on the characteristics of the surface defects. Additionally, they showed that the speed of quenching of C_3S plays an important role in the reactivity via its effect on defect concentration, especially on the induction period [28].

c) What are the kinetics during the nucleation and growth process?

Period III corresponds to the massive nucleation and growth of the C-S-H and CH. This period begins about 1-3 hours after mixing. The reaction rate increases continuously and reaches a maximum that usually takes place around 10-12h. The time at which the peak is reached and the heat liberated is very dependent on the particle size [29,30]. This process is associated with the rapid formation of hydrates that lead to the setting and solidification of the cementitious matrix and the decrease of porosity.

The hydration kinetics for this stage is commonly fit using the Avrami equation [25,31-33]. However, Nonat et al. [34-36] use a new model based on heterogeneous nucleation, in contrast to the Avrami equation which assumes homogeneous process. Thomas, in 2007 [37] proposed a mathematical "boundary nucleation" model in which the nucleation of the hydration product occurs only on the C_3S particle surfaces. This model provides a better description of the early C_3S hydration kinetics than the Avrami equation since the "boundary nucleation" model accounts for the important effect of the C_3S surface on the hydration kinetics.

Investigation of the hydration kinetics by fitting with the Avrami equation:

The Avrami equation [38] relates to the reaction kinetics of processes involving nucleation and growth and has shown to effectively emulate the early kinetics of cement hydration [25,31-33]. The similar shape of the equation and the fact that the initial process of cement hydration can also be viewed as nucleation and growth has generally justified this.

The Avrami equation [32,38] can be written as:

$$\alpha = \alpha_{max}\left(1 - e^{-k(t-t_0)^n}\right) + \alpha_0 \qquad \text{Eq.3. 2}$$

Where α is the degree of hydration calculated from the measured cumulative heat, α_{max} is the maximum possible degree of hydration in percent. t is the time , k is the rate constant and n is an exponent which depends on the dimensionality of the system and on the types of nucleation and growth. The parameters t_0 and α_0 account for any time lag in the reaction (including any measurement delay) and the dissolution peak.

The parameter n is related to the morphological characteristics of the growing crystal through the following relation:

$$n = (P / S) + Q \qquad \text{Eq.3. 3}$$

where P can be equal to 1, 2 or 3 corresponding to the growth of fibres or needles, sheets or plates, spheres or polygons forms, respectively. S can be equal to 1 or 2 corresponding to phase boundary growth or to diffusion of the reacting species through a liquid phase. Q is equal to 0 when there is not nucleation and equal to 1 when there is a continuous nucleation at a constant rate.

Although there is a consensus that the Avrami equation is efficient to fit the kinetics of the hydration of cement, various researchers report a large scatter of fitting coefficients. Table 3. 1 summarise the coefficient values found in literature. The lack of consistency of these puts in question the actual validity of the equation for cementitious materials.

Table 3. 1: Values found in the literature for the main mechanism of hydration of C_3S obtained using different equations

	$k(h^{-1})$	n	α_0	$t_0(h)$	w/c	Radius (μm) or particle fineness (cm^2/g)
Tenoutasse and de Donder (1970)		3				
Brown et al. (1985)						
- Kondo and Ueda (1968)		1.10	0	3	0.5	2-5
		0.67	0	4	0.5	2-5
		1.13	0	3	0.5	5-8
		0.81	0	4	0.5	5-8
		1.12	0	3	1	2-5
		0.79	0	4	1	2-5
Odler and Schüppstuhl (1981) (Triclinic)		1.10	0	3	0.7	3000
(25ºC)		1.02	0	0	0.7	7000
Tarrida et al. (1995) (Triclinic) (20ºC)	0.04	0.85	0	0	0.4	4100
Berliner et al. (1998) (Monoclinic)	0.004	1.86	0	0	0.3	3602
	0.006	1.72	0	0	0.5	3602
	0.007	1.66	0	0	0.7	3602
Fierens et al. (1982) (Triclinic) (25ºC)	0.03	3			0.6	
FitzGerald and al. (1998) (Triclinic)						
- Temperature: 10ºC	0.0019	1.88	0.52	15.5	0.4	3900
- Temperature: 20ºC	0.0074	2.15	0.48	3.5	0.4	3900
- Temperature: 30ºC	0.0174	2.27	0.39	1.5	0.4	3900
- Temperature: 40ºC	0.033	2.59	0.28	0.5	0.4	3900
Thomas and Jennings (1999) (monoclinic)						
- Temperature: 20ºC	0.0933	2.53		3.12	0.4/0.5	3602
- Temperature: 30ºC	0.1497	2.65		1.18	0.4/0.5	3602
- Temperature: 40ºC	0.2421	2.51		0.68	0.4/0.5	3602
Peterson and al. (2006)						
- Triclinic polymorph: 30ºC	0.251	2.65		1.3	0.4	5330
	0.241	2.27		1.3	0.4	5330
- Monoclinic polymorph: 30ºC	0.161	2.65		1.6	0.4	3030

Numerical simulation of the C-S-H growth on a surface from a particle aggregation model

Nonat et al. emulated the degree of hydration with time using an approach also based on nucleation and growth of C-S-H but they assume the mechanism to be dependent on three parameters: one related to the number of initial nuclei, one linked to the growth parallel to the grain surface and one linked to the perpendicular growth [35]. This assumption is based on heterogeneous nucleation and described by a random distribution of nuclei on the anhydrous surface. The growth proceeds through the aggregation and around the initial nuclei of similar particles in an anisotropic way as suggested by atomic force microscopy (AFM) observation [34]. The authors justify their approach compared to Avrami since the latter has been developed for homogeneous processes, which may explain why the parameters obtained from the fit with this equation do not have a clear physical meaning [5].

The nucleation and growth **(Period III)** process is followed by a strong decrease of the hydration rate that has often been considered to be due to transition to a diffusion-controlled process **(Periods IV & V)** [34,39]: the higher the degree of hydration, the greater the thickness of the hydrated layer and consequently the slower the diffusion of water and ionic species through this layer.

Using proton NMR, Zajac [40] shows that the transition to a diffusion-controlled process is associated with a decrease of the available surface area. According to the model described above, this is explained by the fact that up to the second hydration peak, C-S-H can precipitate in the three dimensions around nuclei while after the peak, all nuclei have merged in a continuous layer, 2 dimensions remain available for deposition.
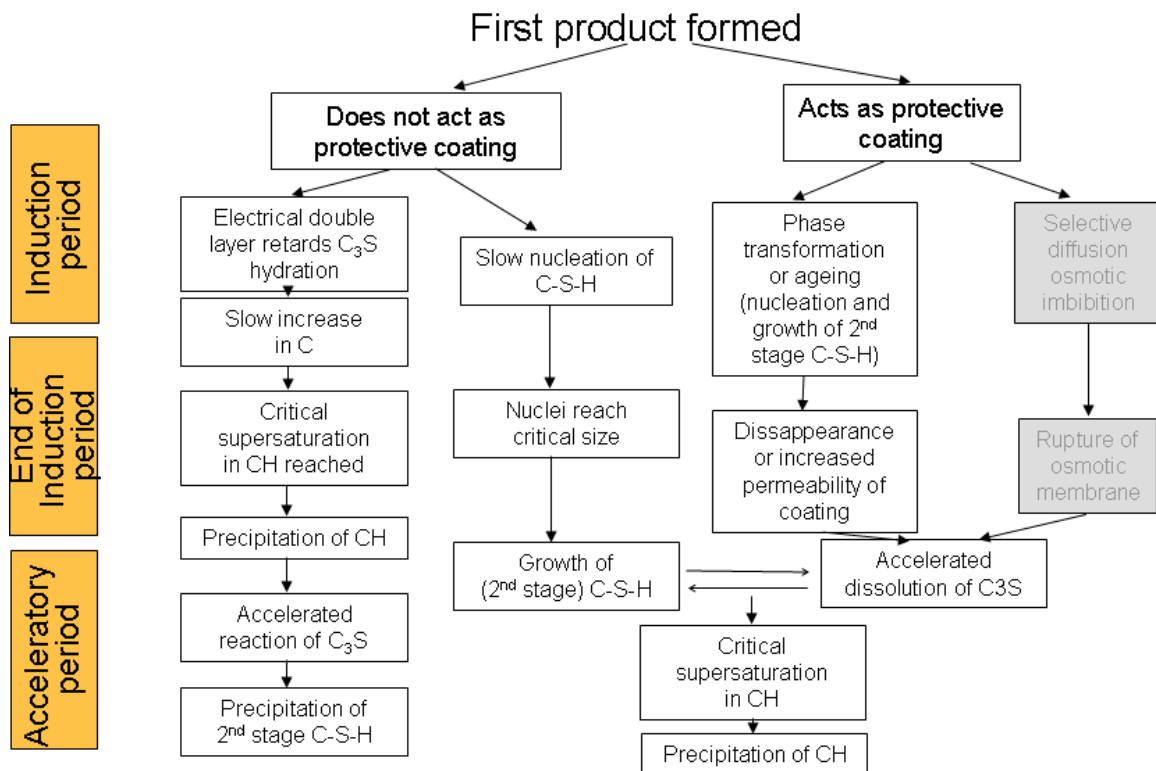
Figure 3.2: Schematic summary of the two different approaches to the induction period. Figure reproduced from RILEM committee 68-MMH (1984). [41]

In 1984, all hydration theories proposed up to that point were summarised by RILEM committee MMH, as shown in Figure 3.2 [41] this show the two schools of thought concerning the induction period (II) and its consequence on further hydration.

d) what is the influence of particle size on hydration kinetics?

Particle size has been shown to play an important role on the hydration kinetics, microstructure and mechanical properties of cementitious materials [1-4].

In 1969, Kondo and Ueda gave the first experimental data concerning the hydration of monodispersed C_3S particles [42] and Tenoutasse and de Donder [31] showed the importance of particle size on the rate of hydration of C_3S pastes (Figure 3.3). Higher hydration rates were observed for the gradations with the highest surface areas (i.e. the smallest particles). Since small particles are being used up rapidly, the transition time from period III to IV occurs earlier for finer particles sizes.
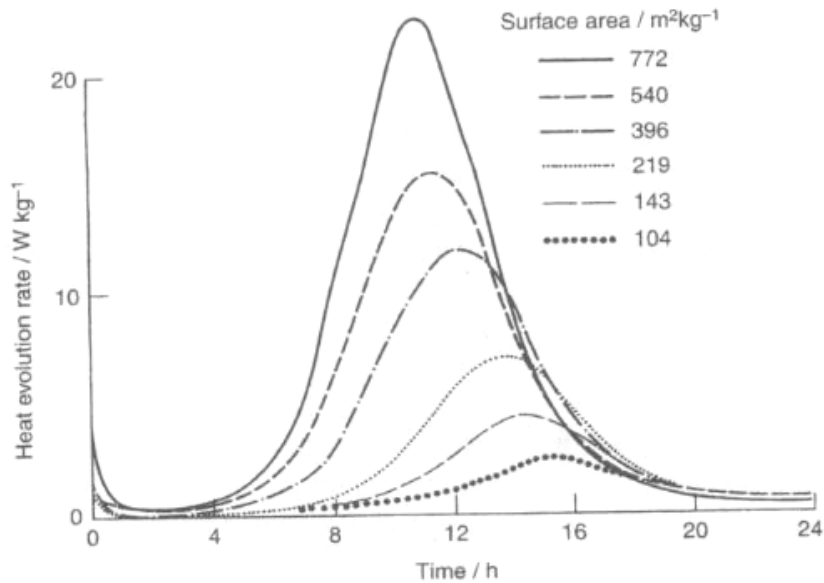
Figure 3.3: Isothermal calorimetry curves for C_3S pastes hydrated (w/s=1.0): effect of surface area on the hydration kinetics[29]. Figure reproduced from Bye [27]

Later on Scrivener [30] observed the same trend when cement samples were produced by fractionating the same cement to different particle sizes (Figure 3.4-a). The same curves normalised by the total surface area of the specimens, calculated by assuming mono-sized particles of radius equal to the geometric mean of the range, are shown in Figure 3.4-b. These graphs show that the heat flow and thus the rate of reaction are approximately proportional to the total surface area of the particles. The downturn in the curves occurs earlier for the smallest particles, which is attributed to the particles getting used up by the reaction. The fact that the reaction rate is affected by the surface area is also supported by the fact that since the initial reaction is governed by the dissolution of material and the nucleation of C-S-H on the surface, higher surface areas would lead to a faster reaction. A similar relationship between the rate of hydration and the specific surface area was observed for the case of tricalcium silicate [6,29,36].

Because of the complexity of the hydration reactions, most kinetic models have only considered the global reaction rather than the reaction of individual particles[43-46]. However, several studies have tried to assess and take into account the influence of particle size to model hydration kinetics. Taplin was the first to point out the importance of incorporating the concept of initial particle size in the development of cement

hydration models [47]. Later on, Knudsen [48] stated that the degree of hydration of a single particle is inversely related to its radius but that in the whole cement system, because of the continuous particle size distribution, the effects of the individual hydration kinetic rates are masked/merged in the global reaction. Afterwards, in 1984 [3] Knudsen developed a dispersion model of hydration for simulating the hydration of Portland cement in which the particle size distribution was explicitly considered. Brown [49] studied the effect of the particle size distribution of 2 gradations of pure C_3S on the hydration kinetics. Using the Jander and Ginstling-Brounshtein model [50,51], he observed that any of the models could emulate the shape of the isothermal calorimetry curves and that the effect of the particle size is mostly important during the acceleratory period while the post-acceleratory appears to be independent of the initial surface area. Later on, Navi and Pignat [52] developed the "Integrated Particle Kinetics Model" in which the hydration and the microstructural development of cement-based materials are modelled as function of the particle size effect and its chemical composition. In they have shown that the microstructural development of hardened cement pastes has a strong dependence with the initial particle size of the cement, particularly at early ages.
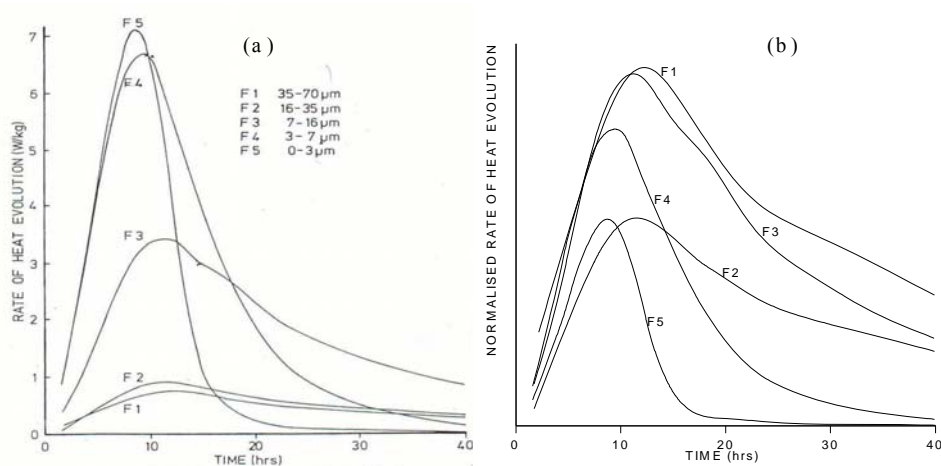
Figure 3.4: a) Rate of heat evolution and b) normalised relative to surface area for different particle sizes [30]

42

3.2 Experimental Study of the Influence of Particle Size Distribution on C$_3$S Hydration Kinetics

3.2.1 Techniques used for the investigation of the hydration kinetics

The hydration kinetics of the different particle sizes presented in the previous chapter were investigated by the combination of several techniques: isothermal calorimetry, chemical shrinkage and SEM-image analysis. Isothermal calorimetry and chemical shrinkage have the advantage of being able to continuously follow the hydration of cement. Isothermal calorimetry experiments were used to measure the heat of hydration over the first 24 hours when the reaction is highly exothermic, while chemical shrinkage was used afterwards when the heat production is low and its signal can hardly be discriminated from the background/noise. SEM-image analysis was employed as a complementary technique for calibrating the two previously mentioned techniques and for following the long term hydration as will be described in more detail in the next Chapter 4.

3.2.1.1 Isothermal calorimetry

Chemical reactions are energetic processes that either release or consume heat. The overall balance of the heat of hydration of C$_3$S is exothermic and the heat released upon hydration can be monitored continuously using isothermal calorimetry. However, the heat evolution rate curve is at any instant a composite of all the on going reactions. Therefore, it can only be used as a global measure of the degree of hydration. Another important limitation of the method is the low rate of reaction of cementitious systems after 24 hours of hydration. The signal is very low and difficult to resolve from the noise due to, for example, the small external temperature variations.

In this work, a TAM Air isothermal calorimeter from Thermometric was used. It consists of 8 parallel twin type measurement channels . One cell is dedicated to the sample, the other to a reference vessel. The reference vessel is used to reduce the signal to noise ratio and to correct measurement and temperature artefacts. 20ml glass ampoules are used for both the sample and the reference container. Each channel is independent from the other channels and was calibrated before any experiments were performed. Water was selected for use as the reference material after several inert materials were tested. This calorimeter allows both in-situ and ex-situ mixing.

In-situ mixing experiments allow the hydration to be followed from the very beginning when water is added to the sample. The in-situ mix is made with a special injection device (Figure 3. 5) which allows for the addition of deionized water (w/c=0.4) to the unhydrated powder (1.5g). The mixing (2 min at 100 r.p.m) is done with the device inside the calorimeter. The main drawback of these in-situ measurements is the poor homogeneity of the mix.
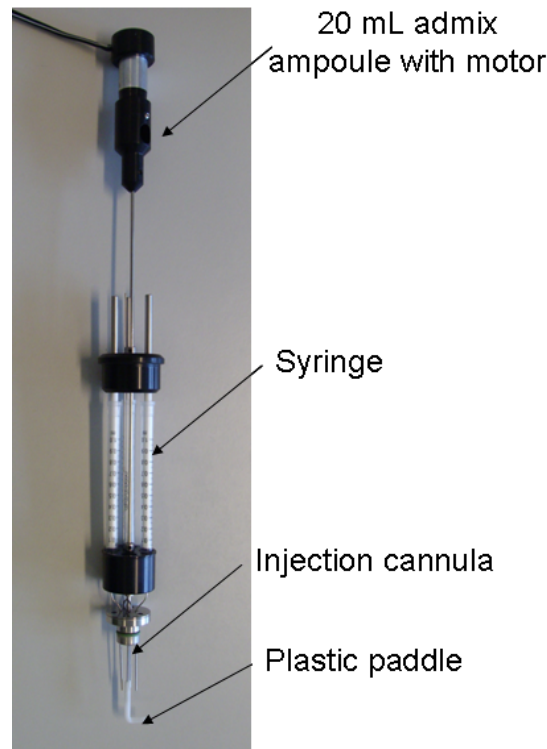

Figure 3. 5: In-situ "Admix-ampoule" from Thermometric

The procedure for the ex-situ mixing was 2 minutes of hand mixing followed by the immediate placement of the ampoules inside the calorimeter, to monitor the hydration from the earliest time possible. All of the different gradations were mixed at a w/c ratio of 0.4 with deionized water. Due to the complexity and time intensive process of alite preparation, the amounts of paste used in the experimentation were reduced to a minimum quantity (3.5 g total paste mass).

The time constant of a calorimeter reflects its thermal inertia and depends on two parameters: the sample heat capacity and the heat transfer properties of the calorimeter. The measured time constant has been used to correct the output signal (Tian correction) for the thermal inertia of the calorimeter especially at very early ages [53] as shown below (Eq.3. 4):

$$P = \varepsilon\left(U + \tau\frac{dU}{dt}\right) \qquad\qquad \text{Eq.3. 4}$$

where P(W) is the thermal power produced in the sample , U(V) is the voltage output of the heat flow sensors, ε (W/V) is the calibration factor, τ (s) is the time constant of the calorimeter which has been calculated to be 4 minutes.

Figure 3.6 compares the heat flow curves of the same powder mixed in-situ and ex-situ. The maximum heat flow peak during the nucleation and growth process is higher and takes place earlier in the castoff ex-situ mixing. Figure 3.7 compares the cumulative heat curves of the same powder mixed in-situ and ex-situ. Higher initial values of cumulative heat in the case of ex-situ curves are observed due to the outside heat introduced in the calorimeter when inserting the sample vessel. The time that the calorimeter needs to stabilize after the vessel is introduced into the calorimeter is about 20 min. This artefact can be taken into account and the ex-situ mix curve can be corrected accordingly as shown in Figure 3.8. However, after a few hours, the two curves are diverging with less heat generated in the case of the in-situ mix procedure. The most probable explanation is the poor homogeneity of the paste which lowers the available surface area for dissolution

and precipitation during the nucleation and growth stage (period III). The experiments were found to be very reproducible up to 24 hours. Therefore, the differences between in-situ and ex-situ measurements cannot be explained as artefacts of the method.

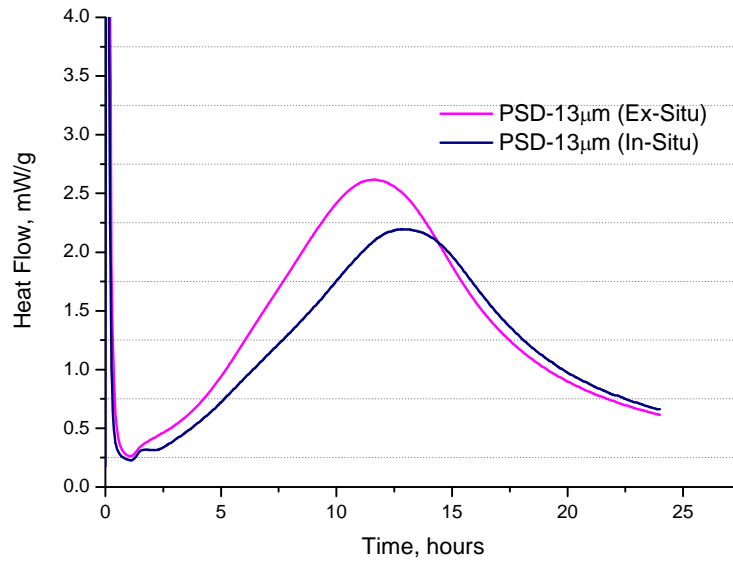Figure 3.6: Comparison between the heat flow curves of a powder (PSD-13µm) made in-situ and ex-situ the isothermal calorimeter
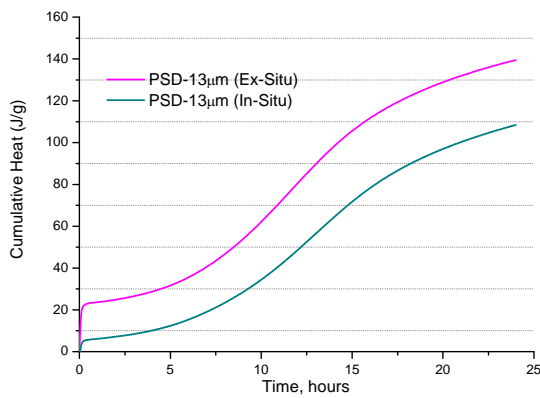

Figure 3.7: Comparison between the cumulative heat curves of a powder (PSD-13µm) mixed in-situ and ex-situ
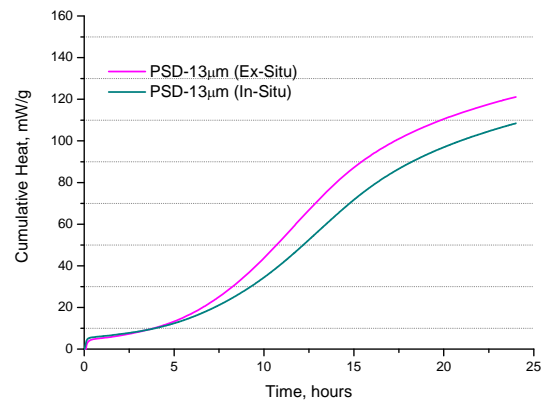
Figure 3.8: Comparison between the cumulative heat curves of Figure 3.7 where ex-situ mix curve has been corrected by subtracting the heat flow induced by the ex-situ mixing

3.2.1.2 Chemical shrinkage

a) Introduction to chemical shrinkage and development of the measuring protocol

Mechanism of chemical shrinkage is a rapid and convenient method for monitoring hydration rates. This method is based on the fact that the volume occupied by the hydration products is lower than that of the reactants. This is due to the fact that water has a lower specific volume when bound to a solid than when free in a liquid as reflected in Eq.3. 5.

$$V_{C_3S} + V_{water} > V_{C-S-H} + V_{CH} \qquad \text{Eq.3. 5}$$

The magnitude of the shrinkage can be calculated using the molecular weights and densities of the compounds as they change from reactants to reaction products and is therefore a direct measure of the progress of the reaction[54].

If the stoichiometry of C_3S reaction (C_3S+ 5.3H $\rightarrow$ $C_{1.7}SH_4$ +1.3CH) and the density of C-S-H are considered constant during the hydration process, the chemical shrinkage can then be calculated according to reactants   Eq.3.6.

$$\Delta V(t=\infty) = \Sigma \text{ (volume ratio)}_{\text{products}} - \Sigma \text{ (volume ratio)}_{\text{reactants}} \qquad \text{Eq.3.6}$$

The main unknown parameter in this approach is the C-S-H density on which the chemical shrinkage is highly dependent. There are several values of C-S-H density reported in the literature [55-58]. They mainly depend on the degree of saturation of the specimens tested and on the method used. According to Jennings they range from 1.9 to about 2.4 g/cm^3, depending on several conditions of measure such as the pre-conditioning of the samples (drying method employed, relative humidity of the samples, etc) or the method employed for its determination (He pycnometry, Archimedes method, backscattered electron image analysis,…) [55].

Table 3. 2 show the values of densities and molar masses used for the calculation.

Table 3. 2: Values used for the calculation of chemical shrinkage in C_3S.
(*) Range values for C-S-H density found in literature

	C_3S	H	C-S-H	CH
Density (g/cm^3)	3.15	1	1.9 to 2.4 (*)	2.24
Molar Mass (g/mol)	228	18	227.2	74

Therefore, using the values in the table, the chemical shrinkage will vary between -7.3 % and -41.7 % for 100 % of reaction of 1 mol of C_3S (Table 3. 3).

Table 3. 3: Variation on the values of chemical shrinkage with the density of C-S-H

Density (g/cm^3)	% $\Delta V_{(t=\infty)}$	$\Delta V_{(t=\infty)}$ (ml/g C_3S)
1.9	-7.3	-0.023
2.4	-41.7	-0.132

There are three main methods commonly used for measuring chemical shrinkage (gravimetry, dilatometry and pycnometry) but all of them have in common that the sample is maintained water saturated and the water needed to replace the volume decrease is measured [59].

a) Gravimetry is based on the indirect measurement of volume change by recording the weight under water as the buoyancy changes with density (Archimedes's law).

b) Dilatometry consists in the direct measurement of length or volume change. Most of the time it involves the measurement of the decrease of water in a capillary connected to the sample flask [60,54].

c) Pycnometry is only applicable for total chemical shrinkage measurement and is carried out by filling a pycnometer with paste and topping it with water. Water is added to refill the pycnometer at different ages, and the weight increase relates to total volume change.

The method chosen here is dilatometry based on the protocol developed by Geiker [54] (Figure 3. 9). It consists of a flask that contains the paste, on top of which a capillary is connected and filled with water. As the hydration proceeds and the paste shrinks, the level of water in the capillary decreases. The water level is monitored using a webcam connected to a laptop. A few drops of oil with a red colorant are added on the top of the water in the capillary to avoid evaporation of water. The coloured oil drops are also used as tracers in the image analysis of the pictures of the capillary taken with the webcam. The flasks are immersed in a thermostatic water bath and maintained at 20 °C. Images were acquired by the webcam every 2 minutes during the first 24 hours and every 5 minutes thereafter. They were then numerically processed to extract the level of water in the capillary. Figure 3. 9 shows the setup used for the measure of the chemical shrinkage.
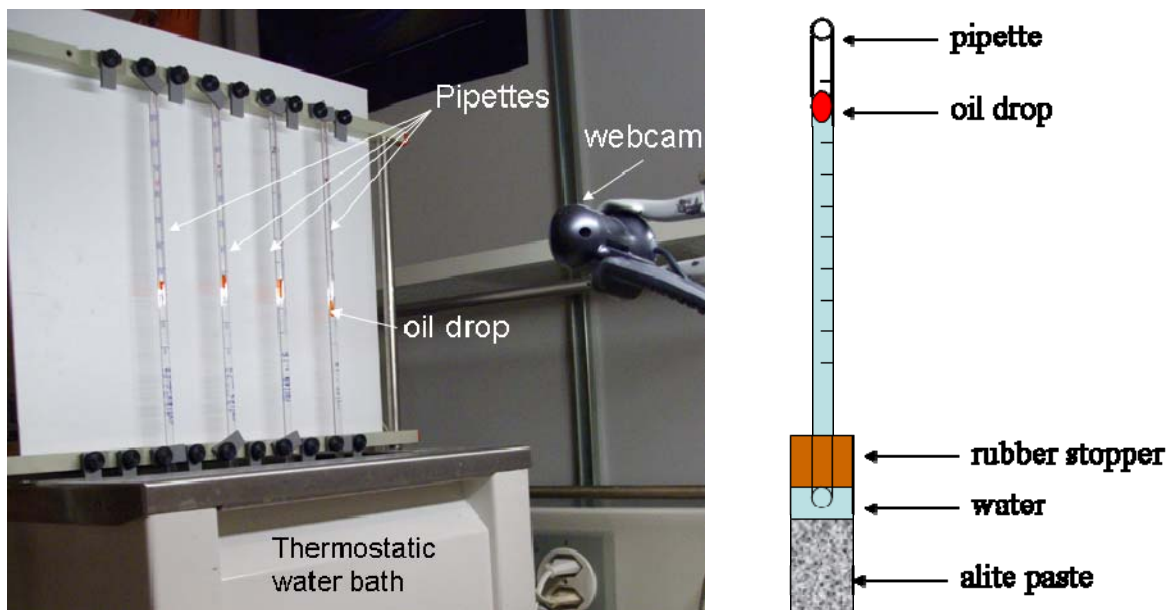
Figure 3. 9: Setup developed for the measure of Chemical Shrinkage (left) and the devise used for the measure by means of dilatometry (right)

The depth of the sample has often been suspected to limit or even prevent the ingress of water in the sample and consequently the measurement of the chemical shrinkage. Boivin [61] investigated the influence of the thickness of the cement paste on the evolution of chemical shrinkage. In order to increase the exposed volume of paste and reduce its thickness she used erlenmeyer flasks. She concluded that there is a critical depth above

which the paste becomes only partially permeable to water, and from which the chemical shrinkage is underestimated. In addition, she stated that this effect is more significant at low w/c ratios.

In this work, two types of flask were compared to develop the best protocol: cylindrical and erlenmeyer shapes to decrease the thickness of pastes and increase the exposed volume. Once filled with paste, the flasks were tapped to avoid entrapped air bubbles. Duplicate experiments were run for each of the particle sizes to check the reproducibility of the method. The maximum thickness of paste in the erlenmeyer flasks (0.5cm) was always lower than 1cm while higher in the case of the cylindrical flasks.

Several amounts of alite pastes were tested with both the erlenmeyer and cylindrical flasks in order to assess the effect of the sample's thickness on the evolution of chemical shrinkage (see Appendix I).

b) Protocol used for the measure of chemical shrinkage

Cylindrical flasks were found to work the best and were used for the remainder of the experiments. Cylinders used for the experimentation had 6 cm height by 2 cm of diameter. The thickness of paste introduced was kept constant in all measurements and equal to 1.7 cm (10 g of alite paste). The paste was tapped in order avoid the presence of entrapped bubbles. Water was added immediately after tapping to the top of the paste, taking special care to minimize mixing risking the dilution of the paste. Duplicate experiments were run for each sample to verify reproducibility of the method.

3.2.1.3 Correlation between chemical shrinkage and isothermal calorimetry

The direct link between chemical shrinkage and degree of hydration measured by non-evaporable water has been shown by previous studies [54,62]. In the present case, the degrees of hydration calculated by isothermal calorimetry curves and chemical shrinkage measurements give the same kind of agreement as shown later (Figure 3. 12).

The procedure for the determination of degree of hydration from isothermal calorimetry curves and chemical shrinkage was the following:

a) The degree of hydration (α) is calculated from the isothermal calorimetry data with Eq.3. 7 [53].

$$\alpha = \frac{Q(t)}{\Delta h} \qquad \text{Eq.3. 7}$$

where Q(t) (J/g) is the specific heat produced at time t and Δh (J/g) is the specific reaction enthalpy at an infinite time i.e. 100% of hydration [6])

b) The degree of hydration is calculated from the chemical shrinkage assuming that the stoichiometry of the reaction remains the same during the whole hydration process, as shown in Eq. 3.8:

$$\alpha = \frac{\Delta v(t)}{\Delta V(t = \infty)} = \frac{\text{Ch.Shr} \times \left(1 + \dfrac{w}{c}\right) \times \rho(C - S - H)}{\Delta V(t = \infty)} \times 100 \qquad \text{Eq.3. 8}$$

where $\Delta V(t)$ is the chemical shrinkage at time t (min), $\rho_{C\text{-}S\text{-}H}$ is the density of C-S-H in (g/cm^3), w/c is the water to cement ratio, **Ch.Shr** (cm^3/g of paste) is chemical shrinkage obtained from the measurements and $\Delta V(t=\infty)$ (cm^3) is the total chemical shrinkage at the end of the process.

The chemical shrinkage is highly dependent on the density of C-S-H [63]. Figure 3. 10 show the development of the degree of hydration for an alite paste (PSD-38μm) for several C-S-H densities. This clearly shows how small changes in the C-S-H density have a big impact on the calculated degree of hydration. This method must therefore be calibrated by an independent method. This was done here using the degree of hydration obtained from SEM-image analysis. The measure of the chemical shrinkage can then be used to estimate the C-S-H density in addition to the volume changes taking place in alite

pastes. By comparison, with the degree of hydration obtained form SEM-Image analysis, the best fit of the chemical shrinkage is obtained for a C-S-H density of 2.04 g/cm^3 [$\Delta V_{(t=\infty)}$ = - 0.186 % (i.e. -0.059 ml/g C_3S) for 100 % of reaction of 1 mol of C_3S] for this particular case.

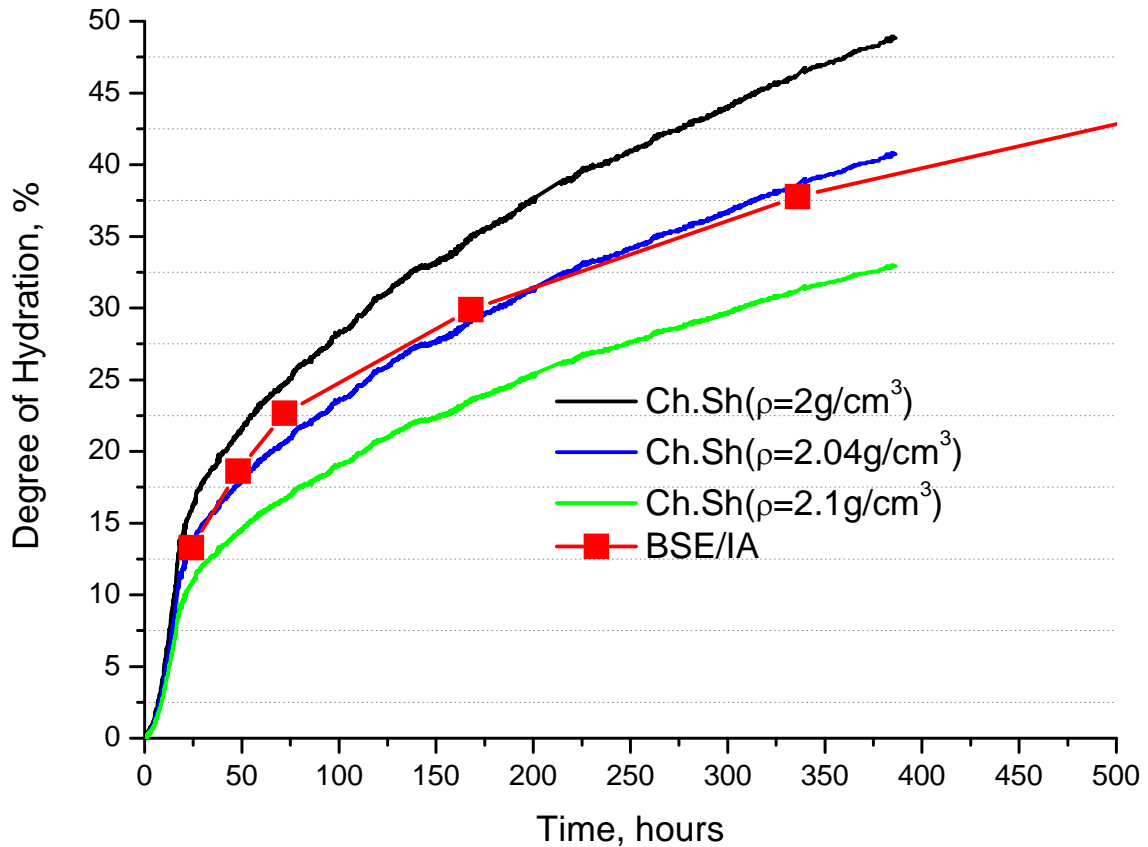Figure 3. 10: Variation of the degree of hydration for an alite paste (PSD-38μm) with the density used for the conversion from chemical shrinkage measurements

All three methods (IC, Ch.Sh, and SEM) can therefore be compared on a common measure (i.e. the degree of hydration), although they are based on totally different approaches and rely on different parameters. This is shown in Figure 3.11.
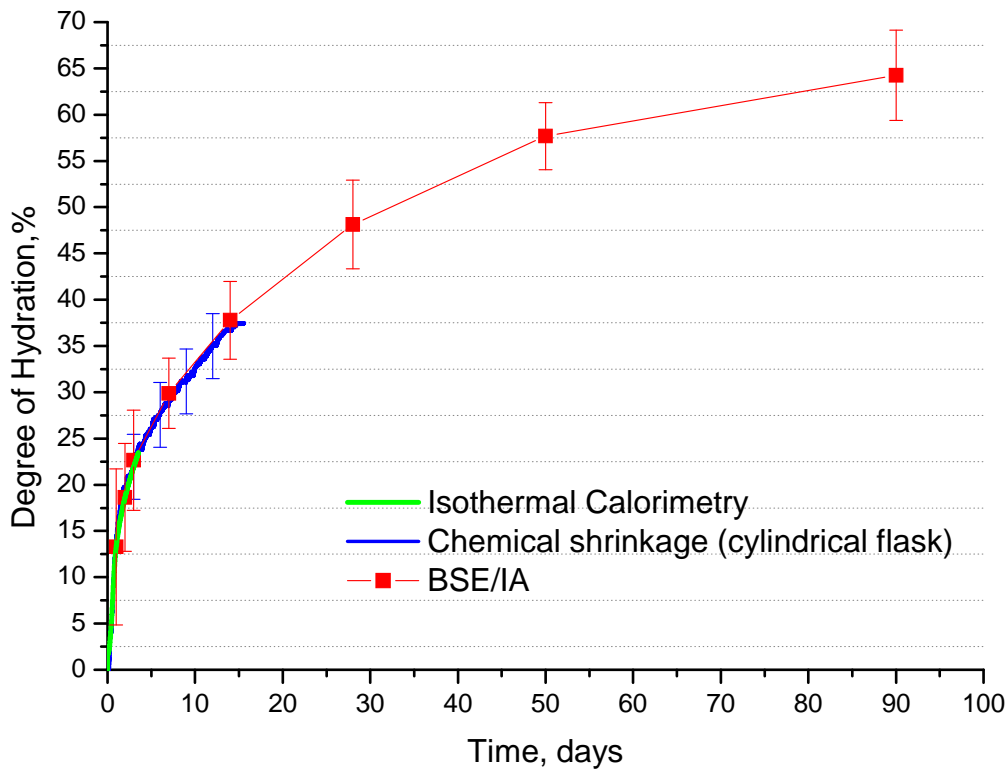
Figure 3.11: Degree of hydration of particle size distribution PSD-38μm calculated using different techniques

Figure 3. 12 shows the linear relationship between the two measurements for PSD-82μm PSD-38μm, PSD-18μm and PSD-6μm between 2 and 27 hours of hydration. The C-S-H densities used in this calculation were obtained from the best fit of the degree of hydration calculated by chemical shrinkage with BSE/IA, and are shown in Table 3. 4. The values are very close, however a slight increase of C-S-H density is observed with increasing the particle size, with the exception of PSD-82μm. For this PSD, the degree of hydration calculated by BSE/IA is slightly underestimated due to the important bleeding of this gradation at the beginning of the hydration (see chapter 4). The calibration of this gradation is therefore questionable. For the other gradations, the observed dependence of the C-S-H density with the particle size of the pastes could be indicative of a different nature of the C-S-H produced. The morphology, composition, chemically bound water and pore size distribution of C-S-H for different gradations of C_3S has been investigated and is presented in Chapters 4 and 5.

Table 3. 4: Values of C-S-H density obtained from chemical shrinkage measurements

	Density (g/cm^3)
PSD-82 μm	**2.09**
PSD-38 μm	**2.04**
PSD-18 μm	**2.05**
PSD-6 μm	**2.07**
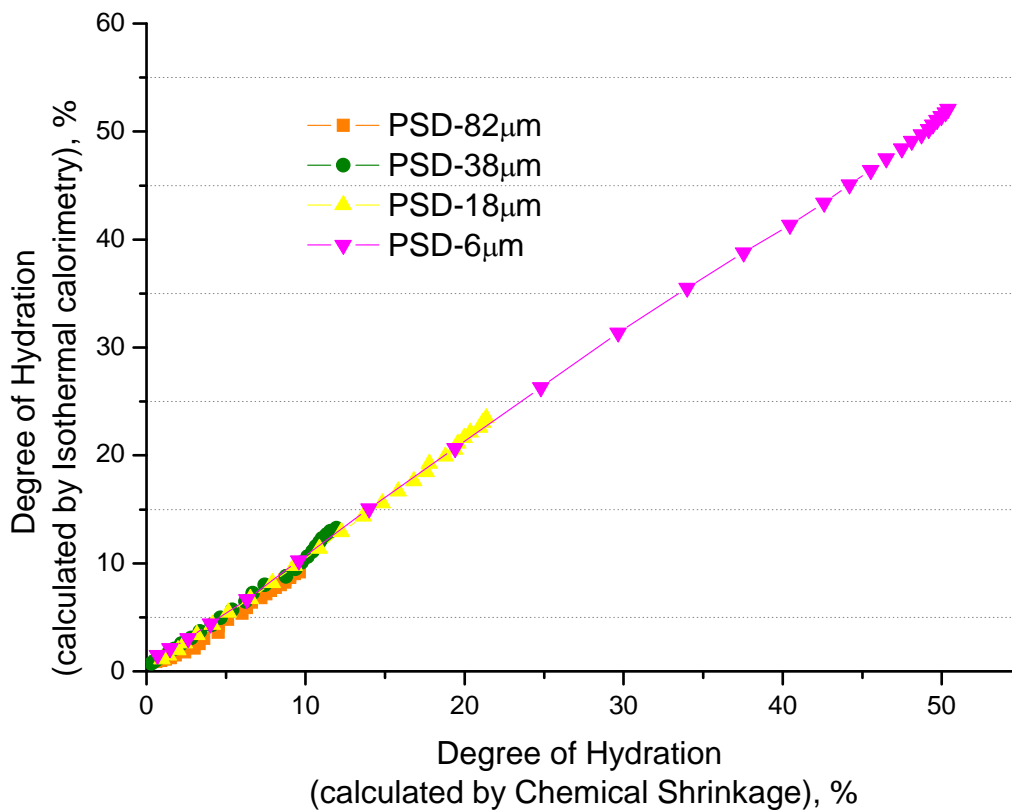
Figure 3. 12: Degree of hydration calculated from isothermal calorimetry curves versus the degree of hydration obtained from the measure of chemical shrinkage for different particle size distributions

Both techniques, isothermal calorimetry and chemical shrinkage, can be considered reliable and complementary for the investigation of hydration kinetics: the sensitivity of isothermal calorimetry to the dissolution processes makes it well adapted for very early age studies while chemical shrinkage is more sensitive to low activity reactions (i.e. late

ages). The period from which chemical shrinkage becomes a more suitable technique to follow the ongoing hydration will depend on the type of material and the particle size.

The two techniques were used according to the protocols defined above to investigate the hydration kinetics of the various particle size distribution of synthesised alite and presented in Chapter 2. These are presented in the following section.

3.3. Effect of the Particle Size on the Hydration Kinetics

Isothermal calorimetry results (Figure 3.13) show higher heat evolution for gradations with finer particles. The degree of hydration (enthalpy of hydration of C_3S = -517±13 J/g [6]) for the different particles calculated by isothermal calorimetry is shown in Figure 3.14 where smaller particles always have the higher values.

A similar trend can be observed in the results from chemical shrinkage (Figure 3.15). The conversion from chemical shrinkage to degree of hydration was made assuming constant density during the hydration process (Table 3. 4).

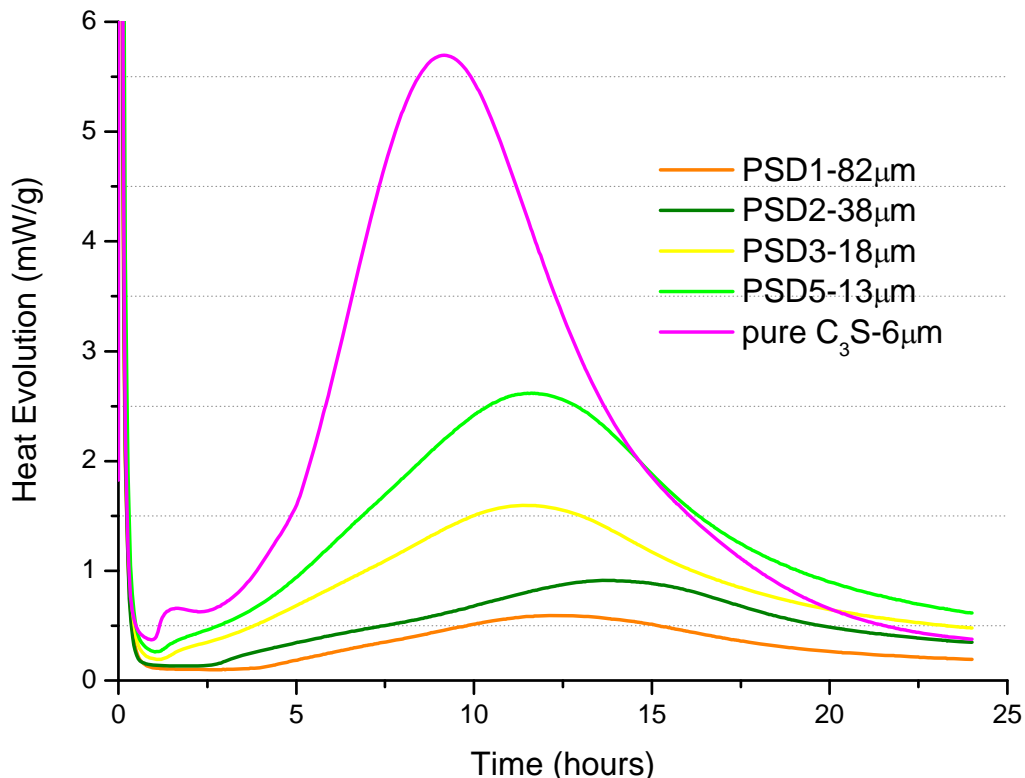

Figure 3.13: Isothermal calorimetry curves of alite pastes with different particle sizes hydrated with a w/c=0.4
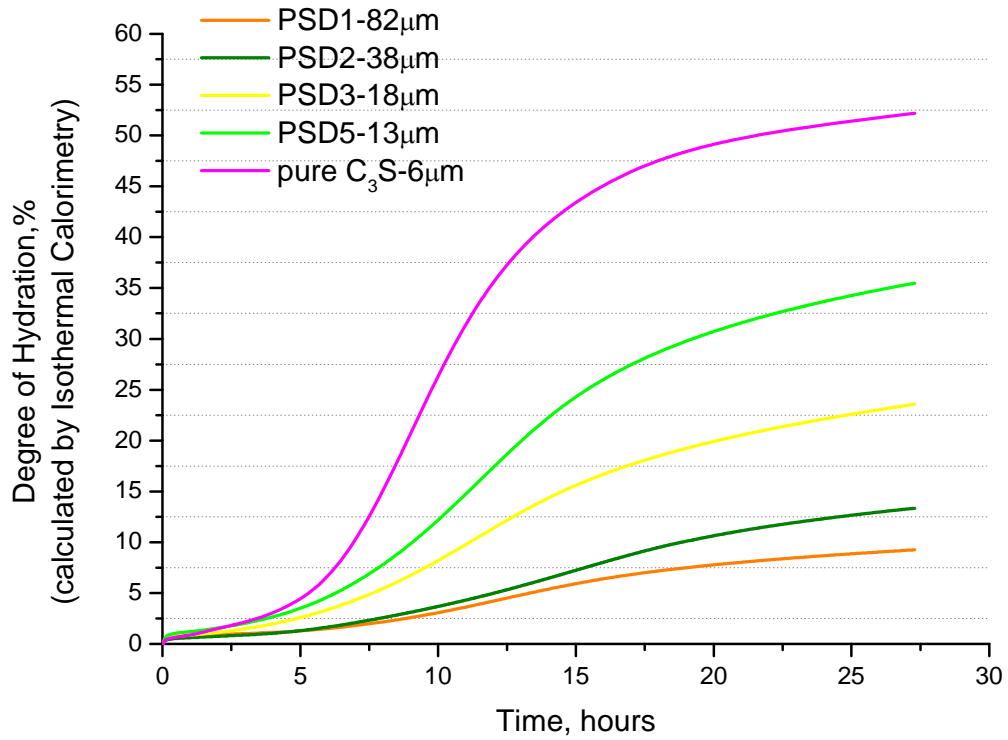
Figure 3.14: Degree of hydration calculated by isothermal calorimetry of alite pastes with different particle sizes hydrated with a w/c=0.4
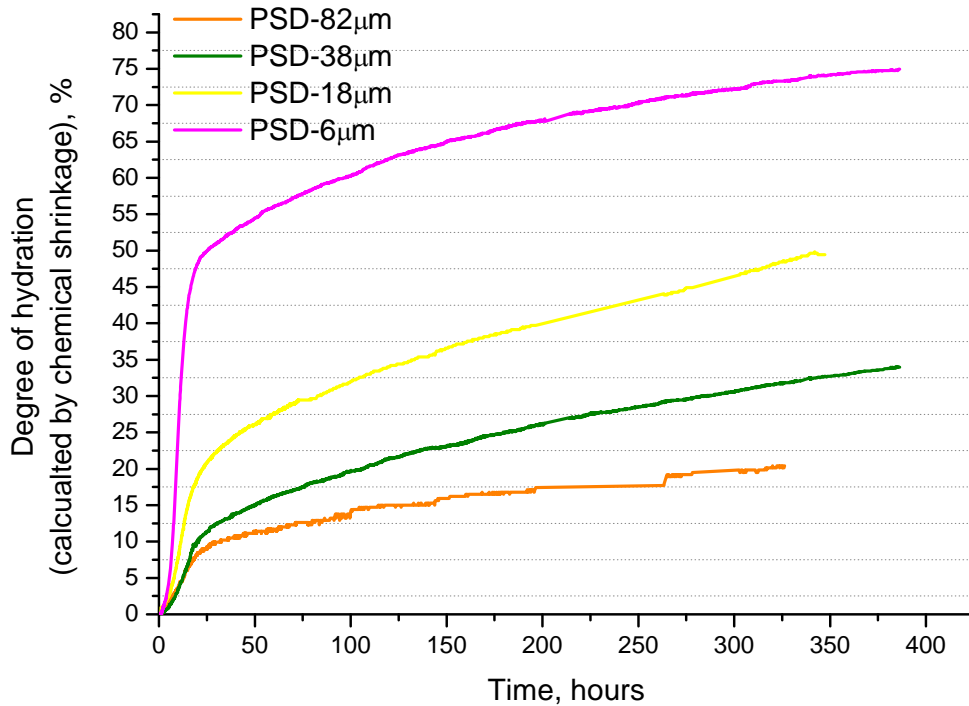
Figure 3.15: Chemical Shrinkage curves of alite pastes with different particle sizes hydrated with a w/c=0.4

The excellent coherence of the degrees of hydration (Figure 3.16) obtained using both techniques (chemical shrinkage and isothermal calorimetry) confirm their reliability for the particle size distribution considered.
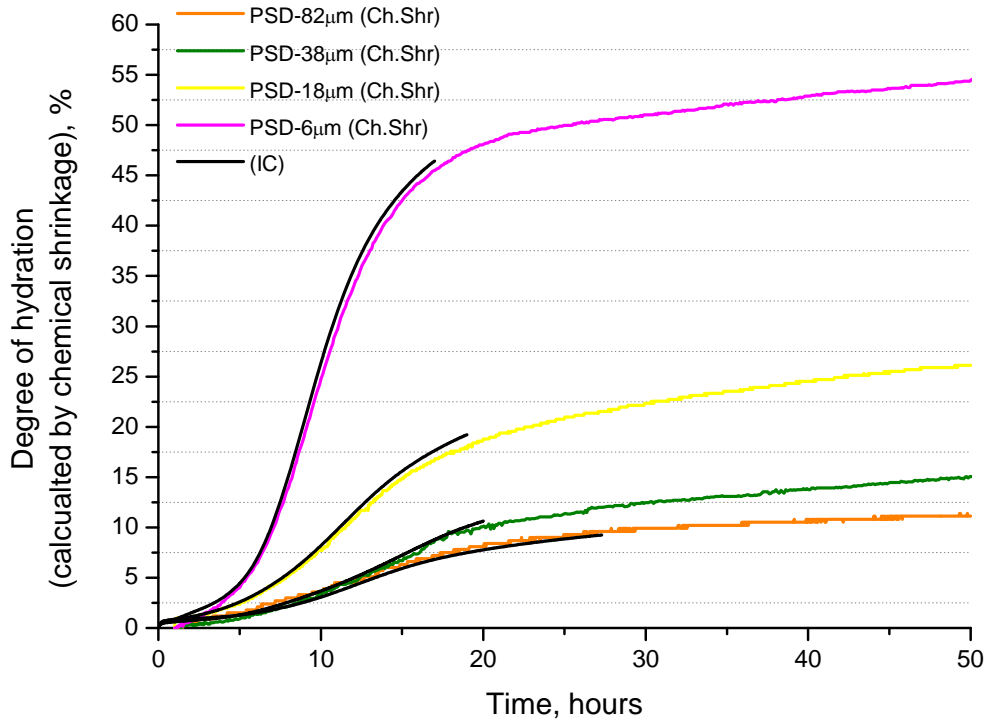
Figure 3.16: Overlapping of degrees of hydration measured by isothermal calorimetry (IC) and chemical shrinkage (Ch.Shr)

The detailed effects of particle size distribution at the different stages of hydration are described in the next sections.

3.3.1 Initial Dissolution

In-situ mixing experiments were carried out to get information about the effect of the particle size on the dissolution peak with a w/c ratio of 0.4. Figure 3.17 shows the dissolution peak for the gradations PSD-82 μm, PSD-38 μm, and PSD-13μm.

Not all the particle sizes were used in this investigation, as some mixes were found to be poorly homogenised after mixing, especially in the case of smaller particles.
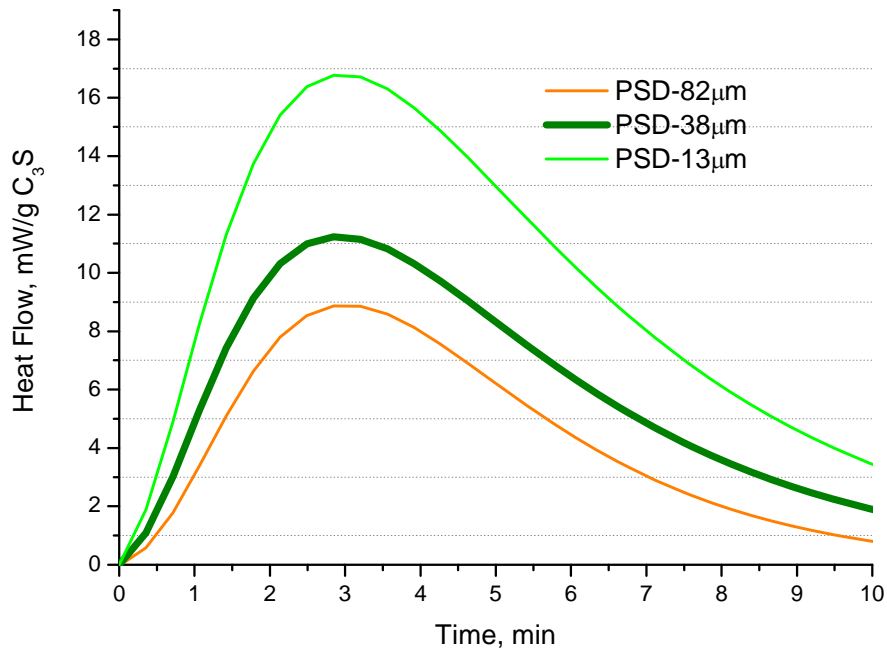
Figure 3. 17: Evolution of the heat flow generated for gradations with different PSDs during the dissolution peak

The general trend observed is the increase of the heat released with increasing specific surface of the particles. This is in agreement with the hypothesis that the dissolution of tricalcium silicate is proportional to its exposed surface. The cumulative heat flow generated at the maximum of the dissolution peak versus the surface area of the grains (calculated by Blaine and the PSDs) is reported in the Figure 3. 18. It shows a dependence of the maximum of heat liberated with the size of the particles, those particles with higher specific surface generating more heat.

However, whether the surface is measured (e.g. Blaine, BET…) or theoretically calculated from the PSD measured from laser granulometry, heat released and surface area follow the same trend: higher heat released for smaller particles. As suggested by some authors and mentioned at the beginning of this chapter, crystalline defects or sub-surface defects due to the grinding of the powders for instance, may be sites for preferential dissolution. In such a case, the dissolution of the particles would rather be related to the density of defects rather than to their surface (although these two could be related).
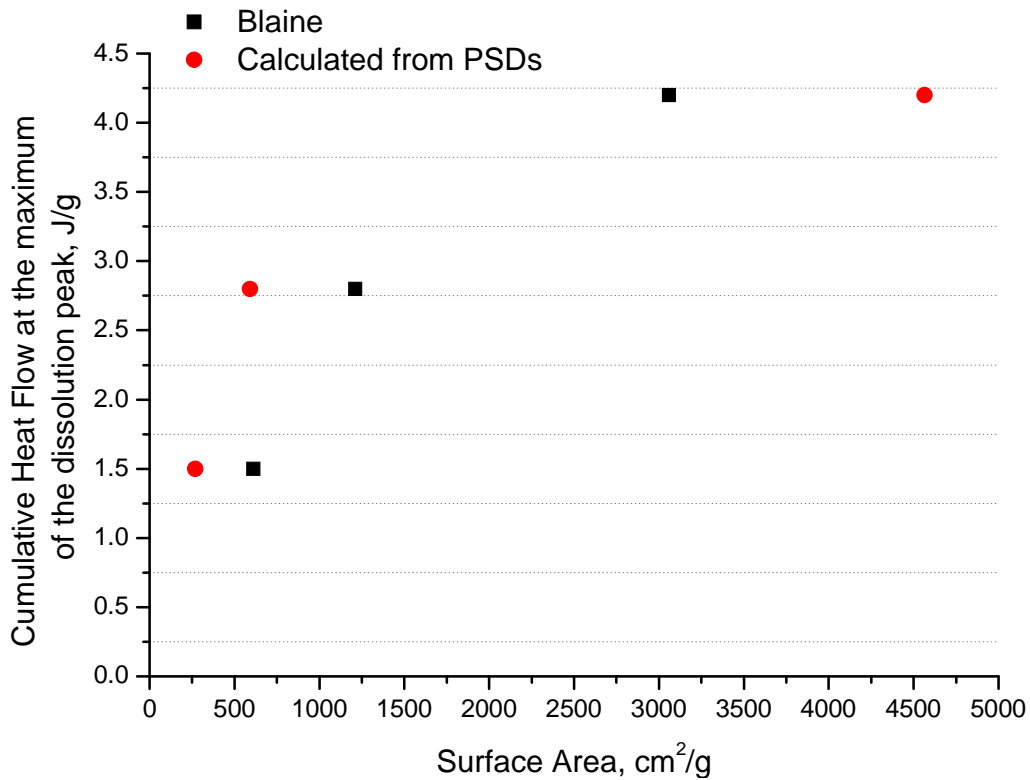
Figure 3. 18: Evolution of t the cumulative heat generated at the maximum of the dissolution peak vs. the surface area (Blaine and calculated) for different PSDs

If we assume that the heat released during the first peak is attributed to the dissolution of Ca^{2+} and silicate ions only [41] then from the heat flows generated for each particle size, the quantity of Ca^{2+} ions dissolved during the hydration process can be, as a first approach and in a very simplistic manner, calculated (Figure 3. 19). Throughout dissolution, C_3S releases 3 mol of Ca^{2+} for 1 mol of silicate ions (Eq. 3.9) for a total enthalpy of -517±13 J/g [6].

$$Ca_3SiO_5 + 3H_2O \rightarrow 3Ca^{2+} + 4OH^- + H_2SiO_4^{2-} \qquad \text{Eq.3.9}$$
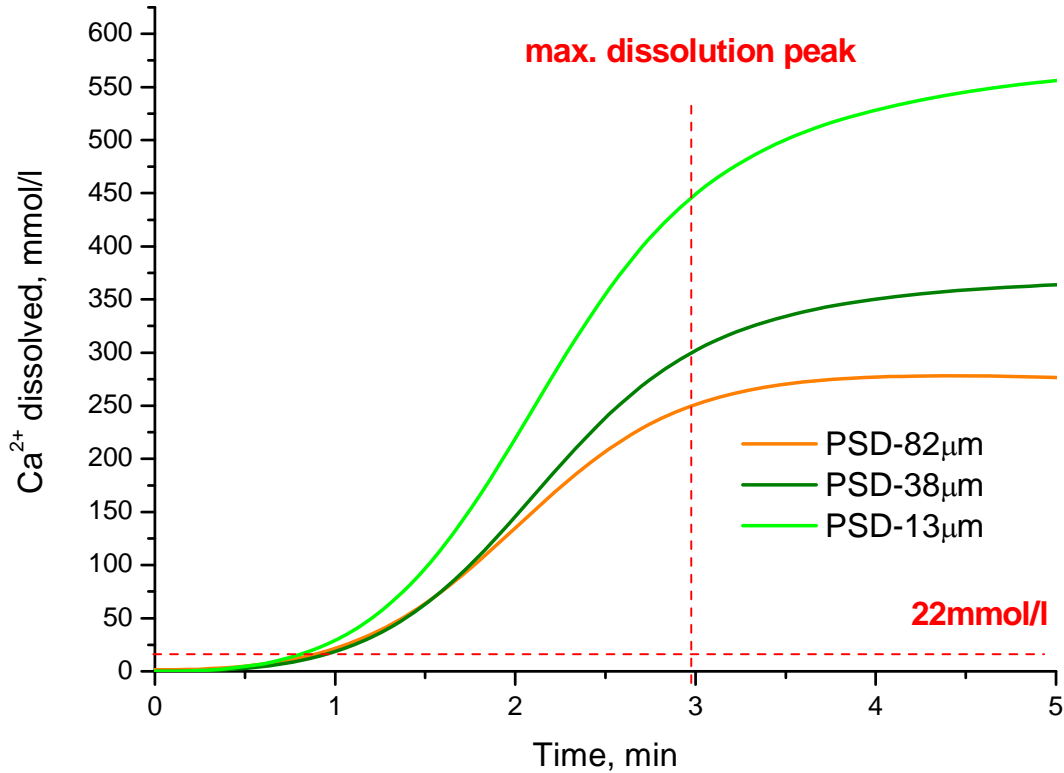
Figure 3. 19: Calcium ion concentrations in solution during the first 10 min of hydration of alite pastes with different particle sizes

In Figure 3. 19, the concentration Ca^{2+} ions dissolved before the maximum of the dissolution period is much higher than the solubility concentration of portlandite in water (22 mmol/ at 25ºC [25,26]). However, in the present study the w/c ratio is much smaller than in the diluted suspensions used in [25,64] (w/c>10) in which the system is always in diluted conditions [5]. This implies that during the first minutes of hydration there are necessarily simultaneous processes taking place, dissolution of C_3S, C-S-H precipitation, and portlandite precipitation.

To gain insight into the effects of defects or lattice distortions on the hydration kinetics of C_3S and particularly on the duration of the dissolution peak, PSD-61µm was annealed at 650ºC for 6 hours and cooled very slowly to reduce the number of defect. Both treated and untreated materials were then hydrated with *in-situ* mixing at 0.7 (w/c). The thermally treated fraction was observed to release less heat than the untreated one (Figure

3.20). Since the particle size distribution before and after the thermal treatment was measured to be the same and no polymorph transformations occurred (Appendix I), the differences found on the kinetics can be only attributed to a lower dissolution of Ca^{2+} and silicate ions for the treated powder. This shows that the dissolution of tricalcium silicate is strongly dependent on the number of defects in its structure.
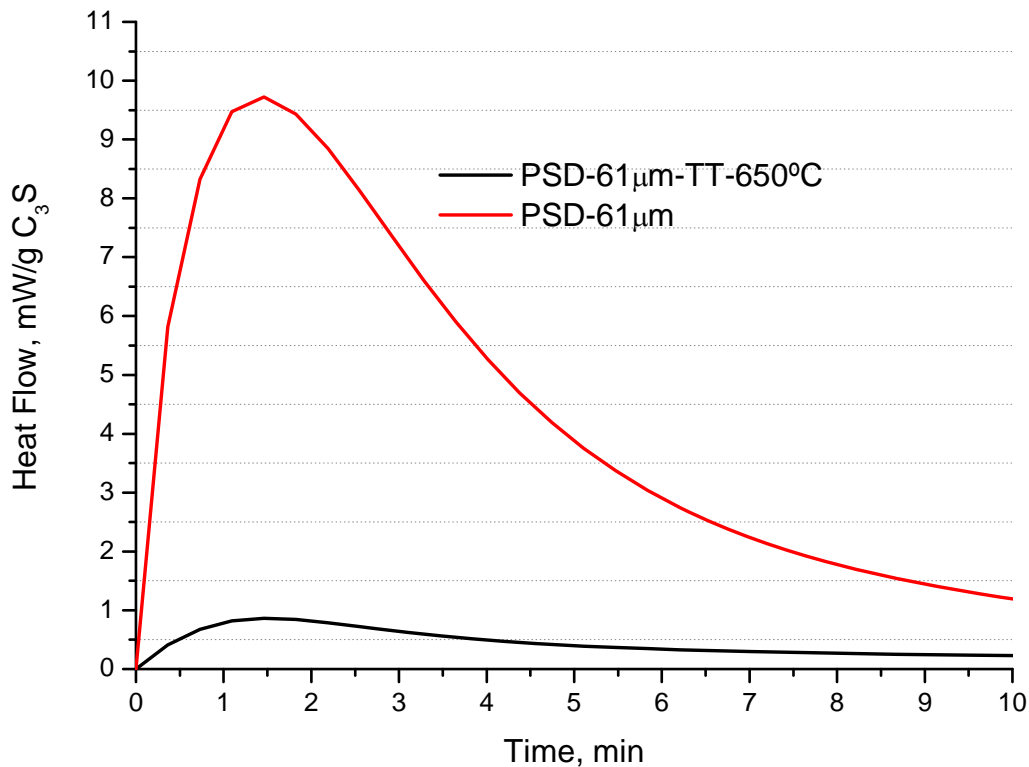
Figure 3.20: Effect of annealing on alite of narrow particle size distribution during the dissolution peak (PSD-61 μm)

To summarize, the dissolution peak has been found to be dependent on surface area and/or lattice distortions. The heat released at the dissolution peak is higher for smaller particles. In the view of being able to describe the hydration kinetics of a mix of various PSDs (e.g. continuous distribution like in alite C2), the dissolution of alite could eventually be simulated based the behaviour of individual particles either semi-empirically from the relation between the heat released and the surface area (Figure 3. 18) or more accurately from the defect density at the surface of each particle (if this is confirmed). In both cases, this implies the generation of knowledge and the collection of very precise data on extremely narrower particles size distributions.

3.3.2 Induction Period

After the end of the dissolution stage (Figure 3. 1) there is a period of slow reaction / low chemical activity commonly termed "induction period". The effect of particle size distribution on the induction period was investigated by isothermal calorimetry using *ex-situ* mixing.

The implications of the particle size for the induction period were investigated on PSD-82µm, PSD-38µm, PSD-18µm and PSD-13µm. Figure 3. 21 shows clearly that the particle size distribution has an influence on the duration of the induction period.
The calorimeter has been calibrated before any measurement to account for the baseline correction.
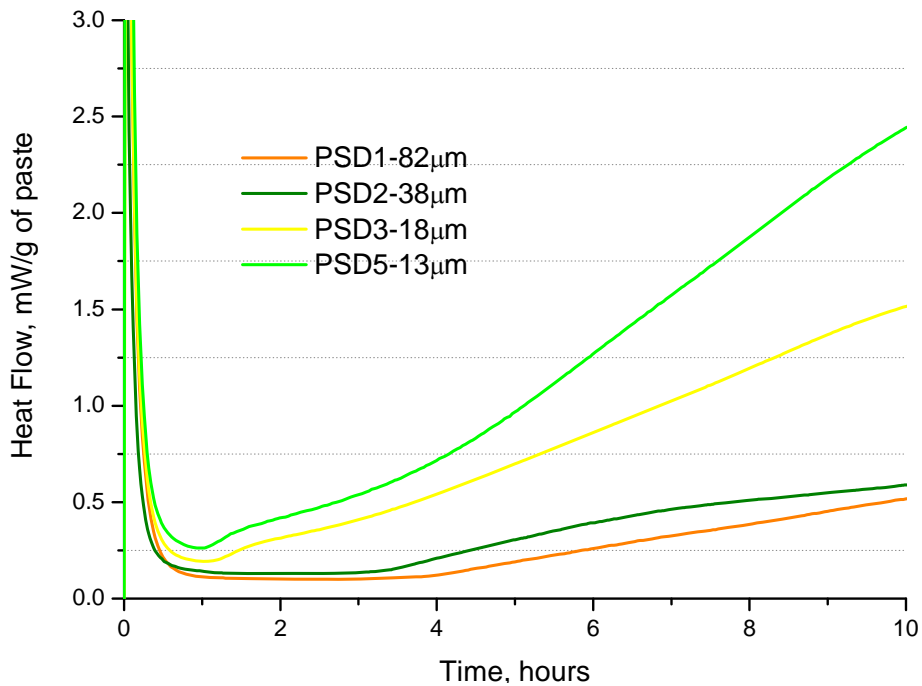
Figure 3. 21: Influence of the particle size on the duration of the induction period

There are two possible ways to define the end of the induction period: (schematised in Figure 3. 22)

- T1: the intersection point between the linear part of the nucleation and growth process and a linear horizontal fit of the induction stage. However, the presence of a small peak before the main peak of the nucleation process makes the definition of this point questionable. The presence of this peak is discussed in § 3.3.3.

- T2: the minimum heat flow after which the heat flow increases.
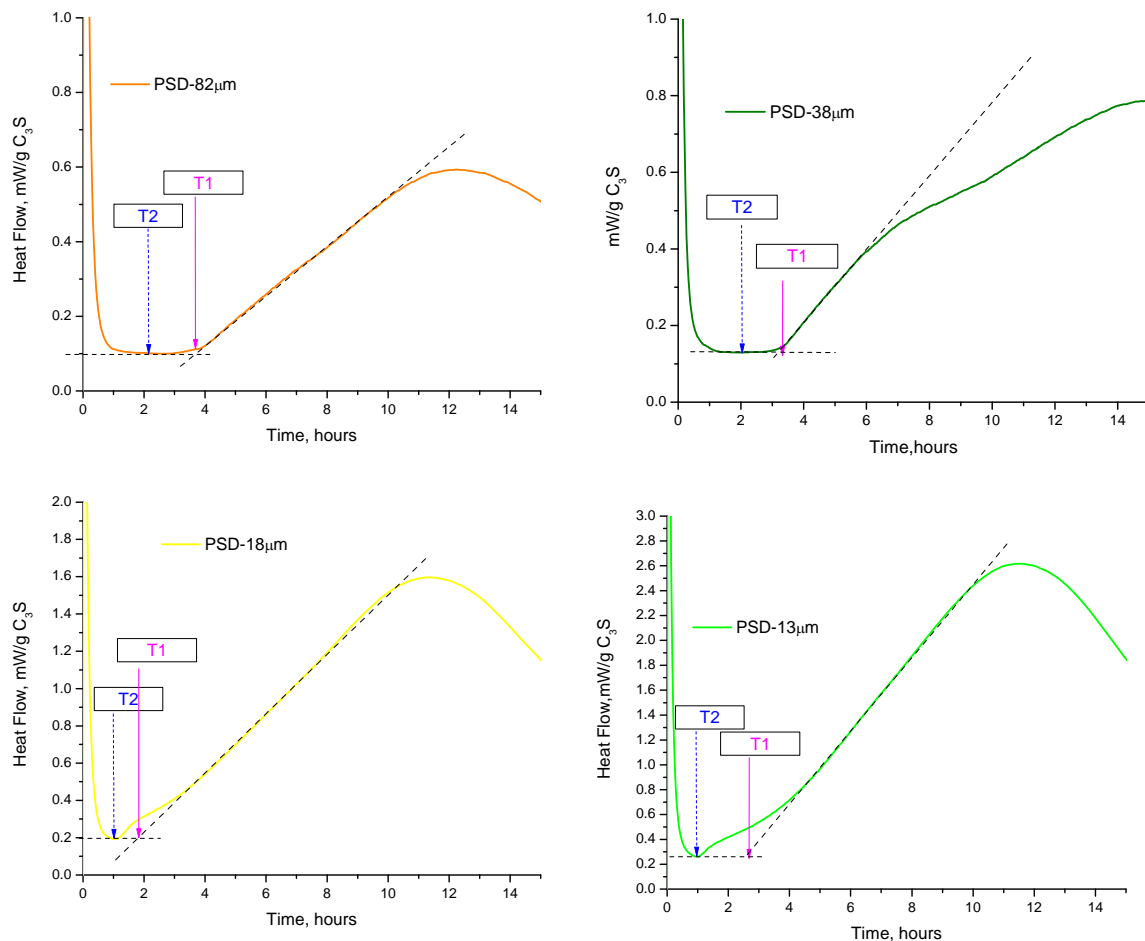
Figure 3. 22: Schematic representation of two possible criteria for the end of induction period taking place:
- T1: intersection point between the linear part of the nucleation and growth process and a parallel line to the time axis in the isothermal calorimetry plot
- T2: minimum heat flow after which the heat flow increases

Table 3. 5 present the values obtained using both criteria for the end of the induction period.

Table 3. 5: End of the induction period attending the two criteria above presented

	T1 (hours)	T2 (hours)	Surface Area (Blaine), cm^2/g	Calculated from PSDs, cm^2/g
PSD-82μm	3.6	2.6	610	268
PSD-38μm	3.2	2.0	1212	591
PSD-18μm	2.0	1.1	2393	1602
PSD-13μm	3.6	0.9	3059	4564

The rate during the induction period is the reciprocal of its length. This quantity is plotted against surface area in Figure 3. 23. Particle size has an influence on the length of this period: longer induction periods were found for particles with smaller surface areas. The same kind of relationship was found between the heat flow released at the end of the induction period and the surface area of the particles as shown in Figure 3. 24. This shows higher heat release at the induction period for particles with higher surface area available for hydration.

The second approach (T2), minimum heat flow after which the heat flow increases, is considered in this work to give the most reliable data: that the point at which the heat flow starts increasing can be considered as indicative of the reaction going into a predominantly nucleation and growth process. T1 values are more questionable due to difficulties for assigning the intersection line, especially because of the small peak before the maximum peak of the nucleation and growth period.
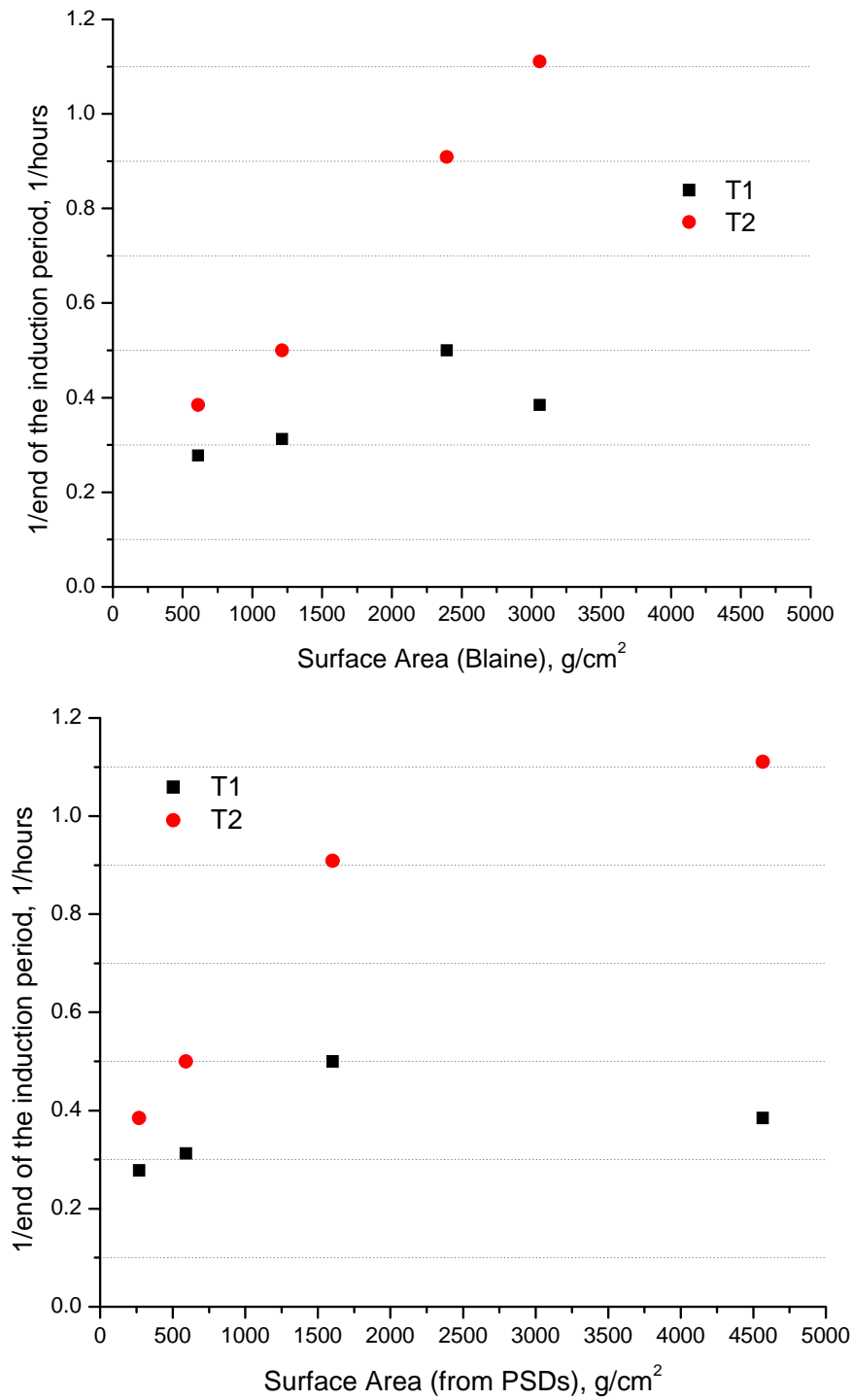
Figure 3. 23: End of the induction period for different particle sizes vs. their specific surface area calculated by Blaine method (top) and from its PSDs (bottom)
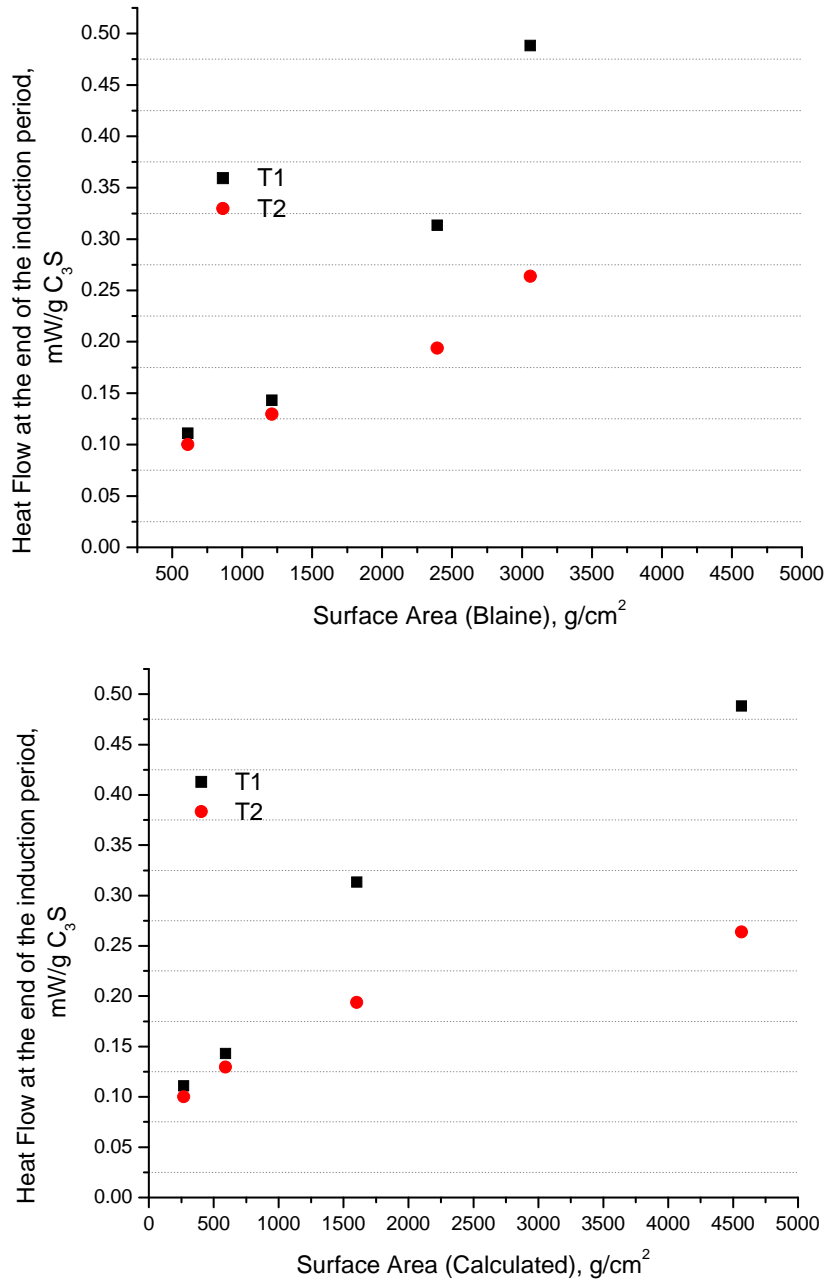
Figure 3. 24: Heat flow released at the end of the induction period for different particle sizes vs. their specific surface area calculated by Blaine method (top) and from its PSDs (bottom)

Figure 3. 25 shows the evolution of the cumulative heat flow at the end of the induction period (assuming T2-the same trend has been also observed assuming T1) with the surface area of the following particle size distributions: PSD-82µm, PSD-38µm and PSD-13µm. The cumulative heat flow has been calculated from in-situ measurements and therefore, considering the heat releases during the dissolution peak. Since the cumulative

heat flow could be related with the amount of hydration product formed it seems, from these experiments, that the end of the induction period does not depend on the amount of C-S-H generated. Nonetheless, this first hypothesis need to be further investigated.
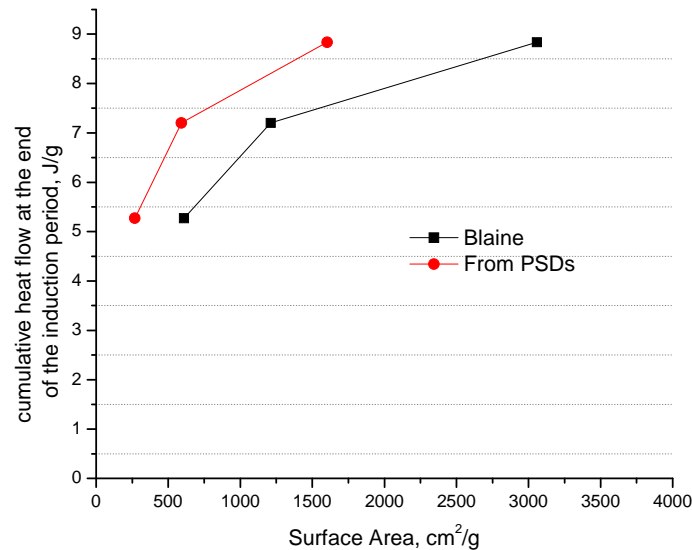
Figure 3. 25: Cumulative heat flow at the end of the induction period for particle size versus surface area for particle size distributions PSD-82µm, PSD-38µm and PSD-13µm

As for the dissolution peak, crystal defects are expected to have some influence on the hydration kinetics. Relating this to the knowledge on the dissolution of minerals from the geo-chemistry point of view [65], these could explain the existence of the so-called 'induction period'. To assess the importance of defects on the duration of the induction period, two narrow particle size distributions (PSD-82µm and PSD-38µm) were annealed at 650ºC for 6 hours and cooled very slowly to reduce the number of defects. Thermal treated gradations showed an elongation of the induction period and therefore a retardation of the time when the maximum heat flow is reached (Figure 3. 26). In addition, the heat flow during the induction period was lower as a result of the drop on their initial activity. Since the psd and XRD patterns are strictly identical before and after the thermal treatment (Appendix I), the change in reactivity observed here can only be attributed to the thermal annealing of structural defects (vacancies, dislocations…)[66].
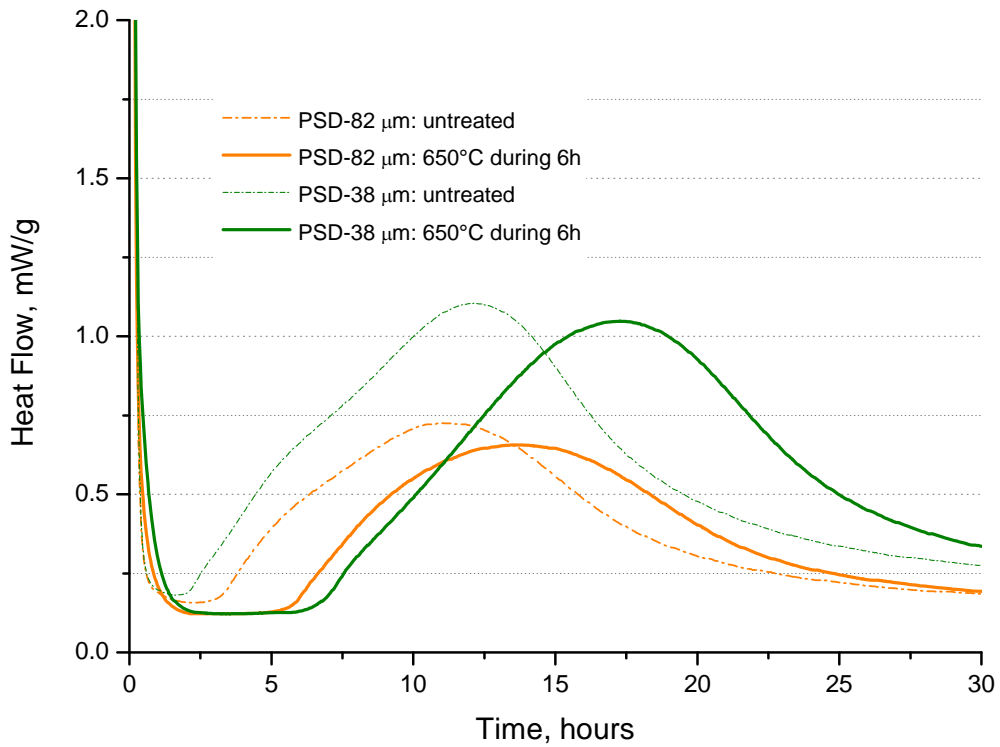
Figure 3. 26: Effect of annealing on alite of narrow particle size distribution

SEM images (Figure 3. 27) of anhydrous alite grains (PSD-82μm) show a surface roughness likely to be related to the presence of lattice defects and thus preferential reactive sites for dissolution.
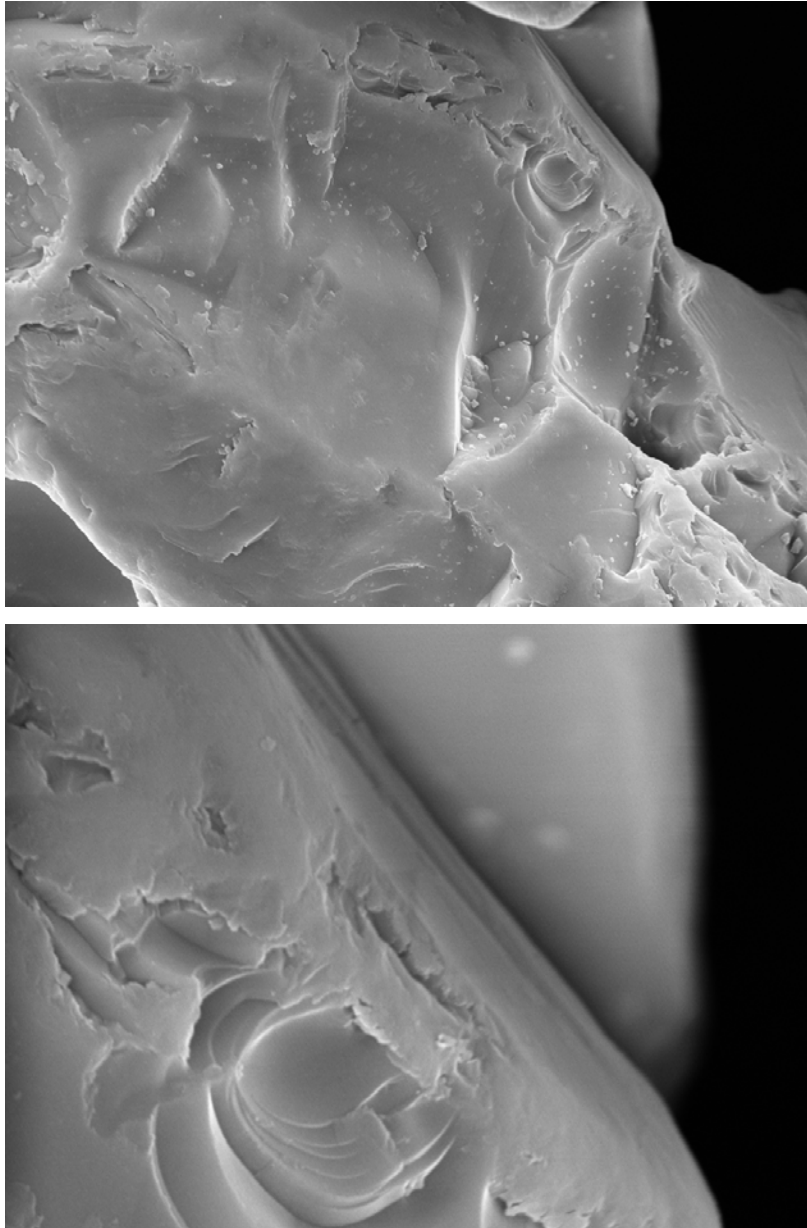
Figure 3. 27: SEM images of anhydrous alite grains (PSD-82μm) showing defects on the grain surface. (This image correspond to the surface of the grains after grinding, not fracture surfaces)

In order to get further insight on the effect of the particle size on the duration of the induction period, two non-overlapping gradations were mixed in the proportion indicated in Table 3. 6 and analysed by isothermal calorimetry (Figure 3. 28).

Table 3. 6: Weight percentage combinations of PSD-82 µm and PSD-13 µm investigated

Sample	% of PSD1-82µm	% of PSD-13µm
100%PSD-82µm	100	0
75% PSD-82µm +25% PSD-13µm	75	25
50% PSD-82µm +50% PSD-13µm	50	50
25% PSD-82µm +75% PSD-13µm	25	75
100% PSD-13µm	0	100

Figure 3. 28: Isothermal Calorimetry curves of the mix of two different PSDs (PSD-82µm and PSD-13µm)during the induction period

Figure 3. 29 shows the evolution of the heat flow at the end of the induction period versus the surface area (calculated from their particle size distribution) of the PSDs at T1 and T2 (assuming the two criteria for the induction period as shown in Figure 3. 24). This shows a strong and almost linear increase in heat flow with the surface area and indicates that an initial level of something has to occur before the end of the induction period to be reached, that is related with the size of the particles.
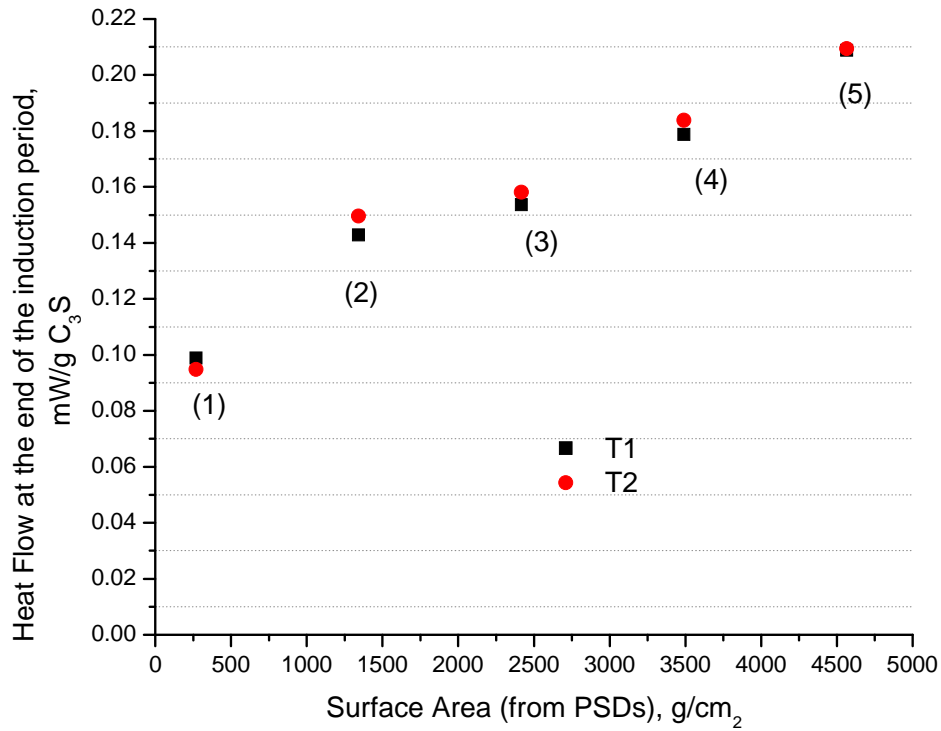
Figure 3. 29: Plot of the heat flow generated at the end of the induction period vs. surface area for the different mixtures

    (1) 100% PSD-82μm

    (2) 75% PSD-82μm + 25% PSD-13μm

    (3) 50% PSD-82μm + 50% PSD-13μm

    (4) 25% PSD-82μm + 75% PSD-13μm

    (5) 100% PSD-13μm

Here again the time at which the induction period take place is related to the surface area of the particles (Figure 3. 30): longer induction period are observed for the mixture with coarse particles.
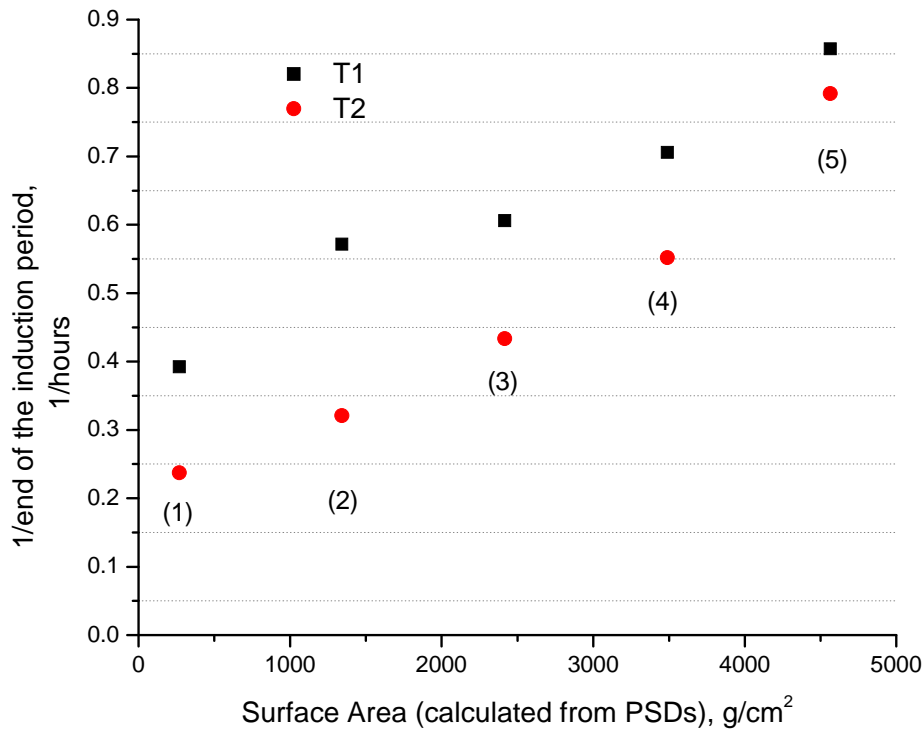
Figure 3. 30: End of the induction period for different particle sizes vs. surface area for the different mixtures:
    (1) 100% PSD-82µm
    (2) 75% PSD-82µm + 25% PSD-13µm
    (3) 50% PSD-82µm + 50% PSD-13µm
    (4) 25% PSD-82µm + 75% PSD-13µm
    (5) 100% PSD-13µm

In Figure 3. 31, the heat flow of these mixtures is compared with the mathematical weighted sum of the heat flow evolution of the two unmixed fractions. The mixtures enter later into the acceleration regime than the calculated average of the two functions separately.

The finer fraction (PSD-13µm) used here contains lot of fines which could give a higher dissolution peak. Since these experiments were carried out *ex-situ*, the energy output during the dissolution peak cannot be taken into account. For instance, the calculated curves in which PSD-82µm (coarser PSD) is predominant are mainly governed by this PSD-13µm (induction period lower than what is actually measured). In the same manner, mixes where PSD-13µm is predominant show calculated heat flow curves which make the transition to the acceleration earlier compare to the measured curves.

In fact, the dissolution of a particle, whatever its size, seems to be highly dependant on of the size of the particles it is mixed with: whatever its size, a particle will behave like a small one and dissolve earlier if the others around are bigger and it will behave like a big one and dissolve later if the others are smaller. Therefore, the calculated curves cannot be corrected to give account of the behaviour of the smallest particles, and the induction period cannot be modelled as a linear addition of the behaviours of individual particles.
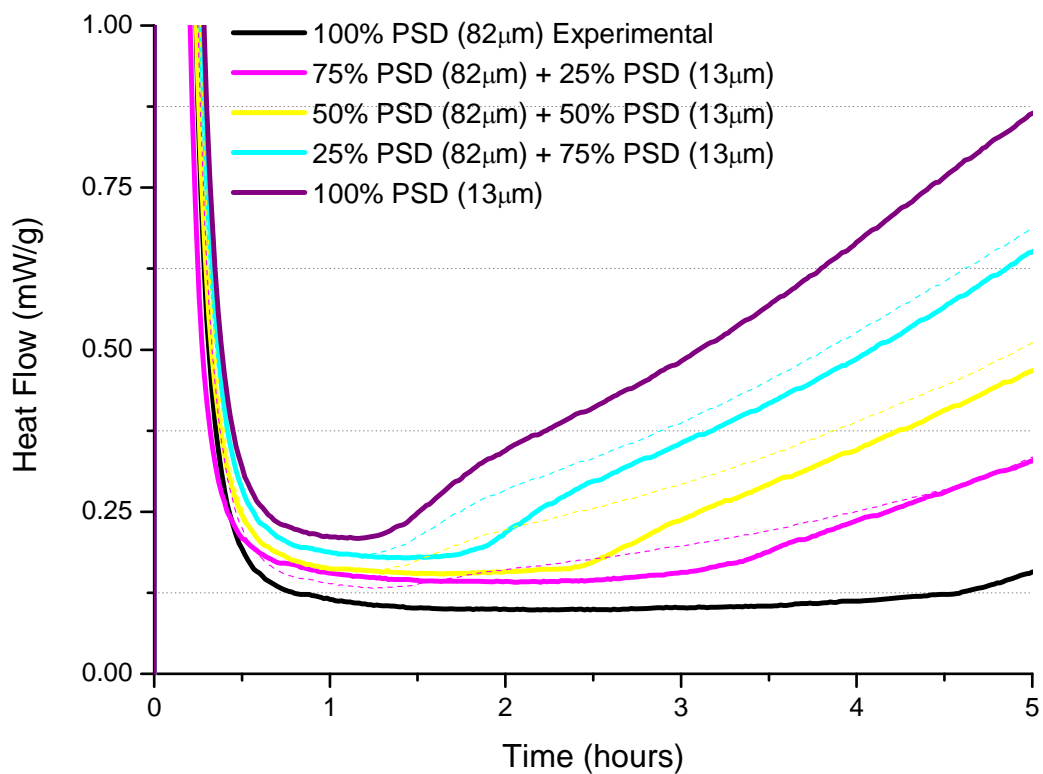
Figure 3. 31: Comparison of the experimental (continuous lines) and calculated (dotted lines) isothermal calorimetry curves of the mix of different PSDs (PSD-82µm and PSD-13µm)

To summarize, two main parameters, which are probably linked, particle size and number of defects in the crystallographic structure of alite, were found to be related with the elongation on the induction period. An increase of the number of defects and of the surface area of the particles leads to an augmentation of reactivity.

3.3.3 Acceleration Period (Nucleation and Growth)

During the so-called acceleration period, the rate of reaction increases continuously until it reaches a main peak.

In the materials studied here (Figure 3.13) a main peak was identified. However, most obviously in the case of PSD-6µm (Figure 3. 32) and also in some other particle sizes a bump at the very beginning of the so-called nucleation and growth process was also observed. Two explanations can be proposed to explain this phenomenon. Firstly, due to the bimodal particle size in the case of PSD-6µm, this peak could be attributed to the reaction of the finest particles. On the other hand, and as suggested by Damidot, Nonat and Barret [64] this could be attributed to the precipitation of portlandite. The precipitation of portlandite is an endothermic process and thus the diminution on the heat flow at this first peak may be attributed to this precipitation.
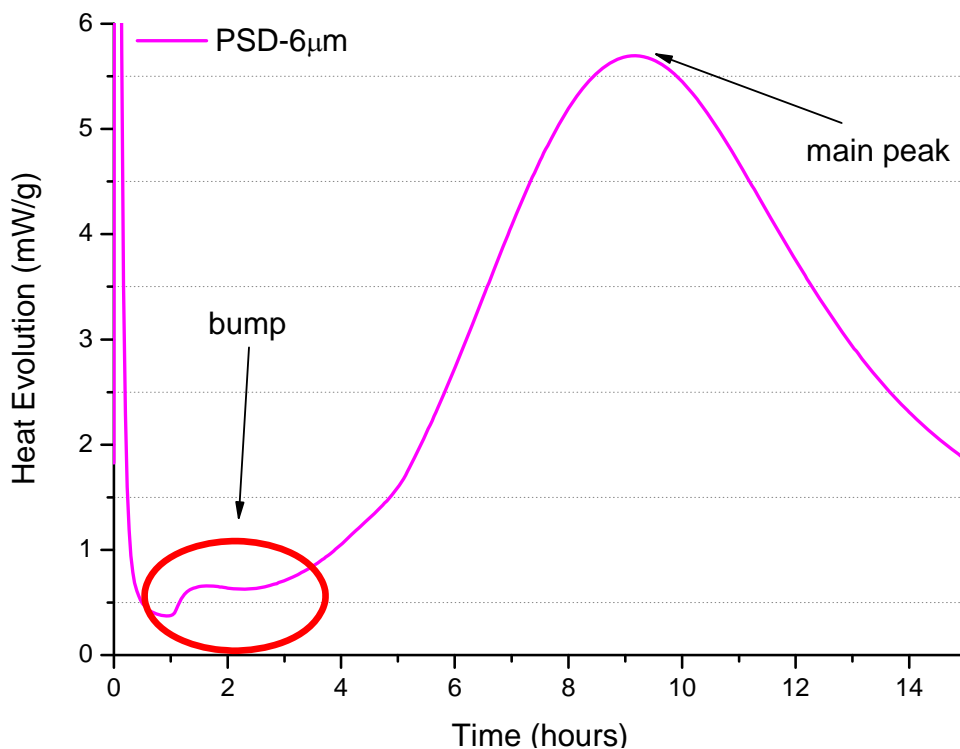
Figure 3. 32: Isothermal calorimetry curve of PSD-6µm

Fitting of the Isothermal Calorimetry curves by the Avrami equation

The generalized form of the Avrami equation discussed earlier (Eq.3.2) can be differentiated. This leads to:

$$\frac{d\alpha}{dt} = knt^{n-1}e^{-kt^n} \qquad \text{Eq.3. 10}$$

For small values of t and k, the exponential part of Eq.3. 10 can be neglected in a first approach. Further, if we assume n equal to 2 (n was obtained from the fit of the linear part of the acceleration period for different particle size distribution with Avrami equation and is shown in more details later on) the equation can be written as:

$$\frac{d\alpha}{dt} = 2kt \qquad \text{Eq.3. 11}$$

Figure 3.11 can be used for a simplified analysis to obtain estimates of k. Since the relation is linear, the linear part of heat-evolution curves (Figure 3. 33) were extracted and fit using linear regression. The obtained values for k are plotted against the specific surface area of the respective powders, calculated by using Blaine method and from the PSDs in Figure 3. 34. The figure shows a predominantly linear variation of k with specific surface.
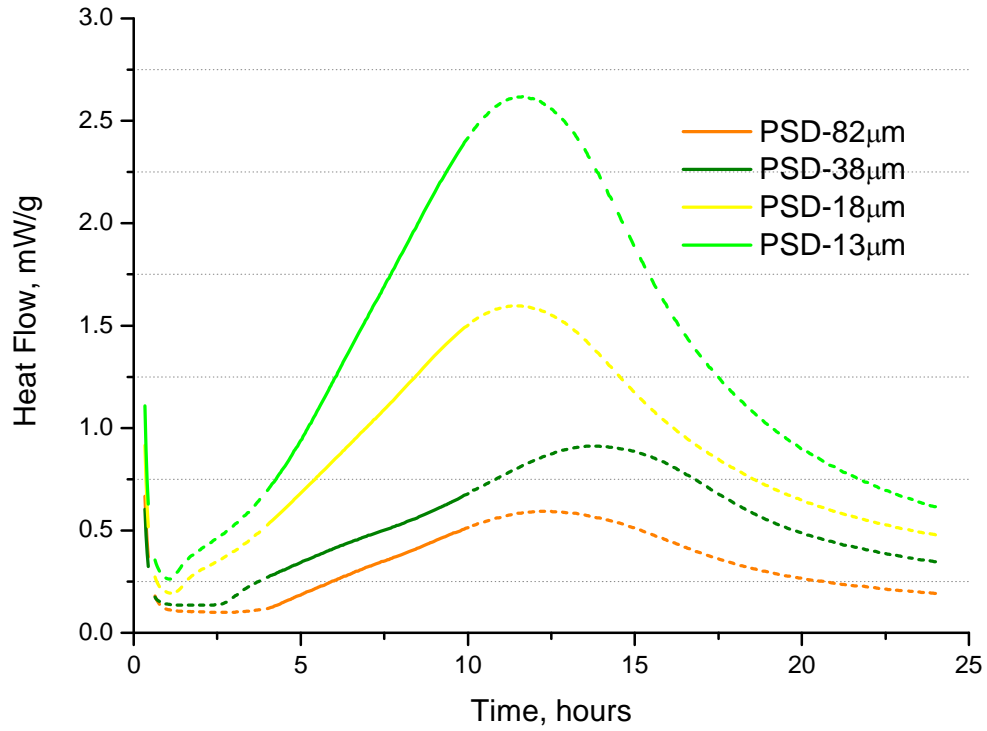
Figure 3. 33: Linear part of the isothermal calorimetry curves (continuous line) for alite pastes of different particle sizes
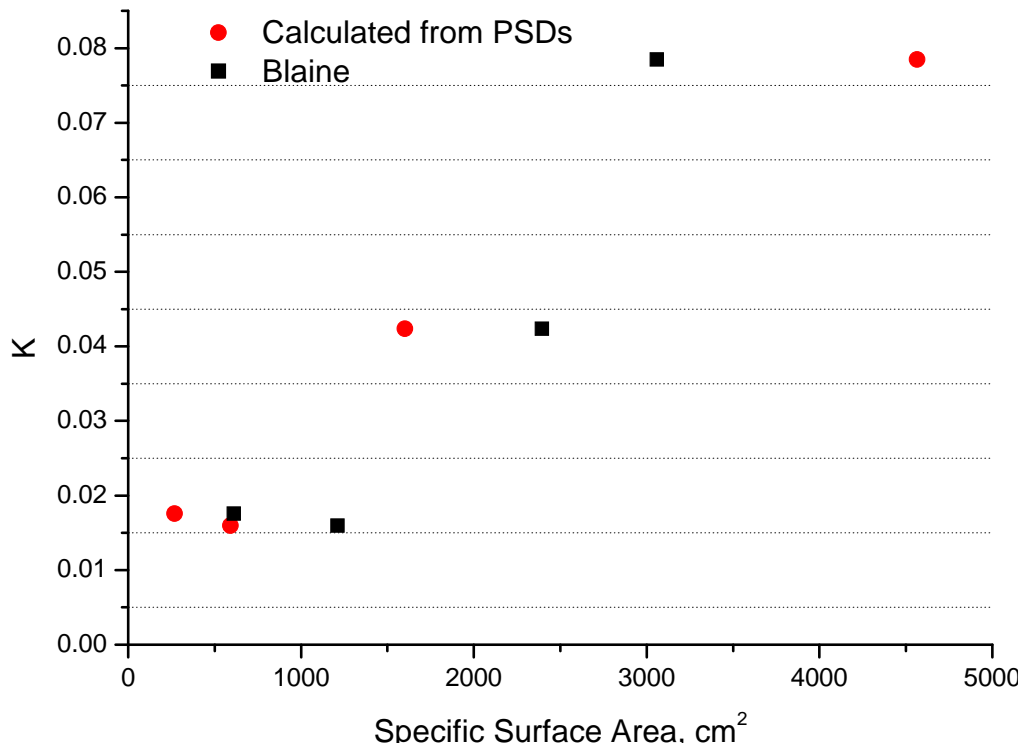
Figure 3. 34: Rate constant against specific surface area calculated by Blaine method and from their PSDs for different fractions of C_3S.PSD-82µm, PSD-38µm, PSD-18µm and PSD-13µm

In the next step, the calorimetric curves of two non-overlapping gradations of Alite (PSD-38μm and PSD-240μm) were measured under isothermal conditions. Another third gradation was obtained by a 50-50 mix of these two powders. A generalized form of Avrami equation was then fit to these results (Figure 3. 35). For the sake of simpler analysis, the equation was modified to the form:

$$\alpha = \alpha_{max}\left(1 - e^{-k(t-t_0)^n}\right) + \alpha_0 \qquad \text{Eq. 3.2}$$

Where α is the degree of hydration calculated from the measured cumulative heat, α_{max} is the maximum possible degree of hydration, which should ideally be 100%. The parameters t_0 and α_0 account for any time lag in the reaction (including sampling delay) and the dissolution peak.

The results show that though the Avrami equation can very well emulate the shape of these curves, the obtained parameters do not make physical sense (Figure 3. 35) [67,68]. For example, the equation calculates widely varying values of α_{max}, which should ideally be 100%. This can be explained by the fact that that since for these rather large particle sizes, the reaction moves to the diffusion regime quite early, the rate of reaction slows down early. The Avrami equation, being based on the assumption of homogenous nucleation and growth being the rate controlling mechanism, fails to correctly emulate this behaviour.

Table 3. 7: n and α_{max} values obtained from the fitting with Avrami eq.

	PSD-38μm	50-50 mix	PSD-240μm
n	3.00±2.11	2.11±0.18	2.34±0.47
α_{max}	15.85±1.123	10.37±0.66	5.56±1.09

However, some other interesting facts can be derived from this analysis. The calculated error estimates in n were observed to be quite large (Table 3. 7). This shows that the fit is

not very sensitive to the value of n and explains the discrepancy in the values in literature, with values varying between 1.5 and 3.

Nevertheless it is important to know if the particles in a given size range have the same kinetics in a mono-sized mixture as in a mixture of several particle sizes. Figure 3. 36 shows the comparison between the degrees of hydration for the mixed powders, plotted against the average of the observed degrees of reaction for the two non-overlapping gradations. It can be seen that not only is this plot linear, the slope of the plot is 1 indicating that in the initial part of the reaction, the hydration of the system could be modelled as the linear addition of individual gradations. This hypothesis need further investigation and is discussed below.
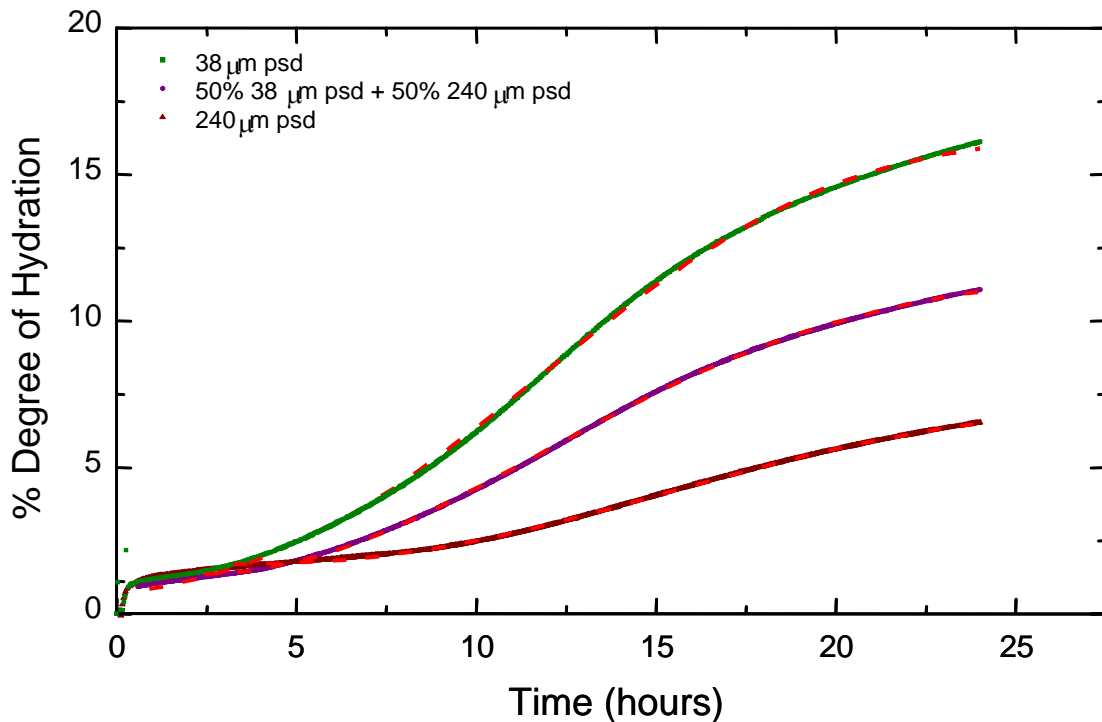
Figure 3. 35: Avrami equation fit for non-overlapping psds
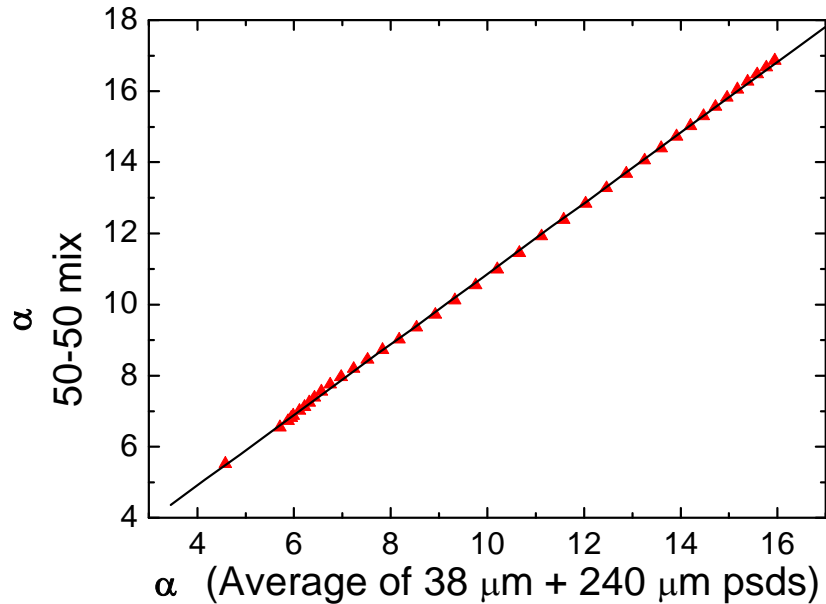
Figure 3. 36: Plot of the degree of hydration for the average of two non-overlapping gradations against the degree of hydration of its 50-50 mixture

<u>Could be the hydration kinetics of alite during the acceleration period be modelled as a linear addition of individual particles?</u>

To verify the hypothesis that the hydration of multi-sized systems could be modelled as the linear addition of individual particles during the acceleration period, several mixtures of 2 different powders (PSD-82µm and PSD-13µm) were investigated (Table 3. 6). When the experimental cumulative heat curves (Figure 3. 37) of the different gradation was plotted against the calculated values, the same linear dependency was found as shown in Figure 3. 38. Consequently with these results, the hydration of the system can be modelled as the linear addition of individual gradations.
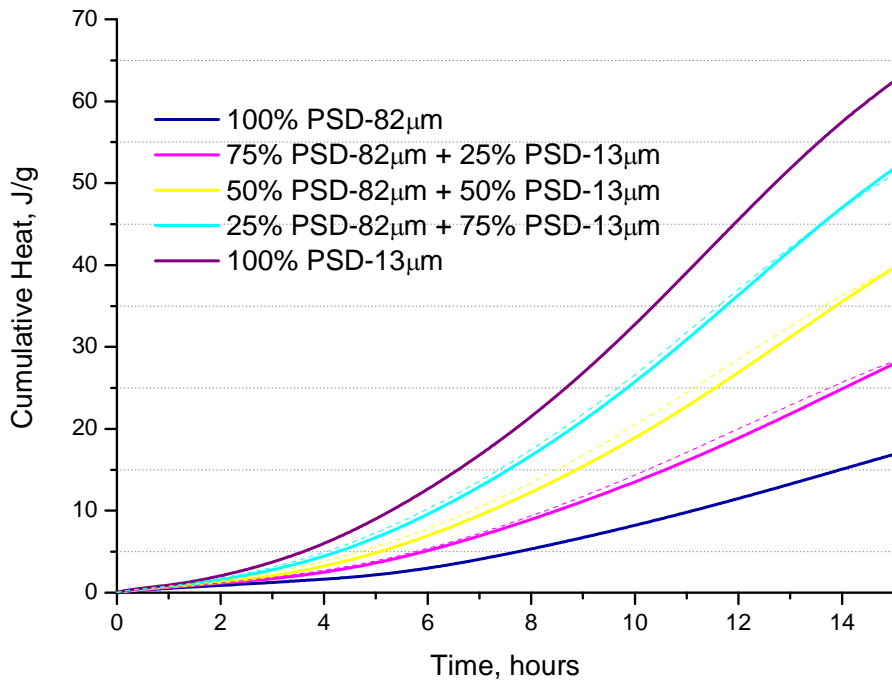
Figure 3. 37: Isothermal calorimetry curves for 2 powders (PSD-82µm and PSD PSD-13µm): comparison of experimental (continuous lines) and calculated (dotted lines) curves.
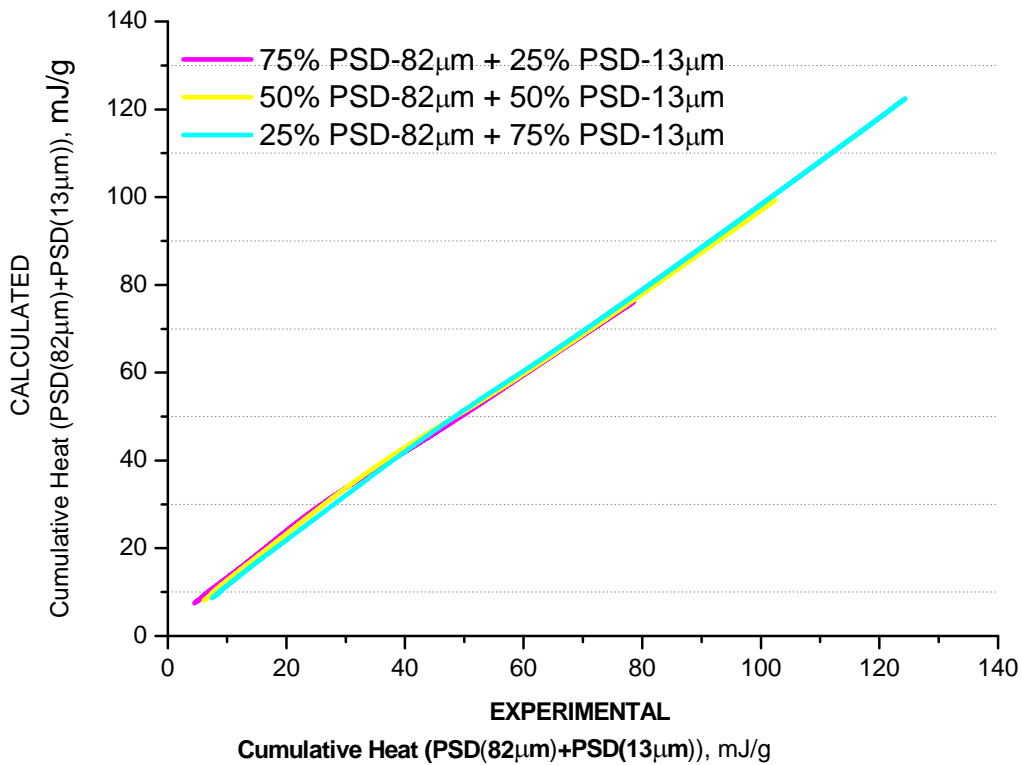
Figure 3. 38: Plot of the experimental cumulative heat for the mixture of two different gradations against the calculated cumulative heat

Figure 3. 39 shows the cumulative heat flow generated at the maximum of the heat flow peak plotted against the surface area (calculated from their particle size distribution) of the different particles. A linear relationship is observed, meaning that instantaneous heat generation can be computed as the linear addition of the heat generated for each particle.
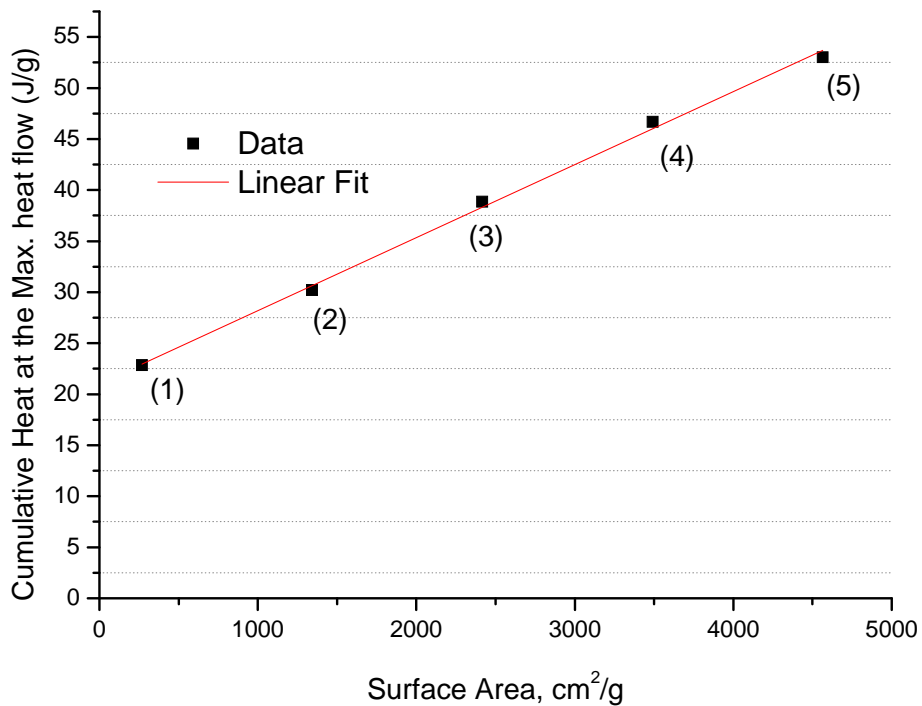
Figure 3. 39: Cumulative heat generated at the maximum of the peak for the acceleration period vs. the surface area for different gradations (Table 3. 6)
    (1) 100% PSD-82μm
    (2) 75% PSD-82μm + 25% PSD-13μm
    (3) 50% PSD-82μm + 50% PSD-13μm
    (4) 25% PSD-82μm + 75% PSD-13μm
    (5) 100% PSD-13μm

3.3.4 Later Period

During this stage the rate of hydration slows down and can continue for as long as water is supplied to the system and anhydrous grains remain. This process is often considered to be governed by a diffusion-controlled mechanism (§.3.1.): upon hydration, the C-S-H layer around un-reacted grains becomes thicker, making the movement of ions through it slower. Chemical shrinkage was used to follow the hydration during this process when isothermal calorimetry is not reliable any longer due to the low rate of reaction: the intensity of the signal cannot be discriminated from the background. The degree of hydration calculated from chemical shrinkage measurements of C_3S pastes with various particle size distributions is given in Figure 3. 40. Although the degree of hydration keeps increasing over time, system stabilizes (the slope of the curves remaintain more or less constant) during the first ~150 hours from which the curves follow the same trend.
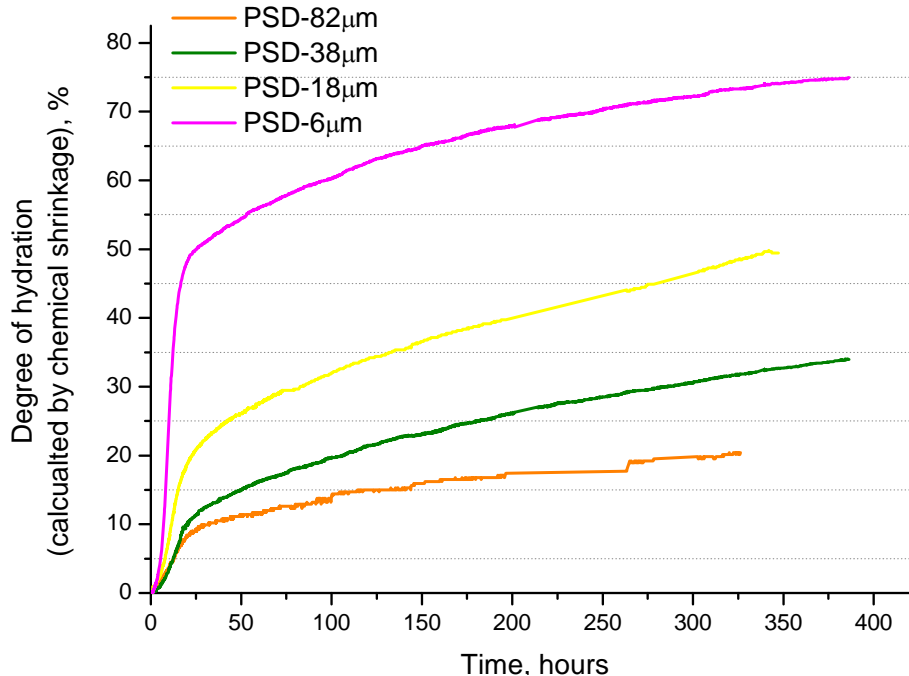
Figure 3. 40: Degree of hydration calculated from chemical shrinkage measurements vs. time for alite pastes with different particle sizes hydrated with a w/c=0.4 (using cylindrical flasks)

As a first attempt to investigate how the particle size is affecting the "diffusion" process, the degree of hydration calculated from the chemical shrinkage for different particle sizes was plotted against time (Figure 3. 44). In a first approach, the curves were fitted using a simple power law (Eq.3. 12).

$$\alpha = At^n \qquad \text{Eq.3. 12}$$

Then, taking the logarithm of both sides of the equation (Eq. 3.13) gives:

$$\log(\alpha) = \log A + n\log(t) \qquad \text{Eq.3. 13}$$

where α is the degree of hydration, log A is the origin and n is the slope of the curve (n should be 0.5 for diffusion-controlled mechanisms.

The logarithm of the degree of hydration versus time is plotted in Figure 3. 41. The time at which the maximum of heat flow during the nucleation and growth process take place is delimited between dotted lines: 9-12 hours, depending on the particle size. If a diffusion-controlled process is assumed, the relation between log(time) and log(degree of hydration) should be linear. This is not the case here from or at least just after the point of maximum heat flow. Therefore, if a diffusion process exists it starts much later.
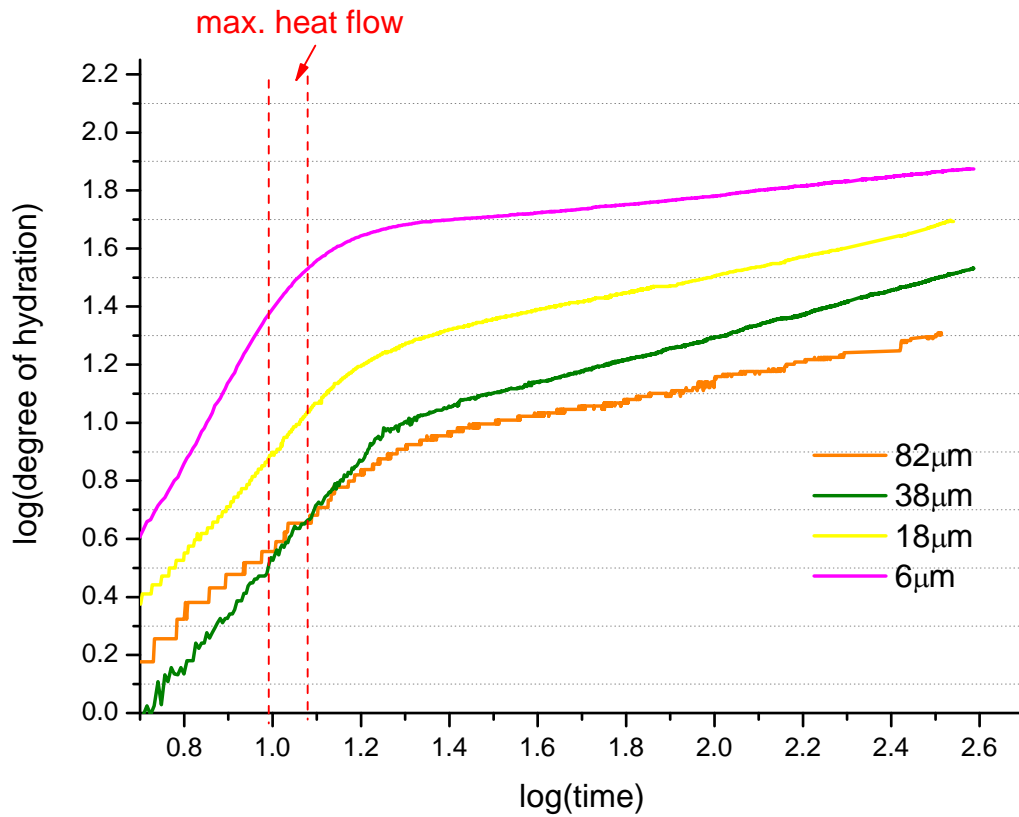
Figure 3. 41: Logarithmic plot of degree of hydration calculated from chemical shrinkage measurements

Another way to look at that question relates to the thickness of the C-S-H. If a diffusion process is assumed to explain the slowing down of the reaction after the main reaction peak, this would imply that it occurs for a same thickness of the CSH layer which will have been formed during the nucleation and growth process.

Assuming spherical particles, the evolution of the C-S-H thickness over hydration can be calculated by the differentiation of the degree of hydration obtained from the chemical shrinkage measurements (Figure 3. 43).

A schematic representation of the approach used for the calculation is presented in Figure 3. 42. Using Eq.3.14 and Eq.3.15 the thickness of C-S-H (e_{C-S-H}) can be deduced from Eq.3.16.

$$R_{in} = R_0 \cdot (1 - DH)^{1/3}$$
Eq.3. 14

$$R_{out} = R_0 \cdot (1 - DH + \chi \cdot DH)^{1/3} \qquad \text{Eq.3. 15}$$

$$e_{C-S-H} = R_{out} - R_{in} \qquad \text{Eq.3. 16}$$

where R_0, R_{in} and R_{out} are the original, remaining and newly generated particle radii (including the original radius of the grain plus the C-S-H rim). DH (α)is the degree of hydration and e_{C-S-H} is the thickness of the total C-S-H layer. χ is a parameter which dependent on the C-S-H density ($\chi = V_{C-S-H}/V_{C3S}$).
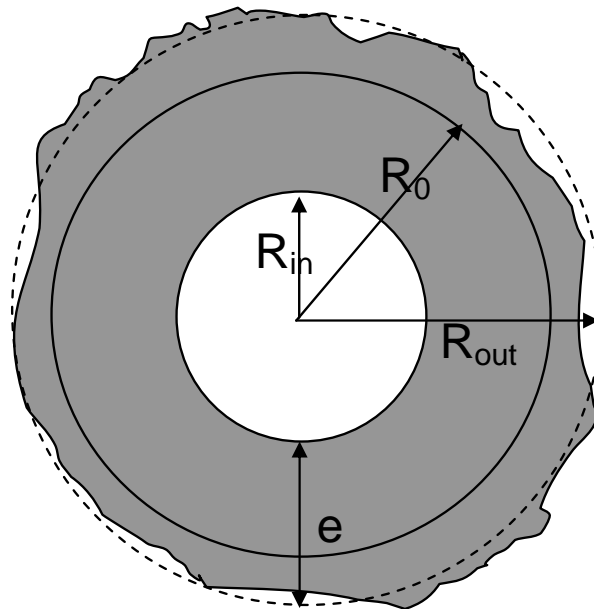
Figure 3. 42 :Schematic representation of the C-S-H growth

In Figure 3. 43 the rate of hydration for different gradations of C_3S obtained from the chemical shrinkage measurements are plotted versus the calculated thickness of C-S-H. As already discussed, the rate of hydration is higher for gradations with higher specific surface area available for hydration. This plot clearly shows that at the maximum of the peak the thickness of C-S-H generated for each particle is different. Zajac [40] proposed that the time from which the maximum heat flow is reached and from which nucleation and growth period becomes diffusion-controlled is dependent on the available surface area for C-S-H deposition. If this is true, then the thickness of the C-S-H layer at which

the process becomes diffusion-controlled must be the same for all gradations at the maximum of the heat flow.

Figure 3. 43 shows that the thickness of the C-S-H layer formed at the peak is different for each gradation. The C-S-H formed for coarse particles is thicker as the result of less surface area per unit mass product deposition. This leads to the hypothesis that the process, at least at the top of the maximum heat flow peak, it is not being governed by a diffusion-controlled mechanism.
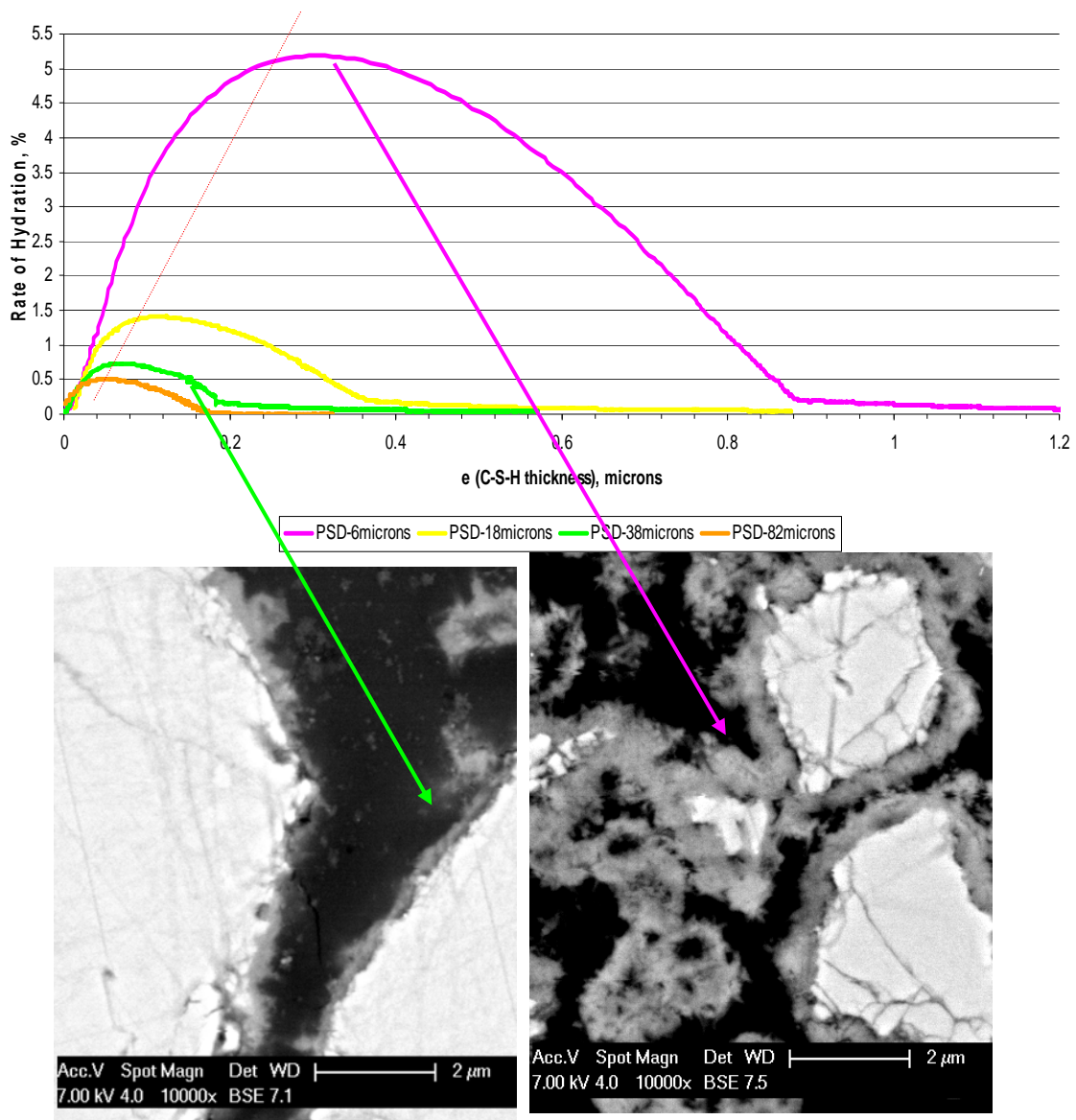
Figure 3. 43: Rate of Hydration calculated from chemical shrinkage measurements versus the thickness of C-S-H at the maximum of the heat flow peak (10-12hours depending on the particle size)

Later on, after about 18 hours, depending on the initial size of the grains, the curves indicate a change of the slope from which the increase of hydration degree becomes more linear. This transition to a linear regime is concluded after 24 hours. At this point we can assume that the mechanism of hydration could be diffusion controlled.

The fit for the relations was therefore done from the time at which the increase of hydration becomes constant (Eq. 3.13).
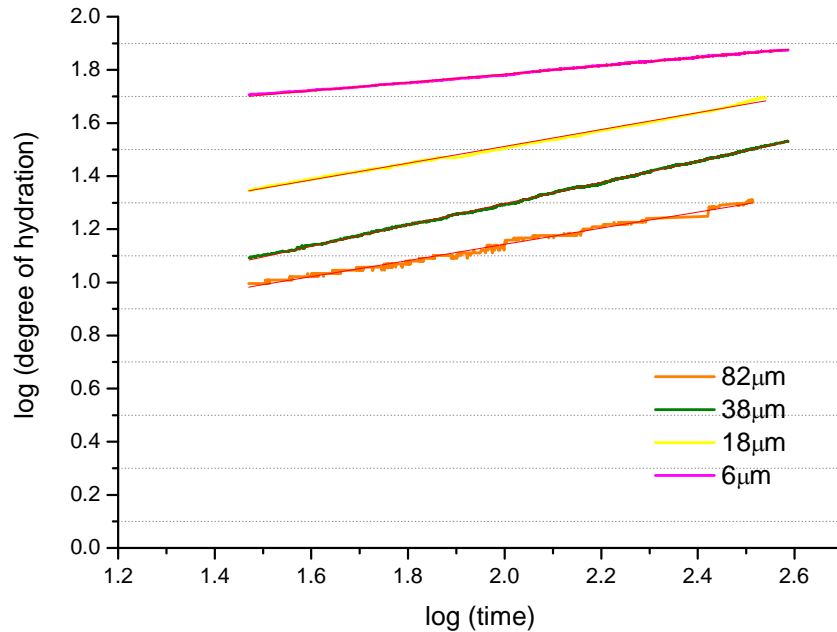
Figure 3. 44: Linear fitting of the degree of hydration obtained by chemical shrinkage after 24 hours of hydration (when the mechanism is diffusion controlled)

Table 3. 8 shows the coefficients obtained from the fitting of the curves for the different particle sizes. With the exception of PSD-82μm for which some inconsistency was regularly experienced -- probably due to bleeding effects -- see chapter 4, the slope of the curves decreases slightly with increasing surface area of the particles. These first results indicate that the later age hydration process could be affected by the initial size of the grains. However, further investigations with narrower gradations are needed to confirm the trend.

On the other hand, the general trend observed for n, specially in PSD-82 μm , PSD-38 μm and PSD-18 μm , is to tend to 0.5 as expected for a diffusion-controlled mechanism, meaning that at that stage the process governing the hydration could be diffusion-controlled or close to it.

The lower values of n for PSD-6μm can be explained by small grains having been completely hydrated. Its small particle size is such that at this stage of the hydration, most of the particles have already completely reacted.

Table 3. 8: Parameters derived from the fit of the degree of hydration (calculated by chemical shrinkage) vs. time using Eq. 3.13 when the process is diffusion controlled

Sample	n	Error n	Surface Area (cm2/g) from PSDs	Surface Area (cm2/g) by Blaine
PSD-82μm	0.30431	0.0004	268	610
PSD-38μm	0.3999	0.0003	591	1212
PSD-18μm	0.3163	0.0003	1602	2393
PSD-6μm	0.1583	0.0003	12735	2952

3.4 Summary

- A combination of chemical shrinkage and isothermal calorimetry has been used to follow continuously the ongoing reaction of different particle size distributions of alite and to investigate their hydration kinetics. The rate of heat generated during the first hours was followed by the means of isothermal calorimetry and afterwards, when this method is not sensitive any longer due to the low reaction rate, chemical shrinkage was employed.

- The degree of reaction calculated from chemical shrinkage is highly dependent on the assumed density of C-S-H which varies very slightly with the gradation. The measured chemical shrinkage was converted into degree of hydration. Good concordance with values given from other techniques such as calibration with the degree of hydration computed from image analysis validates this method to follow the ongoing hydration of alite pastes.

- The dissolution peak was found to depend on the particle size and/or the density of crystallographic defects, higher values of heat liberated were found for smaller particles.

- The duration of the induction period was shown to be dependent on the particle size and the number of crystal defects on the alite grains. The decrease of crystal defects and the decrease of surface area lead to longer induction periods.

- The observed rates of nucleation and growth were found to be higher for powder with higher specific surface. The heat evolution rates were fit against a modified form of the Avrami equation and a roughly linear relationship between the rate constant and the specific surface area was observed. Furthermore, it was observed that the hydration of multi-sized system of tricalcium silicate can be modelled as the linear addition of individual particles.

▪ The later age kinetics were investigated by following chemical shrinkage and were found to be dependent on the particle size. The C-S-H layer at the maximum of the heat flow was calculated and found to be different for each particle size. Contrary to the general assumption, at 18-24 hours, significantly after the maxima of the main heat evolution peak, there appeared to be a change in the mechanism. The power law exponent in this latter regime was around 0.3-0.4, somewhat lower than the values of 0.5 expected for a diffusion controlled regime.

REFERENCES

[1] G. Frigioine, S. Marra, Relationship between particle size distribution and compressible strength in Portland cement, Cement and Concrete Research 6 (1976) pp. 113-128

[2] J.M. Pommersheim, Effect of particle size distribution on hydration kinetics, in Materials Research Society Symposium Proceedings 85, L.J. Struble and P.W. Brown (EDS.) Materials Research Society, Pittsburgh (1987) pp. 301-306

[3] T. Knudsen, The dispersion model for hydration of Portland cement. I. General concepts, Cement and Concrete Research 14 (1984) pp. 622- 630

[4] Dale P. Bentz, Edward J. Garboczi, Claus J. Haecker and Ole M. Jensen, Effects of cement particle size distribution on performace properties of Portland cement-based materials, Cement and Concrete Research 29 (1999) pp. 1663-1671

[5] S.Garrault, T. Behr, A. Nonat, Formation of the C-S-H Layer during the Early Hydration of Tricalcium Silicate Grains with Different Sizes,J. Phys. Chem. B 110 (2006) pp.270-275

[6] H.F.Taylor, Chement chemistry, Tomas Helford, London 1997.

[7] I. Richardson, The nature of the hydration products in hardened cement pastes, Cement and Concrete Research 22, (2000) pp.97-113

[8] Barret P., Menetrier D. Bertrandie D., Cement and Concr. Res. 13 (1983) 728

[9] Trettin R., Wieker W.,Silikattechnik, 85 (1988) 283

[10] Damidot D., Nonat A., In: Nonat A., Mutin C., eds. Hydration and Setting of Cement, E&FN Spon, 1992

[11] Menetrier, D. and Barret, P., Cem. Res. Prog., 1981, 223 (1982)

[12] Barret, P. and Menetrier, D., Cem. Concr. Res., 10, 521 (1980)

[13] Nachbaur et al. J. Colloid Interface Sci., 202, 261-8 (1998)

[14] Stein, H. N. and Stevels, J. M., J. Appl. Chem. (london), 14, 338 (1964)

[15] Stein, H. N., Il cemento, 74, 2 (1977)

[16] Young et al. J. Am. Ceram. Soc., 60, 344 (1977)

[17] Tadros and al J. Am. Ceram. Soc., 59 , 344 (1976)

[18] Jennings, H. M. (1986)). J. Am. Ceram. Soc. 69, 614.

[19]Gartner, Young, Damidot and Jawed. Chapter 3: Hydration of Portland Cement. "Structure and Performance of Cements" 2nd Edition. Edited by J. Bensted and P. Barnes (2002)

[20] Barret, P., Bertrandie, D. and Ménétrier, D., in the 7th ICCC, Vol. 2, p. 261 (1980)

[21] Fierens, P. and Verhaegen, J.P. (1976) Cem. Concr. Res. 6, 337

[22] Odler, I. and Dörr, H. (1979). Cem. Concr. Res. 9, 277

[23] Sierra, R. in 6th ICCC, Vol. 2, Part 1, p. 138 (1976)

[24] S. Garrault, L. Nachbaur, A. Nonat, Pol. Ceram. Bull (2000) p.61

[25] Brown, P.W., Pommersheim, J. And Frohnsdorff, G. (1985) Cem. Concr. Res. 15, 35

[26] E.M. Gartner, J.M.Gaidis, J.M.Mater. Sci. Concrete (1989) pp.95-125

[27] G.C. Bye, Portland Cement, second edition, G.C. Bye and Thomas Telford Limited, London1999

[28] P. Fierens, Y. Kabuema and J. Tirlocq, Influence du Milieu de Temple sur la Cinetique d'Hydratation du Silicate Tricalcique, Cement and Concrete Research 12 (1982) pp. 191-198

[29] Tenoutasse, N., ibid., (1969)

[30] Scrivener, K.L. Development of Microstructure during the Hydration of Portland cement, Ph. D Thesis University of London (1984)

[31] Tenoutasse N. and De Donder A., Silicates Industriels, 35, (1970). pp. 301

[32] Bezjak A. and Jelenic I., On the determination of rate constants for hydration processes in cement pastes, Cem. Concr. Res. 10 (4) (1980) 553-563

[33] Tennis P.D. and Jennings H.M., A model for two types of calcium silicate hydrate in the microstructure of Portland cement pastes, Cem. Concr. Res. 30 (6) (2000) 855-863

[34] S. Gauffinet, E. Finot, E. Lesniewska and A. Nonat, C.R.Acad. Sci. Paris, Earth Planet. Sci. 327 (1998), 231

[35] S. Garrault and A. Nonat, Hydrated Layer Formation on Tricalcium and Dicalcium Silicate Surfaces: Experimental Study and Numerical Simulations, Langmuir 17 (2001) pp.8131-8138

[36] S.Garrault, T. Behr, A. Nonat, Formation of the C-S-H Layer during the Early Hydration of Tricalcium Silicate Grains with Different Sizes,J. Phys. Chem. B 110 (2006) pp.270-275

[37] Jeffrey J. Thomas, A New Approach to Modeling the Nucleation and Growth Kinetics of Tricalcium Silicate Hydration, Journal of the American Ceramic Society 90 (2007) pp. 3282-3288

[38] Avrami M., Journal of chemical physics, Vol. 7 (1939), 1103 – 1112; Vol. 8 (1940) 212 – 224; Vol. 9 (1941), 177 – 184

[39] H.M. Jennings, B.J. Dalgleish and P.L. Pratt, J. Am. Ceram. Soc. 64 (1981) p.567

[40] M. Zajac, Étude des relations entre vitesse d'hydratation, texturation des hydrates et résistance mécanique finale des pâtes et micro-mortiers de ciment portland. Ph. D. Thesis, ICB Istitut Carnot de Bourgogne, UMR 5209 CNRS/Univ. de Bourgogne (2007)

[41] H. F. W. Taylor, P. Barret, P. W. Brown, D. D. Double, G. Frohnsdorff, V. Johansen, D. Ménétrier-Sorrentino, I. Odler, L.J. Parrott, J. M. Pommersheim,and J. F. Young, The Hydration of tricalcium silicate, RILEM Technical Committees 68-MMH, Task Group 3, Materials and Structures, Volume 6 (1984) pp. 457-468

[42] R. Kondo and S. Ueda, Proc. 5th Int. Symp. Chem. Cem. Vol. II, pp.203-248, Tokyo 1969

[43] J. Gronau, Silikattechnik 18 (1967) pp. 143

[44] G.J. Verbeck and C. W. Foster, PCA Research Bulletin 32 (1949)

[45] S. Brunauer, PCA Research Bulletin 80 (1949)

[46] M. D. Cohen, J. Cement Concrete Res. 14 (1983) 305

[47] J. H. Taplin, On the Hydration Kinetics of Hydraulic Cements, in Proc. 5th Int. Symp. Chem. Cem. Vol. II, pp.337 Tokyo (1969)

[48] T. Knudsen, in Proceedings of the 7th International Symposium on the Chemistry of Cement, Vol. I, Paris (1980) pp. 170

[49] P.W. Brown, Effects of particle-size distribution on the kinetics of hydration of tricalcium silicate, Journal Of The American Ceramic Society 72 (1989) p.p1829-1832

[50] W. Jander, Reactions in the Solid State at High Temperatures, Z. Anorg. Allg. Chem. 163 (1927) pp.1-30

[51] A.M. Ginstling and B.I. Brounshtein, Concerning the Diffusion Kinetics of Reactions in Spherical Prticles, J. Appl. Chem., USSR 23 (1950) pp. 1327-1338

[52] P. Navi, C. Pignat, Simulation of cement hydration and the connectivity of the capillary pore space, Adv. Cem. Based Mater. 4 (1996) pp.58-67

[53] L. Wadsö; An experimental comparison between isothermal calorimetry, semi-adiabatic calorimetry and solution calorimetry for the study of cement hydration, Nordtest Report, TR 522, Approved 2003-03

[54] M. Geiker, Studies of Portland Cement Hydration: Measurements of Chemical Shrinkage and a Systematic Evaluation of Hydration Curves by Means of the Dispersion Model. Ph. D. Thesis Technical University of Denmark (1983)

[55] Hamlin M. Jennings, A model for the microstructure of calcium silicate hydrate in cement paste, Cement and Concrete Research 30 (2000) pp. 101-116

[56] T.C. Powers, T.L. Brownyard, Studies of the Physical Properties of Hardened Portland Cement Paste (Bulletin 22), Portland Cement Association, Chicago, IL (1948); reprinted from J. Amer. Concr. Inst. Proc. 43 (1947) pp.469-504

[57] R.F. Feldman, Helium flow and density measurement of the hydrated tricalcium silicate-Water system, Cement and Concrete Research 2 (1972) pp. 123-136

[58] J.F. Young, W. Hansen, Volume relationships for C-S-H formation based on hydration stoichiometries, Mater Res Soc Symp Proc 85 (1987) pp. 313-322

[59] H. Justnes, E.J. Sellevold, B. Reyniers, D. Van Loo, A. Van Gemert, F. Verboven, D. Van Gemert, Chemical shinkage of cement pastes with plasticizing admixtures, Nordic Concr. Res. 24 (2000) pp. 39-54

[60] T. Knudsen, M. Geiker, Chemical Shrinkage as an Indicator of the Stage of Hardening" Proceedings of the International RILEM Conference on Concre of Early Ages, Vol. I. Session V: "Methods of Indicating the Satage of Hardening", Ecole National des pouts et Chausses, Paris, April 6-8, (1982) pp. 163-167.

[61] S. Garcia-Boivin, Retrait au jeune âge du béton développment d'une méthode expérimental et contribution à l'analyse physique du retrait endogène, PhD Thesis, École nationale des Ponts et Chaussées, France (1999)

[62]. L.J. Parrot, M. Geiker, W.A. Gutteridge, D. Killog, Cement and Concrete Research 20 (1990) pp. 919-926

[63] L. Barcelo, Influence des caractéristiques des ciments sur la structuration et le comportement dimensionnel des matériaux cimentaires au jeune ages, PhD Thesis, Ecole Normale Supérieure de Cachan, France (2001)

[64] Denis Damidot, André Nonat and Pierre Barret, Kinetics of Tricalcium Silicate Hydration in Diluted Suspensions by Microcalorimetric Measurements, J. Am. Ceram. Soc. 73 (1990) pp. 3319-3322

[65] Mwakio P. Tole, Antonio C.Lasaga, Carlo Pantano and William B. White, The kinetics of dissolution of nepheline (NaAlSiO$_4$), Geochimica et Cosmochimica Acta 50 (1986) pp. 379-392

[66] H. Henry Teng, Patricia M. Dove and James J.de Yoreo, Kinetics of calcite growth: Surface processes and relationships to macroscopic rate laws, Geochimica and Cosmochimica Acta, Vol. 64 (2000) pp. 2255-2266

[67] M. Costoya, Shashank Bishnoi, E. Gallucci, Karen L. Scrivener, Synthesis and Hydration of Tricalcium Silicate" has been accepted for the 12th International Congress on the Chemistry of Cement , Montreal (Canada) (2007)

[68] M. Costoya, Shashank Bishnoi, E. Gallucci, Karen L. Scrivener, Effect of Particle Size Distribution of Alite on its Hydration, 26th Cement and Concrete Science Conference, Sheffield (UK) (2006)

[69] Parviz Navi, Christian Pignat, Effects of cement size distribution on capillary pore structure of the simulated cement paste, Computational Materials Science 16 (1999) pp.285-293

CHAPTER 4: EFFECT OF PARTICLE SIZE ON THE MICROSTRUCTURAL DEVELOPMENT OF TRICALCIUM SILICATE

Chapter 3 has shown that particle size distribution has a strong influence on the rate of hydration of alite. The interactions between hydration kinetics and microstructural development are not well documented in the literature and there are only a few studies available in which the effect of the particle size on the microstructural development of cementitious materials has been directly investigated.

In this chapter, a quantitative and morphological study of alite pastes is presented with the aim of getting insight into the role of the particle gradation on microstructural development. Scanning electron microscopy has been used as the main technique to investigate qualitatively and quantitatively the evolution of the pastes from different gradations of tricalcium silicate during hydration. SEM-image analysis was used to measure the amount of phases (anhydrous, hydrates and porosity), to calculate the degree of hydration of the pastes and characterise the morphology of the main features of the associated microstructures. Thermogravimetric analysis (TGA), x-ray diffraction (XRD) and isothermal calorimetry (IC) were used as complementary techniques to calibrate and check the validity of the SEM results. The link between the porosity and the density of the various systems was investigated in order to have a better understanding of the role that the particle size plays on the product formation (morphological differences in the C-S-H formation and CH nucleation and growth).

4.1 State Of The Art on the Microstructural Development of Cementitious Materials

A detailed schematic representation of the microstructural development of ordinary Portland cement given by Scrivener [1] is shown in Figure 4. 1. Although quite complex due to the multiphase nature of cement clinker phases and the numerous hydration products (C-S-H, portlandite), AFm and Aft, the microstructure of hardened Portland cement is now well understood. Unreacted grains dissolve and precipitate hydrates that fill in the originally water-occupied space.

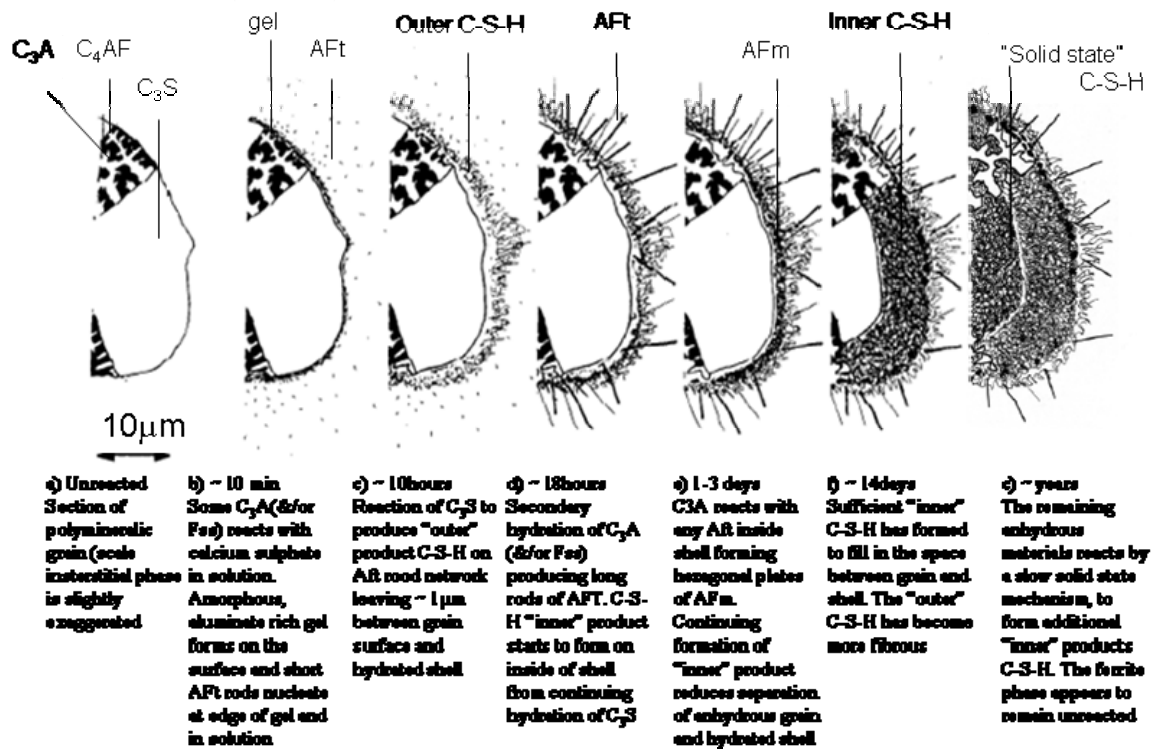Figure 4. 1: Schematic representation of the microstructural development of OPC

The microstructural development of tricalcium silicate is much simpler since this system has only 3 main characteristic features: unreacted grains, C-S-H and portlandite [2-4]. Two morphologies of C-S-H can be distinguished: inner and outer or low and high density. After a few hours of hydration portlandite begins to nucleate and precipitates and

the anhydrous grains are gradually surrounded by a shell of C-S-H product whose thickness increases with time. The morphology of C-S-H is very similar to that observed at the same scale in OPC. Outer C-S-H (Op C-S-H) presents a fibrillar or foil-like morphology and its morphology is affected by the amount of capillary pore space available for precipitation [5]. Inner C-S-H (Ip C-S-H) presents a homogeneous morphology [5]. One of the main differences with the microstructural development of Portland cement apart from the presence of sulphate and aluminate phases concerns the crystallization and precipitation of portlandite: in OPC, portlandite grows with a variable shape and deposits everywhere in the matrix while in C_3S, portlandite grows into large CH clusters. These clusters nucleate at a few random sites. An extended description of the distribution and morphology of portlandite in various cementitious systems was reported by Gallucci and Scrivener [6] in which the authors correlated the differences between the two systems to the presence of other species in OPC such as sulphate, aluminate phases or alkali ions. They suggested that calcium sulphate particles seem to act as nuclei of CH clusters or at least their neighbourhood favours the crystallization of CH.

Effect of particle size on the microstructural development of tricalcium silicate

Although the effect of PSD on hydration kinetics has been known for long time, no rigorous investigation of its impact on the microstructural development has been made. The only work related to the topic was done by Kondo et al. [2,7]. They studied the hydration of C_3S pastes with 2 narrow particle size distributions (2-5μm and 5-8μm) and concluded that during hydration the size and the shape of the initial C_3S particles remain unchanged. However, the particle size distributions used in this investigation were very different compared to the range of 1-50 μm found in cement pastes. Furthermore, this work doesn't discuss at all that the effect of particle size on the microstructural evolution.

Since the particle size has an important effect on the hydration kinetics and the microstructural development of narrow PSDs is poorly documented, this chapter aims to get better insight into the influence of the initial particle size of tricalcium silicate on its

microstructural development. This will help to assess how the microstructural development is connected with the kinetics and therefore, to asses the role that the initial particles sizes play on the final microstructure.

4.2 Sample Preparation and Experimental Techniques

SEM backscattered electron image analysis (BSE/IA) of polished cross-sections was the main technique used to investigate the evolution of different gradations of tricalcium silicate during hydration. Complementary techniques such as isothermal x-ray diffraction/Rietveld refinement and thermogravimetry analysis (TGA) were also used.

4.2.1 Sample Preparation

Alite pastes were prepared by mechanical mixing during 2 min the alite powders with deionizer water at w/c ratio of 0.4. The pastes were poured into plastic vials, sealed and tapped several times to avoid possible entrapped air. After 1 day of hydration the samples were removed from the vials and cured into deionized water. Two drying methods were used for stopping the hydration:

a. *Freeze-drying*: This technique was chosen for the water removal of early age samples (up to 24 hours). This is a very fast drying technique that causes little damage to the cement paste at the microstructural level. In this method the specimen is immersed directly in liquid nitrogen (-196ºC) for about 5 min, or, sometimes immersed in a cold mixture of solid CO_2 and ethanol (-80ºC). For very small specimens, freezing of pore water is almost instantaneous, avoiding the excessive microcraking in the cement paste. Then, the frozen water is removed by sublimation [8].

b. *Solvent replacement*: This technique was chosen for stopping the hydration of samples at later ages (more than 24 hours). Solvent exchange is considered to be gentle to the cement paste microstructure, minimizing the collapse of the C-S-H structure. The solvent used for the replacement was isopropanol in which samples were stored for a week [9].

Afterwards, samples were stored in a desiccator to prevent possible carbonation and further hydration due to humidity.

4.2.2 Principles of Scanning Electron Microscopy (SEM)

Scanning electron microscopy is one of the most versatile technique for investigating the microstructure of materials and has been extensively used to study both quantitatively and qualitatively the microstructural evolution of cementitious materials during their hydration [1,6,10-15].

A FEI quanta 200 SEM microscope and a PGT energy dispersive X-ray analyser were used. Backscattered electron image analysis (BSE/IA) of polished cross-sections at an accelerating voltage of 15 KV was used to quantify the amount and characteristics of all phases (anhydrous and hydrates). Depending on the features and characteristics considered, magnifications from x200 to x20000 were used. For the basic bulk quantifications (amount of phases, degree of hydration …) around 100 images were acquired at a nominal magnification of x800 (i.e. 0.375 microns per pixel).

Prior to SEM examination, all dried samples were epoxy-impregnated (EPOTEK-301) and polished with diamond powder down to ¼ µm. BSE imaging requires highly polished surfaces because improper preparation of the samples may obscure features and create artefacts that may be misinterpreted [16].

Backscattered electrons are one of the several interactions generated upon contact between the electron beam and the material (Figure 4. 2). They are produced by single large-angle or multiple small-angle elastic-scattering events. The energy distribution of backscattered electrons depends on the primary energy of incident electrons, the number of shell electrons, the atomic number of the material and the surface inclination of the specimen. As the atomic number of the material hit by the incident beam decreases, fewer electrons are backscattered, and more energy is lost. In materials with high atomic numbers, many electrons are backscattered by atoms close to the surface, with little

change in energy. Therefore, the yield, energy spectrum and depth of escape of backscattered electrons are directly related to the average atomic number of the considered phase or material, and/or its internal microporosity. This leads to a specific contrast which allows phase discrimination on the basis of their brightness on the screen. In the case of cementitious materials, depending on the acceleration voltage, the depth of interaction volume from which BSE are detected is about 0.3-0.8 μm across [12].
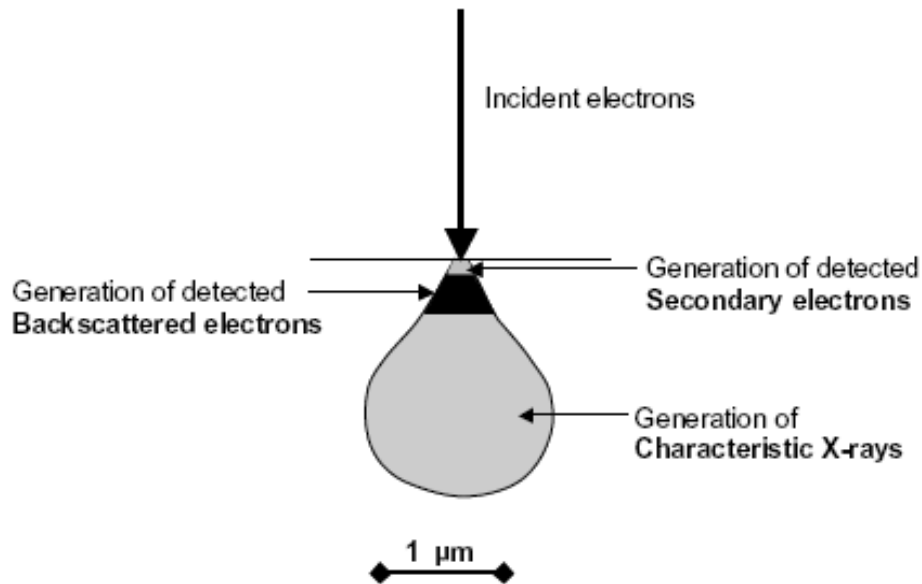
Figure 4. 2: Schematic draw where is represented electron-beam excited- electrons and radiation used in SEM [12]

Image processing

Image analysis is a useful tool for phase quantification of cementitious materials [12]. Since cement microstructures are statistically isotropic the most fundamental rule of stereology applies the possibility of getting 3D quantitative information from 2D analysis (always keeping in mind some limitations in the case of morphological analysis which is biased due to cross-sectioning effects) [17].

_____

Image analysis was carried out based on the greylevel histogram of BSE images. Any image can be described by the distribution of brightness of its pixels (called greylevel histogram) which in a typical 8-bit grayscale image ranges between 0 (black) and 255 (white) with 254 intermediate levels of grey. The brightness of a pixel depends on the average atomic number of the different components present in the sample at that place and their density.

For a BSE image of a polished alite paste, porosity appears black, unhydrated grains bright, portlandite light grey and C-S-H darker grey. A typical example of BSE image for an alite paste and its corresponding grey level histogram is presented in Figure 4. 3.
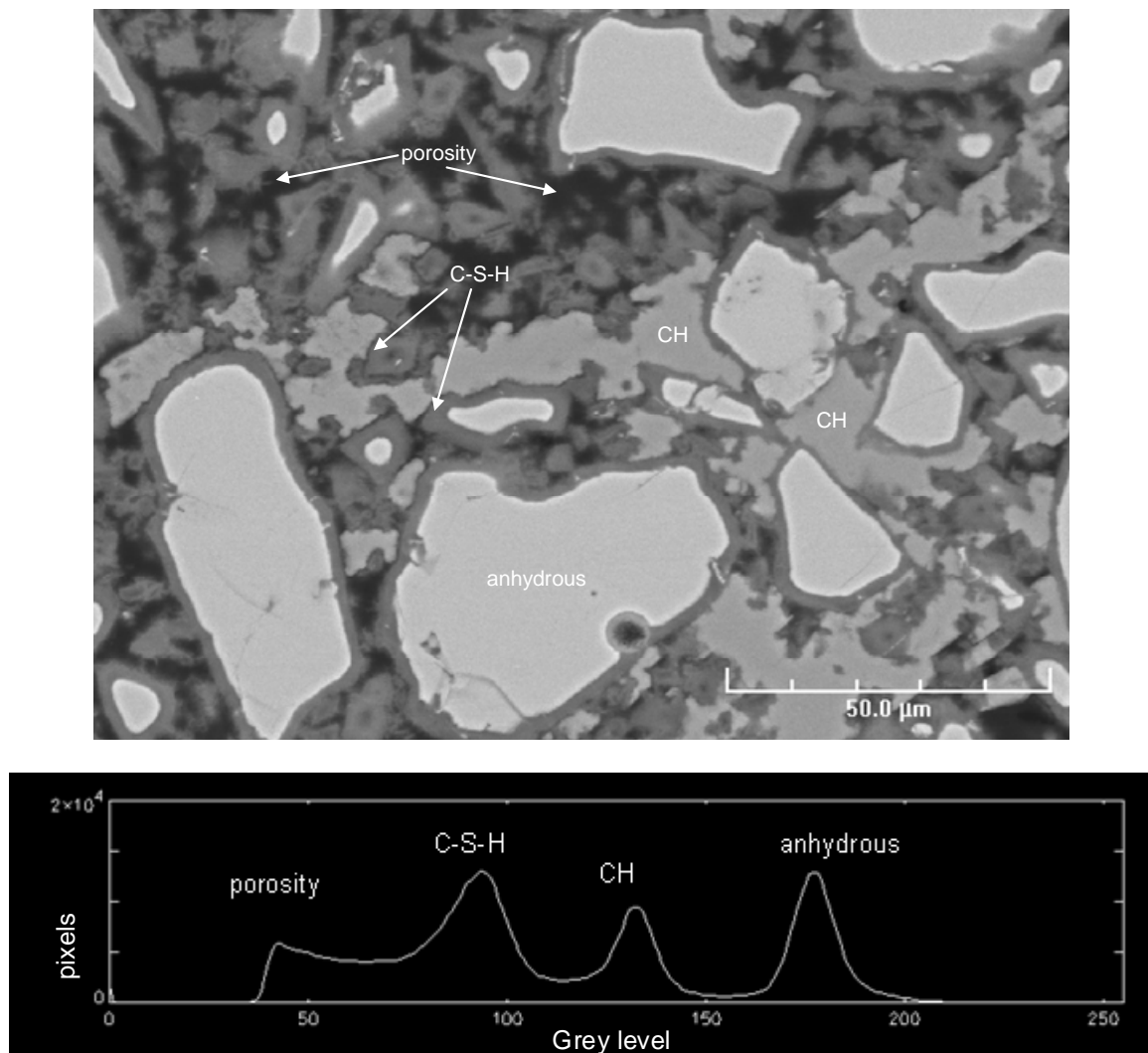

Figure 4. 3: Grey level histogram of an alite pastes after 14 days of hydration

The object of image analysis is to discriminate and isolate individual objects of interest in image. The method used to that effect in this study is histogram segmentation, in which the features of interest are discriminated from the background and the other components by their characteristic grey band. The grey level image is thus converted into several binary images in which the objects of interest are white and all the rest is black. Figure 4. 4 shows the combination of these binary images in which anhydrous C_3S, portlandite, C-S-H and porosity appears represented in white, red, green and black colours, respectively. The most common way of converting gray scale image to binary image is by thresholding, using a range of grey levels that corresponds to the features of interest as the criterion. To reduce the noise produced by imperfections in the image, some image processing such as filtering (median), hole filling, etc. is applied. Once the phases are isolated, a quantitative and qualitative analysis of the microstructure can be done. Some morphological characteristics of the different features such as the area, diameter, shape can be investigated.
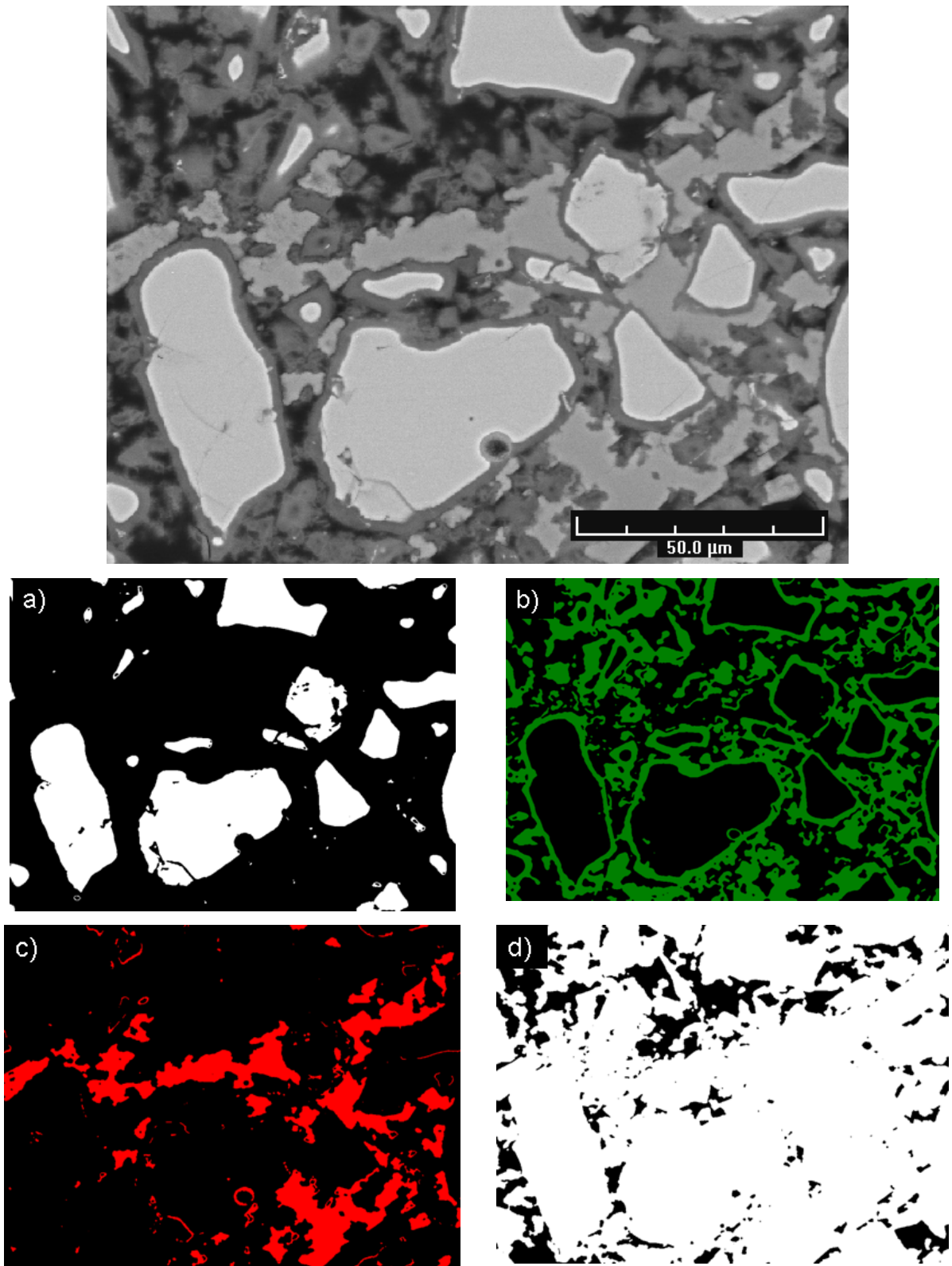
Figure 4. 4: Example of the segmentation process in an alite paste. a) anhydrous C_3S (white), b)C-S-H (green), c) portlandite (red) and d) porosity (black)

4.2.3 Measurement of Density of the Pastes

The density of the products may depend on factors such as de degree of hydration, the temperature, etc. The measure of the density will bring some more information on the nature of the hydrates formed which will be linked with the porosity of the paste. In addition, density of the paste is needed to convert volume fractions by image analysis (IA) to weight fractions measured by techniques such as XRD, TGA and vice versa. Techniques such as helium pycnometry (solid density) and Archimedes methods (apparent density) have been used to determine the density of the hydration products and the evolution of those over time. Both methods are described in more detail below.

Helium pycnometry is the most reliable technique for determining the density of a material. The solid density is calculated by making the ratio between the sample mass and the sample true volume that has been measured from the equipment [8]. This technique has been commonly agreed to give the most reliable results of density. Due to their small size , the He atoms (0.22 nm) are thought to be able to penetrate into the C-S-H layer and thus any changes in its structure would directly be reflected by changes in the values of density over hydration [18,19]. He pycnometry has been extensively used in the past to investigate the microstructure of the C-S-H gel, mainly to give an approximate value of the surface area in the interlayer space [18]. However, either the compression of He gas into the solid or the pre-drying methods can provoke the collapse of the C-S-H, putting into question the reliability of this method for accessing the real interlayer space in C-S-H. This technique also allows determining the pore volume, which makes it very suitable for comparison and modelling purposes. However, it is not possible to have information on the pore size distribution. Here it has been used for the investigation of the solid density (ρ_{solid}) of the dried solid.

Measurements were done using an AccuPyc 1330 [20] from Micromeritics. Each measure included 20 purges prior to analysis and then duplicated the analysis of each sample to verify the reproducibility of the method. The results reported here are the averages of those two determinations.

The Archimedes method determines the density of an object using the displacement principle by weighting the object, immersing it in fluid and measuring its apparent weight. In this study, the apparent density (ρ_{app}) was measured with this technique using isopropanol as the displaced fluid.

The density of C-S-H is directly linked to the water content. Therefore, the density depends on how the sample has been dried. In this study, alite samples were dried by replacing free water by isopropanol in order to avoid or minimize the collapse of C-S-H layer compared to samples prepared using D-drying. Then the samples were immediately placed under vacuum in a desiccator using silica gel as desiccant. Isopropanol was evaporated by introducing the samples into a dessicator connected with a vacuum pump for a few hours (2-4 hours).

4.2.4 Characterization of Porosity

The pore structure of cementitious materials is generally classified in 3 main types of pores: gel pores, capillary pores and macropores. The classification of the pore sizes according to [21] is given in Table 4. 1.

Table 4. 1: Classification of pore size in cementitious materials [21]

Name	Diameter of Pores	Description	Role of Water	Properties of the paste affected
Gel Pores	<0.5 nm	Micropores-Inter layer	Structural water involved in bonding	Shrinkage, creep at all RH
	0.5nm-2.5nm	Micropores	Strongly adsorbed water	Shrinkage, creep at all RH
Capillary Pores	2.5nm-10nm	Small (gel) capillaries	Strong surface tension forces generated	Shrinkage between 50% and 80% RH
	10nm-50nm	Medium capillaries	Moderate surface tension forces generated	Strength, permeability, shrinkage at high RH,>80%
	50nm-10µm	Large capillaries	Behaves as bulk water	Strength, permeability
Macropores	0.1 µm-1mm	Entrained air		Strength

There are a few techniques that have been used in the last years to characterize the pore size distribution of cementitious materials. Mercury intrusion porosimetry, gas adsorption and solvent exchange are the most used techniques.

There are several factors such as the composition, the w/c ratio, temperature, the degree of hydration, the fineness of the sample, etc. that can significantly affect the pore structure. However, the most important limitation for the characterization of either the pore volume or the pore size distribution is the drying of the sample. Most of the commonly used methods require the pre-drying of the sample leading to the collapse of

the C-S-H gel. Other important limitations are for example assumptions made in the models used for the transformation of pore volumes into pore size distributions or assuming the shape of the pores.

The initial particle size of cement has an important effect on the hydration kinetics as seen in Chapter 3. In addition, the packing of these particles has also an important influence: smaller particles leads to a larger proportion of small pores. In coarse gradations where the packing leaves larger voids between particles more hydration is needed to close off the capillary porosity [22].

The investigation of the effect that the initial particle size distribution has on the capillary porosity is presented in this chapter. The capillary porosity was investigated by backscattered electron image analysis (BSE/IA) as described in § 4.2.2 [23]. The pore size characterization of C-S-H is described in Chapter 5.

The drying method chosen for stopping the hydration of the samples was isopropanol exchange as it is considered less destructive for the C-S-H structure.

4.3 Effect of PSD on the Microstructural Development of Tricalcium Silicate

This section describes the microstructural development of tricalcium silicate, first giving a general description of its evolution upon hydration and in a second part, the emphasis is put on the effect of the initial particle size on the progress of hydration. Table 4. 2 summarizes the experiments carried out for each of the particle sizes used in the investigation in chapters 4 and 5. PSD-82µm, PSD-38µm and PSD-33µm are gradations obtained from alite and PSD-6µm from pure C_3S powders.

As a consequence of the large size of the particles in gradation PSD-82µm the reaction rates are very low. These large particles could lead on some occasions to bleeding. Since image analysis is a volumetric method, it will be very sensitive to the reference volume which itself depends on the w/c ratio. As a result, some of the quantitative results presented for this particle size are sometimes inconsistent. When possible (i.e. when the quantity of supernatant water could be measured), data have been corrected to take into account the lower w/c ratio due to bleeding and has been indicated with an asterisk (*).

Despite of the fact that PSD-33µm has a very wide particle size distribution when compared to PSD-38µm, both have almost the same average particle size. Thus, for most of the experiments, similar results are obtained for these two particle size distributions. The most important differences are observed when those are compared with the smallest of the gradations (PSD-6µm/ pure C_3S) as discussed in this chapter.

Table 4. 2: Summary of experiments made for each of the particle sizes in Chapters 4 and 5

		PSD-82µm	PSD-38µm	PSD-33µm (Alite)	PSD-6µm (pure C3S)
Microstructure	**SEM**	X	X	X	X
	TEM			X	X
Density	**bulk**	X	X	X	X
	appartent	X	X	X	X
Quantification	**Porosity**	X	X	X	X
	AN	X	X	X	X
	DH	X	X	X	X
	CH	X	X	X	X
	C-S-H relative brightness	X	X		X
	Ca/Si	X	X	X	X
	bound water	X	X	X	X
	NAD			X	X

Nomenclature:
SEM: scanning electron microscopy, TEM: transmission electron microscopy, AN: anhydrous C_3S, DH: degree of hydration, CH: portlandite, NAD: nitrogen adsorption

4.3.1. Global (bulk) Description of Tricalcium Silicate Microstructural Development

The microstructural development of 2 pastes mixed from different particle size distribution is compared in Figure 4. 6 for the early ages and Figure 4. 7 at later ages. PSD-33µm has the closest PSD compared to OPC and PSD-6µm is the smallest PSD synthesized.

With PSD-6µm, as its reaction rate is higher, the matrix is filled with hydration products much earlier than in the case of PSD-33µm. Preferential reaction of the grains is observed at very high magnification,described in section §4.4.1, in both systems.

For C_3S samples, portlandite was found to precipitate randomly in the matrix, forming small clusters which increase in number and size. Small portlandite clusters are observed from 4 hours, the first age investigated. Some of them grow on the semi-hydrated grains stopping or slowing down their future hydration.

A clear differentiation between inner and outer C-S-H can be observed at high magnification even after 14 days of hydration. This differentiation is observed earlier for smaller particle sizes. An example of this inner and outer C-S-H in an alite paste from PSD-33µm after14 days of hydration is shown in Figure 4. 5. However, the thickness of the inner C-S-H layer differs from one system to the others. The increase of the C-S-H thickness with hydration for different gradations of alite was investigated and is shown in section §4.4.2. The capillary porosity of both systems has been considerably reduced at this age. The total porosity for the different gradations of C_3S was measured by BSE/IA and is introduced in section §4.4.2.

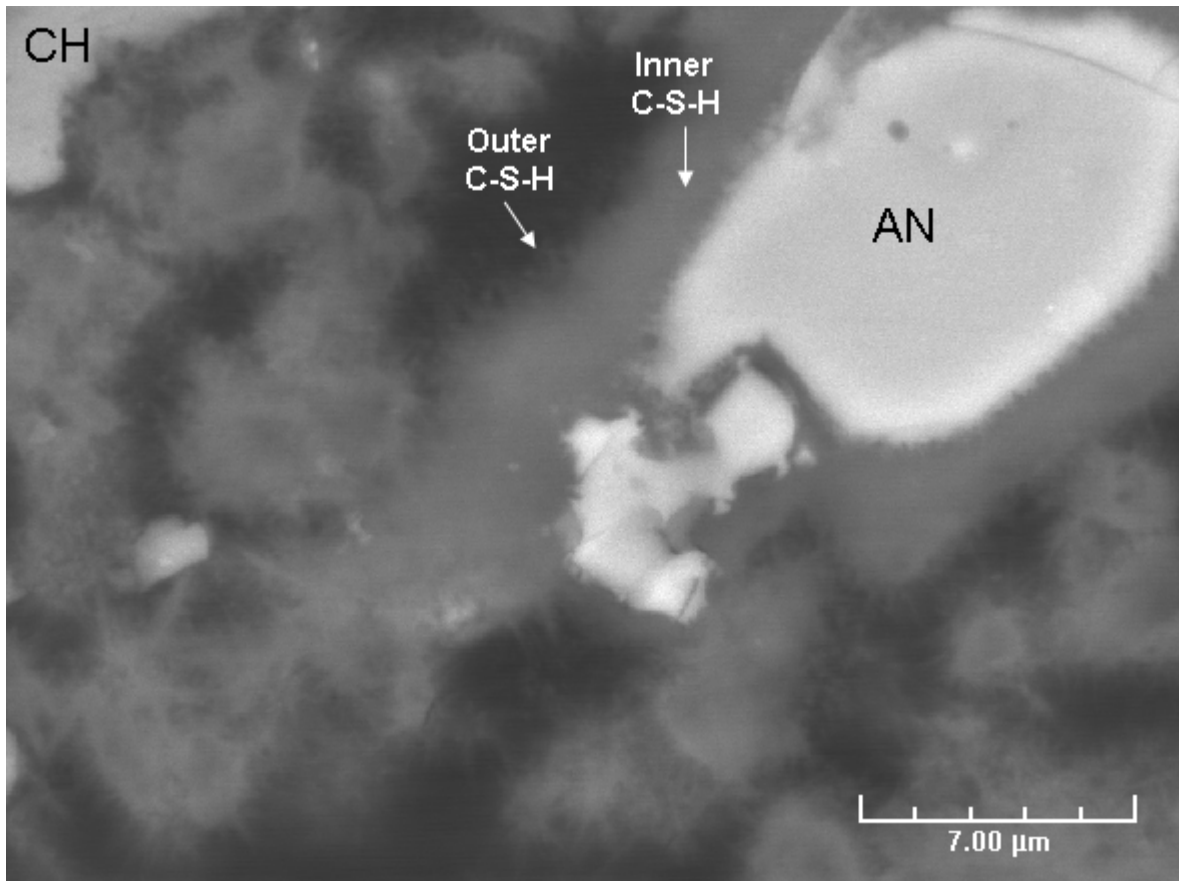
Figure 4. 5: BSE image of an alite paste (PSD-33µm) showing the inner and outer C-S-H after 14 days of hydration

In general, the microstructural development of PSD-33µm compared with PSD-6µm seems to be similar and present the same type of hydration product features. The most

relevant difference concerns earlier microstructural development of the PSD-6µm paste which has higher hydration rates.
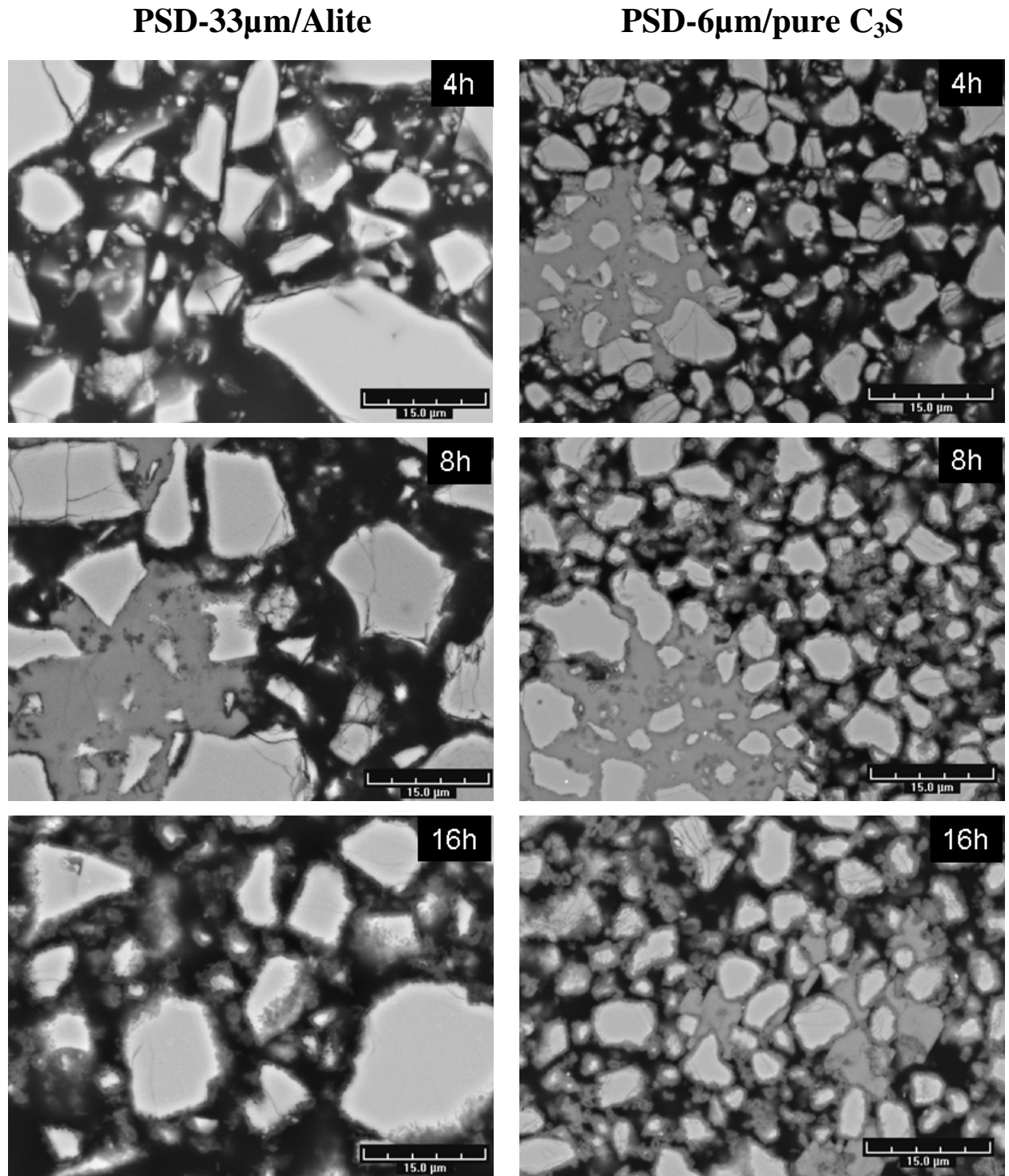
PSD-33µm/Alite   **PSD-6µm/pure C$_3$S**

Figure 4. 6: Microstructural development of PSD-33µm/Alite (left) and PSD-6µm/pure C$_3$S (right) pastes during the first   hours of hydration(4, 8 and 16 hours (w/c=0.4))

PSD-33µm/Alite   **PSD-6µm/pure C₃S**
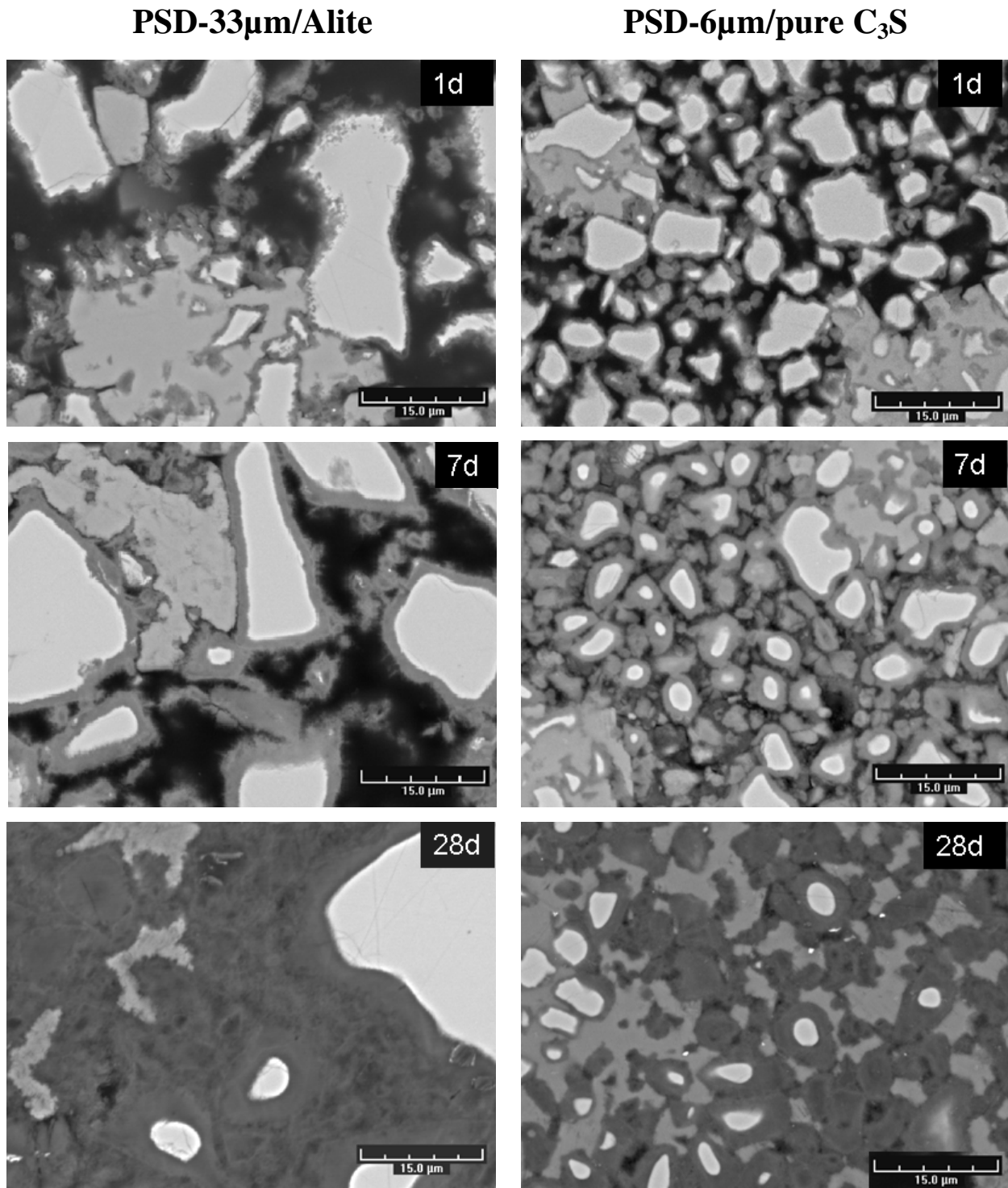

Figure 4. 7: Microstructural development of PSD-33µm/Alite (left) and PSD-6µm/pure C₃S (right) pastes over hydration at later ages (1, 7 and 28 days (w/c=0.4))

4.3.2 Quantification of Phases

The quantification of the different phases was mainly investigated by backscattered electron image analysis (BSE/IA).The description of the method can be found in section §4.2.2.

4.3.2.1 Unhydrated C_3S and degree of hydration

The consumption of anhydrous tricalcium silicate was measured by BSE/IA (§4.2.2.) and is shown in Figure 4. 8. Lower amounts of anhydrous content are observed in the PSD-6µm system. As discussed in Chapter 3, the degree of hydration for this particle size is much higher than the others at the same age, and subsequently there is less remaining anhydrous phase. The data collected for the coarse PSD-82 µm has been corrected to take into account the bleeding of the sample.
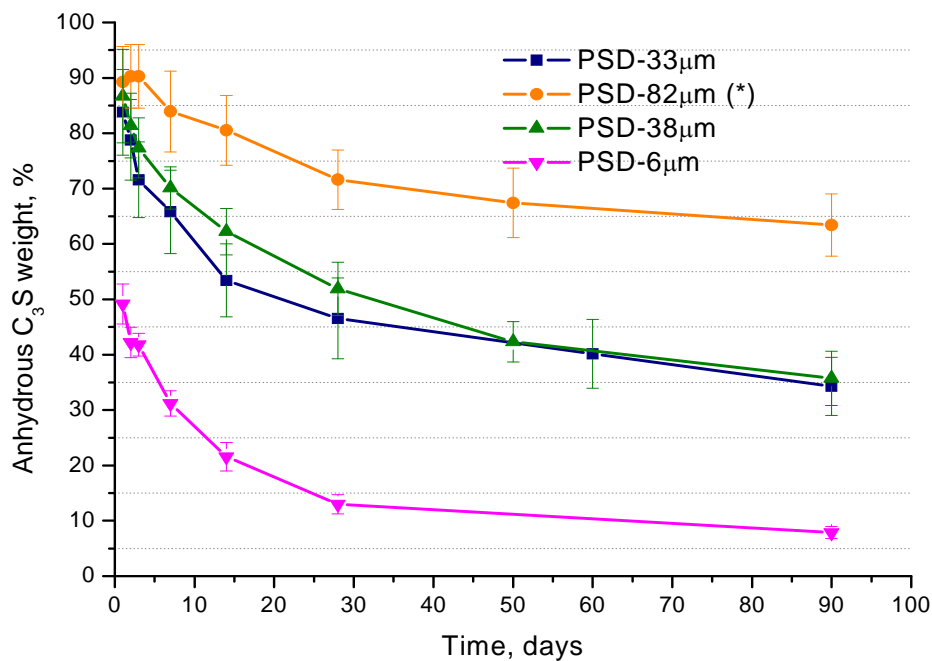

Figure 4. 8: Anhydrous C_3S weight percentage over time for different gradations calculated by BSE/IA. (*) PSD-82µm was corrected to take into account the bleeding effect

The degree of hydration (α) can be calculated by relating the anhydrous amount of alite measured this way to its original content in the mix design according to :

$$\alpha = \frac{V_{AN}(0) - V_{AN}(t)}{V_{AN}(0)} \times 100 \qquad \text{Eq.4. 1}$$

where $V_{AN}(0)$ is the initial volume fraction of anhydrous and $V_{AN}(t)$ is the volume fraction of anhydrous after a given time, t.

As seen in Chapter 3, the BSE-IA, isothermal calorimetry and chemical shrinkage (using a C-S-H density of 2.04g/cm^3 (for PSD-38µm) calculated from the measure of chemical shrinkage) give consistent results (Figure 4. 9).

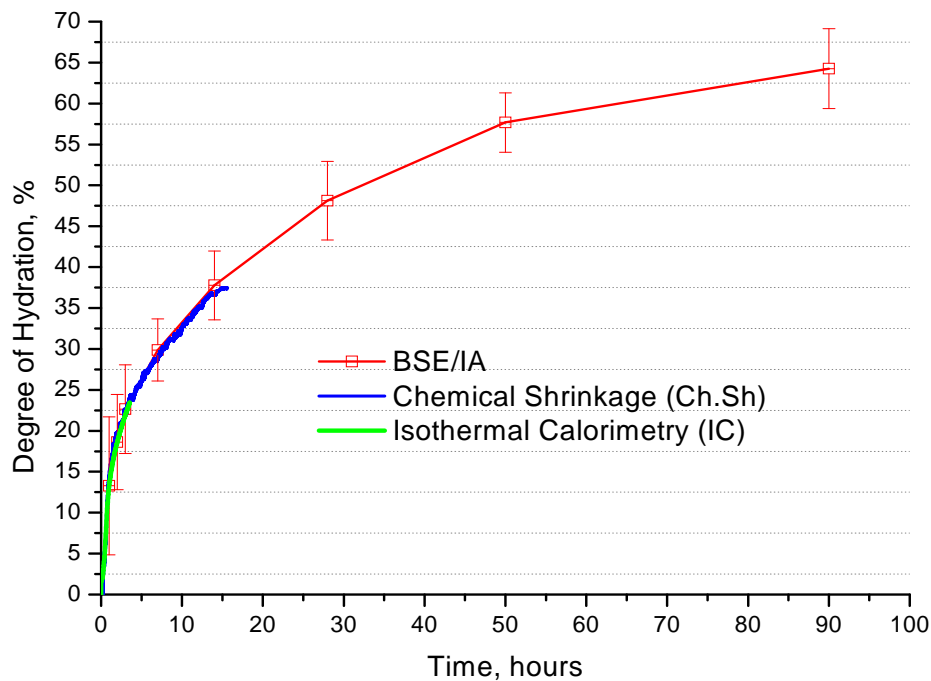

Figure 4. 9: Comparison between the degrees of hydration calculated by isothermal calorimetry, chemical shrinkage and BSE/IA for PSD-38µm

The development of the degree of hydration for C$_3$S pastes with different particle sizes calculated by BSE/IA and is plotted in Figure 4. 10. Here again, as a consequence of their

higher hydration rates, gradations with smaller particle sizes reach higher degrees of hydration earlier. This was explained in chapter 3 as a consequence of higher surface area available for hydration.
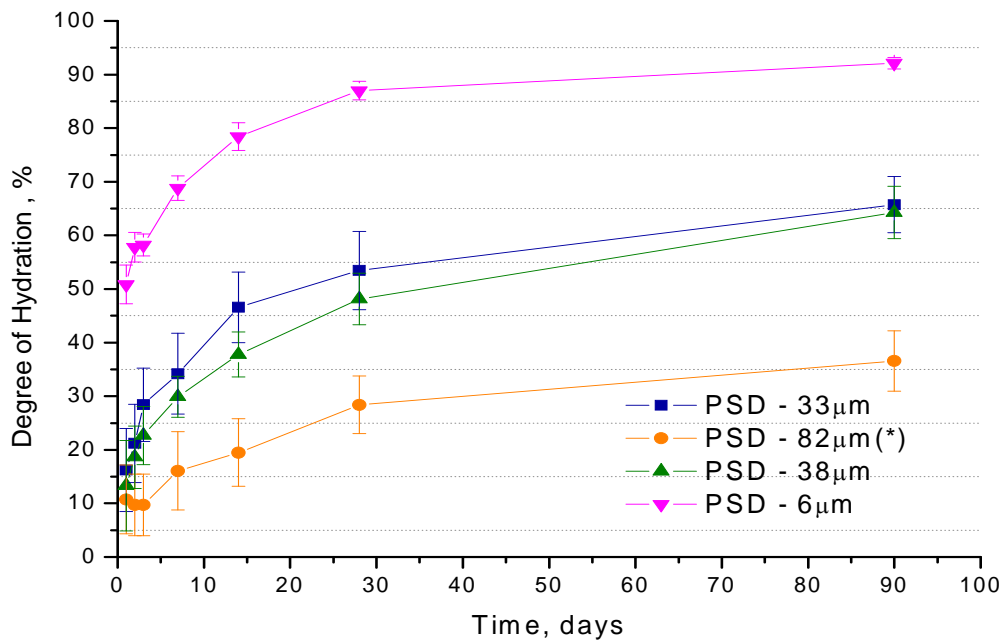

Figure 4. 10: Comparison of the degree of hydration of different gradations measured by BSE/IA. (*) PSD-82µm was corrected to take into account the bleeding effect

4.3.2.2 Quantification of portlandite

Portlandite content was measured using BSE/IA, XRD-Rietveld, mass balance calculations and thermogravimetric analysis. The experimental conditions used in the experimentation are presented in Appendix II.

The amount of portlandite measured for the different systems from 1 to 90 days is presented in Figure 4. 11. The higher content of portlandite for the smallest PSDs is in good agreement with the higher degrees of hydration measured.

Independently from particle size, the amount of portlandite generated as a function of degree of hydration is the same for all systems (Figure 4. 12). Mounanga et al. [24] found

the same linear trend between the portlandite content and the degree of hydration for cement pastes at different temperatures and w/c ratios. However, in [24] the portlandite is assumed to precipitate when the degree of hydration, calculated by thermogravimetric analysis, is about 7%). In the present study, in which the degree of hydration was calculated from BSE/IA, the linear extrapolation of the CH percentage versus degree of hydration has an intercept at about 3%. This indicates that that the precipitation of portlandite occurs earlier than at a degree of hydration of 7%. Furthermore, this fits well with found in chapter 3 as the levels of Ca^{2+} found in solution after a few minutes of hydration where much higher than the saturation concentration. This indicates that the precipitation of portlandite starts within a few minutes after the first contact with water and not after 7% of hydration.
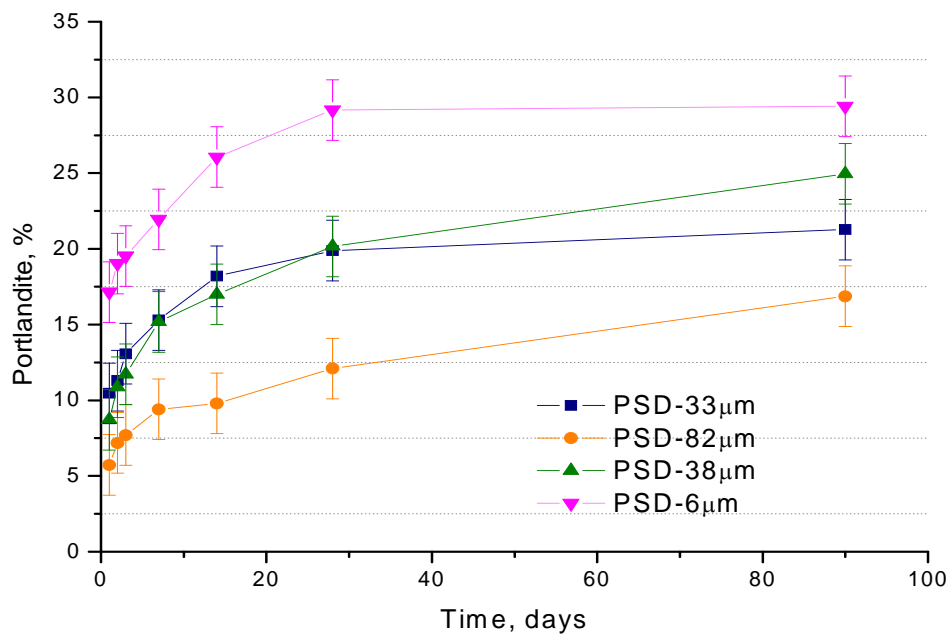

Figure 4. 11: Evolution over time of the weight % of portlandite determined by TGA alite pastes with different particle sizes
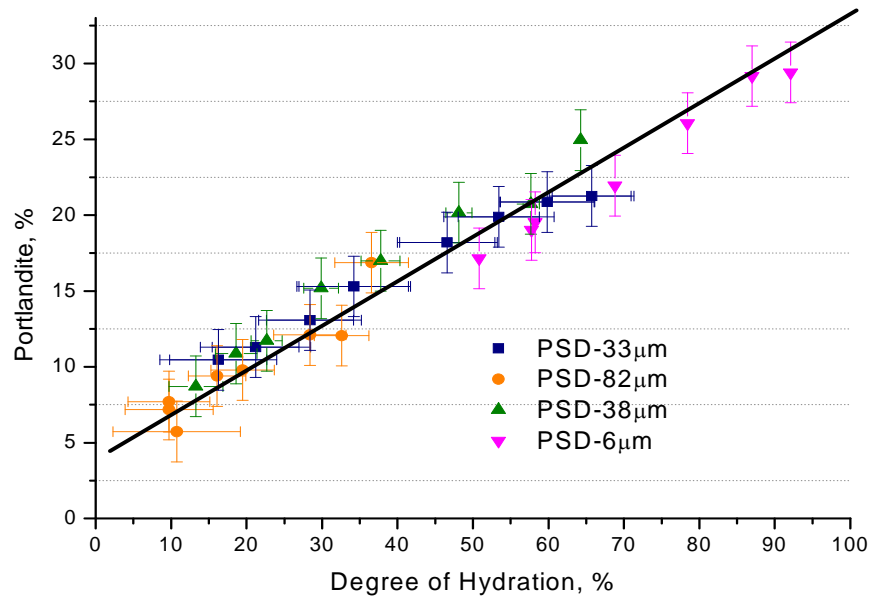
Figure 4. 12: Portlandite % (calculated by TGA) for different particle size distribution vs. the degree of hydration calculated by BSE/IA (the line correspond to an extrapolation to the Y axes)

4.3.2.3 Measure of capillary porosity from BSE-image analysis

Figure 4. 13 shows the evolution of capillary porosity over time for the different gradations measured by BSE-IA. As mentioned in §4.2.2, the pixel size used is 0.375 microns so capillary pores smaller than 0.5µm are not measured. Nevertheless, it has been shown that the values measured by image analysis are generally close to those measured by classical methods [25]. The variation of the percentage of porosity varies from one particle size to the other but in general decreases from approximately 37 to 0.2 %. PSD-6µm, the smallest particle size investigated, presents the smallest values of porosity. In this system the capillary porosity decreases faster compared with coarser gradations which fit well with the observed faster hydration.
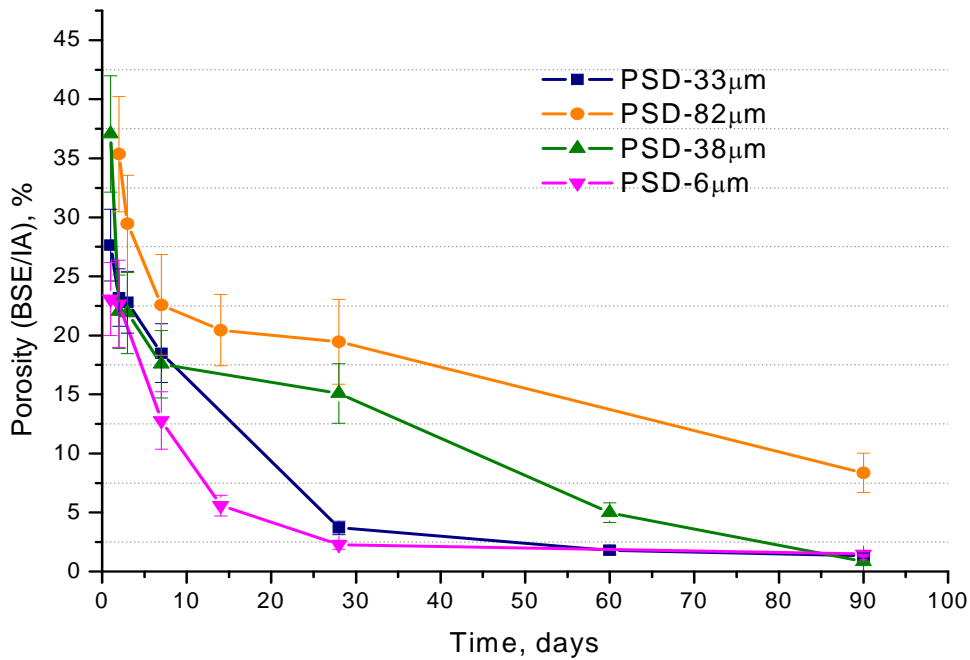
Figure 4. 13: Comparison of the porosity calculated by BSE/IA for different gradations of C_3S

In Figure 4. 14 porosity is plotted against the degree of hydration. All particle size distributions follow a similar trend: they decrease with the increase of the degree of hydration. A possible trend could be an increase of the porosity with the decrease of the size of the particles. Hypothesis for such behaviour could be explained either by a change in density of the products formed or from different filling of the microstructure related to the degree of constriction of the inter-particle space.

The porosity content calculated from volume balance calculations using the data given in Table 4. 3. and the C-S-H densities measured in chapter 3 is plotted in dotted line in Figure 4. 14. The slight C-S-H differences measured using chemical shrinkage do not explain change in the content of porosity calculated this way, therefore only one curve has been plotted. This result tends to show that the density of the C-S-H formed is not responsible for the differences in the measured porosities and by consequence that the chemical nature of the starting material (Alite vs pure C_3S) has probably no influence in the microstructural development.

Table 4. 3: Values used for calculating the porosity

	C$_3$S	H	C-S-H	CH
Density (g/cm^3)	3.15	1	2.04-2.09(*)	2.24
Mass ratio	1	5.3	1	1.3
Molar Mass (g/mol)	228	18	227.2	74

(*) Values obtained from the measure of chemical shrinkage (Table 3.4 in Chapter 3)

[26] stated that "the influence of particle size distribution on the porosity is dependent on both the packing density and the rate of hydration" and that at low degrees of hydration, the packing density is the main factor while at high degrees of hydration, both parameters must be considered. Packing density is considered in this work as the distribution of solids in the volume.
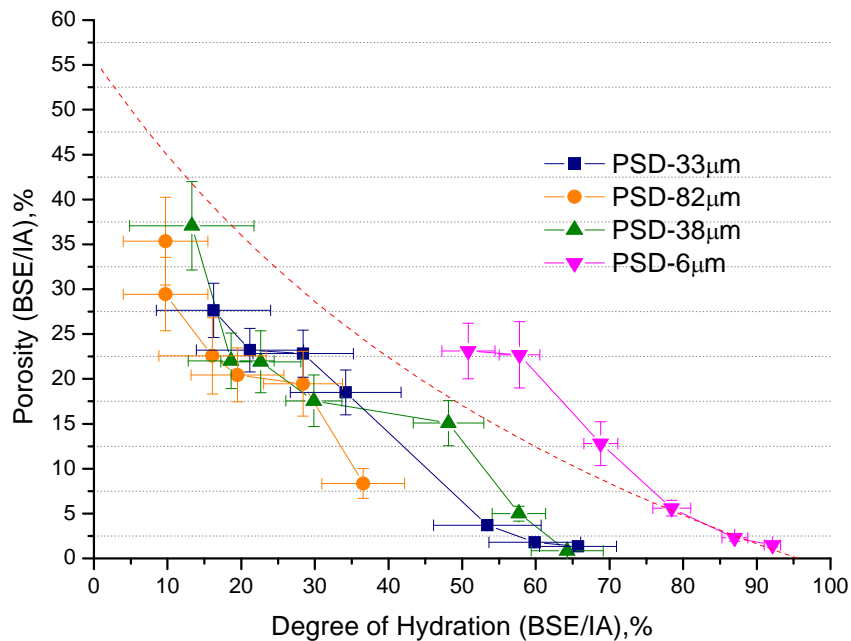

Figure 4. 14: Porosity (BSE/IA) versus degree of hydration of different particle size distributions

Another important fact that should be taken into account and could explain the differences found in porosity is the formation of different morphologies of the outer C-S-H. Richardson [27] suggested that when C-S-H grows in large capillary pores it forms

more coarse fibrils. Whereas, when it grows with limitation of pore space then grows in a more fine fibrillar morphology.

4.3.2.4 Quantification of C-S-H

C_3S systems are only constituted of four main components (C_3S, C-S-H, CH and pores), thus the C-S-H content can be deduced from the three others. Figure 4. 15 shows the evolution of the C-S-H content renormalized to C_3S by image analysis compared with results obtained from XRD-Rietveld analysis and mass balance calculations.

Mass balance calculation was made by assuming the following stoichiometry [28] for the hydration of C_3S:

$$C_3S+ 5.3H \rightarrow C_{1.7}SH_4 +1.3CH \qquad Eq.4.\ 2$$
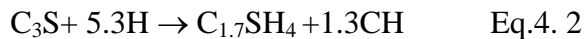
Good agreement is observed between XRD and mass balance calculation while BSE/IA diverges significantly after a few days. This is certainly explained by the fact that fine capillary pores are not measured by image analysis and since these are more numerous upon hydration, the overall capillary porosity measured is therefore underestimated which in turn increases the apparent C-S-H content. This limited resolution issue is addressed in the following section.
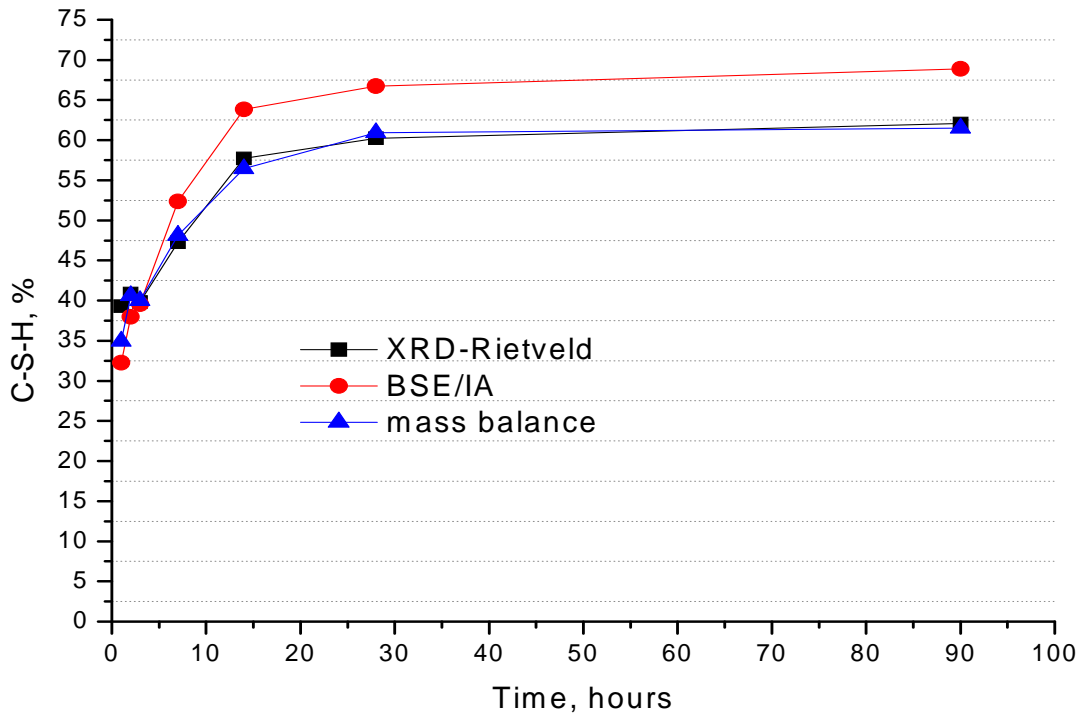
Figure 4. 15: Quantification of amorphous phase by XRD-Rietveld, BSE/IA and mass balance calculations for C_3S paste over hydration

4.3.3. Measure of the Density

The variation of the density with hydration for the different gradations investigated was determined by helium pycnometry and by the Archimedes method. The Archimedes method gives insight on the apparent density (ρ_{app}), including the pores. ρ_{app} increases over hydration since water is gradually bound to the solid. The density measured by helium pycnometry excludes the pores and only gives information on the solid density of the material (ρ_{solid}) which decreases over hydration as anhydrous content is replaced by less dense hydrates.

4.3.3.1 Apparent Density

The evolution of the apparent density of the different gradations of tricalcium silicate pastes is given in Figure 4. 16. The same trend as for the capillary porosity measured by

BSE-IA is observed since at constant degree of hydration the PSD-6µm paste shows lower values of apparent density compare to all other systems (Figure 4. 14).

The density calculated assuming values in Table 4. 3 is shown in dotted line in the same plot. The differences obtained in the calculated apparent density, due to the slight changes in the density of the C-S-H for the different gradations, cannot account for the differences found in the measured apparent density. Since there is almost no variation, only one of the calculated apparent densities for one of the gradations is showed in the plot.

However, PSD-82µm, the coarser particle size investigated, shows the highest densities (this can partially be explained by the observed bleeding with coarse PSDs as signalled above). The bleeding effect can not be corrected in this case.
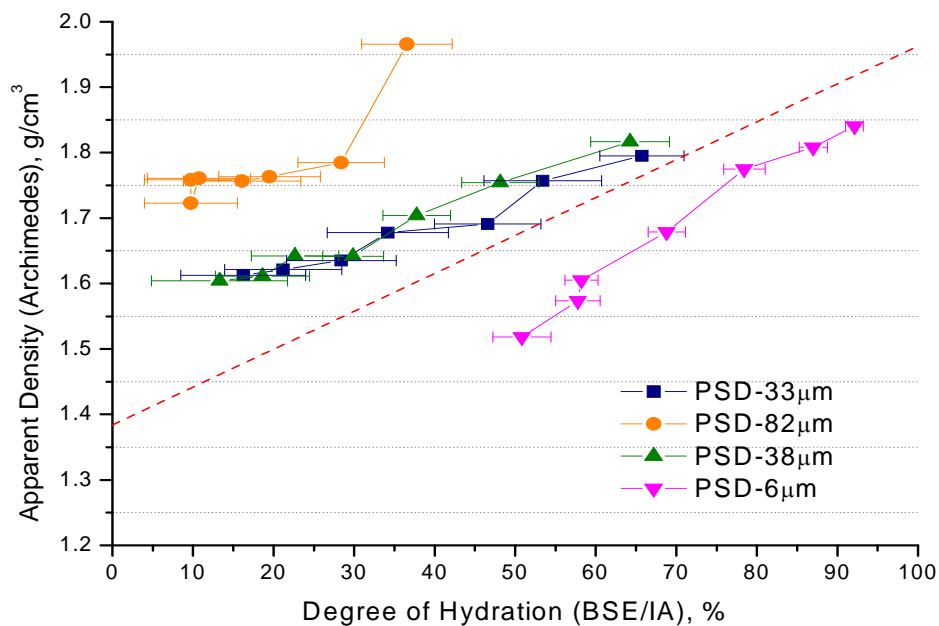

Figure 4. 16: Evolution of the density of the different gradations calculated by Archimedes methods versus the degree of hydration obtained from BSE/IA

4.3.3.2 Density of Solid Phases

The solid density measurements by Helium pycnometry for PSD-33µm, PSD-82µm, PSD-38µm, PSD-6µm pastes are shown in Figure 4. 17. The density decreases over hydration and varies from 2.80 g/cm^3 (most of the solid phases are still unreacted alite (ρ=3.15 g/cm^3)) to 2 g/cm^3 (most of the solid is hydrated) depending on the system: at a same degree of hydration, it increases with the decrease of the PSD.

In Figure 4. 17 a common trend is observed for the different particle sizes. Smaller gradations show higher values of solid density. This result clearly shows that in the case of PSD-6µm paste, the smallest of the gradations, the C-S-H formed is much denser or more packed than in the other systems. As hypothesised above, this might be due to a higher constrained space for product deposition: at a same degree of hydration, this would lead to a much higher capillary porosity, which is observed when measured using BSE-IA (Figure 4. 14). In the case of coarser particle size distributions (for instance PSD-38 µm) C-S-H should have less restrictions for deposition which could eventually allow a lower density, which in turn would lead to much lower values of capillary porosity (Figure 4. 14).

As for the investigation of the capillary porosity and the apparent density the calculated solid density was calculated for the different particle size distributions using the values shown in Table 4. 3. Here again, the density of the C-S-H formed for the different gradations does not induce significant changes on the value of the calculated solid density . Therefore, the most probable is that the different nature of the powders (PSD-33µm, PSD-82µm, PSD-38µm gradations from Alite and PSD-6µm from pure C_3S) does not cause the differences in the density. However, to completely discard the effect that the Al and Mg ions may provoke in the morphology and subsequently in the porosity and density of the C-S-H this need to be further investigated in more detail.
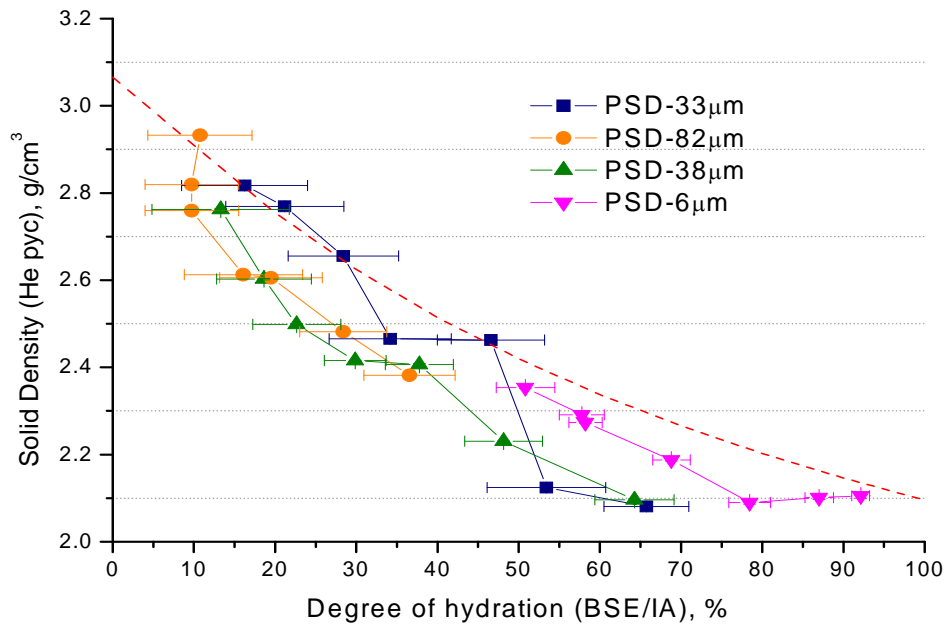
Figure 4. 17: Solid density (He pycnometry) versus degree of hydration (BSE/IA) for the PSD33µm, PSD-82µm, PSD-38µm and PSD-6µm pastes

From these results, the most probable hypothesis that could explain the differences found in density between the PSD-6µm and the other gradations of alite may lay on differences of available pore space morphology for deposition of C-S-H or in a different proportion of inner and outer products formed for the different gradations.

The value of solid density here obtained is a mix between the density of unhydrated C_3S, C-S-H and CH.

By definition, the apparent density in these systems can be written as Eq. 4.3:

$$\rho_{app} = \frac{m_{C3S} + m_{C-S-H} + m_{CH}}{V_{C3S} + V_{C-S-H} + V_{CH}} \qquad \text{Eq. 4.3}$$

$$V_{C-S-H} = \frac{m_{C-S-H}}{\rho_{C-S-H}} \qquad \text{Eq. 4.4}$$

Combining Eq. 4.3 and Eq. 4.4 the density of C-S-H can thus be calculated by using the following equation (Eq. 4.5):

129

$$\rho_{C-S-H} = \frac{m_{C-S-H}}{\left(\dfrac{m_{C3S} + m_{CH} + m_{C-S-H}}{\rho_{app}} - V_{C3S} - V_{CH} \right)}$$
Eq.4. 5

The molar mass and the stoichiometry of reaction used for the calculation were previously shown in Table 4. 3

The back-calculated density of C-S-H is plotted in Figure 4. 18. In this graph the C-S-H densities for the different gradations are compared at the same degree of hydration (50 % DH). A slightly increase of the C-S-H density while decreasing the size of the grains is observed giving the proof the different nature of the C-S-H packing. Incompatible values with the trend were measured for PSD-82µm but as already mentioned, this may be probably due to some bleeding at early age. C-S-H densities shown in Figure 4.18 are lower than the values presented in Table 3.4 derived from chemical shrinkage methods. Feldman [35] suggested that the lower values of solid density measured by this technique can be explained by the poor penetration of helium into the C-S-H layer leading to lower C-S-H densities.
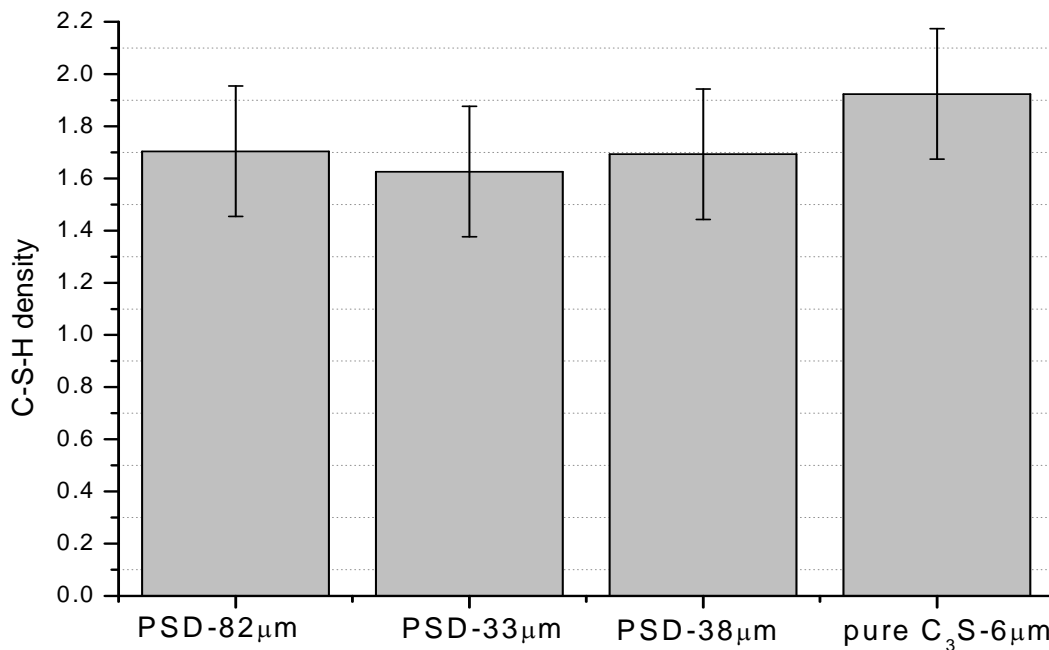
Figure 4. 18: Comparison of the C-S-H density for different particles sizes at the same degree of hydration (50%)

Parameters such as the composition, chemical bound water and interparticle space between C-S-H sheets are directly linked to the final density of the C-S-H and thus their investigation should bring important information to assess the effect of particle. These parameters have been investigated and discussed in Chapter 5.

4.3.3.3. C-S-H relative density from its BSE brightness

C-S-H composition and porosity are known to depend on factors such as curing temperature, water content and degree of hydration of the sample [29]. As said in §4.2.2 the relative brightness of phases in BSE imaging is a function of its composition and apparent density. He pycnometry measurements have shown that depending on the particle size, the density of the C-S-H which is produced can vary. This is confirmed qualitatively in which shows the differences in term of grey level histogram calculated from the average of inner and other C-S-H of PSD-82μm and PSD-6μm pastes: although CH and alite have the same grey level, that of C-S-H is higher in the case of PSD-6μm

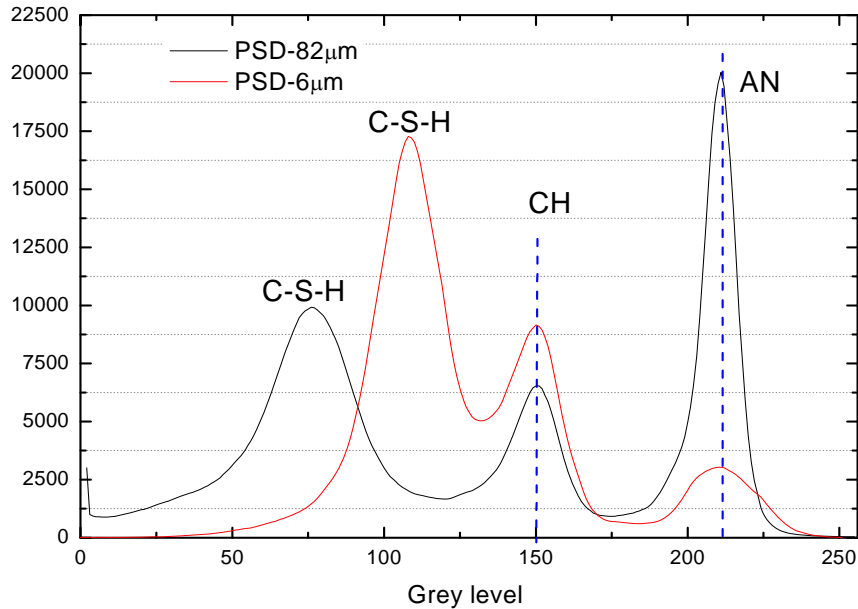than in PSD-38µm for a constant composition, this implies a higher density for the C-S-H produced from PSD-6µm.

Figure 4. 19: Comparison of the PSD-82µm and PSD-6µm grey level histograms

This can be semi-quantitatively assessed by measuring the C-S-H relative brightness using the following relation:

$$\textbf{C-S-H relative brightness} = \left(\frac{I_{AN} - I_{CSH}}{I_{AN} - I_{CH}} \right) \qquad \text{Eq. 4.7}$$

where I_{AN}, I_{CSH} and I_{CH} are the brightness of the anhydrous C_3S grains, C-S-H and portlandite, respectively. An increase of this so-called 'relative brightness' accounts for an increase of the density of C-S-H.

The differences in the C-S-H relative brightness of PSD-82µm, PSD-38µm and PSD-6µm pastes are shown in Figure 4. 20. Even if values are quite close and the standard error overlap, a clear trend that the C-S-H brightness increases gradually with increases in the finesse of the gradations. This approach agrees well and confirms the results obtained using He pycnometry (Figure 4. 17) as long as the C-S-H grey level evolution is only dependant on its internal porosity. It will be seen in chapter 5 that the Ca/Si ratio of C-S-

H is affected neither by the tricalcium silicate polymorphism nor by the presence of Al^{3+} and Mg^{2+} ions. The levels of these ions in alite are not high enough to have any significant influence on the C-S-H grey level. The variations observed in Figure 4. 20 are therefore probably due to a change in the C-S-H density/internal porosity
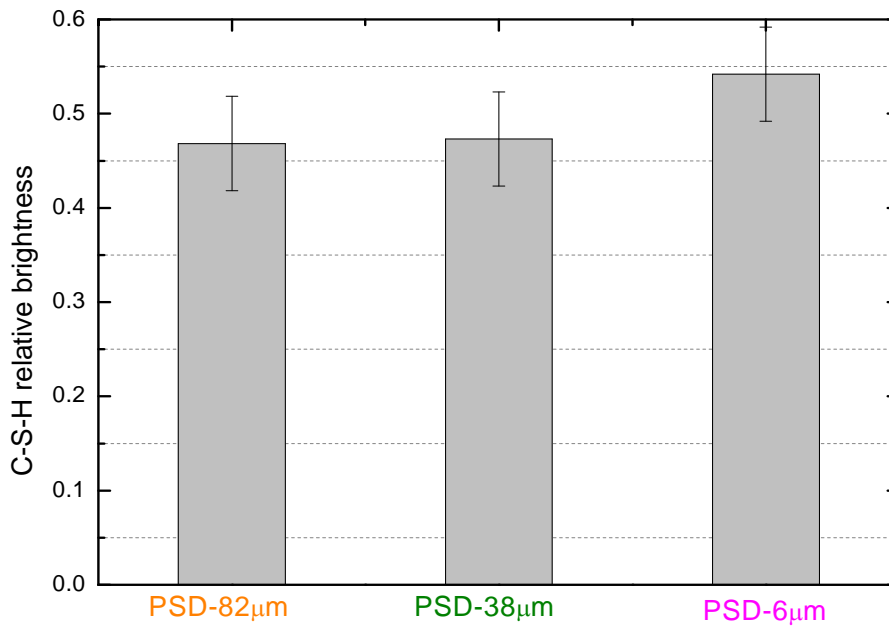

Figure 4. 20: C-S-H relative brightness different gradations

4.4 Morphological / Local Analysis of the Microstructure

In this section, a local analysis of the main phases observed in the C$_3$S hydration is described.

It especially emphasizes the effect of the initial size of particles on the formation, consumption, development, size, shape and arrangement of phases.

4.4.1 Reactivity of C$_3$S Grains

Figure 4. 21 shows micrographs of the gradations PSD-82µm, PSD-38µm, PSD-33µm, and PSD-6µm. These micrographs show that in some parts of the surface the reaction proceeds faster. Some parts of the surfaces behave as preferential reaction sites for hydration. Selective reaction at the surface of the grain was found to be a characteristic phenomenon for all ages and gradations investigated.

This selective reaction was previously reported by Mathur [30]. In his study of OPC pastes, the surface of the alite grains showed ridges, indicating signs of preferential reaction along some planes. He pointed out that the reaction of the cement grains progressed by the inward movement of a reaction front. The different alite systems investigated follow the same trend.

Figure 4. 22 shows high magnification images of an alite grain with a medium size of 13 microns after 12 hours of hydration. The reaction is seen leaving a non-homogeneous distributed C-S-H layer as it progresses inward. No gap between the formed C-S-H layer and the anhydrous core has been observed. The same features are shown in a bigger particle (82-µm) in Figure 4. 23.

In Chapter 3, the defects found in alite grains have been considered as a hypothesis to explain the differences in the dissolution rate and induction period lengths between

different particles. Particles with higher surface areas are expected to have a higher number of defects per unit volume and therefore higher hydration rates. The strong etching of the alite grains observed here agrees well with a selective reactivity (as already mentioned by Mathur [30]) which could be strongly correlated with the impact of defects as reactive sites. Further investigation is required to determine the number of defects in the structure and understand the changes that foreign ions introduce in the lattice parameters of C_3S.
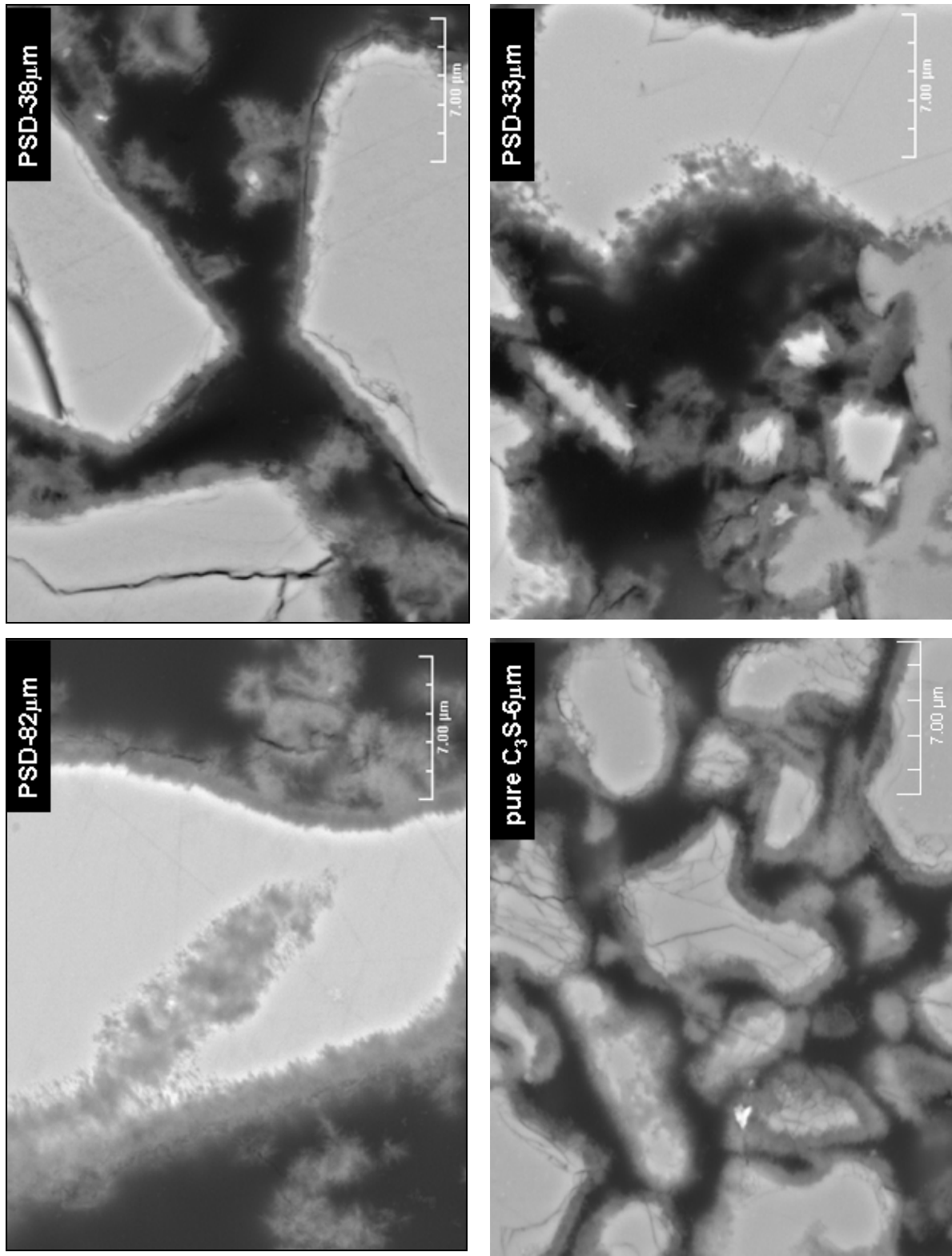
Figure 4. 21: Micrographs of alite pastes with different particle size illustrating the preferential reaction on the grains. PSD-82μm (3 days), PSD-38μm (1day), PSD-33μm (1day) and PSD- 6μm (1day)
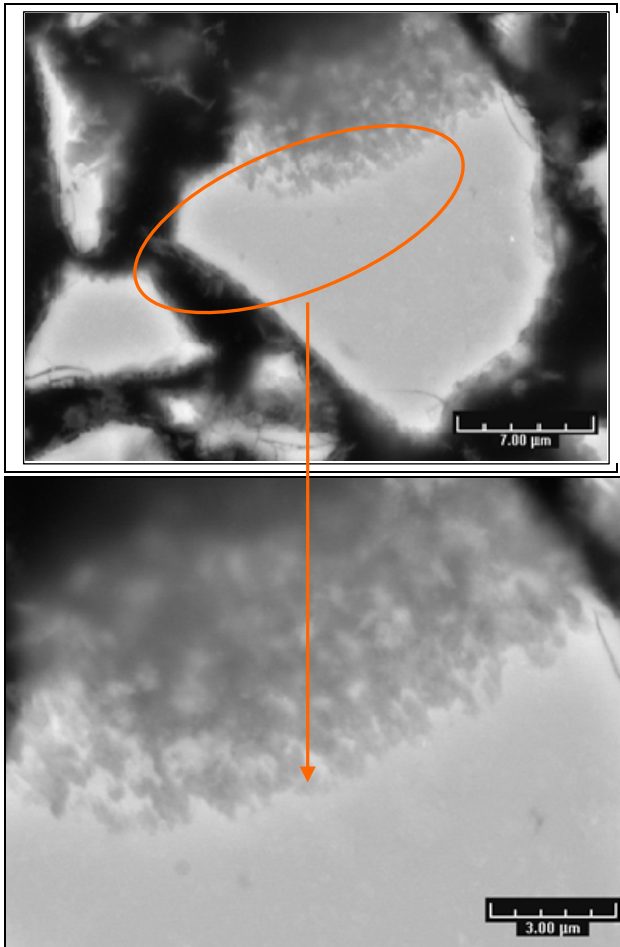
Figure 4. 22: BSE image which illustrate the "preferential reaction" in a alite grain after 12h of hydration in PSD-13µm.
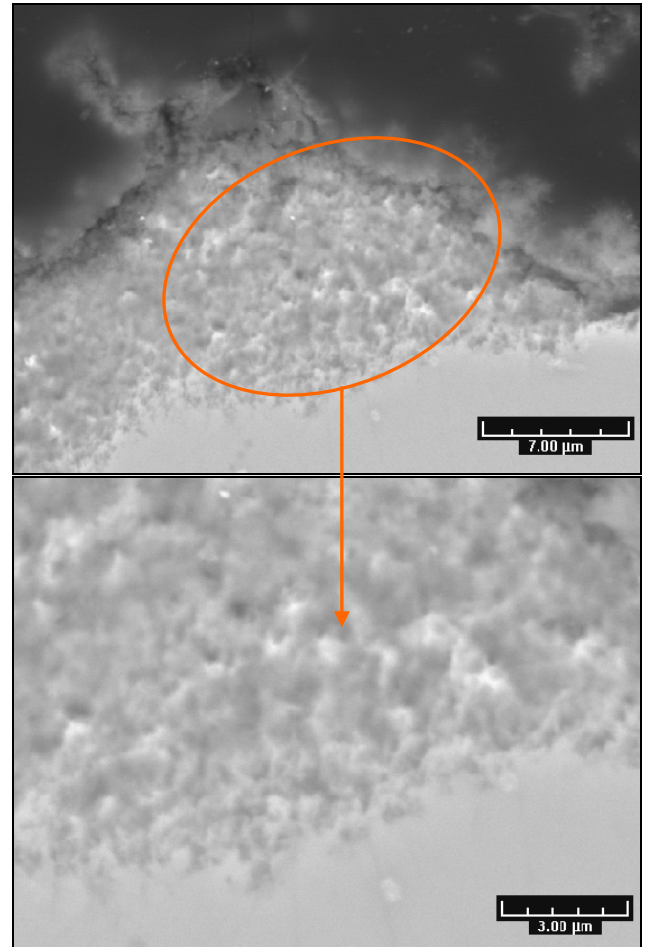
Figure 4. 23: BSE image which illustrate the "preferential reaction" in a alite grain after 24h of hydration in PSD-82µm.

4.4.2 Development of C-S-H

The morphology of C-S-H has been largely reported [5,31,32]. In both, OPC and C_3S pastes, the morphology of this hydration product is very similar. Richardson [5] described the morphology of the inner product (Ip) as having a fine-scale and homogeneous morphology. The outer product, in the other hand, is constituted by foil-like morphology.

In his colloidal model for C-S-H, Jennings [33] defined C-S-H packing densities as either low-density (LD) or high-density product (HD). The high density product was characterized by microporosity in which the N_2 cannot get into during the measurement. Figure 4. 24 presents BSE images of the PSD-82µm paste after 50 days of hydration in which 2 types of C-S-H are distinguished: fibrillar and directional C-S-H and higher density inner C-S-H.

The same type of morphology for C-S-H is observed for all gradations investigated (Figure 4. 25). At the same age, smaller particles which have higher degrees of hydration. The thickness of the C-S-H layer as a function of degree of hydration for the different gradations has been measured by means of image analysis at high resolution (0.147 microns) on 500 individual grains. For each alite particle the surface fraction of C-S-H was compared to that of the unreacted grain and converted to a shell thickness assuming spherical particles.
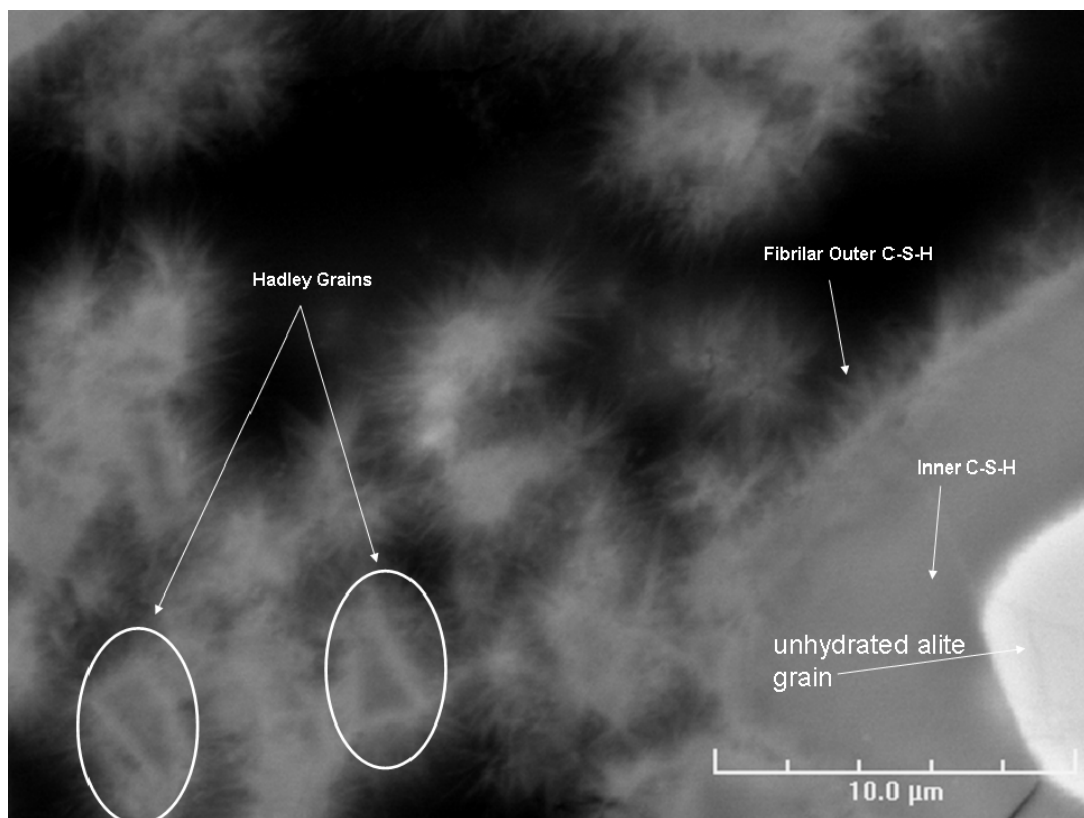

Figure 4. 24: BSE image of PSD-82µm paste after 50 days of hydration showing two types of C-S-H: inner and outer C-S-H
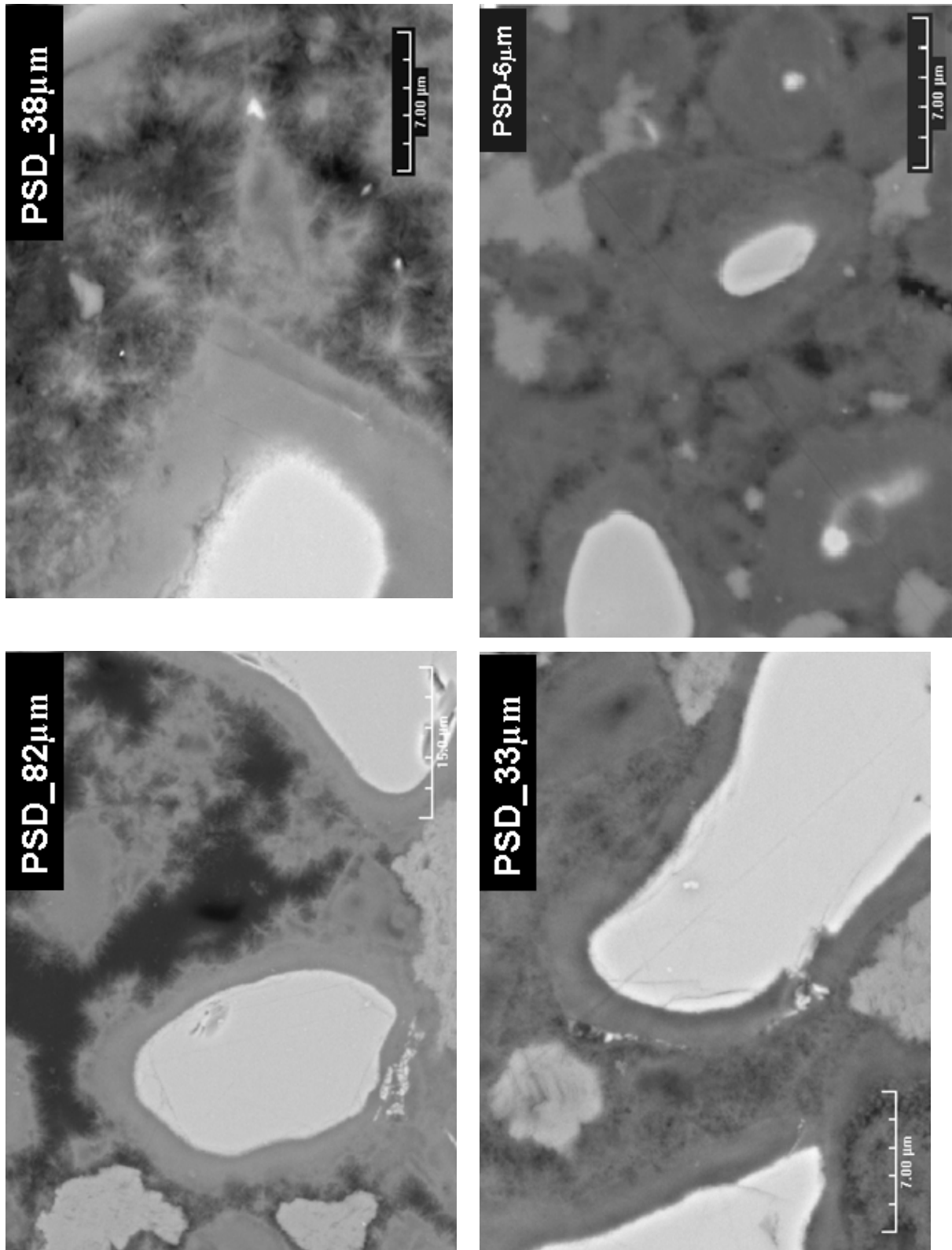
Figure 4. 25: BSE images of alite pastes of different particle sizes after 28 days of hydration showing two types of C-S-H: inner and outer C-S-H

During hydration, the thickness of the C-S-H layer formed increases. In the case of the PSD-33µm system, after 24 hours of hydration the shell thickness has a medium value of 0.7 µm and goes up to 5.5 µm at 90 days.

The variation of the C-S-H thickness over hydration for two narrow gradations (PSD-82 µm and PSD-38 µm) is given in Figure 4. 26 which shows that it is strongly dependent on the grain size. At a same degree of hydration PSD-82µm has a much thicker C-S-H layer than PSD-38µm which is explained by the fact that there is less surface for C-S-H deposition.

Assuming spherical particles, the degree of hydration can be back-calculated from the measured shell thicknesses. The thicknesses of 2.2 and 4.2 microns, shown in Figure 4. 26, give a degree of hydration of 23% for PSD-38µm and 21% for PSD-82µm. This compares nicely to the 25% degree of hydration measured by BSE-IA for these shell thicknesses, confirming the reliability of the IA approach.
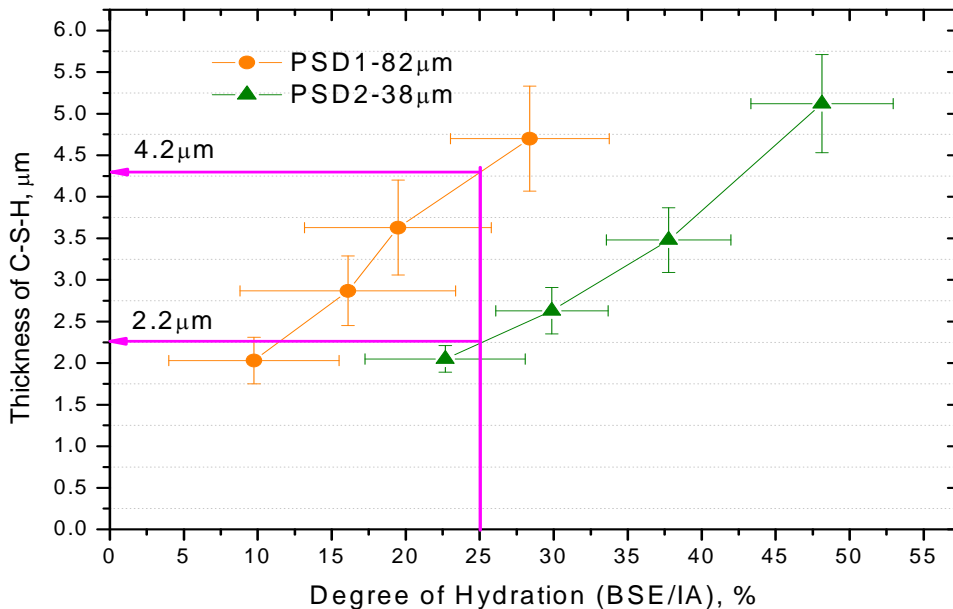

Figure 4. 26: Calculated C-S-H thickness versus the degree of hydration measured by BSE/IA in C_3S pastes at different ages for two different particle sizes

Figure 4. 24 shows some Hadley grains, recognizable by the porous space that occupies the space left from the fully hydrated alite particle. The median size of those Hadley

grains over time was measured using image analysis from several BSE images of alite grains, and is shown in Table 4. 4. This in agreement with [4] in which Kjellsen, investigating the microstructure of C_3S didn't reported the existence of any Hadley grain with a median size bigger than 4µm.

Table 4. 4: Median size of Hadley grains over time calculated from BSE images

Time (days)	Hadley grain size (µm)	Standard Deviation
0.6	1.20	0.22
0.7	1.62	0.22
1	1.68	0.52
2	2.37	0.50

4.4.3 Nucleation and Growth of Portlandite over Hydration

As previously mentioned in § 4.1, the nucleation and growth of CH in tricalcium silicate systems is different than in OPC. Figure 4. 27 compares the microstructure of OPC and alite pastes at 24 hours of hydration. In OPC paste, portlandite crystallizes and grows everywhere in the matrix with a variable shape [4,6,34]. On the other hand, in alite pastes portlandite forms clusters which grow from arbitrary places in the matrix, and which number and size increase during hydration.
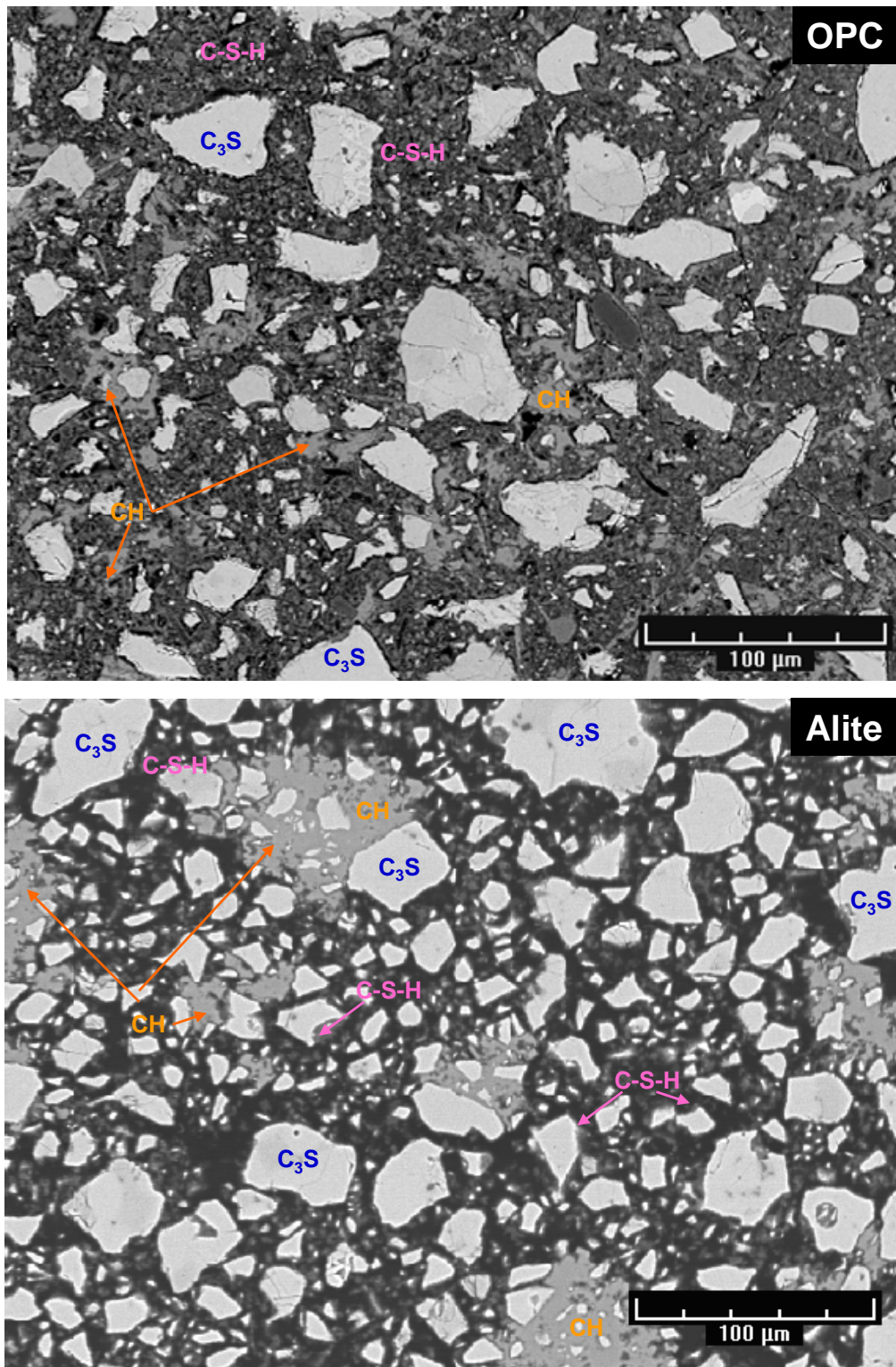
Figure 4. 27: BSE image comparing the differences in morphology of portlandite in OPC (top) and alite (bottom) pastes with w/c= 0.4 at 24 hours of hydration

In C$_3$S pastes, portlandite first grows forming a few nuclei increasing in number and size upon hydration (Figure 4. 29). The first nuclei are formed very early in the hydration. Small CH clusters were observed at 4 hours, the earliest age investigated. These clusters deposit randomly occupying capillary porosity and semi-hydrated grains stopping or slowing down their further hydration. Figure 4. 28 shows the close packing of the CH (light gray) and C-S-H (dark gray) in PSD-33µm paste after 14 days of hydration in which the CH clusters have grown occupying the available capillary space.
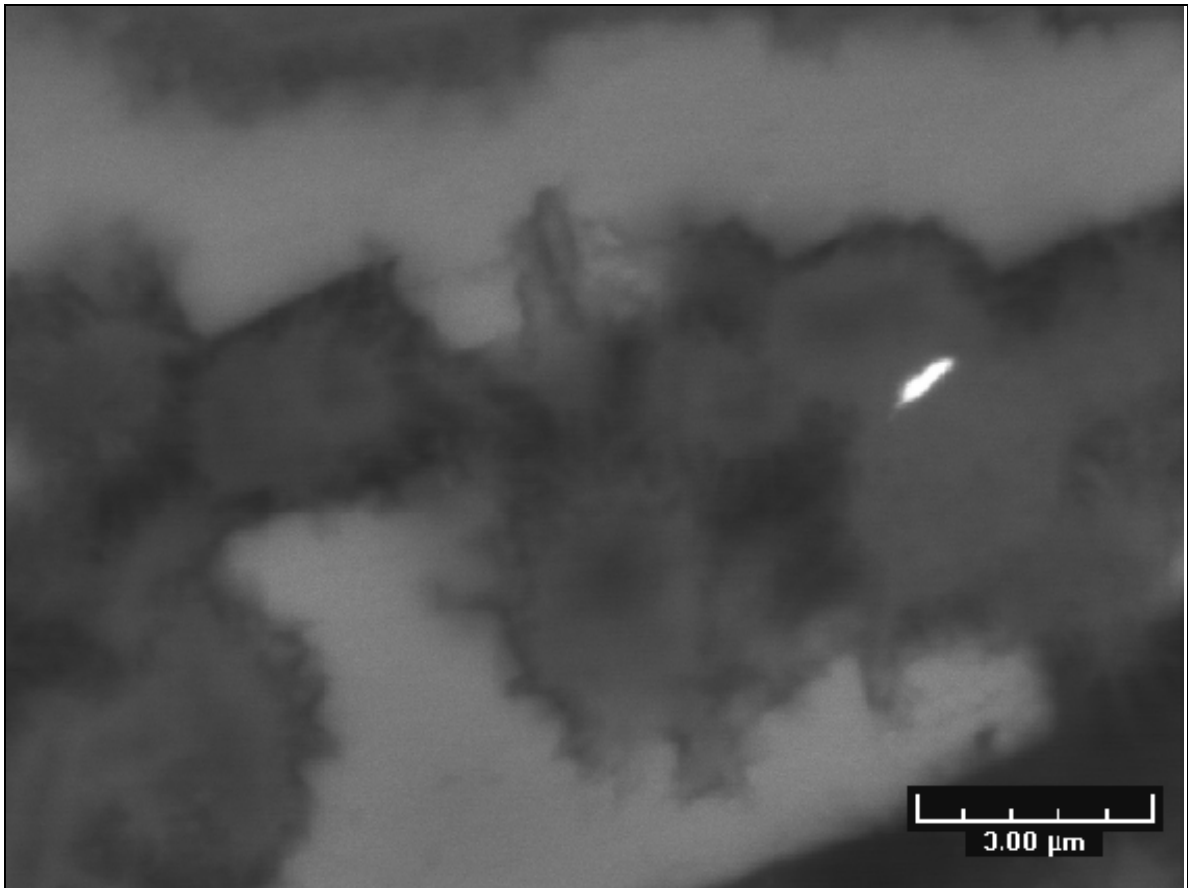

Figure 4. 28: BSE image of PSD-33µm paste (14days) in which the grains are completely reacted and portlandite clusters are filling in the available capillary porosity

Figure 4. 29 quantitatively shows that smaller gradations seem to present a higher number of CH clusters whereas for large PSDs, their number seems more limited while their size much bigger.
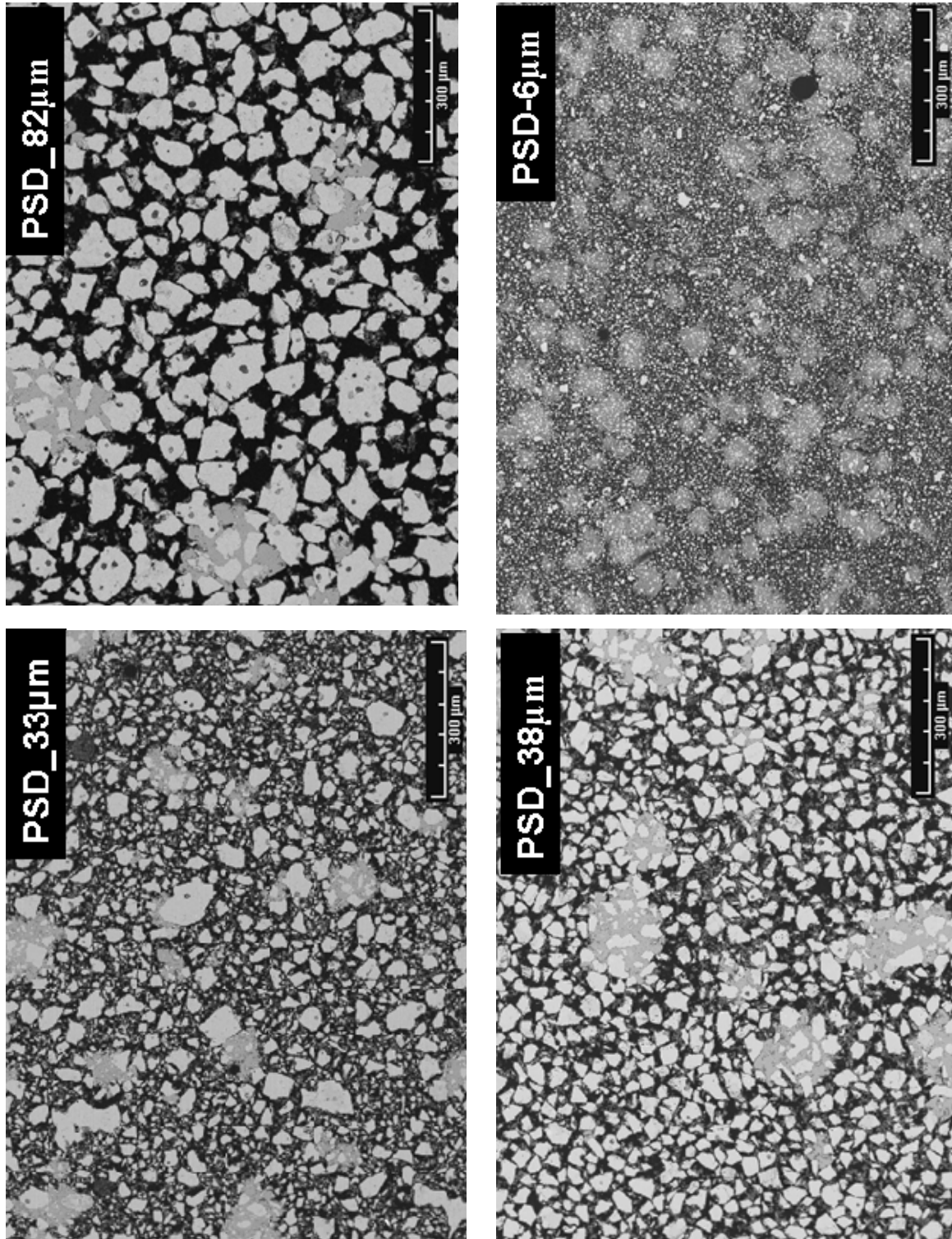
Figure 4. 29: BSE images showing the portlandite morphology and distribution of portlandite clusters for the following particle sizes: PSD-33µm, PSD-82µm, PSD-38µm and PSD-13µm pastes with a w/c= 0.4 at 24 hours of hydration

This has been quantitatively investigated by image analysis on large reconstructed cross sections (Figure 4. 30) made of 400 individual BSE images acquired at a nominal magnification of 200x (pixel size of 1.464 μm). The analysed surface in the reconstructed image was therefore corresponding to a 15x15 mm cross-section of the sample. The idea of working with this kind of large reconstructed map is to avoid field-cross-sectioning effects on large features such as the CH clusters which can be several hundreds of micron wide. Once reconstructed, the map is processed as any BSE image and CH clusters were extracted through grey-level histogram segmentation (Figure 4. 31). The number, size and distances between clusters have been quantified for 4 gradations: PSD-33 μm PSD-82 μm, PSD-38 μm and PSD-6 μm.
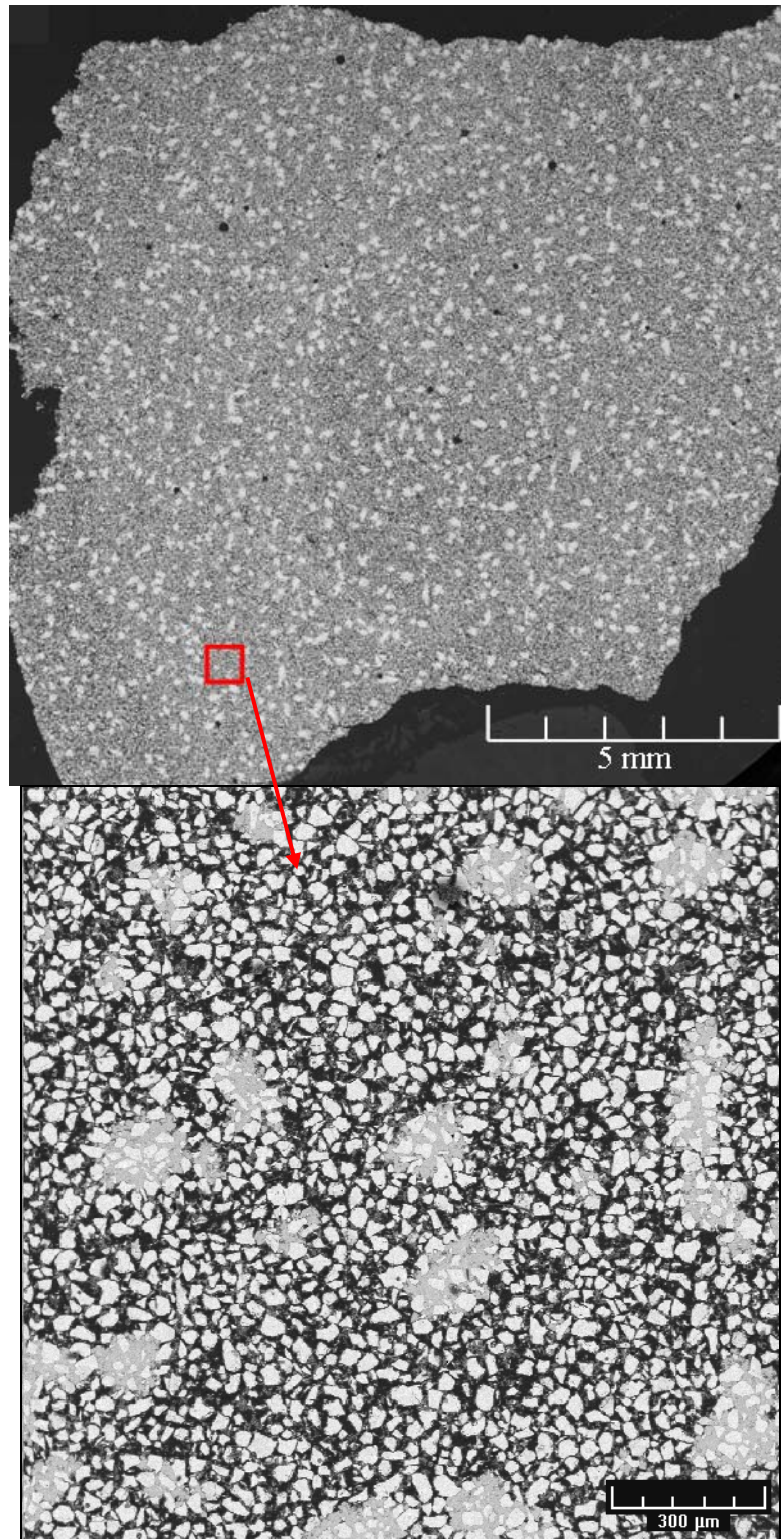
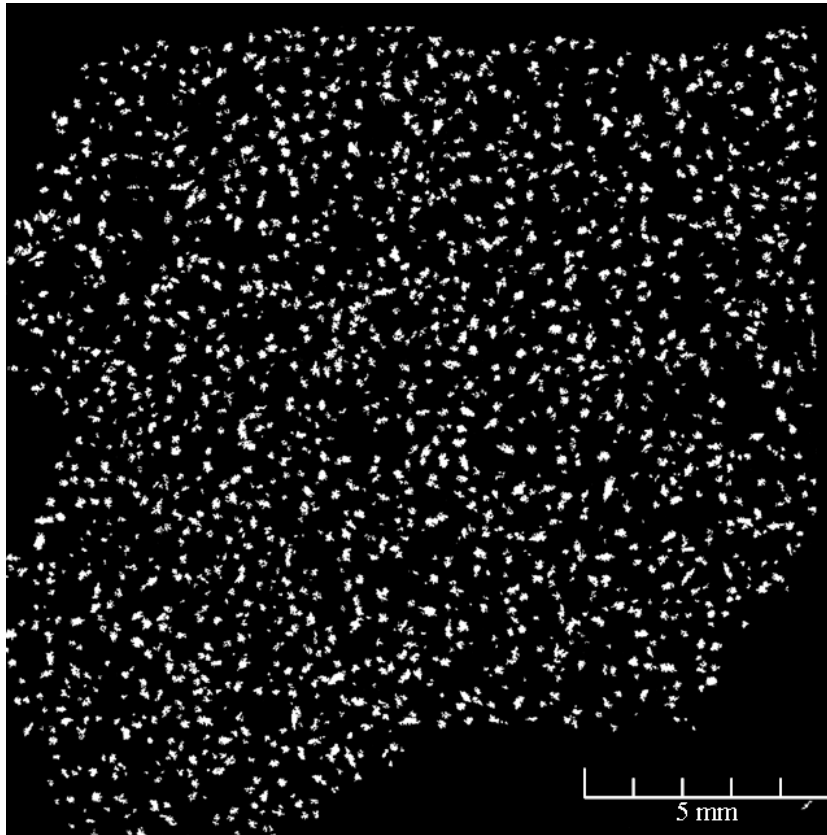Figure 4. 30: Reconstructed map PSD-38μm paste after 1 day of hydration

Figure 4. 31: Reconstructed map PSD-38 μm paste (Figure 4. 30) after image segmentation to isolate CH clusters

The calculation of the mean diameter of CH clusters is very complex due to the tortuous nature of the CH clusters. In this investigation, the portlandite cluster size distribution was calculated using the mean Feret diameter. *Feret's Diameter* is defined as the longest distance between any two points along the selection boundary. This is used to correct for the effects of image edges which reduce the error induced for the shape of the particle in the measure [17].

The number of portlandite clusters for PSD-33 µm, PSD-82µm, PSD-38µm and PSD-6µm pastes versus their mean size at 50% degree of hydration is plotted in Figure 4. 32. The distribution of sizes, especially for coarser particles, is very broad ranging between 0 and 600 µm. An increase of the mean size of the portlandite clusters while increasing the particle size distribution has been observed. In the smaller gradations, due to the higher specific surface area of the grains, the concentrations of calcium ions that go into solution

at the beginning of the reaction are greater (Figure 3. 19),   favouring the formation of CH nuclei. Therefore, the initial number of nuclei will be higher in smaller gradations. The precipitation of portlandite will preferentially occur on the portlandite nuclei rather forming new nuclei. Once the portlandite nuclei had been formed, rather that forming new nuclei. Bigger clusters are developed in the case of coarse particles as a consequence of the fewer number of initial nuclei formed.
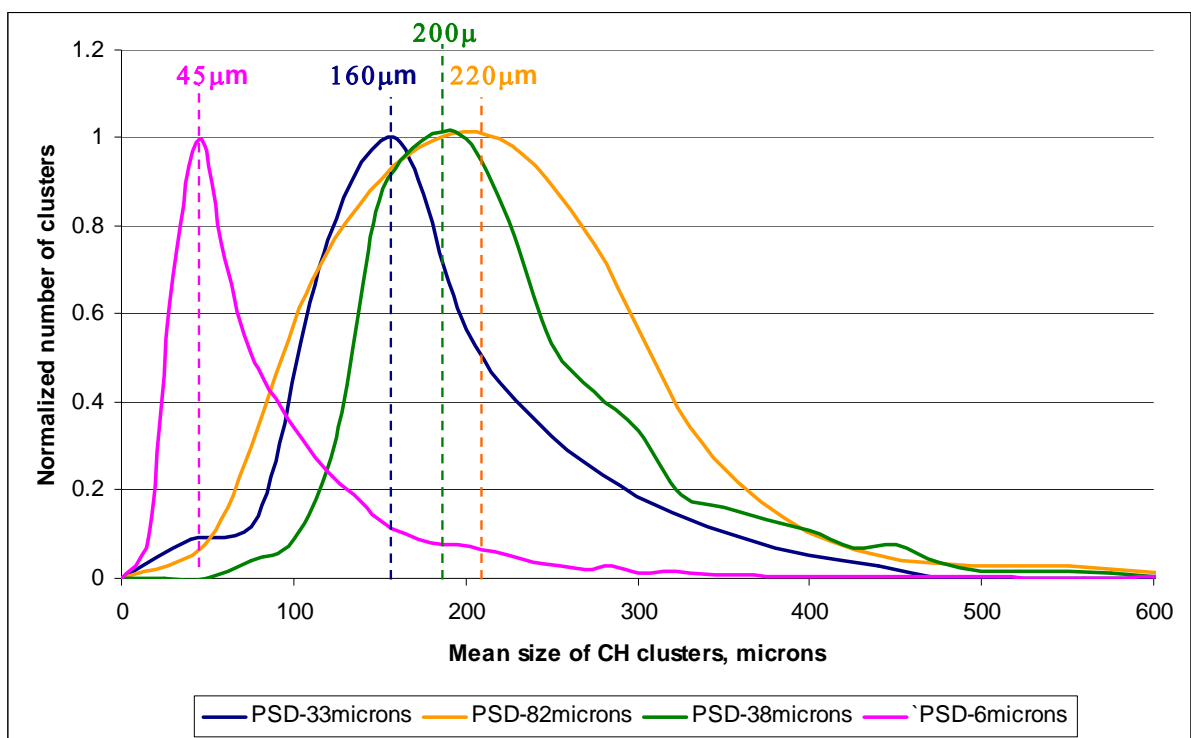
Figure 4. 32: Evolution of the number of portlandite clusters versus their mean size (PSD-82µm PSD-38 µm, PSD-33µm and PSD-6µm)

The mean distances between these clusters (more than 1000 clusters for each of the particle size distributions) at 50% degree of hydration are presented in Figure 4. 33. It shows that the distances between clusters are shorter when the initial particle size of the grains is small. This accounts for a better distribution of the clusters within the microstructure which is then more homogeneous. This again is a consequence of the greater number of initial nuclei formed which is linked to the higher availability of calcium ions in the pore solution at early age.

Figure 4. 33: Distribution of distances between portlandite clusters

4.5 Summary

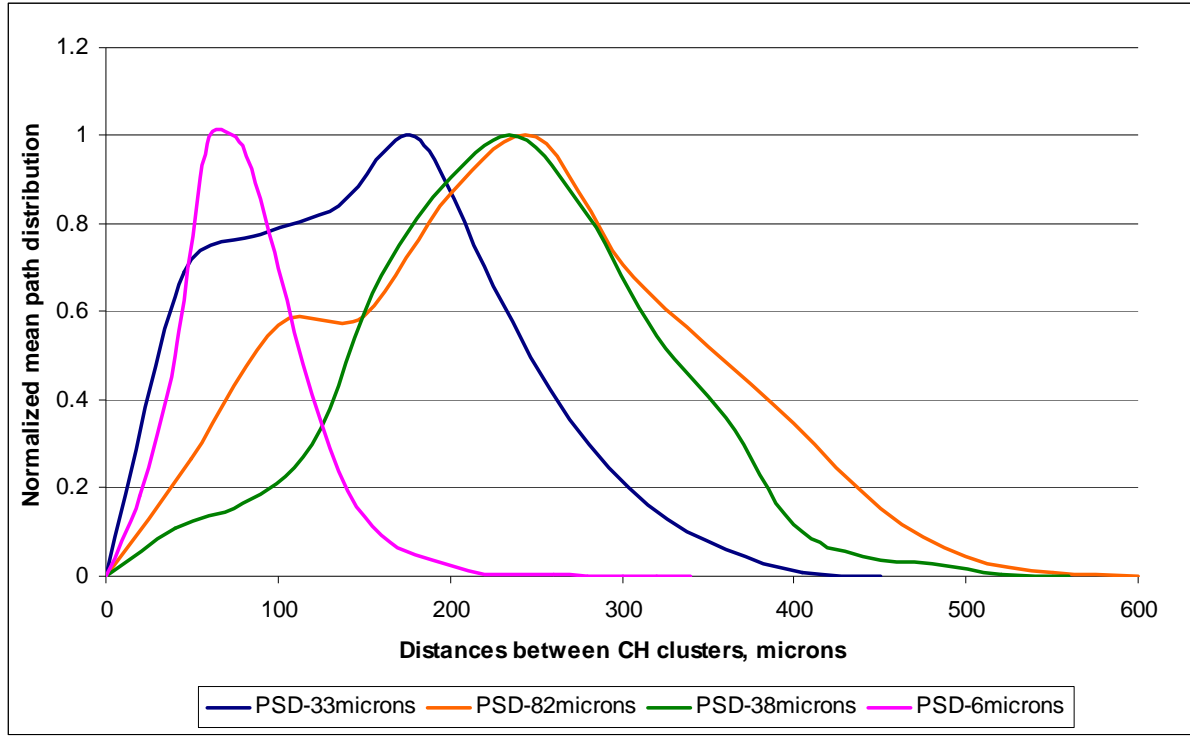Quantitative and morphological image analysis of SEM-BSE of polished cross sections was performed in order to get insight on the microstructural differences between hydrated pastes of alite with different particle size distribution.

The main results obtained for the different particle sizes considered are:

- A preferential reaction of the surface of alite grains is observed independently from the initial size of the grains. This has already been shown in the case of Portland cement and supports the hypothesis of the large influence of the density of defects in the sub-surface region of alite. This tends to support the observation made in chapter 3 to explain the faster rates of dissolution of the smallest particles. However further investigation is needed to really confirm the link between defects and dissolution rate for alite.

- Two types of C-S-H, inner and outer, were identified in all of the investigated systems. The boundary between inner and outer product was delimited sooner for powders with smaller particle size since those hydrate faster. At the microstructural level, no significant changes were observed between the various systems except the BSE grey level of the inner C-S-H which tend to be brighter while the PSD decreases. This could account for either a change in composition or a change in density of the C-S-H. The C-S-H thickness was measured by BSE/IA and found to be strongly dependent on the initial particle size. At the same degree of hydration, this layer is thicker for coarser particles since less surface area is available for C-S-H deposition.

- The capillary porosity was investigated by BSE/IA and found to be greater for smaller gradations. The same trend was observed when the pore volume was back-calculated from the solid density of the material. The differences observed for the different gradations were hypothesized to be directly related with the different initial arrangement of the grains. The grains pack closer for smaller gradations and therefore the available space for product deposition is more constrained. This leads to higher values of capillary porosity and higher density of

the solid. Another possibility would be related to the different morphology of the outer product [27]. Finer outer fibrils would form for smaller particles with more pore constrains, leading to higher values of capillary porosity. In coarse particles, there are fewer pore constraints, leading to a coarser outer product formed and lower values of capillary porosity.

- Portlandite grows in all particle size, forming randomly placed clusters in the matrix. Some of those clusters grow on C_3S grains, blocking or slowing down their further hydration. The amount of portlandite as quantified by both TGA and BSE/IA was found to be independent of the initial size of the grains when compared at the same hydration degree. The number, size and distances between clusters were found to be directly dependent on the initial particle size. For smaller gradations, as shown in chapter 3, the concentration of calcium ions available in solution is much higher at early ages favouring the formation of CH nuclei. During these early ages, the smaller gradations have a higher number of CH nuclei. Upon hydration, the precipitation of portlandite preferentially occurs on the previous formed nuclei leading to smaller clusters and shorter distances between them when the PSD decreases.

The results obtained in this study show that the microstructure at late ages is not affected much by the initial particle size of the powder. The main observed differences are the density of the C-S-H and the capillary porosity content, which was measured to be higher as the PSD decreases. The most probable explanation for this may be connected to the different initial arrangement of the grains.

REFERENCES

[1] Scrivener, K.L. Development of Microstructure during the Hydration of Portland cement, Ph. D Thesis University of London (1984)

[2] M. Diamon, S. Ueda and R. Kondo, Morphological study on hydration of Tricalium silicate, Cement and Concrete Research 1 (1971) pp. 391-401

[3] Jennings HM, Parrott LJ. Microstructural analysis of hydrated alite paste. Part 2: Microscopy and reaction products. J Mat Science 21 (1986) pp.4053-4059

[4] K.O.Kjellsen, H.Justes, Revisiting the microstructure of hydrated tricalcium silicate-a comparison with Portland cement, Cement and Concrete Composites 26 (2004) pp.947-956

[5] I.G. Richardson, The nature of C-S-H in hardened cement, Cem. Concr. Res. 29 (1999) pp. 1131-1147

[6] E. Gallucci, K. Scrivener. Crystallisation of calcium hydroxide in early age model and ordinary cementitious systems. Cem Concr Research 37 (2007) pp.492-501

[7] R. Kondo and S. Ueda, Proceedings of the 5th International Symposium on the Chemistry of Cement, Tokyo (1968)

[8] Kalliopi K. Aligizaki, Pore Structure of cement-based Materials: Testing, Interpretation and Requirements, Modern Concrete Technology 12, London and New York (2006)

[9] H.F.Taylor, Chement chemistry, Tomas Helford, London 1997

[10] Jennings H.M., Pratt P.L., On the hydration of Portland cement, Proc. Brit. Ceram. Soc. 28 (1979) p.179-193

[11] Scrivener K.L., Bentur A, Pratt P.L, Quantitative characterization of the transition zone in high strength concretes, Advances in Cement Research 1, p.230-237 (1988)

[12] Scrivener K.L., Backscattered electron imaging of cementitious microstructures: understanding and quantification, Cement and Concrete Composites 26 (2004) p. 935-945

[13] Scrivener K.L., Pratt P.L, Characterisation of Portland cement hydration by electron optical techniques, In Electron microscopy of materials. Proc Mat Res Soc Symp 31 (1983) p. 351-356

[14] D.W. Hadley, W.L. Dolch, S. Diamond, On the occurrence of hollow-shell hydration grains in hydrated cement paste, Cem. Concr. Res 30 (2000) p.1-6

[15] S. Diamond, K.O.Kjellsen, Resoltion of fine fibrous C-S-H in backscatter SEM examination, Cem. Concr. Res 28 (2006) p.130-132

[16] L.J.Struble; P.E. Stutzman, Epoxy impregnation of hardened cement for micro-structural characterization, Journal of Materials Sicence Letters 8:632-634 (1989)

[17] John C. Russ, Practial Stereology, Plenum Press, New York (1986)

[18] R. F. Feldman, Density and porosity studies of hydrated Portland cement, Cement Technology, (1972) pp.5-14

[19] M. Krus, K.K. Hansen, H.M. Künzel, Porosity and liquid adsorption of cement paste, Materials and Structures, Vol. 30, 201 (1997) pp. 394-398

[20] http://www.micromeritics.com/

[21] S. Mindess, J.F. Young, D. Darwin, Concrete, 2nd Edition (2002), Prentice Hall, Englewood Cliffs, NJ

[22] Dale P. Bentz, Edward J. Garboczi, Claus J. Haecker, Ole M. Jensen, Effects of cement particle size distribution on performance of properties of Portland cement-based materials, Cement and Concrete Research 29 (1999) pp. 1663-1671

[23] K.L. Scrivener and P.L. Pratt, Characterisation of Portland cement hydration by electron optical techniques. In: W. Krakow, D.A. Smith and L.W. Hobbs, Editors, Electron Microscopy of Materials, Materials Research Society Symposium Proceedings vol.31, Elsevier Science Publishing (1984), pp. 351–356.

[24]Pierre Mounanga, Abdelhafid Khelidj, Ahmed Loukili, Ve´ronique Baroghel-Bouny, Predicting Ca(OH)$_2$ content and chemical shrinkage of hydrating cement pastes using analytical approach, Cement and Concrete Research 34 (2004) pp. 255–265

[25] Scrivener K.L., Backscattered electron imaging of cementitious microstructures: understanding and quantification, Cement and Concrete Composites 26 (2004) pp.935-945

[26] Wang Aiquin, Zhang Chengzhi, Zhang Ningsheng, The theoretic analysis of the influence of the particle size distribution of cement system on the property of cement, Cement and Concrete Research 29 (1999) pp.1721-1726

[27] Richardson I.G., The nature of the hydration products in hardened cement pastes, Cement and Concrete Composites 22 (2000) p.97-113

[28] K. Fujii and W. Kondo, Kinetics of the hydration of tricalcium silicate. J. Am. Ceram. Soc. 57 (1974), pp. 492–497

[29] C. Famy, K. L. Scrivener and A. K. Crumbie, What causes differences of C-S-H gel grey levels in backscattered electron images?, Cement and Concrete Research 32 (2002) pp. 1465-1471

[30] Mathur, P.C., Study of Cementitious Materials using Transmission Electron Microscopy, Ph. D Thesis École Polytechnique Fédéral de Lausanne (2007)

[31 J.H. Taplin, Aust. J. appl. Sci. 10 (1959) pp.329-345

[32] I.G. Richardson , Tobermorite/jennite- and tobermorite/calcium hydroxide-based models for the structure of C-S-H: applicability to hardened pastes of tricalcium silicate, β-dicalcium silicate, Portland cement, and blends of Porland cement with blast-furnace slag, metakaolin, or silica fume, Cement and Concrete Research 34 (2004) pp.1733-1777

[33] Hamling M. Jennings, A model for the microstructure of calcium silicate hydrate in cement paste, Cement and Concrete Research 30 (2000) pp. 101-116

[34] S. Diamond, Calcium hydroxide in cement paste and concrete-a microstructural appraisal, in: J. Skalny, J. Gebauer, I. Odler (Eds.), Material Science of Concrete, Special volume: Calcium Hydroxide in Concrete, The American Ceramic Society, Westerville (2001) pp. 37-58

[35] R.F. Feldman, Cem. Technol. 3 (1972) p.5

CHAPTER 5: CHARACTERIZATION OF C-S-H IN TRICALCIUM SILICATE PASTES

In the previous Chapter, the microstructural development of C_3S pastes with different particle sizes was investigated and discussed. It was concluded that the microstructure develops in primarily the same manner, regardless of the initial particle size. The only differences observed were related to the deposition and microporosity of C-S-H. The most probable hypothesis that can explain the observed differences found in bulk density and porosity is the higher constrained space for deposition of product in systems with small particle size distributions. For coarse particles, these constraints are smaller leading to much lower values of capillary porosity and lower values of C-S-H density.

Since the only major differences were connected to the C-S-H and in order to assess the veracity of the drawn hypothesis, the present chapter focuses on its formation and intrinsic characteristics. This includes the analysis of its morphology using scanning and transmission electron microscopy, its solid and water composition by EDS and thermogravimetric analysis and its porosity and specific surface investigated by nitrogen adsorption/desorption using Density Functional Theory (DFT).

5.1 State of the Art on Calcium Silicate Hydrate C-S-H

Calcium silicate hydrate (C-S-H) is the main binding phase and is formed from the hydration of C_3S with water as shown in Eq.5. 1:

$$C_3S + (3-x+n)H \rightarrow C_xSH_n + (3-x)CH \qquad \text{Eq.5. 1}$$
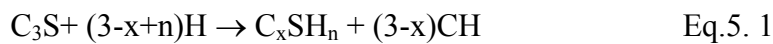
Where n is the water to silica ratio (H/S) and x is the calcium to silica ratio (C/S).

5.1.1 Ca/Si (C/S) ratio in C-S-H

There is a large range of Ca/Si (C/S) ratio values of C-S-H found in the literature, ranging from 1.2 to 2.3. There is a general consensus however, that for C_3S pastes it is around 1.7-1.8 [1,2]. The intermixing of C-S-H with portlandite or the substitution of Si^{4+} by Al^{3+} in alite pastes could explain some of the higher values of C/S found in the literature [3]. Some researchers [3-5] have reported constant values of C/S ratio over hydration.

5.1.2 Bound water in C-S-H (H/S)

As a consequence of the hydration of cement and the formation of products, the microstructure gradually becomes denser. Part of the initial water becomes chemically combined in the hydration products during the hydration,while some water is adsorptively bonded to the surfaces of the hydration products by surface forces. The remaining water fills the interstitial spaces as liquid water [6].

Chemically bound water is defined in this work as the amount of water which reacts with solid and leads to the formation and precipitation of hydrates. In C-S-H, *bound water* includes the structural water which is chemically connected to the crystalline structure, the interlayer water and the adsorbed water.

The calculation of the bound water in C-S-H (H/S) is very difficult and controversial since there is no sharp distinction between water present as part of C-S-H structure and water held in micropores, isolated mesopores and as multilayer adsorbed films. The chemically bound water decreases when the curing temperature increases. The measured values depend on the drying conditions and the time at which the material is held under these conditions before heating to drive off all of [1,7]. Young and Hansen [8] reported values of H/S of 2.1 for C_3S pastes equilibrated in an atmosphere of 11% RH. For fully hydrated C_3S pastes dried by D-drying method the typical values obtained are between 1.3-1.5 [5]. Other researchers [4,5] reported no variation of the H/S ratio of C-S-H with the degree of hydration in C_3S pastes. However it was found to increase within increasing the w/c ratio[9].

5.1.3 Structure of C-S-H

C-S-H has a poorly-crystalline structure. It is generally agreed upon that C-S-H has a disordered layer structure composed of calcium ions in which silicate ions and hydroxyl groups attached together with the interlayer of calcium ions and water molecules. There are several models proposed that describe the structure of C-S-H. Taylor proposed a model composed of the mix of structural units derived from jennite ($C_9S_6H_{11}$) and 1.4 − nm tobermorite ($C_5S_6H_9$) [1]. Figure 6. 1 illustrate this type of structure [1].
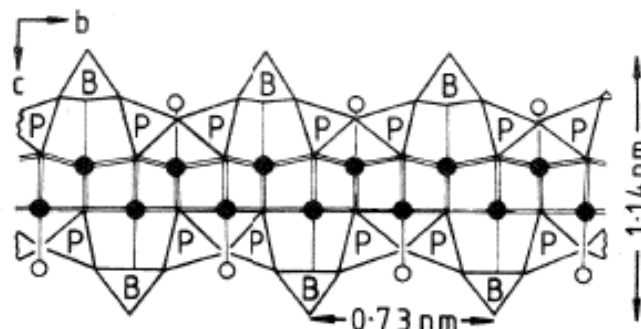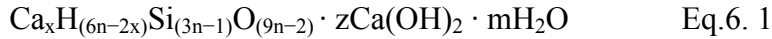

Figure 6. 1: Silicate chain of the type present in 1.4-nm tobermorite and jennite (dreierkette). Reproduced from [1]

Richardson and Groves [10] proposed a generalized model for the C-S-H and expressed as Eq. 6.2

$$Ca_xH_{(6n-2x)}Si_{(3n-1)}O_{(9n-2)} \cdot zCa(OH)_2 \cdot mH_2O \qquad \text{Eq.6. 1}$$

This model was extended later on to cement pastes by allowing the possibility of various ionic substitutions [10] and seems to be implicitly based on altered 1.4 nm tobermorite.

5.1.4 Morphology of C-S-H

The two types of C-S-H layer can be distinguished from the reaction of C_3S or OPC pastes. Taplin [11] classified them as inner product which grows within the original boundaries and outer product which lies outside the original grain boundaries. Later on, Jennings [12] classified the two types of C-S-H as high density (HD) and low density (LD) that corresponds with the inner and outer products, respectively, denoted by Taplin.

Outer product forms before inner product during the nucleation and growth period. This grows outwards from the grain boundary and in free pore space. Outer C-S-H has a fibrillar and directional morphology. The shape of these fibrils is postulated to depend on the capillary porosity available for hydration. Richardson suggested that more coarse fibrillar C-S-H is formed when it grows in large capillary pores, however when there is more constrained space for product deposition, the C-S-H grows in a much finer morphology[3]. Later on the C-S-H starts to form inwards from the shell and grows with a homogeneous and fine-scale morphology, forming a pore size somewhat under 10nm in diameter [2].

5.1.5 Pore size characterization of C-S-H

Several different microstructural models have been proposed to describe the structure of C-S-H and its porosity. The most well known models are the ones presented by Powers and Brownyard [13], Feldman and Sereda [14], and Wittmann [15] and Jennings and Tennis [16]. Figure 6. 2 give a schematized representation of these models[1,17].

Powers and –Brownyard [13] proposed a C-S-H model composed of particles having a layered structure, made up of two to three layers randomly arranged which are bonded by surface forces. Later on, Feldman and Sereda [14] proposed a new model very similar to the model of Powers-Brownyard. In this model, the sheets composing the C-S-H gel are considered to not have an ordered layered structure. The C-S-H formed subparallel groups a few layers thick and which enclosed pores of dimensions ranging from interlayer spaces upwards. In the model proposed by Wittmann ("The Munich model") [15] the C-S-H structure is consider as a three dimensional network of amorphous colloid gel particles forming a "xerogel". Xerogel consist of separate particles without a preconceived particular internal structure. Jennings and Tennis proposed in 1994 [16] a new model based on the assemblage of basic building blocks formed of spherical units that group together. These basic building blocks are arranged together, leading to high density (HD) and low density products (LD) that corresponds with the inner and outer C-S-H, respectively.

C-S-H is often considered as an amorphous gel which contains pores of approximately a few nanometers in size that are called gel pores. Jennings et al. [18] and Diamond [19] have indicated that the C-S-H gel exists in a variety of forms such as irregular grains, fibrous particles, honeycombs, flattened particles.

Various techniques can be used to characterize the pore structure and the surface area of cement pastes like MIP, SAXS, SANS, NMR and gas sorption. Nitrogen adsorption is one of the most popular techniques used to study the pore structure of materials which

contain both micropores and mesopores. In the case of cement, nitrogen adsorption is one of the most used techniques to characterize the C-S-H pore morphology.

In this study, the pore size characterization of a calcium silicate hydrate (C-S-H) gel was studied by means of nitrogen sorption. Although the technique is not new, the analysis of the adsorption/desorption isotherms was carried out using new tools such as the Density Functional Theory (DFT). The approach was first applied to pillared clays, a model slit pore system and then to pure C-S-H. Thereafter, the pore size distribution of different gradations of C_3S was investigated in order gain to insight into the effect that the initial particle size has on their development over hydration. The distribution of pores has been calculated using different models, including new tools like the DFT model using both cylindrical and slit shaped pores. The evolution of the specific surface area as a function of hydration has also been investigated.
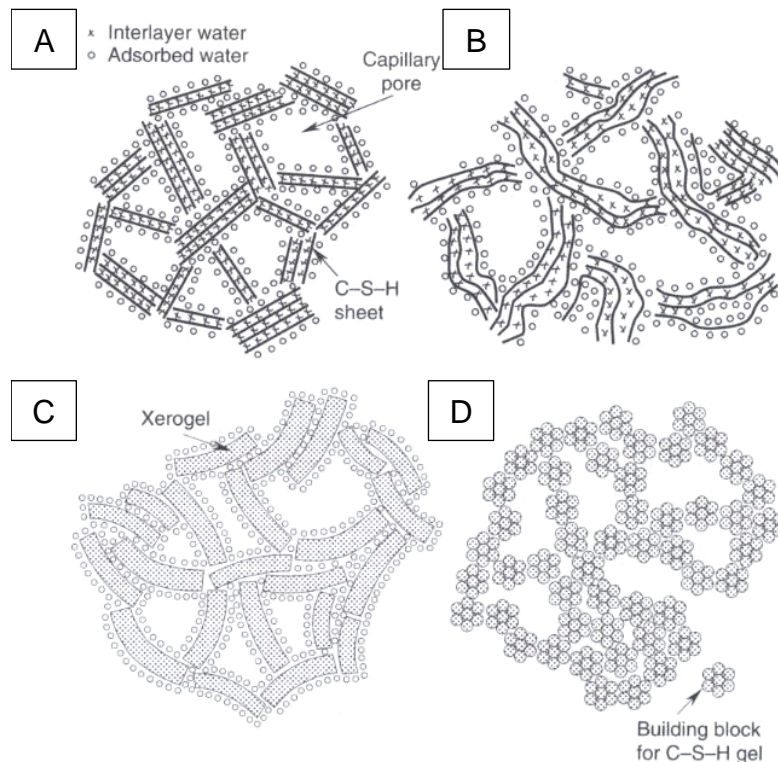

Figure 6. 2: Schematic representation of some of the existente models of C-S-H (reproduced from [17]). **A**: Powers and Brownyard (1948), **B**: Feldman and Sereda (1970), **C**: Munich model proposed by Wittmann (1977), **D**: Jennings and Tennis (1994)

5.2 Growth/Precipitation of C-S-H During Hydration in Tricalcium Silicate Pastes

The hydration development was shown to be related with the initial particle size of the grains (Figure 3.14). Therefore, the nucleation and growth of the hydration products occurs earlier for smaller particles. The morphology of this first C-S-H is fibrillar, regardless of the initial size of the particles, and grows outwards from the surface of the grain. An example of the fibrillar and directional morphology of the outer C-S-H formed is shown in Figure 5. 1.
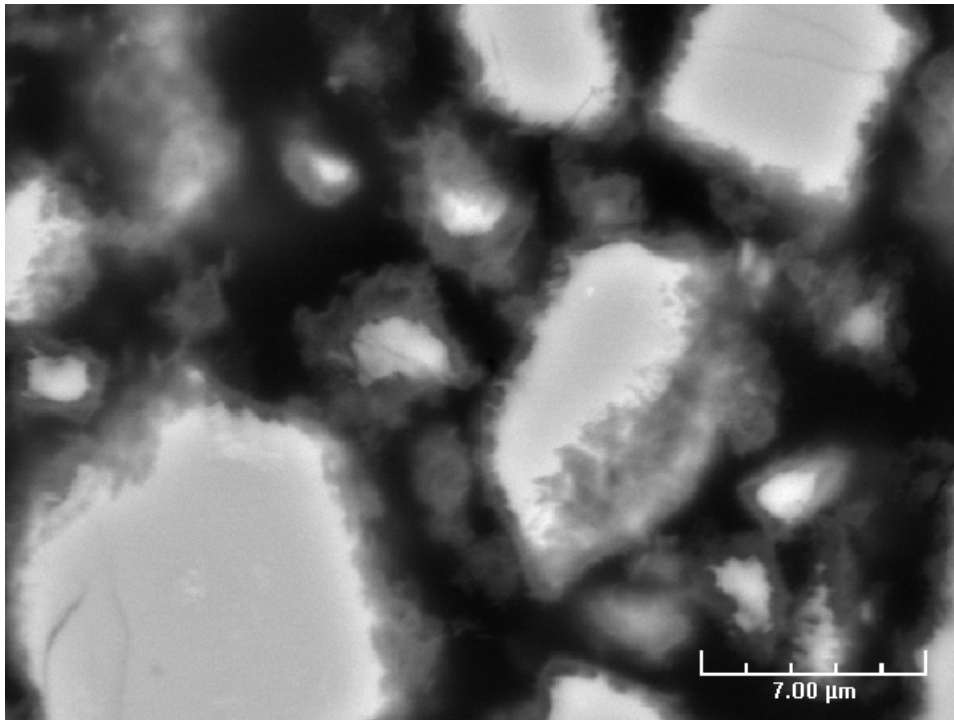

Figure 5. 1: High magnification BSE image of full hydrated alite grains (PSD-33μm)after 16 hours of hydration showing the fibrillar morphology of the outer C-S-H

It is more or less agreed upon that once a first shell of hydration products is formed, it is more difficult for dissolved calcium and silicate ions to migrate through this layer and C-S-H starts to form inwards from the shell. The time at which this happens depends on grains size and occurs earlier in the case of smaller particles. As calculated in Chapter 3 for early ages (Figure 3. 40) and in Chapter 4 for later ages (Figure 4. 26), the thickness of this layer is directly dependent on the initial size of the grain, being thicker for bigger

particles. In the systems with larger PSD, the specific surface area available for deposition is smaller leading to thicker C-S-H layers for a fixed degree of hydration. Inner C-S-H reveals a denser and closer packed morphology than the outer C-S-H previously formed and is illustrated in Figure 5. 2 for PSD-82 μm and PSD-38 μm at 28 days of hydration. A clear defined boundary between inner and outer C-S-H is observed in the case of all the studied particle sizes distributions, happening earlier for smaller particles.
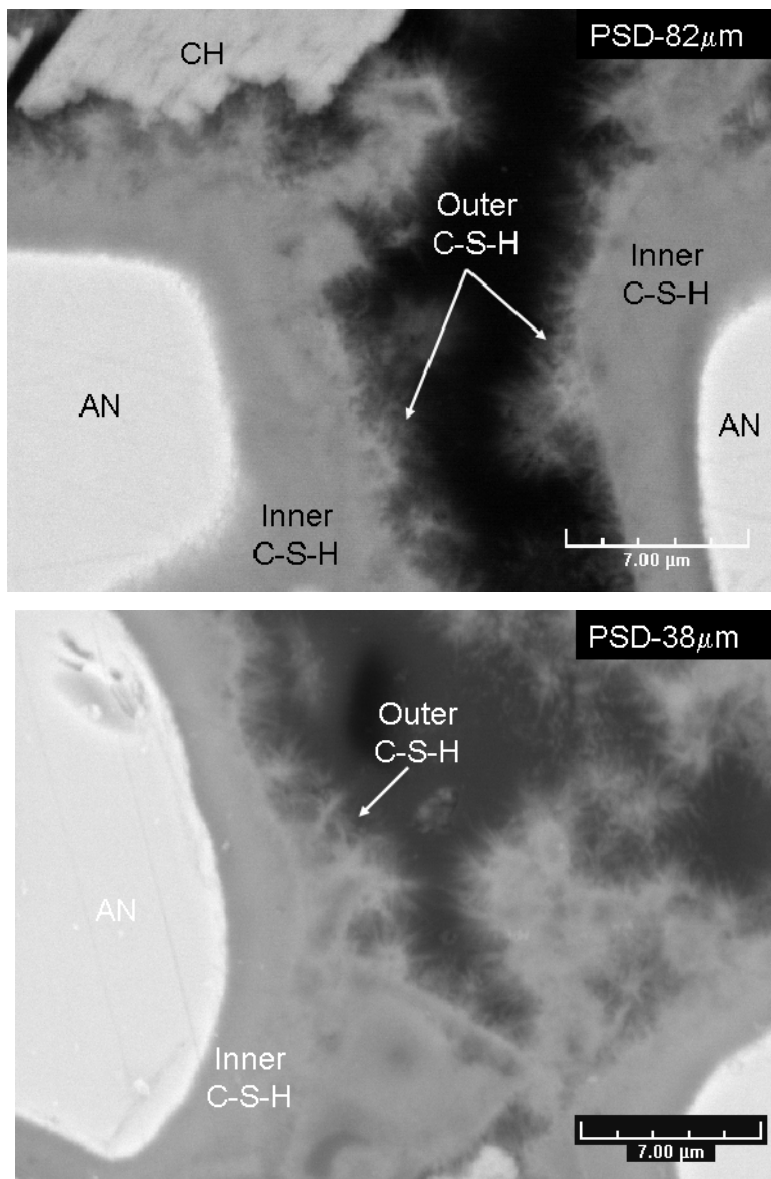

Figure 5. 2: BSE images of tricalcium PSD-82μm and PSD-38μm after 28 days of hydration illustrating the boundary between inner and outer C-S-H

After 28 days of hydration the capillary space becomes almost completely filled with hydration products (Figure 5. 3). However, as quantified in Chapter 4 (Figure 4.14), PSD-6μm pastes show greater capillary porosity when compared with other gradations at the same degree of hydration. One hypothesis to explain this could be due to the difference in available space for product deposition. In this way, coarse gradations with less restriction for deposition of C-S-H could lead to a much lower values of capillary porosity and a much lower values of solid density (Figure 4.17).
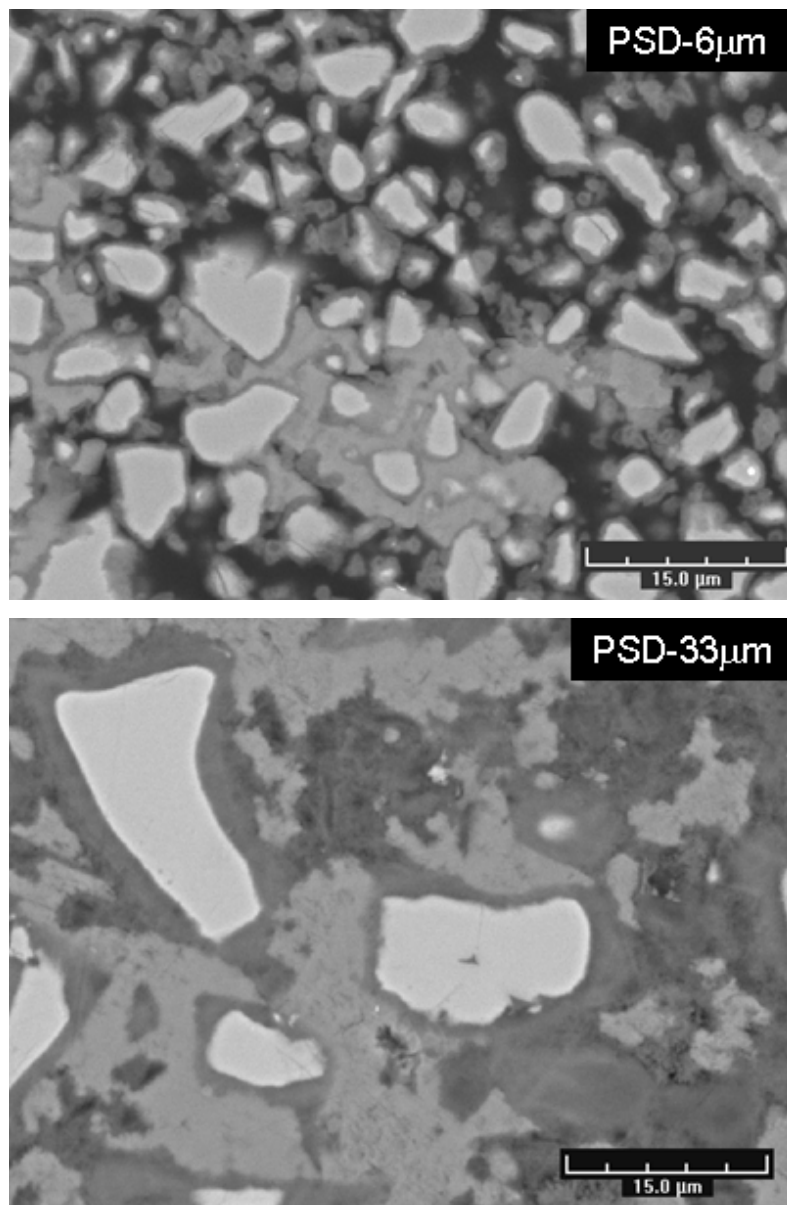

Figure 5. 3: BSE images of PSD-6μm (top) and PSD-33μm (bottom) pastes at a hydration degree of 50% illustrating differences on the capillary porosity

TEM was used to get more information about the nanoscale morphology of C-S-H. A Transmission electron microscope, CM200 (FEG-STEM) at an operating voltage of 200 KeV, was used for examining the structure of PSD-6μm/pure C_3S paste at high resolution and at high magnification.

Figure 5. 4 shows a transmission electron image of fully hydrated PSD-6μm/pure C_3S grains after 24 hours of hydration. A magnified image of the inner and outer C-S-H is shown in the same figure. The outer product has foil-shape or fibrillar morphology and precipitates preferentially outwards from the shell in the capillary porosity. The precipitation of this low density product will depend on the available pore space for deposition. Richardson distinguished two types of outer product as a function of the space constraints: "coarse fibrillar" when it grows in large pore spaces and "fine fibrillar" when it grows in a more constrained space) [3]. On the other hand, the inner C-S-H is much denser and is composed of small globular particles more homogeneously distributed [20]. As already reported by Groves and Richardson [20,21], the size of the pores in the inner product is less than 10nm. Pore size characterization of pastes with different particle sizes has been investigated in this thesis work by nitrogen adsorption and is discussed in section §5.4.
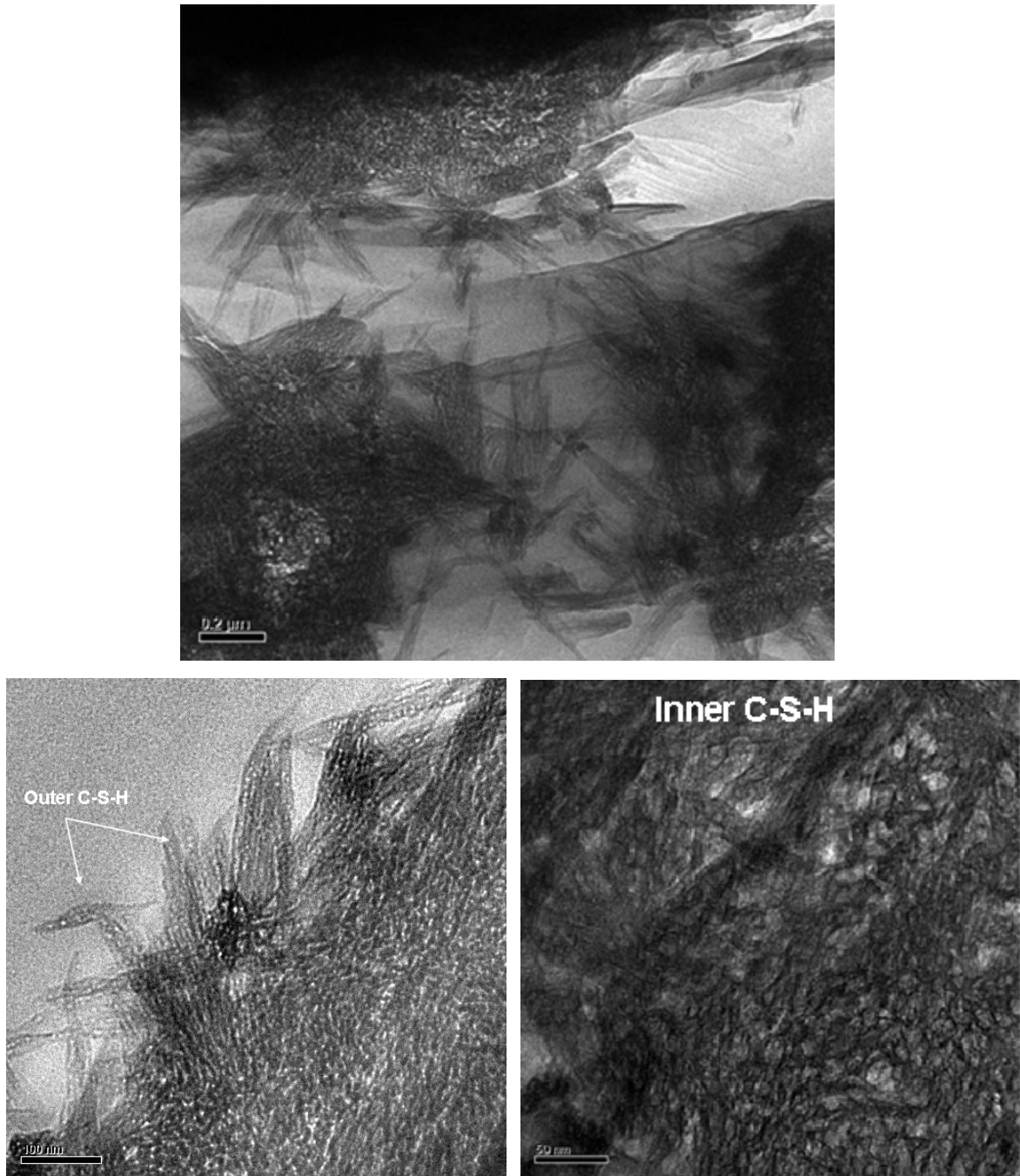
Figure 5. 4: TEM (bright field) micrograph of PSD-6µm/pure C_3S grains after 24 hours of hydration (left). Right image shows a zoom in the inner C-S-H layer

5.3 Chemical Composition of C-S-H

5.3.1. Phase composition as measured by Energy Dispersive Spectroscopy (EDS)

This section describes the evolution of the C/S ratio for pastes of different gradations (PSD-82μm, PSD-38μm PSD-33μm and PSD-6μm) at a constant w/c ratio of 0.4. The Ca/Si ratio (expressed as atomic ratios) in the C-S-H layer has been determined form energy dispersive X-ray analysis (EDS) in the SEM.

A FEI quanta 2000 SEM microscope and a PGT energy dispersive X-ray analyzer were used in this study at an accelerating voltage of 15 KV and using pertinent mineral standards for quantitative analysis.

The EDS analysis was made in the inner C-S-H shells with a sampling depth of 1-2 microns. About 100 points were analyzed for each sample for statistical accuracy. The crosses shown in Figure 5. 5 illustrate the type of areas selected for analysis. EDS analysis was only performed in the thicker parts of the inner product to avoid areas in which the C-S-H would be intermixed with portlandite and/or anhydrous particles. The average value of all measured points was taken.
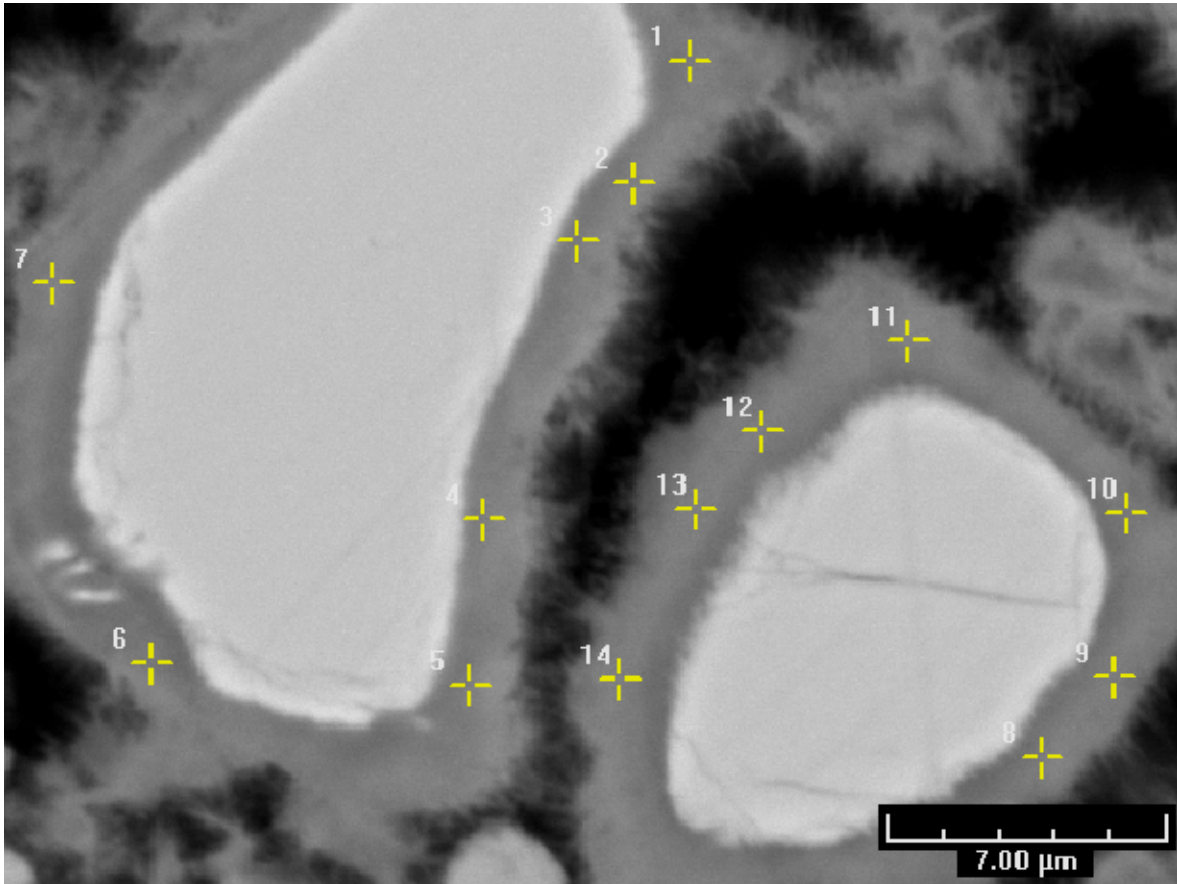
Figure 5. 5: BSE image of PSD-33 µm paste after 14 days of hydration

a) Influence of aging on the C-S-H composition

First step in the investigation was to study the influence of the age on the Ca/Si ratio. Figure 5. 6 shows the evolution of this ratio for PSD-33µm. The mean of (Ca+Mg)/(Si+Al) (alite has Al and Mg ions that substitutes Si and Ca, respectively) remains constant during hydration, presenting an average value of 1.7 ± 0.1. Previous studies have also found constant values for the C/S ratio during hydration [3,4,5].
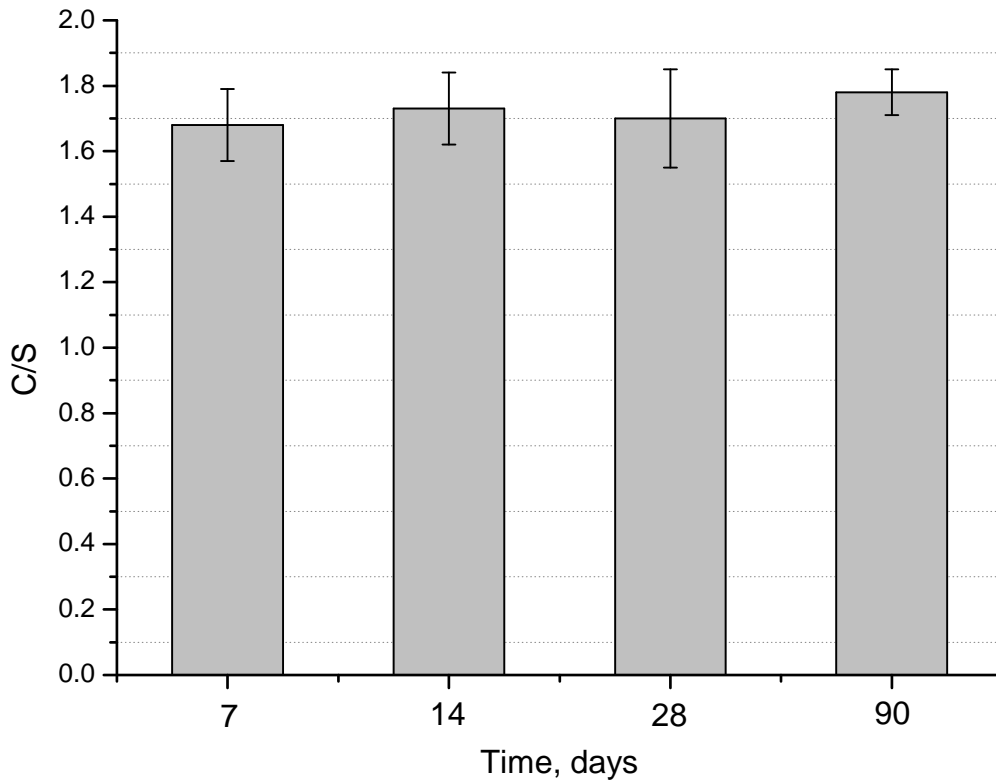
Figure 5. 6: Evolution of the C/S (Ca+Mg)/ (Si+Al) ratio during hydration for PSD-33μm pastes with w/c = 0.4

b) <u>Influence of PSDs o the C-S-H composition</u>

The composition of C-S-H for different particle size distributions of tricalcium silicate (PSD-82μm, PSD-38μm PSD-33μm and PSD-6μm) at a degree of hydration of 50% is shown in Figure 5. 7. The average C-S-H (Ca+Mg)/(Si+Al) was found to be 1.7 ± 0.1 without any significant variations in terms of composition.
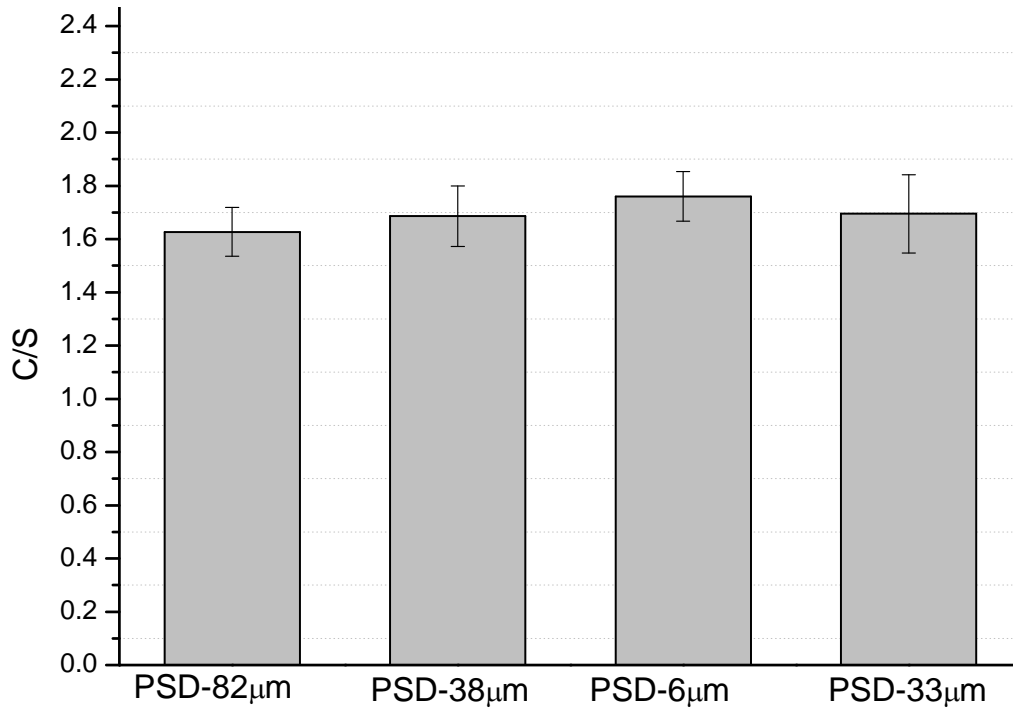
Figure 5. 7: Variation of the C/S ratio for pastes with different particle size distribution (50% of hydration degree)

5.3.2 Chemically bound water in C-S-H

Calculation of the bound water in C-S-H

The evolution of the chemically bound water content over hydration has been investigated for pastes with different particle size (PSD-82µm, PSD-38µm PSD-33µm and PSD-6µm) (w/c= 0.4). The drying method used here was solvent exchange with isopropanol.

Assuming that all free water has been eliminated by solvent exchange, the total amount of combined water has been calculated from 25 up to 900ºC. Therefore, the weight percentage of bound water in C-S-H (H/S) has been calculated using Eq. 5. 2:

$$W_{C\text{-}S\text{-}H} = W_{Total} - W_{CH} - W_{calcite} \qquad \text{Eq.5. 2}$$

where W_{C-S-H} , W_{Total} , W_{CH} , $W_{calcite}$ are the weight percentage of combined water in the total sample (from 25 to 900ºC), portlandite (from 415 to 525ºC) and calcite (from 415 to 715ºC) coming from undesireable CH carbonation, respectively (Figure 5. 8).
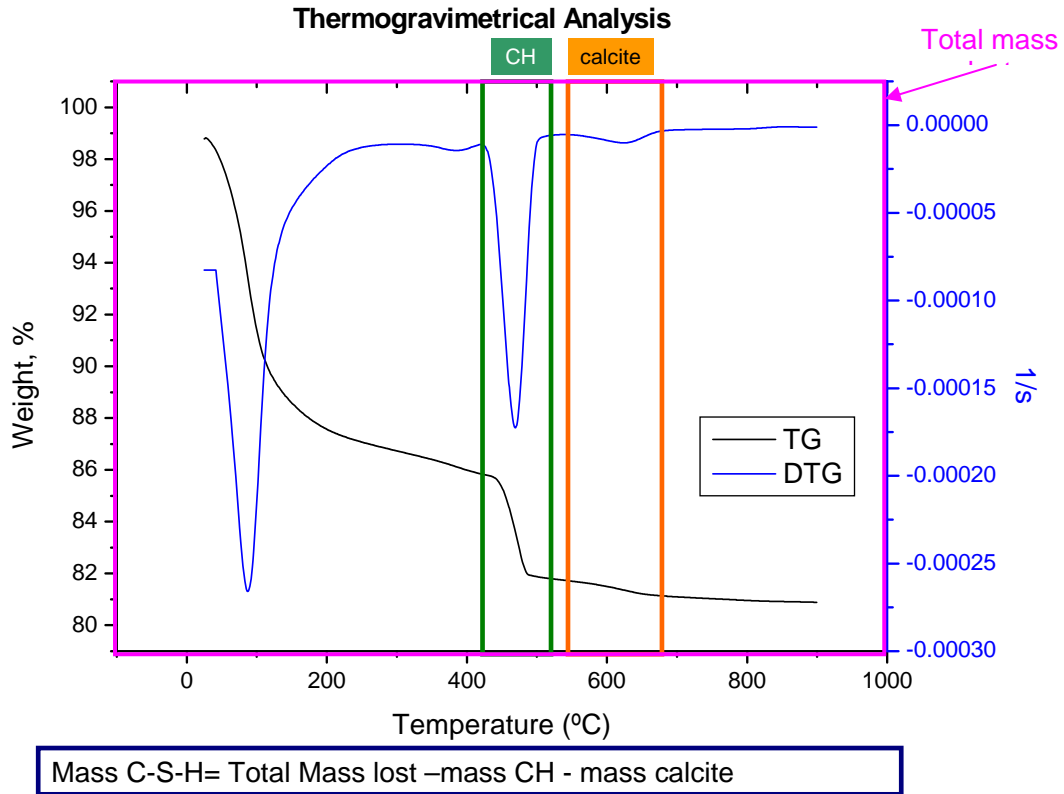

Figure 5. 8: TGA and DTG curves of PSD-33μm paste at 24 hours of hydration

If we assume C/S (x) ratio equal to 1.7 as the average value obtained from EDS analysis, then Eq. 5.3 can be rewritten as shown in Eq. 5.4:

$$C_3S + (3-x+n)\, H \rightarrow C_xSH_n + (3-x)\, H \qquad \text{Eq.5. 3}$$

$$C_3S + (1.3+ n)\, H \rightarrow C_{1.7}SH_n + 1.3\, H \qquad \text{Eq.5. 4}$$

Equation 5.4 can then be used to calculate the molar ratio of H (n) in C-S-H.

Figure 5. 9 shows the relationship between chemically bound water versus the age for different gradations of C_3S pastes. This graph clearly shows that the bound water content

maintains constant upon hydration. Some authors have also reported no variation on the H/S ratio in C-S-H with the degree of hydration in C_3S pastes [4,5,6].
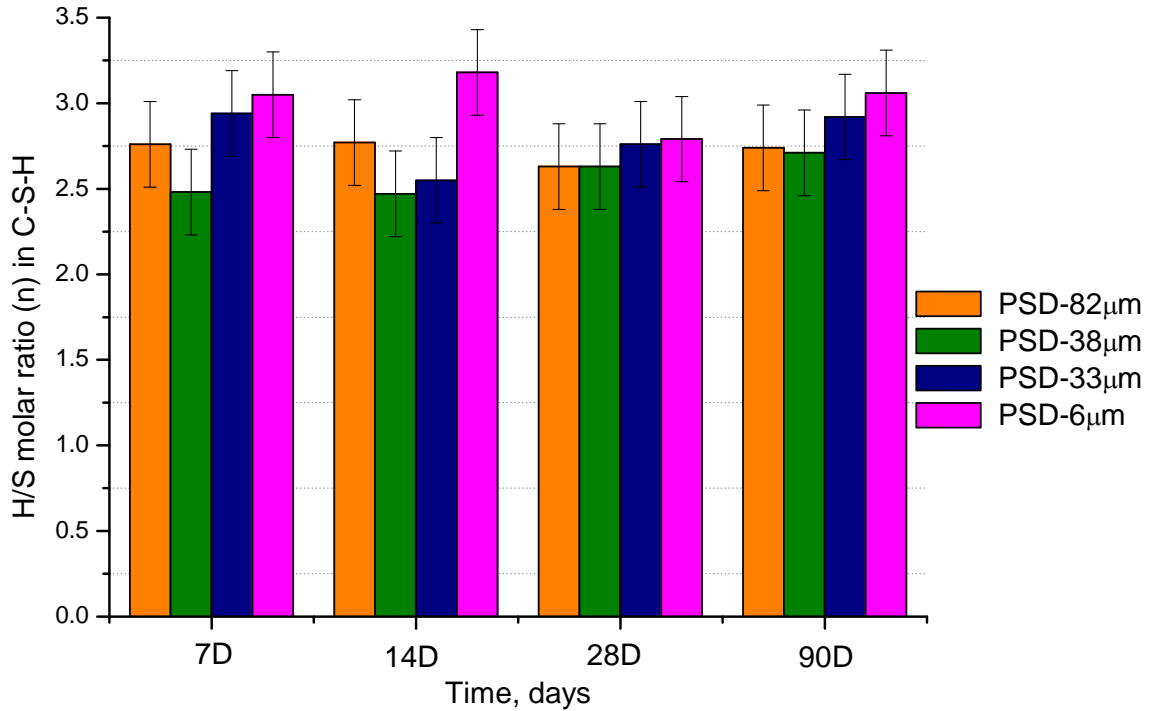

Figure 5. 9: Chemical bound water for different particle size distribution upon hydration

Since the chemical composition and the bound water were found to be independent from the particle size, the measured differences in density come from differences in the packing or microstructural arrangement of C-S-H sheets. This has been investigated by means of nitrogen adsorption in the following section.

5.4 Characterization of C-S-H porosity by nitrogen adsorption.

The investigation of the C-S-H porosity that is described in this section was done using nitrogen adsorption. A reference material with similar structure to C-S-H was first used in order to validate the method selected for characterization of the pore size distribution. Later on the pore size distribution of 2 different gradations (PSD-33µm/Alite and PSD-6µm/pure C_3S were compared to have a better understanding on the effect that the initial particle size has on the C-S-H porosity.

5.4.1 Materials and methods

C_3S pastes were mechanically mixed at a w/c ratio equal to 0.4. At the ages of 1, 3, 7, 14 and 28 days the hydration was stopped using both solvent exchange with isopropanol and D-drying. The samples were then stored under vacuum.

Pure C-S-H was obtained from fully hydrated pure C_3S pastes. Pastes were ground and repeatedly washed with de-ionised water until no CH was detected by XRD (Figure 5. 10).
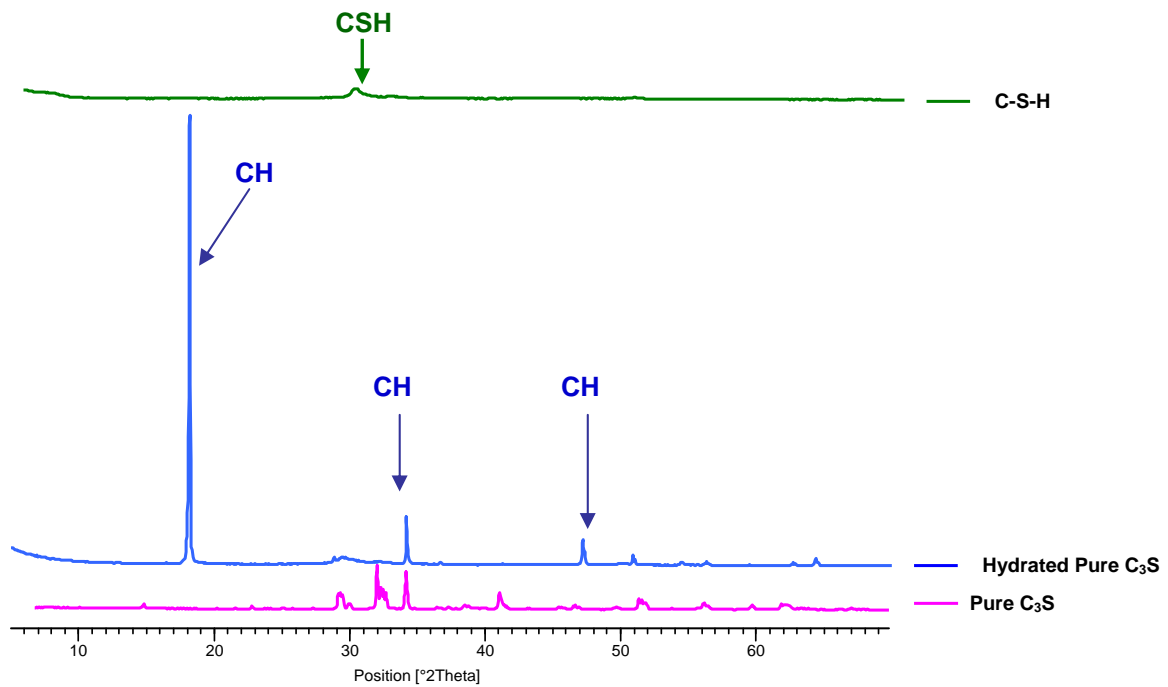
Figure 5. 10: Evolution of the XRD patens during the synthesis of C-S-H

Surface areas and pore size distributions were measured by N_2 adsorption performed with an ASAP 2020 surface area and porosimetry analyzer from Micromeritics. The reproducibility of the measurements was found to be higher than 98% percent.

The degree of hydration of each tested specimen was measured by SEM-BSE image analysis (BSE/IA).

5.4.2 Choice of a model for pore size analysis

The approach used in this work was first tested with a reference material to assess the reliability of the method. Montmorillonite was chosen as a model material because of the similarity of its adsorption/desorption isotherm with that of C-S-H. Montmorillonite is a well characterised material and has a slit-shaped pores structure (IUPAC H3 type) [17].

Figure 5. 11 presents the isotherms of the synthesized C-S-H and Montmorillonite. The amount of gas adsorbed on the surface of the solid depends on factors such as the surface area of the specimen, the nature of both the specimen, the gas and the pressure of the gas

at which the adsorption takes place. The gas is adsorbed inside the pores of the material forming first a monolayer, then a multilayer, and finally capillary condensation. The relative pressures at which the hysteresis loop closes depend on the temperature and the nature of the adsorbent. In the case of using nitrogen the loop is known to close at a relative pressure of about $P/P_o=0.4$. At this point the capillary condensation starts to occur in the smallest pores and thereafter continues in the larger ones. From the analysis of the adsorption/desorption isotherms, both materials present the same type of pore structure, identified as slit-shaped pores according to the H3 type (IUPAC).
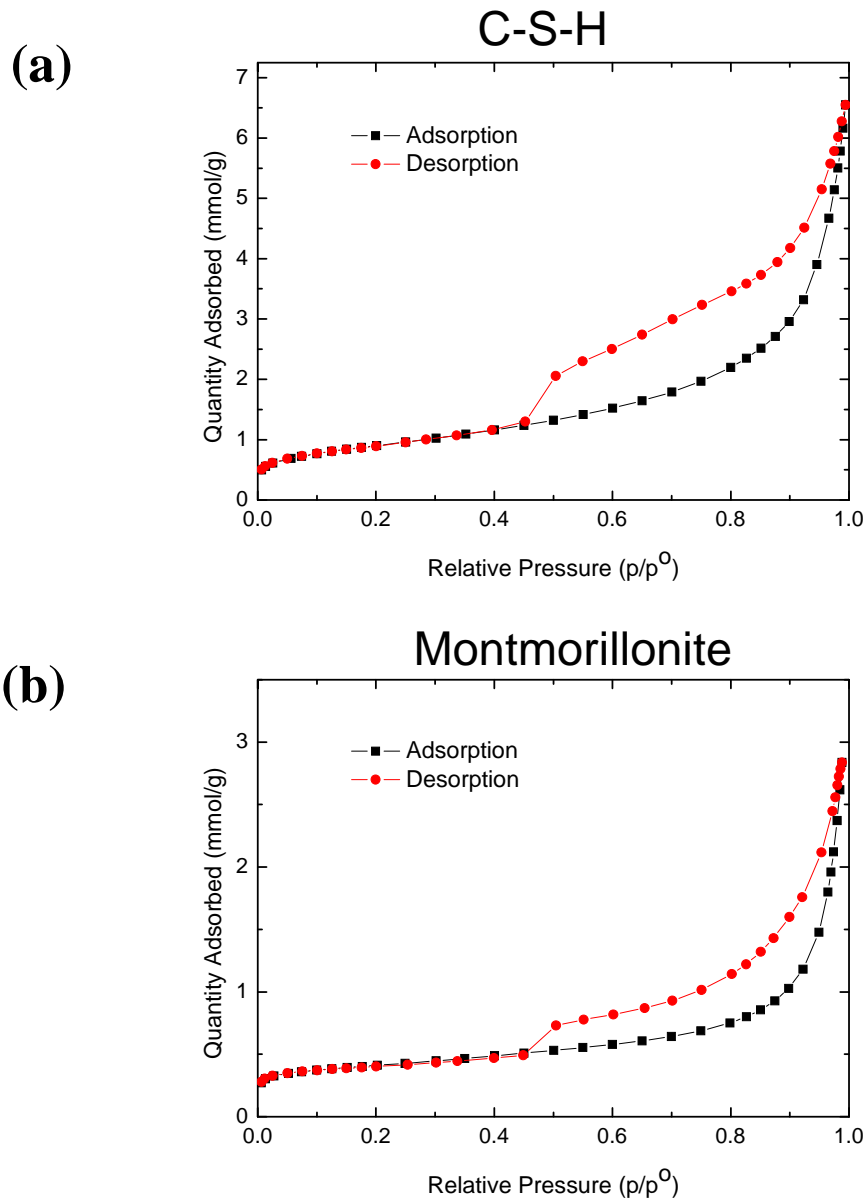
(a)

(b)

Figure 5. 11: Nitrogen adsorption-desorption isotherms for an PSD-33µm paste hydrated for 7days (a) and the montmorillonite clay with slits of 1.2nm (b)

The TEM micrographs (bright field) shown in Figure 5. 12 illustrate the compatibility between the nanostructure of calcium montmorillonite (top) (reproduced from [22]) and that of pure C-S-H (bottom). These figures show the similar morphology, both forming elongated or fibrous particles with a lamellar structure very closely packed at a nanoscale level.
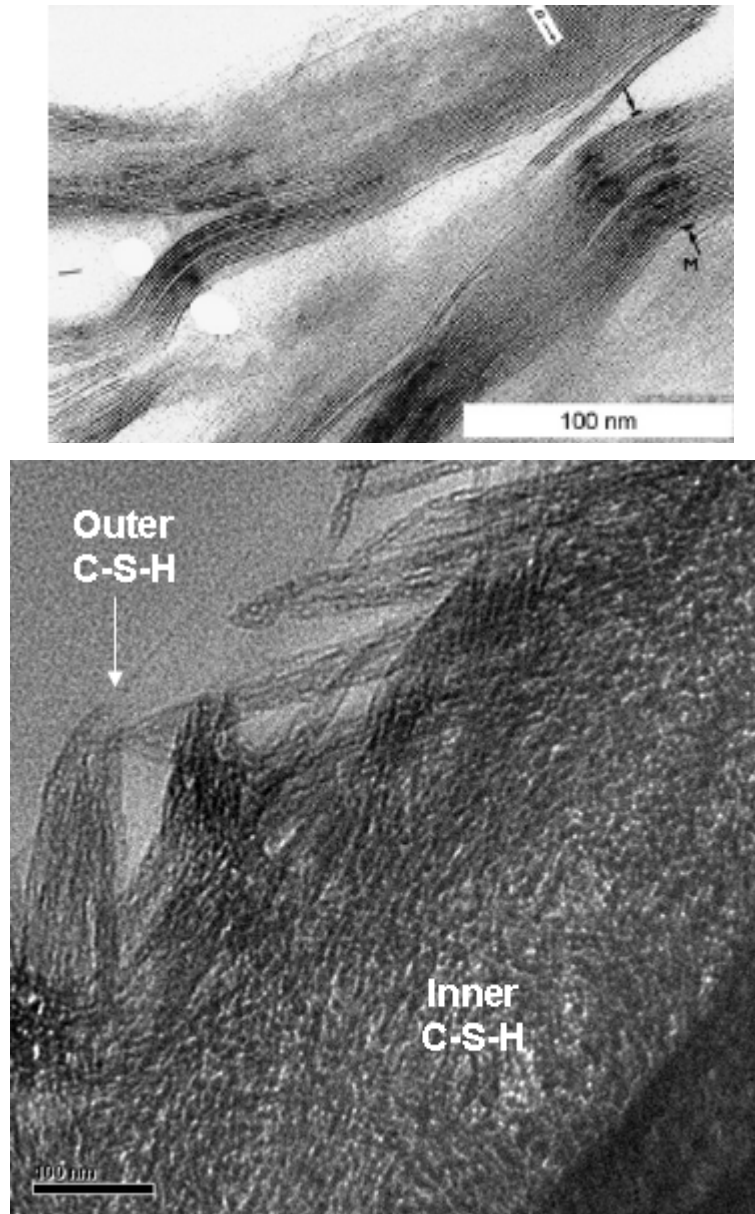
Figure 5. 12: TEM micrographs of Montmorillonite (top) (reproduced from [22]) and synthesized C-S-H (bottom)

The pore size distribution of the montmorillonite and the synthesized C-S-H were then investigated using both the Classical and DFT methods for slit-shaped pores (see Appendix III). Classical models usually fail at very low partial pressures due to the limitation of the Kelvin equation assumptions leading to an overestimation of pores at that range [23]. The DFT approach partially overcomes those problems and allows for a better fit of the isotherms, especially at low partial pressures.

5.4.3. Pore size characterization of Tricalcium Silicate: effect of particle size and evolution upon hydration

The characterization of the pore size distribution of C_3S pastes (PSD-33µm/Alite and PSD-6µm/pure C_3S) is done in this study using the DFT model and assumes a slit-shaped pores in C-S-H. Figure 5. 13 shows the nitrogen adsorption/desorption isotherms for pastes made from different PSD at different ages. Type H3 (slit-shaped pore nature) isotherms are obtained for all ages, only differing in the magnitude of the hysteresis. The area of the hysteresis increases as the quantity of adsorbed N_2 increases. The sizes and shape of the hysteresis indicate a continuous distribution of pore sizes which increase during hydration.
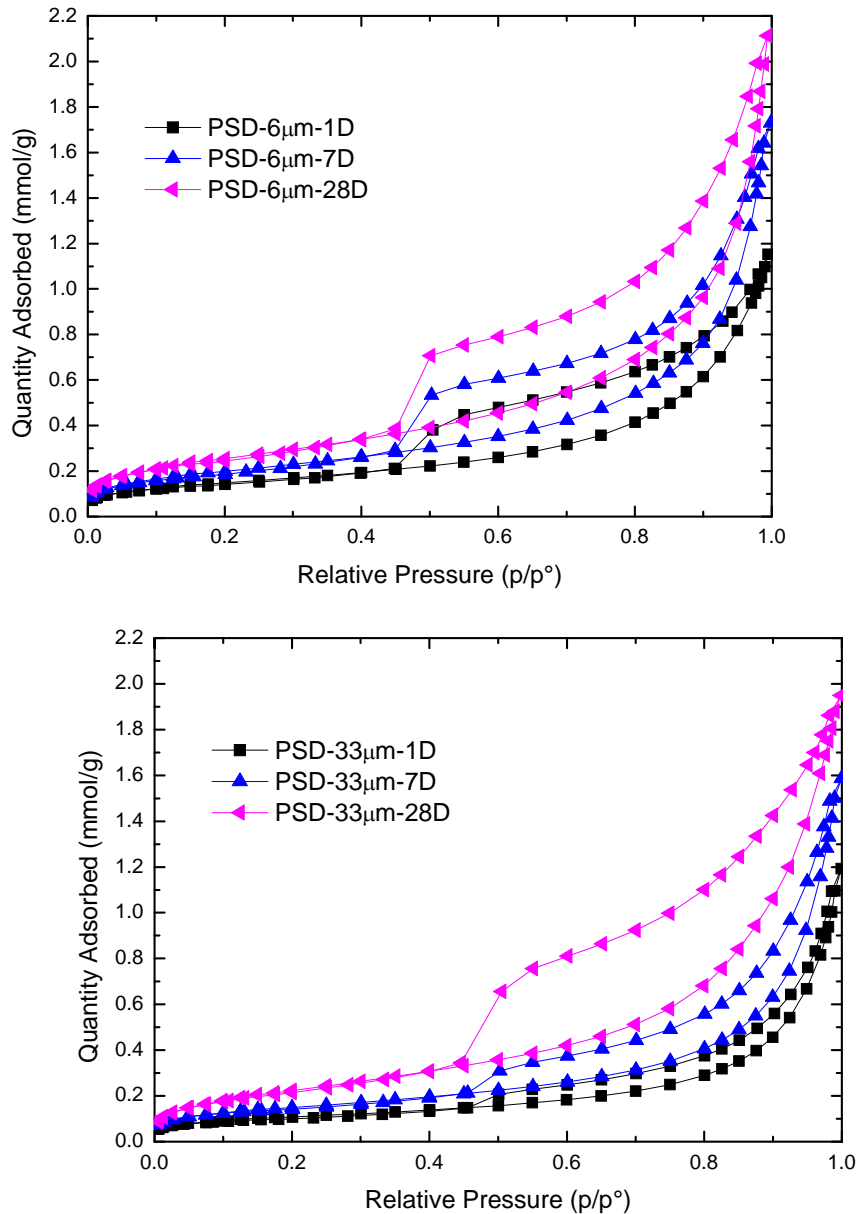
Figure 5. 13: Nitrogen Adsorption/Desorption isotherms for PSD-6μm/pure C$_3$S (top) and PSD-33μm/Alite (bottom) pastes at different ages (1, 7 and 28 days)

Some information of the pore size distribution can be deduced form the adsorption isotherms by converting the relative pressures (P/Po) to pore widths. As earlier mentioned, classical adsorption theories extract this information from a limited fragment of the adsorption isotherm rather than the entire curve. Density functional Theory (DFT) is the most recent theory based on the principles of statistical thermodynamics in which the whole range of the isotherms is considered and is not restricted to a confined range of

relative pressures or pore sizes [23]. In this work, the DFT model for slit-shaped pores has been used to gain insight into the differences in pore size distribution between the different tricalcium silicate pastes. Nevertheless, the transformation from relative pressure to pore size distribution should be interpreted with care to avoid erroneous conclusions.

The cumulative pore volume versus the pore size for PSD-6μm and PSD-33μm pastes at different ages are shown in Figure 5. 14. The cumulative pore volume increases with the degree of hydration for both systems. Only gel porosity is being reflected in this type of measurements (pores<300nm).
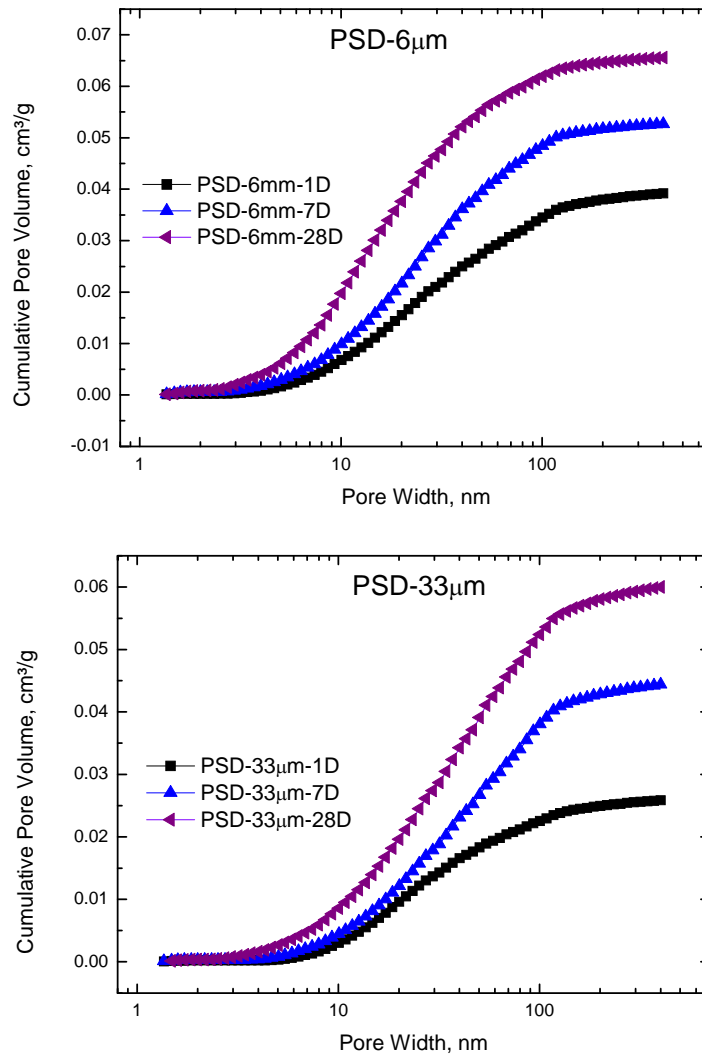

Figure 5. 14: Evolution of the cumulative pore volume vs. pore size over hydration for PSD-6μm/pure C_3S and PSD-33μm/Alite pastes

The most important information is extracted when the cumulative pore volume curves for the two different gradations are compared at the same degree of hydration (50%). Figure 5. 15 shows that for the smallest gradation forms more of smaller pores. As earlier discussed, this could be a consequence of their different initial packing or arrangement of the grains. Due to the more important limitation for product deposition in the smallest gradations, the outer fibrillar C-S-H grows more closely packed, leading to a higher number of small pores and greater values of capillary porosity as shown in Chapter 4 (Figure 4.14)
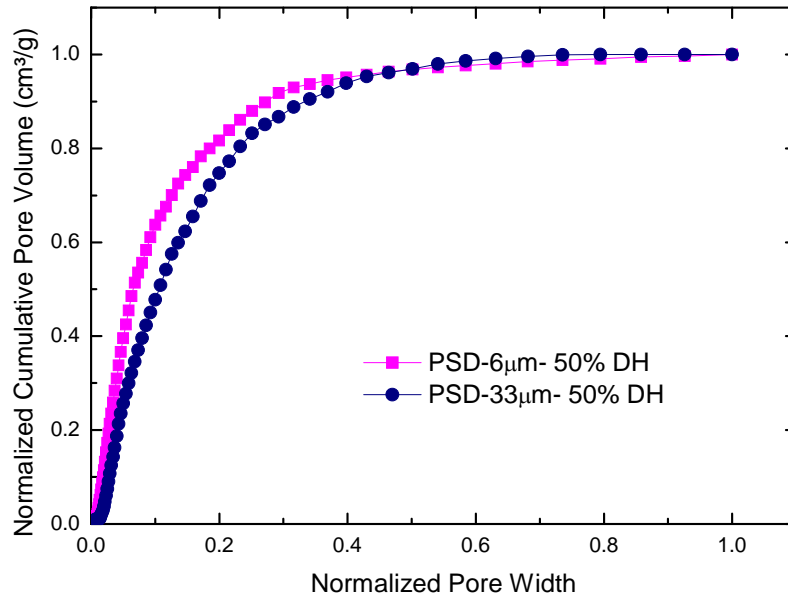

Figure 5. 15: Comparison of cumulative pore volume versus pore width for different gradations of tricalcium silicate (50% of hydration degree)

The transformation from relative pressures to pores size distribution is shown in Figure 5. 16 (normalized curve is presented). This indicates that the amount of smaller pores for the smallest gradation (PSD-6μm) is greater. Even though the DFT model has been shown to better describes the adsorption isotherm than the classical methods, the pore size volume for pores smaller than 4nm determined from nitrogen adsorption must be viewed as suspect. Additionally, the discontinuities found above 30 nm are an indicative of the poor mathematical differentiation when the relative pressures are converted into pore sizes and also related to the resolution of the number of experimental points in the P/Po during the data collection. Nevertheless, two main families of pores were obtained

for both gradations. The smaller of the families was found around 1.5 nm. These pores could correspond with the C-S-H model presented by Jennings [24], to the space in between sheets from which the smallest units (globules) make up the fractal solid/pore system. The second family found at about 10 nm could correspond to the space between aggregates or globules (Jennings [24]).
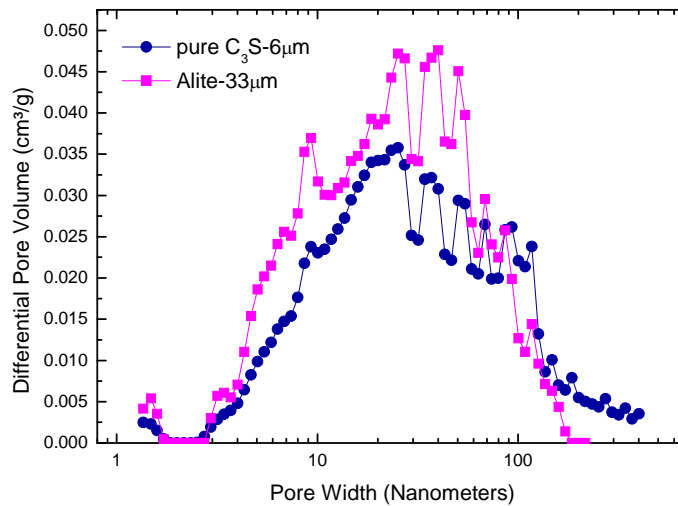

Figure 5. 16: Normalized pore size distribution versus pore width for PSD-33µm/Alite and PSD-6µm/pure C$_3$S pastes at 50% of hydration degree using DFT model for slit-shaped pores

5.4.4. Evolution of the surface area upon hydration

The effect of the drying method (solvent exchange versus D-drying) used to stop the hydration on the measured surface was investigated for the case of PSD-33µm/Alite paste (Figure 5. 17). The specific surface area was found to be about 2 times lower when D-drying was used than when solvent exchange with isopropanol. Samples dried by solvent exchange have been found to increase the accessibility of nitrogen into the small pores given the bigger surface areas. When isopropanol is used, due to its lower surface tension, the capillary pressure is reduced, preventing collapse of the pores [25,26]. In the case of D-drying the water present in the very small gel pores (<2nm) is not removed and N$_2$ molecules do not have access to these pores leading to smaller surface areas [27].
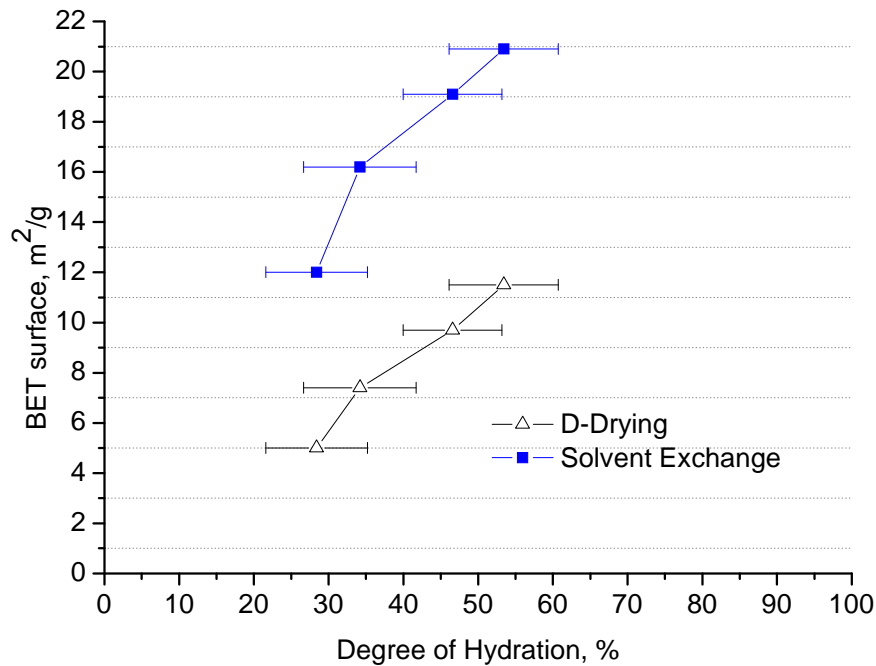
Figure 5. 17: Evolution over hydration of the BET surface area and average pore diameters for PSD-33μm/Alite pastes dried by isopropanol exchange and D-drying

The comparison of surface areas and average pore diameters for PSD-33μm and PSD-6μm pastes was performed using solvent exchange with isopropanol as the drying method because this was considered less damaging for the C-S-H structure.

Jennings [12] stated that none of the pores in HD C-S-H are accessible to nitrogen while some of the pores in LD C-S-H are accessible. In this way, the LD C-S-H will be the one contributing more significantly to the specific surface area measurement.

The increase of C-S-H content due to the evolution of the hydration is reflected in the linear increase of the specific surface area as shown in Figure 5. 18. From this graph, it can also be seen that for a given degree of hydration, the PSD-6μm paste has lower specific surface area values. This means, that for the case of PSD-6μm, the amount of LD C-S-H, which is the type of C-S-H contributing most of the surface area calculated by nitrogen adsorption, should be lower. This agrees well with the results of bulk densities measured by He pycnometry (Chapter 4). In there, we see that higher values of density are obtained for the PSD-6μm pastes and as a result, most probably, to a much higher

constraint space for product deposition and subsequently leading to much higher capillary porosities.
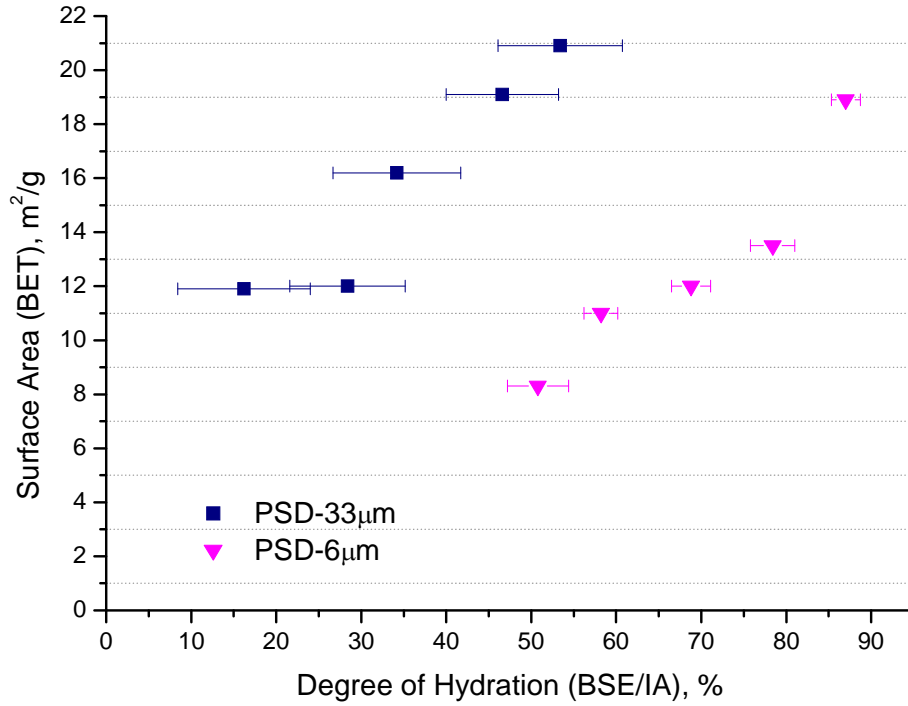

Figure 5. 18: Evolution of the surface area upon hydration for PSD-6µm/pure C_3S and PSD-33µm/Alite pastes

5.5 Summary

➢ Two types of C-S-H, inner and outer, were identified in all gradations of tricalcium silicate pastes. Outer product grows outward from the grains with fibrillar morphology. Inner product consists in a much denser and packed morphology of particles homogeneously distributed.

➢ The Ca/Si ratio of the inner C-S-H layer was investigated by EDS analysis and was found to be the same for all of the particle sizes at all measured degrees of hydration and equal to 1.7.

➢ The amount of chemically bound water was investigated by thermogravimetrical analysis. Assuming C/S ratio equal to 1.7 (as obtained by EDS), the bound water content was constant regardless of the degree of hydration or the particle size. However, for the smallest gradation (PSD-6μm/pure C$_3$S) the amount of chemical bound water was found to be slightly higher than the other gradations of tricalcium silicate.

➢ From the analysis of the adsorption/desorption isotherms, C-S-H was identified to have slit-shaped pores (H3 type form IUPAC). The goodness of fit data indicated that Classical methods fail at very low partial pressures leading to an overestimation of the volume of the smallest pores. The pores size distribution was obtained from the transformation of relative pressures using the DFT model. Two main families of pores, one at 1.5 nm and another around 10 nm, were identified. When the normalized cumulative pore volume versus the pore width curves for 2 different particle size distributions were compared at the same degree of hydration, the smallest gradations showed to have higher amounts of small pores. This means that the space between fibrils (outer C-S-H) is greater for the case of coarser gradations. The specific surface area of PSD-33μm pastes was investigate over time and found to be strongly dependent on the degree of hydration. When the C-S-H specific surface areas of PSD-6μm and PSD-33μm

were compared at the same hydration degree, higher values were observed for PSD-33μm pastes.

Since the composition and the amount of chemically bound water in C-S-H did not change when the particle size distribution changed. The higher values of capillary porosity and C-S-H density reported for the smallest gradations (Chapter 4) can probably be related only to the difference in the distance between fibrillar particles of outer C-S-H. As observed from the nitrogen adsorption measurements, the space between fibrils of C-S-H (outer product) was found to be shorter for the smaller gradation as a result of its more constraint space for product deposition.

REFERENCES

[1] H.F.Taylor, Chement chemistry, Tomas Helford, London 1997

[2] I.G. Richardson, The nature of C-S-H in hardened cements, Cement and Concrete Research 29 (1999) pp. 1131-1147

[3] Richardson I.G., The nature of the hydration products in hardened cement pastes, Cement and Concrete Composites 22 (2000) p.97-113

[4] L.J, Parrot, R.C. Patel, D.C Killoh, H.M. Jennings, Journal of the American Ceramic Society 67 (1984) pp.233

[5] I. Odler and H. Dorr, Early Hydration of tricalcium silicate. I: Kinetics of the hydration process and the stoichiometry of the hydration products, Cement and Concrete Research 9 (1979) pp. 239

[6] Friederich W. Locher, Cement princples of production and use, Verlag Bau+Technik GmbH, Düsseldorf, 2006

[7] Zhang, Xinyu, Quantitative and microstructural characterization of concrete cured under realistic temperature conditions, Ph. D Thesis École Polytechnique Fédéral de Lausanne (2007)

[8] J.F. Young and W. Hansen, Volume relationships for C-S-H formation based on hydration stoichiometries, In: Microstructural Development During Hydration of Cement, L.J. Struble and P.W. Brown (Eds.), Mat. Res. Soc. Symp. Proc. vol. 85 (1987) pp. 313-322.

[9] H. Koster and I. Odler, Investigations on the structure of fully hydrated portland cement and tricalcium silicate pastes. I. Bound water, chemical shrinkage and density of hydrates, Cement and Concrete Research 16(1986) pp. 207-214

[10] I. G. Richardson and G. W. Groves. The incorporation of minor and trace elements into calcium silicate hydrate (C-S-H) gel in hardened cement pastes, Cement and Concrete Research,23(1993) pp.131–138,.

[11]J.H. Taplin, A method for following the hydration reaction in Portland cement paste, Australian J Appl Sci 10 (1959) pp. 329–345

[12] Hamling M. Jennings, A model for the microstructure of calcium silicate hydrate in cement paste, Cement and Concrete Research 30 (2000) pp. 101-116

[13] Powers T.C., Brownyard T.L. "Studies of the physical properties of hardened Portland cement paste" Research Bulleting 22, Portland Cement Association, Chicalgo, IL (1948)

[14] Feldman R.F., Sereda P.J. "A new model for hydrated Porland cement and its practical implications" Engineering Journal of Canada, 53 (8-9), 1970, pp. 53-59

[15] Wittmann F. "Grundlagen eines Modells zur Beschreiburg charakteristischer Eigenschaften des Betons" Deutscher Ausschuss für Stahlbeton, Heft 290, Berlin, 1977, pp. 45-100

[16] Jennings H.M., Tennis P.D. "Model for the developing microstructure in Portland-cement pastes" Journal of the American Ceramic Society 77 (1994) pp. 3161-3172

[17] Kalliopi K. Aligizaki, Pore Structure of cement-based Materials: Testing, Interpretation and Requirements, Modern Concrete Technology 12, London and New York (2006)

[18] Jennings H.M., Dalgleish B.J., Pratt P.L. "Morphological development of hydrating tricalcium silicate as examined by electron microscopy techniques", Journal of the American Ceramic Society 64 (1981) pp. 567-572

[19] Diamond S. "Cement paste microstructure-an overview at several levels" in Proceedings of Conference on Hydraulic Cement Pastes: Their Structure and Properties, Sheffield, Cement and Concrete Association, 1976, pp. 2-30

[20] I.G. Richardson , Tobermorite/jennite- and tobermorite/calcium hydroxide-based models for the structure of C-S-H: applicability to hardened pastes of tricalcium silicate, β-dicalcium silicate, Portland cement, and blends of Porland cement with blast-furnace slag, metakaolin, or silica fume, Cement and Concrete Research 34 (2004) pp.1733-1777

[21] G.W. Groves, TEM studies of cement hydration, Mater. Res. Soc. Symp. Proc. 85 (1987) pp.3-12

[22] R.J.-M. Pellenq, N. Lequeux, H. van Damme, Enginneering the bonding scheme in C-S-H : The iono-covalent framework, Cement and Concrete Research 38 (2008) pp. 159-174

[23] Paul A. Webb and Clyde Orr "Analytical Methods in Fine Particle Technology", Micromeritics Instrument Corporation, 1997, pp.81

[24] Hamling M. Jennings, Jeffrey J. Thomas, Julia S. Gevrenov, Georgios Constantinides, Franz-Josef Ulm "A multi-technique investigation of the nanoporosity of cement paste" Cement and Concrete Research 37 (2007) pp. 329-336

[25] Litvan G.G. "Variability o the nitrogen surface area of hydrated cement paste" Cement and Concrete Research 6 , 1976, PP. 139-143

[26] Lawrence C.D. "The interpretation of nitrogen sorption isotherms on hydrated cements" Cement and Concrete Association Technical Report 530, 1980, PP. 28

[27]A. Korpa, R. Tretting "The influence of different drying methods on cement paste microstructures as reflected by gas adsorption: Comparison between freeze-drying (F-drying), D-drying, P-drying and oven-drying methods" Cement and Concrete Research 36, 2006, pp.634-649

CHAPTER 6: DISCUSSION, CONCLUSIONS AND FUTURE WORK

The aim of this thesis is to gain insight into the effect of the initial particle size distribution on hydration kinetics and microstructural development of tricalcium silicate pastes. The most important findings are summarized and discussed here to try to have a better understanding of C_3S hydration and the implications of the particle size.

6.1. Discussion

The discussion focuses on the following points:

- Effect of the particle size on the hydration kinetics
- Microstructural development of C_3S pastes: development of C-S-H layer

6.1.1 Effect of Particle Size on the Hydration Kinetics

The effect that the particle size has on the hydration kinetics at the different stages of hydration: dissolution, induction period, nucleation and growth process, and diffusion were investigated by the combination of isothermal calorimetry (early ages: up to 24 hours) and chemical shrinkage (later ages). Both methods show the same tendency; higher heat evolution rates were observed for smaller gradations.

a) Dissolution Period: the initial dissolution process was found to be dependent on the particle size and/or the amount of lattice defects of the grains. More heat is released for particles with higher specific surface area and higher defect concentration.

When the isothermal calorimetry curves of a same powder, raw and thermally treated, are compared, the powder treated thermally shows lower values of heat release during the dissolution peak (Figure 6. 1) and longer induction periods. The particle size distribution and the XRD patterns before and after the thermal treatment were compared and no significant differences between both were observed, meaning that the differences found in the kinetics can not be attributed to changes in the size of the particles or polymorphism. This indicates that the dissolution of C_3S could be related to defect concentrations as previous suggested by [1]. Microstructural investigation of the hydration of C_3S pastes during the first hours of hydration revealed the presence of preferential sites for reaction on the surface of the grains. This same preferential reaction of alite grains was observed earlier by Mathur [2] in the case of cement pastes. However, further investigations are needed to asses and quantify the actual effect of defects for each gradation and its influence on the mechanisms of early hydration.
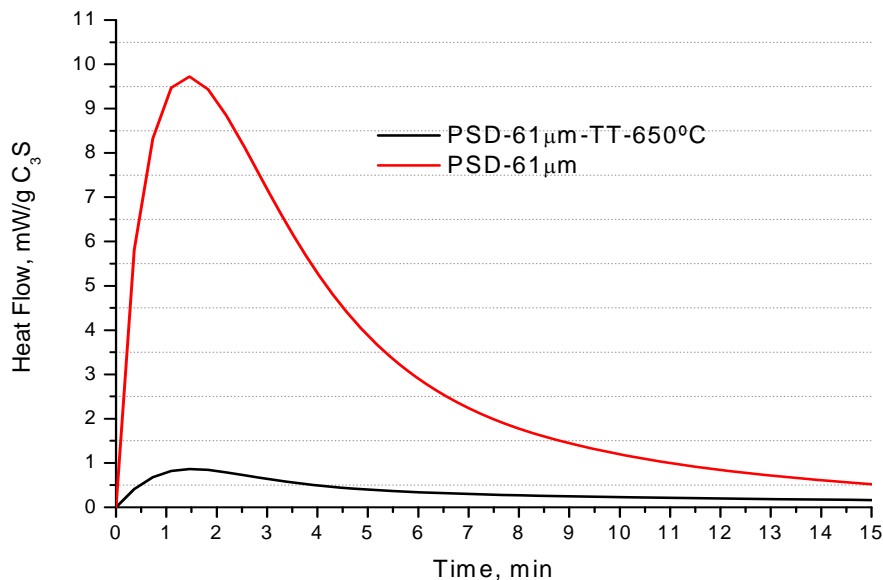

Figure 6. 1: Effect of annealing on alite of narrow particle size distribution during the dissolution peak (PSD-61 µm). TT: treated termically

b) Induction Period: The heat evolution and the length of the period of low chemical activity was observed to be related to the particle size and or/the density of crystallographic defects of the powder. The calcium concentrations during this period were found to be much higher than the solubility concentration of $Ca(OH)_2$ (22 mmol/ at 25ºC [3,4]. Therefore, in this case (low w/c ratio) precipitation of portlandite must be taking place. From the investigation of the isothermal calorimetry of the mixture of 2 different gradations a relationship between the heat and the duration of the induction period with the surface area was observed: smaller particles release more heat during the induction period and go into the nucleation and growth period earlier (Figure 6. 2). There is a critical amount of reaction to bring the induction period to an end. When the powders are treated thermally, the duration of the induction period increases and subsequently the reaction goes into nucleation and growth process much later (Figure 6. 3).
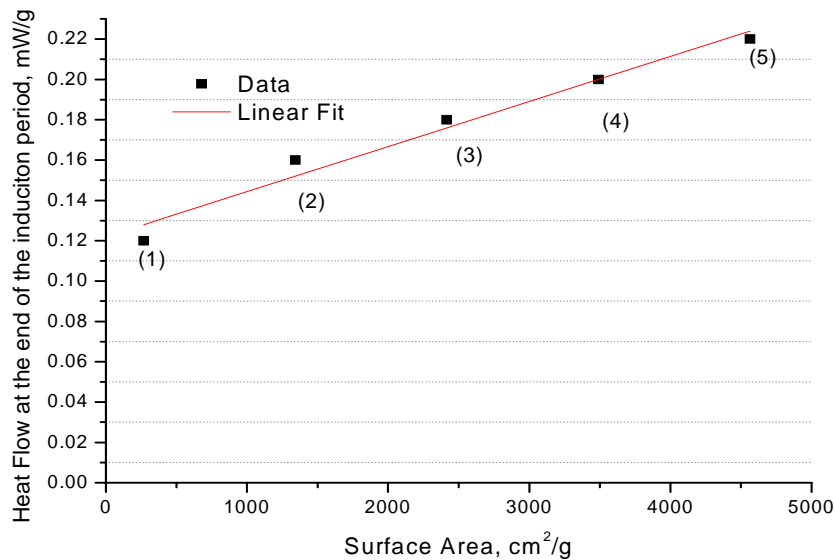

Figure 6. 2: Plot of the heat flow generated at the end of the induction period vs. surface area for the different mixtures
    (1) 100% PSD-82μm
    (2) 75% PSD-82μm + 25% PSD-13μm
    (3) 50% PSD-82μm + 50% PSD-13μm
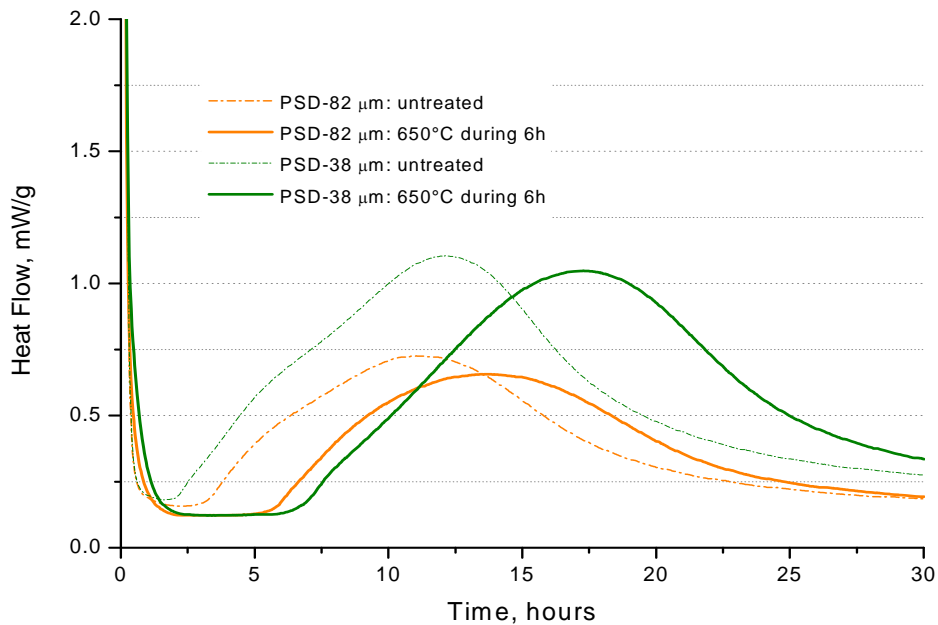   (4) 25% PSD-82μm + 75% PSD-13μm
    (5) 100% PSD-13μm

Figure 6. 3: Effect of annealing on alite of narrow particle size distribution

c) Nucleation and Growth Period: higher rates of nucleation and growth were obtained for finer powders (higher surface areas). A linear relationship between the rate constant and the specific surface area was obtained when the linear part of the isothermal calorimetry curves during the nucleation and growth period were fit against the Avrami equation. In addition, it was shown that the nucleation and growth process can be modelled as a linear addition of individual particles in the case of tricalcium silicate system.

d) Later Period: the analysis of the chemical shrinkage curves indicated that, contrary to general belief, at the top of the peak (in which the nucleation and growth process slows down) the process is not governed by a diffusion-controlled mechanism. Furthermore, the C-S-H thickness at the top of the peak was found to be different for the different gradations. Therefore, the slowing down of the reaction can not be explained by the process being controlled by a diffusion regime. The same C-S-H thickness would be expected for all gradations at the top of the peak if at this stage of the hydration is diffusion-controlled. If the diffusion process exists, this occurs much later at about 18 hours, depending on the particle size of the grains.

The data here generated has been complementary used for the development of a model *μic*, developed in our laboratory [5]. In this model, the evolution of the microstructure of cement is calculated based on the hydration of individual particles. Subsequently, the study of the hydration kinetics plays a major role. The derivation of individual reaction rates for different particle sizes was attempted in order to understand the various rate-controlling mechanisms in the reaction. This was done by investigating the hydration kinetics of the mix of various narrow particle size distributions. However, the interpretation of these results is still difficult due to the presence of a wide range of particle sizes in the powders. A linear relationship between the heat-evolution from a mix of two different particle size gradations and the weighted mean of the heat-evolution measured from individual gradations was observed (Figure 6. 4). Furthermore, the observed slope of this relationship is 1, indicating that the nucleation and growth process can be modelled as linear addition of the reaction of individual particles. More work is required to understand if the overall reaction during the diffusion-controlled regime can be modelled as a sum of the hydration of individual particle sizes.
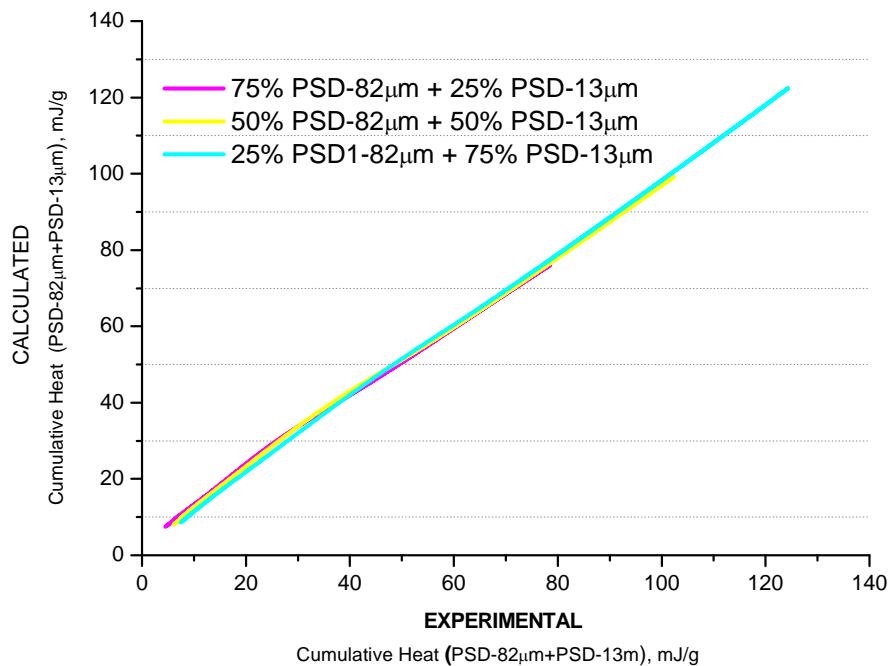

Figure 6. 4: Plot of the experimental cumulative heat for the mixture of two different gradations against the calculated cumulative heat

Using the model μic, the data obtained from various particle size distributions has been used to further study the hydration kinetics of cement [5].

6.1.2 Development of C₃S Pastes: Development of C-S-H

The investigation of the microstructural development of C₃S pastes at later ages has shown to be little poorly affected by the initial particle size of the powder (Chapter 4). All gradations form the same type of hydration products and with similar morphology.

In general, the C-S-H morphology is the same regardless the particle size of the grains. An example of the C-S-H morphology is illustrated in Figure 6. 5. Outer C-S-H forms earlier in a fibrillar and directional morphology as described in Chapter 5. Inner C-S-H is densely packed and homogeneously distributed [6]. However, the layer is much thicker for bigger particles as a consequence of their lower specific surface area for C-S-H formation leading thicker shells.
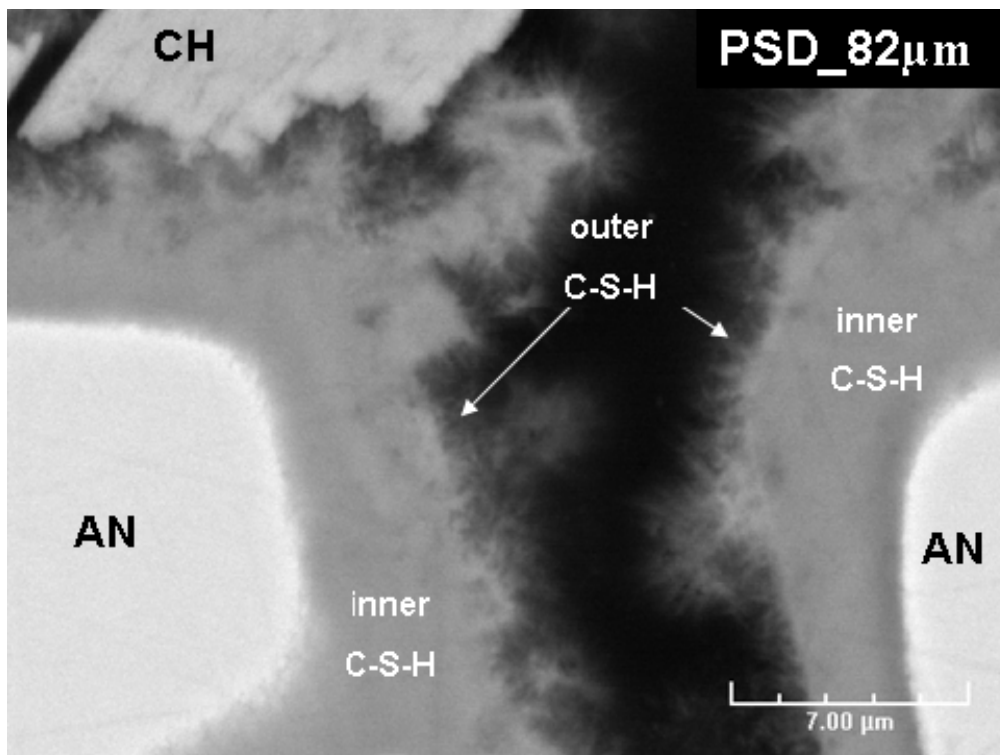

Figure 6. 5: BSE images of tricalcium PSD-82μm after 28 days of hydration

However, slight differences were observed concerning the density of C-S-H and the capillary porosity of the different pastes of C_3S. An increase of the bulk density and an increase of the capillary porosities were observed for smaller particle size distributions at the same degree of hydration.

Density measurements indicate a slight difference between the smaller fraction (PSD-6μm/pure C_3S) and, for instance, the larger PSD-33μm/Alite fraction. Higher values of density were found for smaller gradations. Corresponding to these differences in density, the capillary porosities measured for the small C_3S fraction was observed to be higher at the same degree of hydration. The dotted line corresponds to the theoretical evolution of the porosity upon hydration using the values of density, molar mass and molar ratio shown in Table 4. 3.
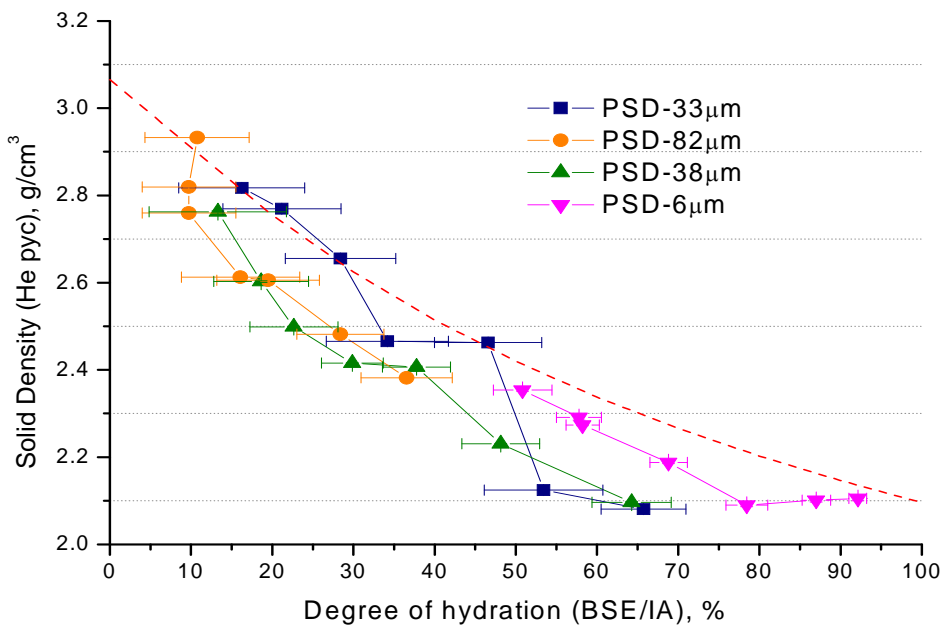

Figure 6. 6: Porosity (BSE/IA) versus degree of hydration of different particle size distributions
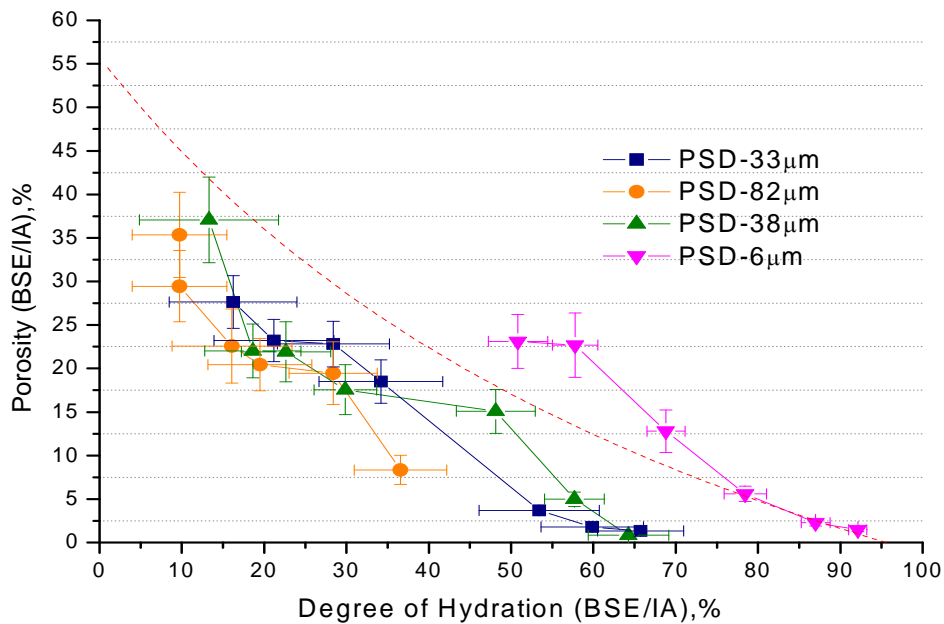
Figure 6. 7: Solid density (He pycnometry) versus degree of hydration (BSE/IA) for the PSD33µm, PSD-82µm, PSD-38µm and PSD-6µm pastes

One hypothesis for explaining these differences could be related to differences in initial pore space available for product deposition. Smaller grains are more closely packed or distributed so that the available space for product deposition is more confined. Therefore, the C-S-H would grow more closely packed leading to higher values of C-S-H density and consequently higher capillary porosity for the smallest gradations.

In order to have a better understanding of what causes the differences found in the capillary porosity and the bulk density, parameters such as the composition, the chemical water and the space between inter-fibrils of C-S-H were investigated in Chapter 5. Both, the mineralogy and the chemically bound water in C-S-H were found to be very similar independent of the particle size. Therefore, the differences in density may come from differences in the packing of C-S-H sheets. Nitrogen adsorption measurements made on different gradations of tricalcium silicate revealed higher values of surface area (as shown for capillary porosity by BSE/IA) and greater fraction of smaller pores for the smallest particle size distribution. The comparison of cumulative pore volume versus pore width of two different gradations of tricalcium silicate (at 50% of hydration degree) is given in Figure 6. 8. In smaller particles, due to the more confined space available for product deposition, the C-S-H fibrils may grow much closely packed leading to higher bulk-

densities of the product and therefore higher capillary porosities. However, from these experiments is no possible to confirm if the differences found in the C-S-H density are due to different arrangement of outer C-S-H fibril. It is not clear how much the N_2 is capable to penetrate in the C-S-H and how much the drying of the sample has damaged the C-S-H structure.
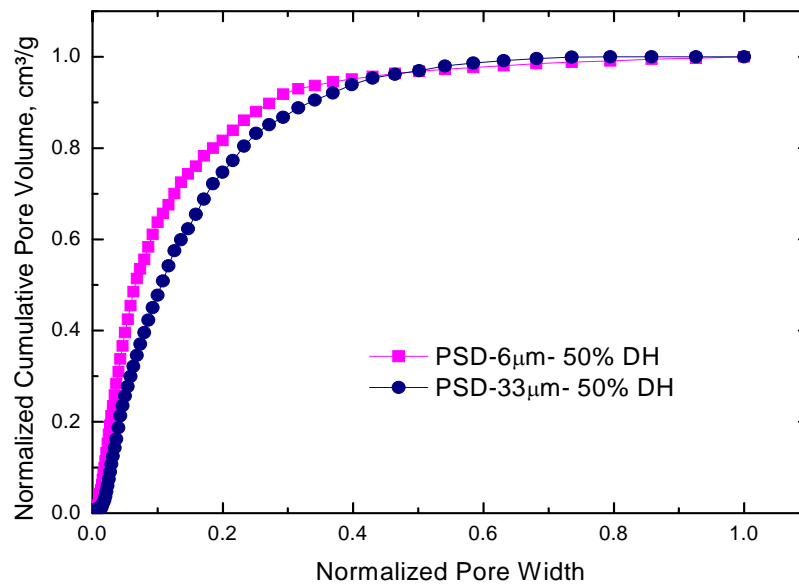

Figure 6. 8: Comparison of cumulative pore volume versus pore width of two different gradations (PSD-33 μm and PSD-6 μm) of tricalcium silicate (50% of hydration degree)

6.2 Conclusions

- The hydration kinetics of tricalcium silicate were found to be dependent on the initial particle and/or defect concentration of the grains. Smaller particles release more heat, have higher dissolution peaks and go into the nucleation and growth process much earlier. In addition, the hydration kinetics of multi-sized system during the nucleation and growth period can be modelled as the linear addition of individual particles.

- The microstructural development of the different gradations was found to be, in general, the same independent of the initial particle size of the gradations, forming the same hydration product features: C-S-H and portlandite. A preferential

reaction on the surface of the grains was observed for all particle sizes. Slight differences in the capillary porosity, C-S-H density and space between outer C-S-H fibrils were observed. Smaller particles give higher values of capillary porosity, solid density and shorter distances between C-S-H fibrils, as measured by N_2 adsorption.

6.3 Future Work

- This thesis work has shown that the particle size and/or the density of crystallographic defects could have a big impact on the different hydration steps of tricalcium silicate pastes. However, more work has to be carried out in order to better correlate the number of crystallographic defects and the surface area of the grains.

- In the same line, to have a better understanding of the interaction of changes in the lattice parameters of C_3S, caused by a combination of different foreign oxides such as Al and Mg, as used in this study, and changes in hydration reactivity would be a very powerful tool to predict the reactivity of cement.

- It was demonstrated that the nucleation and growth process can be modelled as the linear addition of individual particle size gradations. Although, the investigation of the interaction of particles in a system of three or more different narrow particle size distributions could provide more insight into the process.

- NMR studies would be helpful in for the investigation of possible differences in the structure of C-S-H from different particle size gradations of tricalcium silicate.

REFERENCES

[1] J.N. Maycock, J. Skalny and R.Kalyoncu, Crystal defects and hydration. I. Influence of lattice defects, Cement and Concrete Research 4 (1974) pp. 835-847

[2] Mathur, P.C., Study of Cementitious Materials using Transmission Electron Microscopy, Ph. D Thesis École Polytechnique Fédéral de Lausanne (2007)

[3] Brown, P.W., Pommersheim, J. And Frohnsdorff, G. (1985) Cem. Concr. Res. 15, 35

[4] Denis Damidot, André Nonat and Pierre Barret, Kinetics of Tricalcium Silicate Hydration in Diluted Suspensions by Microcalorimetric Measurements, J. Am. Ceram. Soc. 73 (1990) pp. 3319-3322

[5]Shashank Bishnoi, Vector modelling of hydrating cement microstructure and kinetics, Ph. D Thesis École Polytechnique Fédéral de Lausanne (2008)

[6] I.G. Richardson, The nature of C-S-H in hardened cement, Cem. Concr. Res. 29 (1999) pp. 1131-1147

APPENDIX I

Development of the measuring protocol for Chemical Shrinkage

Several amounts of alite pastes were tested with both the erlenmeyer and cylindrical flasks in order to assess the effect of the sample's thickness on the evolution of chemical shrinkage (Figure I. I). In this figure, curves were normalised to 100 g of paste and show, as mentioned by Boivin [1] that the higher the volume of paste, the lower the chemical shrinkage. However, unexpectedly, the measured chemical shrinkages were systematically lower in the case of erlenmeyer flasks.
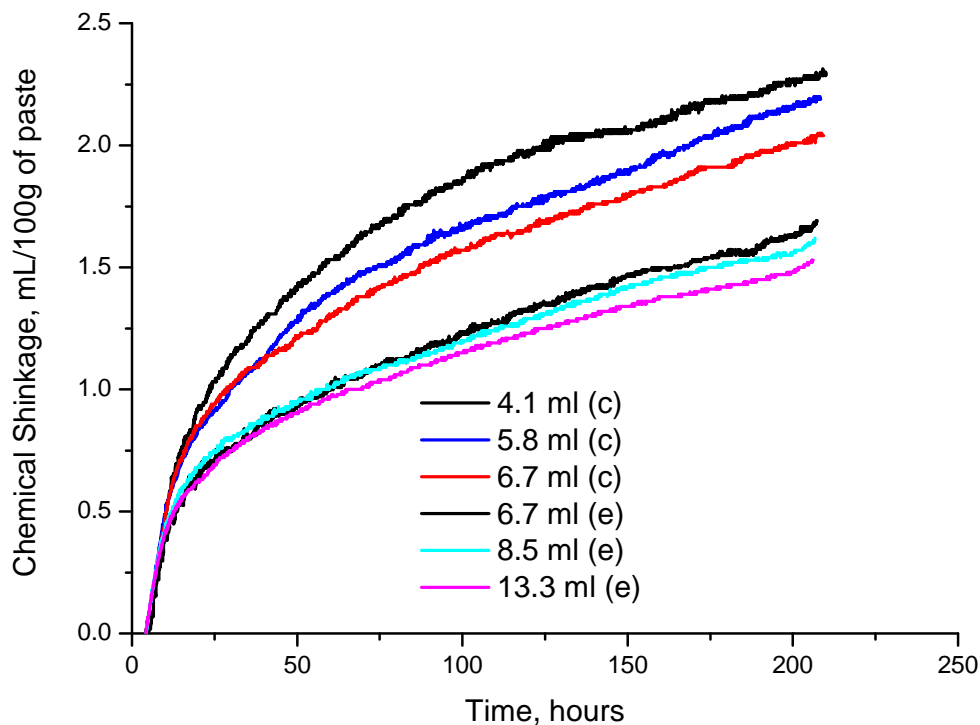
Figure I. I: Comparison of the chemical shrinkage for different volumes of alite pastes measured in cylindrical and erlenmeyer flask.
- (c): cylindrical flask
- (e): erlenmeyer flask

Figure I. II shows the chemical shrinkage curves for 6.7ml alite pastes in cylindrical and erlenmeyer flasks. The volume reduction was the same during the first 10 to 15 hours but became much higher in the cylindrical flask afterward [2]. Boivin [1] observed the same

behaviour and related it to a higher amount of air voids (bubbles) entrapped in the thicker samples (i.e. cylindrical). In the present case, special care was taken to avoid this artefact and examination of specimen cross-sections did not showed any difference. Boivin [1] based her conclusions in the study on the cross-sections of the pastes at a magnification of x10, not accuracy enough like for stating that is the presence of more bubbles in the thicker paste is there reason of having higher values of shrinkage. In Figure I. II, the difference in chemical shrinkage is 0.25 ml/100g after 200 hours i.e. 0.5 vol. % of the paste (corresponding to thousand bubbles of 200 μm size in the paste). Then, there is not possible that this difference in shrinkage could be explained by higher number of bubbles in samples hydrated in cylindrical flask.
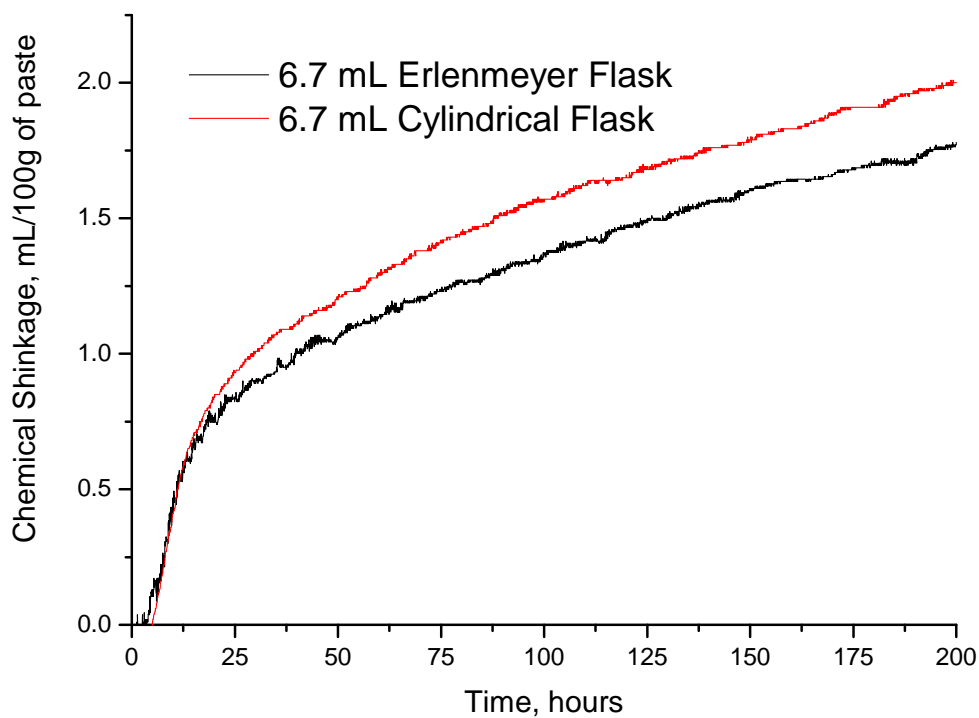

Figure I. II: Comparison of the chemical shrinkage for alite pastes measured by using cylindrical and erlenmeyer flask.

Another possible hypothesis that could explain the differences in shrinkage is the quantity of water that is added on the pastes for the measure. In the case of using erlenmeyer flask, the amount of water that is added is much higher that in the case of cylindrical (~6 times more). Another inconvenience in the case of using erlenmeyer flask is attributed to the fact that high surface of paste are in contact with water (before setting time) and in

consequence high amounts of Ca^{2+} ions go rapidly into solution. Massive precipitation of portlandite takes place preferentially on this surface. EDS and XRD analysis made on the surface in contact with water confirms high concentration of CH. An secondary electron image showing the portlandite crystal is given in Figure I. III. Figure I. IV shows the surface of an alite paste which has been in contact with water during the measurement in a erlenmeyer flask where it is show that there are big crystals of calcium hydroxide with its characteristically hexagonal shape. However, when cylindrical flasks is used the dilution effect on the paste is reduced while filling up the flak with water and therefore the shrinkage would be expected to work better at early ages, before the setting time.
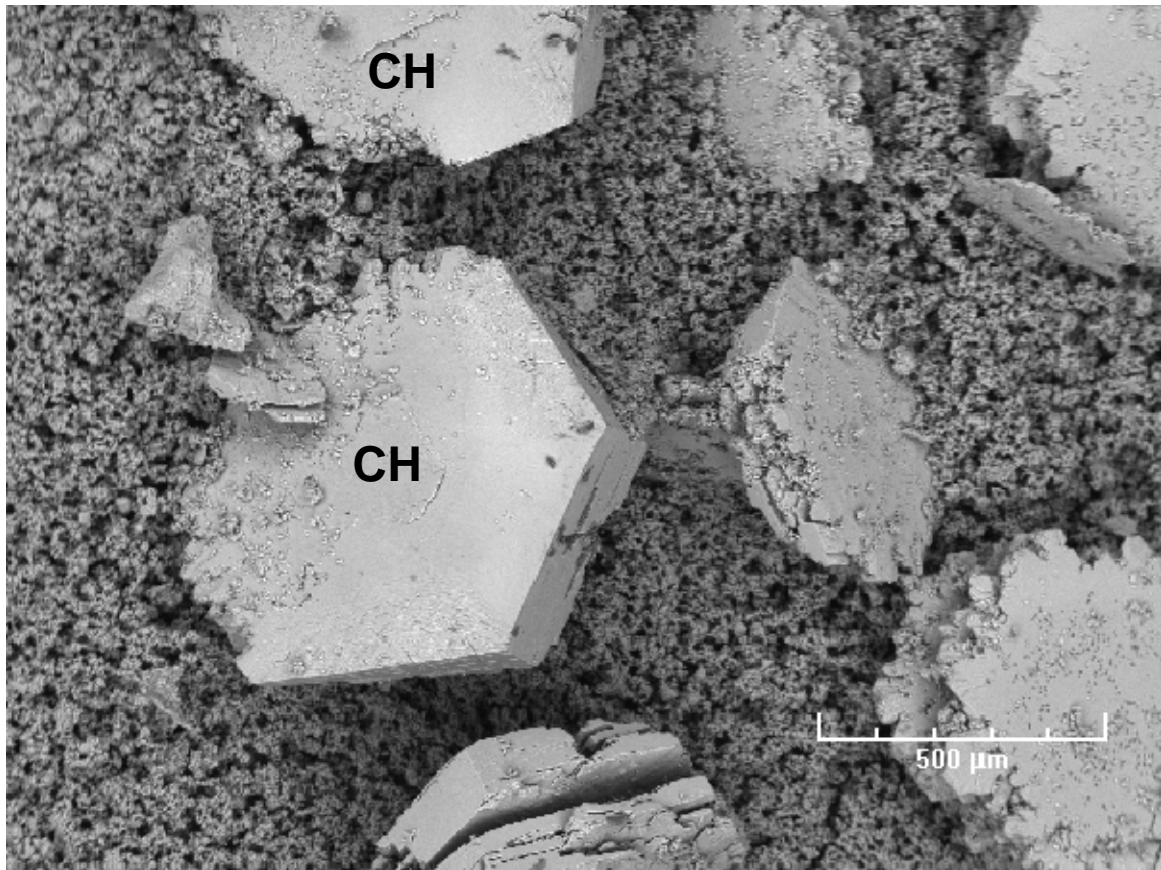

Figure I. III: SEM image an alite paste at the surface in contact with water during the measure of chemical shrinkage in a erlenmeyer flaks putting in evidence the presence of big crystals of CH on the surface in contact with water

Figure I. IV: Surface in contact with water of the alite at 28 days of chemical shrinkage measurement (in an erlenmeyer flask)

To access the influence of dilution on the shrinkage two alite pastes were mixed in the same conditions (as previously reported) and let to set for 24 hours in sealed containers. After 24 hours, one of the pastes was ground and place in an erlenmeyer flask and the other was let in the same erlenmeyer flask where was set. Water was added very carefully on the top of the ground paste and the chemical shrinkage was started to record after 24 hours. The chemical shrinkage of this pastes are compared in Figure I. V. with the chemical shrinkage obtained using cylindrical and erlenmeyer flask.
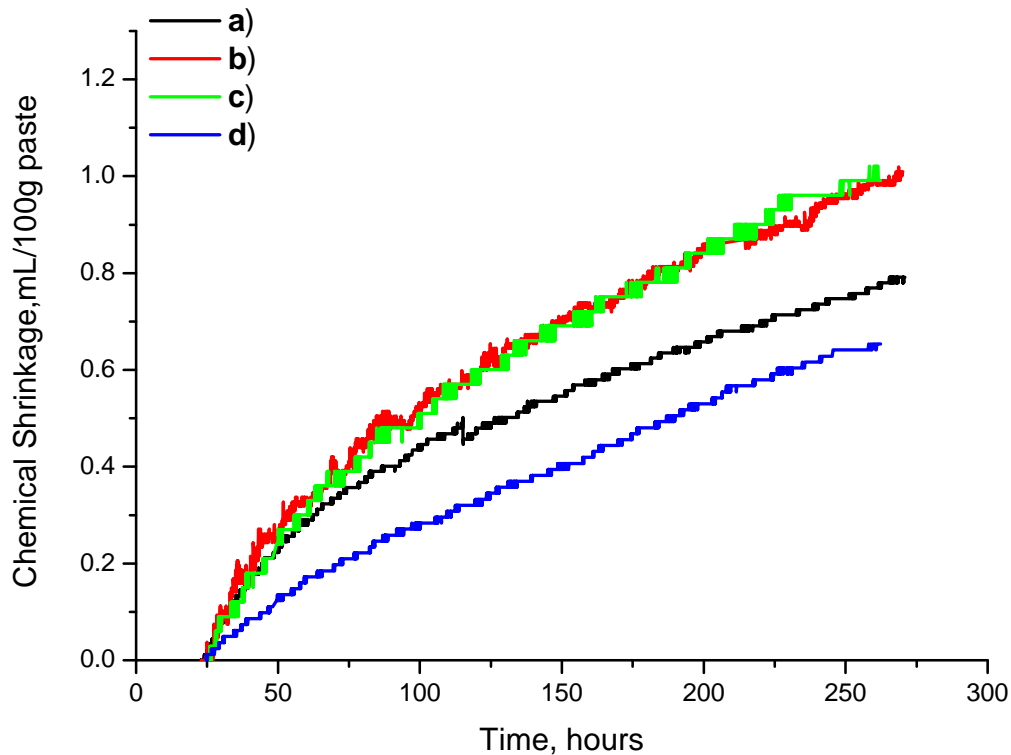
Figure I. V: Evolution of the chemical shrinkage curves of:
  a) alite pastes casted in a erlenmeyer flask
  b) alite paste casted in a cylindrical flask
  c) set ground alite paste measured after 24 hours in a erlenmeyer flak
  d) set alite paste measured after 24 hours in a erlenmeyer flak

The fact that the measured values of chemical shrinkage of an alite pastes that it was placed in a cylindrical flask (b) is equal to the shrinkage of a ground paste (c) leads to think that the thickness of the paste in the cylindrical paste is not a limiting factor in the measure of shrinkage. In this study, the thickness of the alite paste in the cylindrical tubes is not large enough for preventing the diffusion of water through the paste.

These results confirm that chemical shrinkage measured using cylindrical flasks give more reliable results than in the case of using erlenmeyer flask.

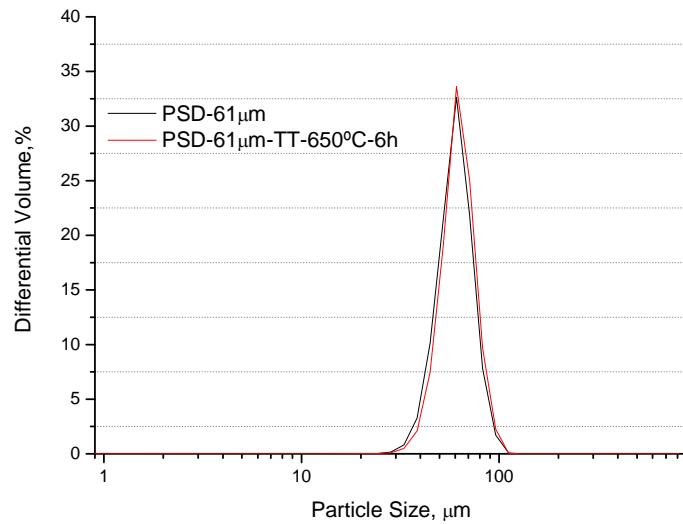## **Thermically treated powders**

a) PSD-61µm

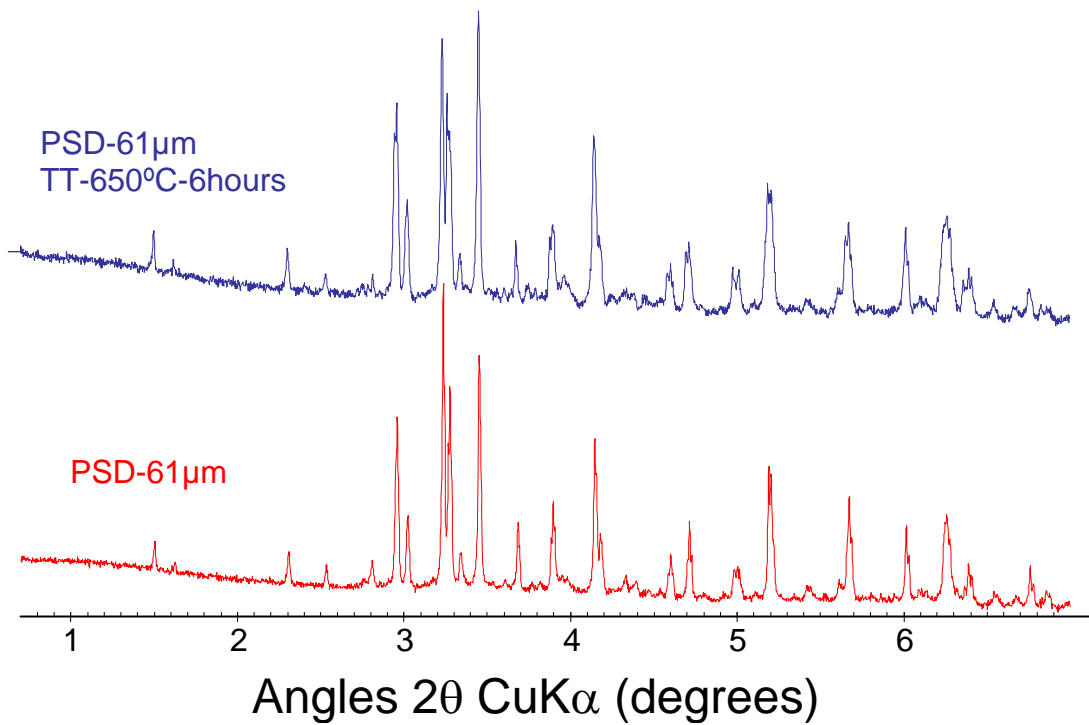Figure I. VI: Particle size distribution of PSD-61m before and after treated thermically

Figure I. VII: Powder X-ray diffraction patterns of PSD-61µm before and after treated thermically
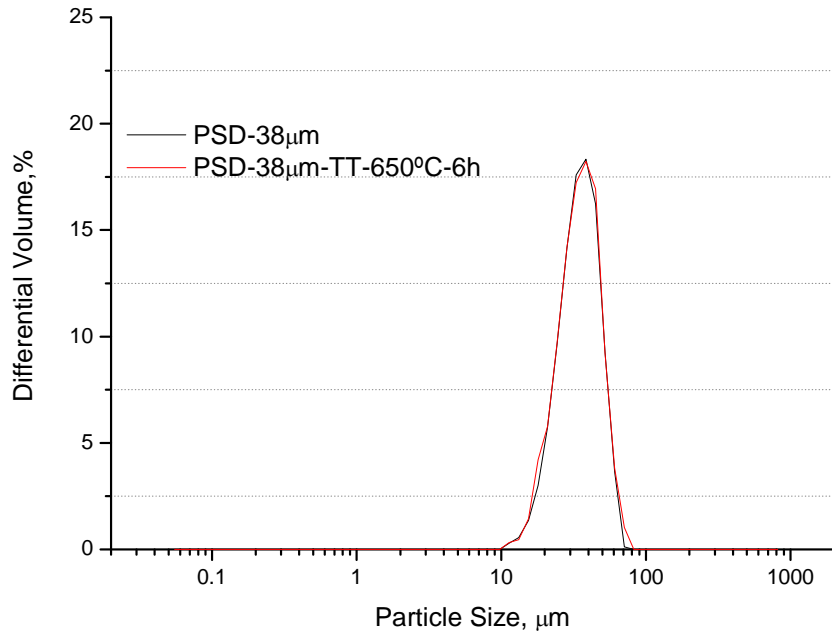
b) PSD-38μm

Figure I. VIII: Particle size distribution of PSD-38m before and after treated thermically
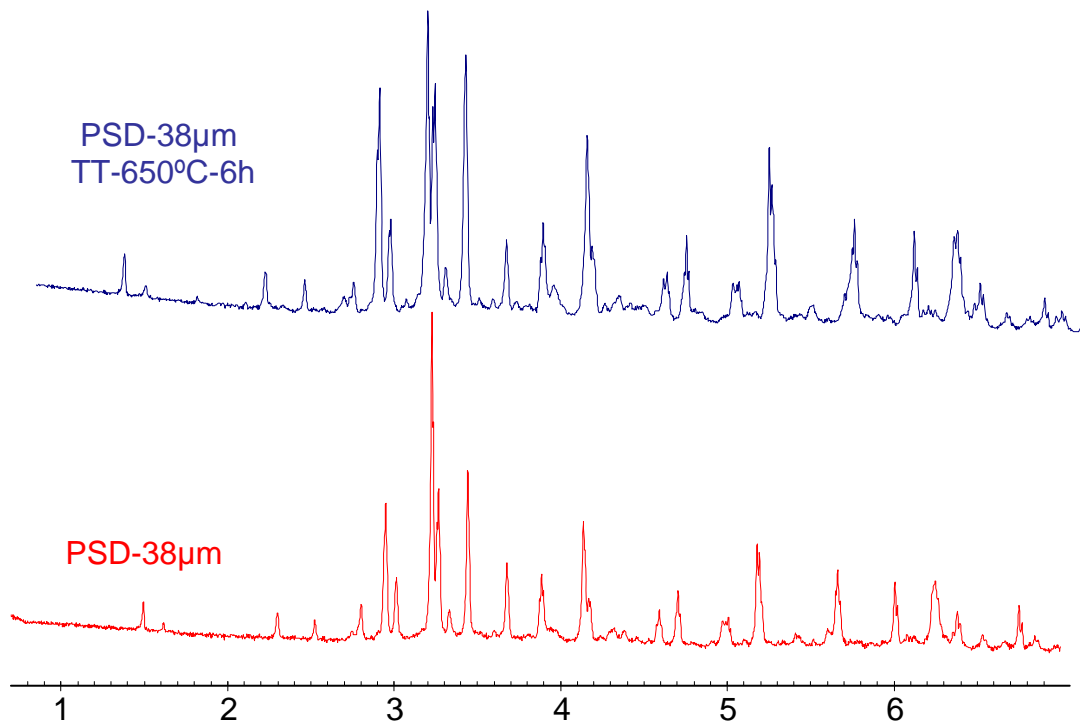

Figure I. IX:Powder X-ray diffraction patterns of PSD-38μm before and after treated thermically

APPENDIX II

The quantification of CH by X-ray diffraction was made through the angular range of 7 to 70º 2θ with an interval step of 0.017º and an active length of 120s. The amorphous content was calculated from the apparent content of the internal standard (Al_2O_3) [3].

Mass balance calculations were made assuming H/S of 4 and Ca/Si of 1.7 in C-S-H (Ca/Si for the different gradations was preferentially calculated and detailed in Chapter 5). The H/S ratio has an approximate value of 4 in case of saturated pastes and the Ca/Si ratio in C-S-H has been found to range 1.7 to 1.8 in C_3S pastes [4, 5]. The stoichiometry used for the mass balance calculation is the following:

$$C_3S + 5.3H \rightarrow C_{1.7}SH_4 + 1.3CH \qquad \text{Eq. II.1}$$
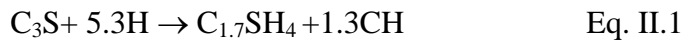
Thermogravimetrical analysis were carried out in the 25-900ºC temperature range with a heating rate of 10ºC/min in a nitrogen atmosphere, with a Thermogravimetric Analyzer TGA/DSC1 from Mettler Toledo. The percentage of calcium carbonate has been taken into account in the calculation of CH.

An example of DTG/TGA analysis of a cement paste is shown in Figure II.I where mass losses are generally assumed as being due to:

- 25-415: part of the bound water in C-S-H escapes (in our case, not free water should be remaining after solvent exchange with isopropanol)
- 415-525: dehydroxylation of CH
- Above 525: is a combination between the decarbonation of calcium carbonate (product of the carbonation of the sample partly during the cutting process or during the storage) and part of the bound water.
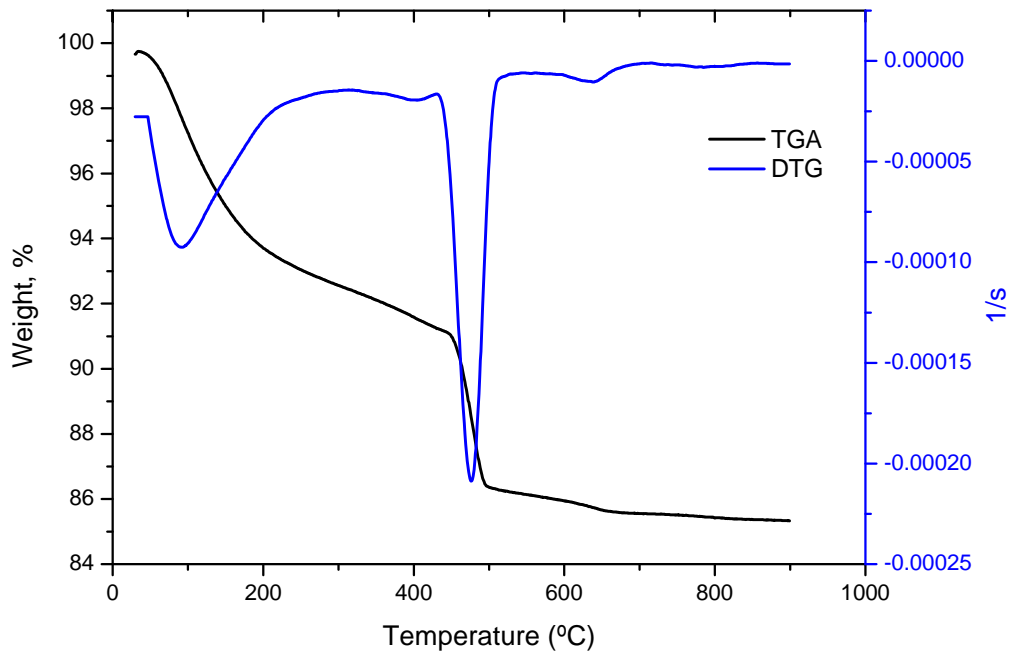
Figure II.I: Typical Thermogravimetrical Analysis curve found for cement pastes

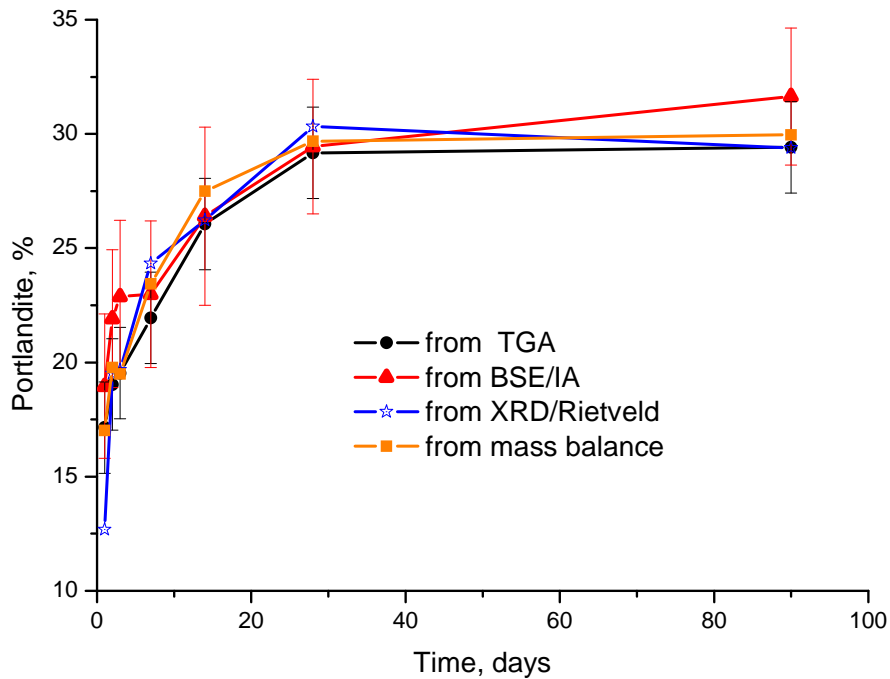Figure II.II illustrates the good agreement is observed between all approaches (PSD-6µm).

Figure II.II: Good agreement for the calculation of the portlandite % between all approaches (PSD-6µm)

APPENDIX III

Choice of Model for Pore Size Analysis

The pore size distribution of the montmorillonite and the synthesized C-S-H were investigated using both the Classical and DFT methods for slit-shaped pores. From the analysis of accuracy of the fit (Figure III.I) is concluded that the DFT methods fit better, especially at low partial pressures. Classical models fail at very low partial pressures due to the limitation of the Kelvin equation assumptions leading to an overestimation of pores at that range. However, on the other hand the DFT method makes much accurate assumptions and practically overcomes these limits with modern mathematics and is the only method available that can realistically analyze a broad pore size distribution ranging from 0.4 to 100 nm in porosity [6].
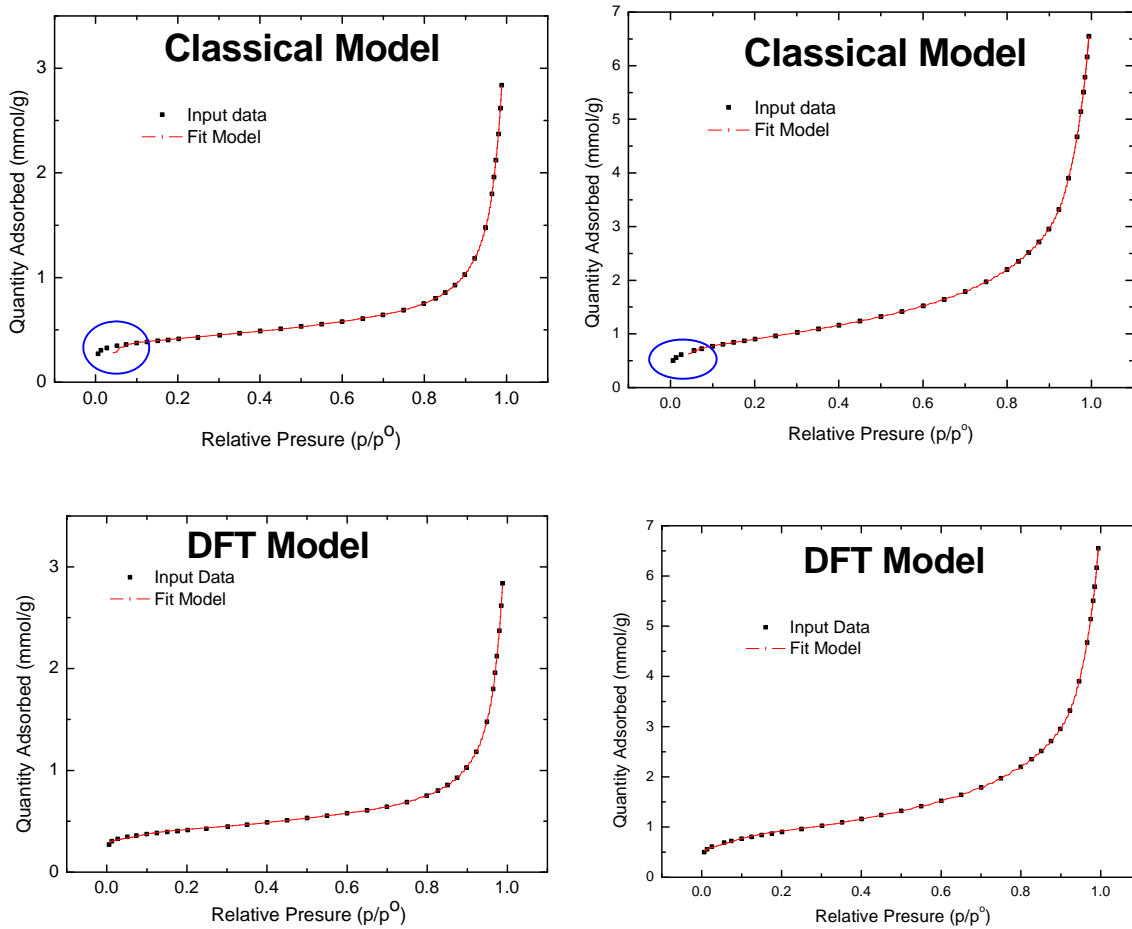
Figure III.I: Goodness of fit graph for Montmorillonite (left) and synthesized C-S-H (right) using Classical and DFT methods for slit-shaped pores

This is overestimation of the microporosity while using the classical methods is clearly seen when the normalized cumulative pore volume calculated by DFT and classical methods versus the pore width are compared. An example of this is shown in Figure III.II for the case of the synthesized C-S-H.
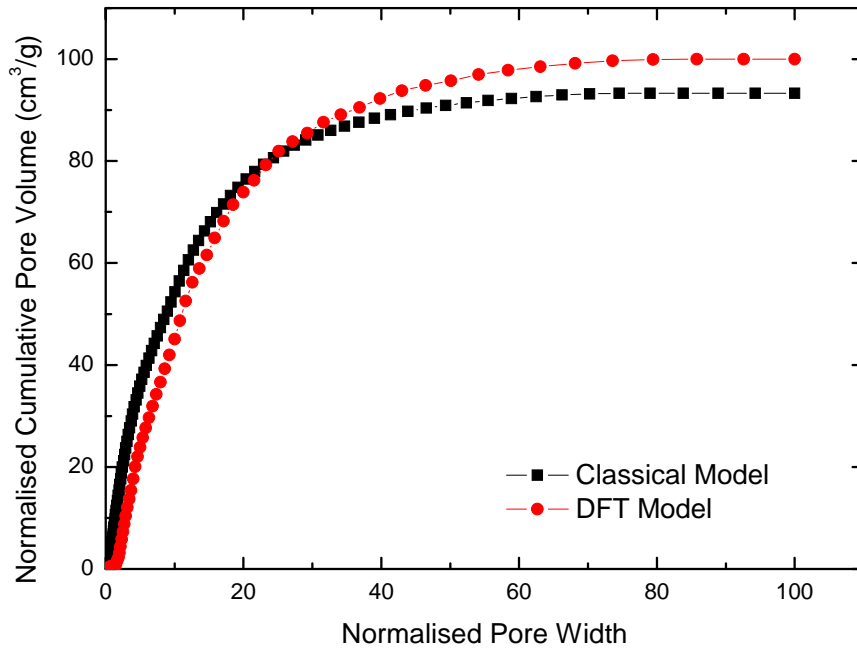
Figure III.II: Normalized cumulative pore volume versus the pore size for synthesized C-S-H

REFERENCES

[1] S. Garcia-Boivin, Retrait au jeune âge du béton développment d'une méthode expérimental et contribution à l'analyse physique du retrait endogène, PhD Thesis, École nationale des Ponts et Chaussées, France (1999)

[2] M. Geiker, Studies of Portland Cement Hydration: Measurements of Chemical Shrinkage and a Systematic Evaluation of Hydration Curves by Means of the Dispersion Model. Ph. D. Thesis Technical University of Denmark (1983)

 [3] Scrivener K.L., Füllmann T., Gallucci E., Walenta G., Bermejo E., Quantitative study of Portland cement hydration by X-ray diffraction/Rietveld analysis and independent methods, Cement and Concrete Research 34 (2004) p.1141-1547

[4] H.F.Taylor, Chement chemistry, Tomas Helford, London 1997

[5] Richardson I.G., The nature of the hydration products in hardened cement pastes, Cement and Concrete Composites 22 (2000) p.97-113

[6] Paul A. Webb and Clyde Orr "Analytical Methods in Fine Particle Technology", Micromeritics Instrument Corporation, 1997, pp.81

Curriculum Vitae

Mercedes COSTOYA

Date and Place of Birth: 6 June 1979, Spain
Nationality: Spanish
Marital Status: married
Email: mercedes.costoya@gmail.com

EDUCATION

2005-2008: PhD Laboratory of Construction Materials, EPFL-Switzerland

2003-2005: MSc in Chemical Engineering, Vigo University -Spain

2004: Master in **"Quality** :ISO 9001:2000, ISO 17025:1999, AIMEN, Spain

2004: Master in **"Environmental Management"**: ISO 14001:2000, AIMEN, Spain

2004: Master in **"Accident Prevention at Work"**, AIMEN, Spain

1997-2002: **BSc in Chemical Engineering**, Vigo University, Spain

WORK EXPERIENCES

From 2005: PhD. Assistant in Material Sciences, Laboratory of Construction Materials, École Polytechnique Fédérale de Lausanne (EPFL), Switzerland
2003-2004: Researcher in the Department of Chemical Engineering and the Department of Materials in the Faculty of Engineers at Vigo University.

TECHNICAL COMPETENCES
Scanning Electron Microscopy (SEM/EDS), Transmision Electron Microscopy (TEM), X-ray Driffraction (XRD), Thermogravimetrical Analysis (TGA), Isothermal Calorimetry, Chemical Shinkage, Helium pycnometry, Granulometry Laser Analysis, Surface Area (BET and Blaine), Gas Adsoption (nitrogen), Mercury Intrusion Porosimetry (MIP), Impedance Spectroscopy, Contact Angle in Mercury Intrusion Porosimetry, etc.

LANGUAGES
Spanish : Mother tongue
Galician : Mother tongue
English: Speak, read and write (High Level)
French : Speak, read and write (Medium Level)
Portuguese : Speak, read and write(Fluent)

INTERESTS
Writing, reading and listening music
Excursions and sports
Traveling